
306318775/

STATISTICAL MECHANICS OF FLUIDS

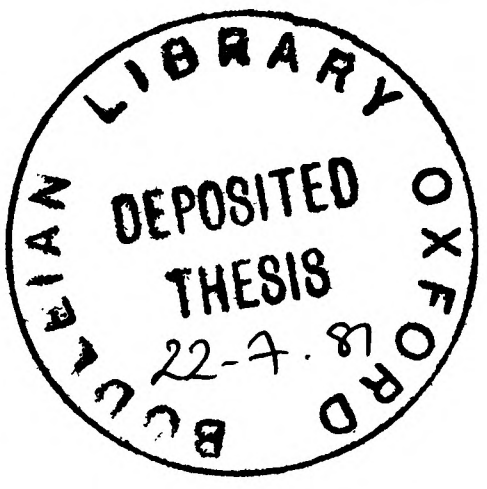
ABSTRACT

of a thesis for the Degree of Doctor of Philosophy

in the University of Oxford

by

E.S. Severin



St Catherine's College
Physical Chemistry Laboratory.

May 1981

ABSTRACT

The statistical mechanics of the interfacial region is studied using the Monte Carlo and molecular dynamics simulation techniques.

The penetrable-sphere model of the liquid/vapour interface is simulated using the Monte Carlo method. The pressure equation of state is calculated in the one-phase region and compared to analytic virial expansions of the system. Density profiles of the gas/liquid surface in the two-phase region are calculated and are compared to profiles solved in the mean-field approximation. The effect of the profile near a hard wall is investigated and as a consequence the theory is modified to account for a hard wall. The theory agrees well with the computer result. This is a simple model for adsorption of a gas at a solid surface.

A model for methane adsorbed on graphite is proposed. A number of simplifying assumptions are made. The surface is assumed to be perfectly smooth and rigid, and quantum effects are neglected. An effective site-site pair potential for the methane-graphite interaction is adjusted to fit the rotational barriers at 0K.

The isosteric enthalpy at zero coverage is predicted in the range 0K to 200K, by averaging the configurational energy during a molecular dynamics simulation of one methane molecule. The surface second virial coefficients are calculated in the range 225K to 300K and agree with the experimental measurements. The effective pairwise potential predicts the height of the monolayer above the surface and the vibrational frequency against the surface. The translational and rotational behaviour of a single methane molecule are examined.

Solid $\sqrt{3} \times \sqrt{3}$ epitaxial methane is studied at a constant coverage of $\theta = 0.87$ by molecular dynamics simulation. The specific heat and configurational energy are monitored. A slow phase transition occurs between 0K and 30K and a sharp transition is observed at 90K. Calculation of the centre-centre distribution functions and order parameters indicates the first transition is due to a slow rotational phase change. At 90K some molecules evaporate from the surface and the remaining bound molecules relax into a 2-d liquid. Between 10K and 25K the adsorbed methane floats across the surface and the question remains open whether this phenomenon is an artifact of the model system or does occur in nature.

The dynamical behaviour of adsorbed methane is compared to incoherent inelastic neutron scattering. The principal peaks in the self part of the incoherent structure factor $S_s(0,\omega)$ should correspond to the peaks in the Fourier transforms of the velocity and angular velocity auto-correlation functions. The peaks calculated from the Fourier transform of the auto-correlation functions agree with all the assignments in the experiments.

The reorientational motion in the monolayer is monitored and the reorientational auto-correlation functions characterize the slow phase transition from 11K to 30K. Three methane molecules are scattered on top of the $\theta = 0.87$ monolayer at 30K. Reorientational correlation functions are compared for the single adsorbed molecule, the monolayer and a few particles in the bilayer. Rotation is less hindered in the monolayer than for a single adsorbed molecule and least hindered in the second layer.

Adsorbed methane is studied at coverages of $\theta < 0.87$ over a wide range of temperature in order to unravel various conflicting solid and liquid phases predicted by experiment. By careful monitoring of the structure via changes in the specific heat, the distribution functions and order parameters a liquid/gas coexistence is not observed in the region 56K to 75K. This result is confirmed by calculating the self diffusion coefficients over two isotherms at 65K and 95K. The diffusion coefficients decrease with increasing coverage over both isotherms. If liquid and gas coexist the diffusion coefficient should not change with increasing coverage.

The statistical mechanical expression for the spreading pressure of an adsorbed fluid is derived and reported over a wide range of temperature and coverage. Experimental techniques are not as yet sufficiently highly developed to measure this quantity directly.

An expression for the coherent neutron scattering structure factor for a model of liquid benzene adsorbed on graphite is derived. This expression is a function of the 2-dimensional centre-centre distribution function and we solve the Ornstein-Zernike equation in the Percus-Yevick approximation to obtain the 2-d distribution functions for hard discs. Agreement with present experimental results is reasonable, but a more highly orientated substrate needs to be used in experiment before a more exact comparison can be made.

STATISTICAL MECHANICS OF FLUIDS

A Thesis submitted for the Degree

of

Doctor of Philosophy

in the

University of Oxford

by

Emery Stephen Severin

St Catherine's College
Physical Chemistry Laboratory

May 1981

ACKNOWLEDGEMENTS

I wish to thank Professor John S. Rowlinson for the opportunity to study in his group and for his expert supervision over the past three years. (Professor Rowlinson extended the analytic theory to the mean field profile of the penetrable sphere model near a hard wall). I am greatly indebted to Dr. Dominic J. Tildesley for his continual interest and guidance throughout the years, and without whom the formulation of much of this work would not have been possible.

I would also like to thank Dr. R.K. Thomas and Dr. T. Rayment for many helpful discussions about the experimental aspects of the adsorption problem and for Dr. Thomas's permission to reproduce an unpublished experimental diffraction pattern in this work (Figure 6.5). I also thank many colleagues in the Physical Chemistry Laboratory for their help during the preparation of this thesis especially Steve Hemingway and Andy Laughton for performing the arduous task of proof reading. I extend much gratitude to Frankie for her very capable typing.

Finally I wish to thank the Rhodes Trust for a scholarship to attend Oxford and for the Australian Army in allowing me complete freedom in the pursuit of this degree.

Contents

	Page
Acknowledgements	i
Contents	ii
List of Figures and Tables	v
List of Principal Symbols	ix
CHAPTER 1 - Introduction	
1.1 Monte Carlo and Molecular Dynamics - a brief history	1
1.2 The Gas/Solid Potential	12
1.3 Experimental Measurements on the Gas/Solid Surface	17
Thermodynamic Measurements	20
Structural Measurements	21
Dynamical Measurements	24
1.4 What is to follow	26
CHAPTER 2 - Monte-Carlo Simulation of the Gas-Liquid Interface of the Penetrable-Sphere Model	
2.1 Introduction	30
2.2 The Models	33
The grand partition function.	34
The phase diagram of the two component system.	38
Thermodynamic functions in the mean-field approximation.	40
2.3 The Monte-Carlo Method	47
The Monte-Carlo program.	53
2.4 Simulation of the Penetrable-Sphere Model in the One Phase Region.	56
2.5 Simulation in the Two Phase Region.	63

CHAPTER 3 - A Methane Molecule Adsorbed on Graphite — Page

3.1 Introduction. 69

3.2 The Simulation. 72

3.3 The Potential Model. 83

3.4 The Potential Parameters of the Methane-Surface Interaction

The initial guesses. 95
The rotational barriers. 101
Isosteric enthalpy at zero coverage. 107
Surface second virial coefficient. 112

3.5 Some Properties of the Model. 119

CHAPTER 4 - Solid Methane Adsorbed on Graphite

4.1 Introduction - The Phase Diagram. 132

4.2 The Simulation and Thermodynamic Properties. 138

4.3 Translational Order and Structure of the Adsorbed Methane 148

The Dynamical Behaviour of the Monolayer. 159

4.4 Orientational Behaviour of the Adsorbed Methane. 170

4.5 Orientational Behaviour in the Bilayer. 177

CHAPTER 5 - Liquid Methane Adsorbed on Graphite

5.1 Introduction. 182

5.2 Thermodynamics and Structure. 185

5.3 Translation Across the Surface - the Diffusion Coefficient. 197

5.4 The Spreading Pressure 218

CHAPTER 6 - The Structure Factor of Benzene Adsorbed on Graphite	Page
6.1 Introduction - Theory.	227
6.2 Solution to the PY Approximation for Hard Discs.	235
6.3 Structure Factor for a Molecular Liquid in the Free Rotation Limit.	239
6.4 Results and Discussion.	248
CHAPTER 7 - SUMMARY	253
APPENDIX A - Listings of Computer Programs on Microfilm.	262
Bibliography	263

List of Figures and Tables

Figures

		Page
1.1	A graphite lattice.	16
1.2	Schematic first layer adsorption isotherm.	20
2.1	Phase diagram of the binary primitive system of the penetrable-sphere model.	39
2.2	Surface density profiles of the penetrable sphere model in the mean field approximation.	48
2.3	g(r) for a system of hard spheres at $\rho^* = 0.7071$.	57
2.4	An instantaneous plot of a configuration at $\rho_a = \rho_b = 0.8$.	60
2.5	$g_{ab}(r)$ at densities $\rho_a = \rho_b = 0.7$, 0.8, and 0.9.	61
2.6	Sketches of starting configurations for simulation in the two phase region.	64
2.7	Density profile at an overall density of $\rho_a = 2.0$.	66
2.8	Density profile at an overall density of $\rho_a = 2.4$.	67
3.1	Plan of the basic simulation cell and graphite surface.	73
3.2	Flow diagram of molecular dynamics program.	82
3.3	Potential models for methane adsorbed on graphite.	85
3.4	Comparison of two potential models.	93
3.5	The methane-surface potential as a function of the methane orientation.	94
3.6	Potential energy curve resulting from translation of methane across the surface at a fixed height.	96-98
3.7	Comparison of Williams and Lennard-Jones site-site potentials.	102-103
3.8	$\sqrt{3} \times \sqrt{3}$ epitaxial structure and the barrier to the h_4 rotation.	105
3.9	The barrier to the h rotation.	106
3.10	Isosteric enthalpy at zero coverage compared to experiment.	108
3.11 – 3.13	Translation of a methane molecule across the surface at T = 19.8, 53.4 and 108K.	121-123

		Page
3.14	Vibration of methane against the surface.	125
3.15	Single particle reorientational correlation function, $C^{\perp}(t)$, over a wide range of temperature.	129
3.16	Single particle reorientational correlation function, $C^{''}(t)$, compared to a 2-d free rotor.	131
4.1	A phase diagram of methane adsorbed on graphite at sub-monolayer coverages.	134-135
4.2	Configurational energy and specific heat at $\theta = 0.87$ over a range of temperature, $10 < T < 130$ kelvin.	144
4.3	Distribution of molecular centres for an adsorbed $\sqrt{3} \times \sqrt{3}$ monolayer.	150
4.4	An instantaneous configuration at $\theta = 0.87$, T = 127.2K.	153
4.5	Trajectories of the centre of mass of methane at $\theta = 0.87$, T = 19.8K and 51.8K.	156-157
4.6	Average distribution of molecular heights above the surface.	160
4.7	The velocity auto-correlation functions of the centre of mass of the adsorbed solid, $\theta = 0.87$, T = 19.8K.	164-166
4.8	The velocity auto-correlation functions at T = 51.8K.	168-169
4.9	Reorientational auto-correlation functions of the adsorbed solid perpendicular to the surface, $C^{\perp}(t)$ and parallel to the surface, $C^{\parallel}(t)$.	172-173
4.10	Angular velocity auto-correlation function at 19.8K.	175
4.11	Comparison of reorientational correlation functions for single particle, monolayer and bilayer adsorption.	179
4.12	Trajectory of $\sqrt{3} \times \sqrt{3}$ solid methane plus three molecules scattered in the bilayer at 30K.	181

		Page
5.1	Two experimental phase diagrams of methane adsorbed on graphite at submonolayer coverages.	184
5.2	Configurational energy and specific heat at $\theta = 0.46$, $20 < T < 95$ kelvin.	186
5.3	Distribution of molecular centres at $\theta = 0.46$.	189
5.4	Trajectories of the centre of mass at $\theta = 0.46$, T = 21.7, 36.6, 49.9 and 90.6K.	190-191
5.5	Site-site distribution functions at $\theta = 0.77$, T = 72.1K.	193
5.6	Distribution of molecular centres above the surface at $\theta = 0.77$, T = 72.1K and 94.4K.	198
5.7	The "inter" site-site structure factors at $\theta = 0.77$, T = 72.1K.	199
5.8	The velocity auto-correlation functions at $\theta = 0.77$, T = 72.1K and 94.4K.	203-205
5.9	The root mean squared displacement of molecules over a range of temperature and coverage in the liquid region of the phase diagram.	207-208
5.10	The diffusion coefficients calculated from the simulation compared to experiment.	211
5.11	Reorientational correlation functions plotted on a logarithmic scale.	214
5.12	The self part of the Van Hove function $G_s(r,t)$ at $\theta = 0.77$, T = 94.4K.	217
5.13	The reduced spreading pressure ϕ^* over a wide range of temperature and coverage.	226
6.1	The intra axis system.	240
6.2	The inter axis system.	243
6.3	A hard core model for benzene.	247

Page

6.4 The intra, inter and total structure factors at $\rho\sigma^2 = 0.694$. 249

6.5 Comparison of the total structure factor with experiment at $\rho\sigma^2 = 0.760$. 251

Tables

2.1 Coefficients of the virial expansion of the equation of state. 43

2.2 Comparison of simulation, mean field approximation and virial equation in the one phase region of the penetrable sphere model. 62

3.1 Potential parameters used in the simulation. 100

3.2 The second virial coefficients of methane adsorbed on graphite. 118

3.3 The single molecule vibrational frequency against the surface as a function of temperature. 126

4.1 The thermodynamic properties of methane adsorbed on graphite at $\theta = 0.87$. 143

4.2 The order parameters O_1 and O_2 for adsorbed methane at $\theta = 0.87$. 154

5.1 The order parameters O_1 and O_2 for adsorbed methane at $\theta = 0.46$. 188

5.2 The diffusion coefficient as a function of temperature and coverage for adsorbed liquid methane. 209

5.3 Comparison of the two routes to the diffusion coefficient. 240

6.1 The hard disc diameter as a function of temperature. 246

List of Principal Symbols

A	free energy
A_s	surface area of adsorbent
B_{as}	surface second virial coefficient
$c(1,2)$	direct correlation function
$C_\ell(t)$	ℓ^{th} order correlation function
C_v	specific heat
D	diffusion coefficient
E	total energy
F	force
$g(r_{12})$	pair distribution function
$g_{cc}(R_1R_2)$	distribution of molecular centres
$g^+(\sigma)$	value of the pair distribution function at point of contact for hard spheres
$h(1,2)$	correlation function $g(1,2) - 1$
$\hbar$	Plancks constant divided by 2π
I	moment of inertia
$J_\ell(kr)$	ℓ^{th} order Bessel function
k	wave vector/reciprocal of r space
k_B	Boltzmann's constant
k_z	elastic force constant
L	Avogadro's number
m	particle mass
N_s	number of adsorbed molecules
O_1, O_2	order parameters
p	pressure
P_ℓ	ℓ^{th} order Legendre polynomial

$q_{st}^{\ominus}$	isosteric enthalpy at zero coverage
Q	wave vector
Q_N	canonical ensemble
$\underset{\sim}{r}_i$	position of particle i
R_{12}	separation of centres of mass of molecules 1 and 2
$\underset{\sim}{r}_{i\alpha j\beta}$	separation of atom α on molecule i from atom β on molecule j
S(k)	structure factor
$S(k,\omega)$	dynamic structure factor
t	time
T	temperature
U	internal energy
v	velocity
v_o	volume of sphere of diameter σ
$W(N_a)$	volume covered by N_a interpenetrating spheres
y(r)	$e^{\beta U(r)}\ g(r)$
Z	configurational energy
$Z(\omega)$	fourier transform of velocity auto-correlation function
$\beta = 1/k_B T$	inverse temperature
$\delta(1,2)$	Dirac delta function
Γ	torque
ε	energy scale of intermolecular pair potential
θ	1) inverse reduced temperature $\varepsilon/k_B T$
	2) extent of adsorption
ϕ	spreading pressure
λ	dimensionless activity
μ	chemical potential

Ξ	grand canonical partition function
$\Pi = Pv_o/k_BT$	reduced pressure to temperature ratio
ρ	density
ρ_a	reduced density $N_a v_o/V$
σ	1) hard sphere diameter
	2) range of intermolecular repulsion
τ	correlation time
ω	angular velocity
$< >$	canonical average

CHAPTER 1

Introduction

On the basis that the laws of physics can be applied to chemical phenomena, then all problems in chemistry are ultimately reduced to those of applied mathematics. The task of the theoretician is to bridge the gap between experimental knowledge and the laws of physics, producing theories to explain observable phenomena. In the physical chemistry of condensed matter we are interested in the nature of the intermolecular forces, the thermodynamics, structure and dynamics of the system. Even for the simplest of realistic systems it is impossible to produce exact theories which will calculate the partition functions, the key to the equilibrium structure. For dynamical propertes no exact framework has been proposed and the models we build are phenomenological. The purpose of the theoretician is twofold; to prepare interesting realistic models and to solve these models analytically or numerically. The art of the theoretician is then to obtain a successful balance between the realism of the model and the complexity of its solution. In this thesis the second of these problems is tackled using computer simulation as the numerical tool. This brute force numerical attack on the many body problem enables us to choose complicated models for the gas-liquid surface and molecules physically adsorbed on surfaces, and to establish a useful link with experimental work on adsorption.

In this chapter we give a brief historical account of computer simulations and highlight a few of the many important results. The difficulties that arise when choosing a potential model are discussed. The adsorption problem is introduced and the experimental techniques for measuring the properties of physically adsorbed species are summarized. Finally the problems we wish to answer in the proceeding chapters are outlined.

1.1 Monte Carlo and Molecular Dynamics Methods - a brief history.

Over the past fifteen years computer "experiments" have come to play an important role in liquid-state physics. From a theoretician's point of view simulations are important because they provide an exact set of quasi-experimental data on well-defined models. This data is used as the basis for comparison with analytical and numerical solutions of approximate theories of liquids such as integral equations, perturbation theory, etc. We can also access microscopic information about a system which is difficult to examine experimentally. The simulation of realistic molecular systems is also of interest to the experimentalist. For example it may be possible to obtain spectra of condensed matter which are difficult to interpret. If these spectra can be obtained from a simulation, then it is likely we can associate certain peaks in spectra with particular structural or dynamical fluctuations in the liquid.

Fluids and solids can be simulated at a molecular level in a number of ways. The commonest techniques are Monte Carlo and

and molecular dynamics. The term Monte Carlo (MC) refers to the Markov-chain ensemble averaging technique introduced by Metropolis et al., (1953). Molecular dynamics (MD) refers to the time averaging technique used to sample the microcanonical (N,V,E) ensemble. MD was pioneered by Alder and Wainwright (1959) for hard core and square-well interactions and by Rahman (1964) for continuous potentials.

The MC method is restricted to the calculation of static equilibrium properties usually in the canonical (N,V,T) ensemble, while the MD method can estimate time-dependent correlation functions as well as equilibrium averages. If equilibrium properties alone are required the Monte Carlo method is generally favoured because it is the easier technique to program and the simulation can be performed in a variety of ensembles. The MC method can also be used to calculate statistical properties, (free energy, entropy) in addition to mechanical properties (energy, pressure and specific heat) using the umbrella sampling technique (Valleau and Torrie, 1977). Until recently MD could only be performed at constant volume, particle number and total energy which can be inconvenient. The technique for performing molecular dynamics at constant temperature and/or pressure has been developed (Andersen, 1980).

With either of these machine methods, only small numbers of particles (compared to Avagadro's number) can be studied. Depending on the nature of the system of interest it is feasible to study systems of 10^2 ~ 10^3 molecules. Periodic boundary conditions

are typically used in order to reduce the effects of such small system sizes. This condition is applicable to strictly finite range potentials (Wood and Erpenbeck, 1976) such as hard cores and square wells, as well as the weakly long range interactions like the Lennard-Jones (LJ) potential. For potentials that decrease relatively rapidly at large separations, such as r^{-6} attraction in the LJ case, the common practice is to truncate the potential at some convenient distance $r = R\sigma < L/2$ (where σ is some scale parameter of the potential and L is the period of the system) and sum only the "minimum image distance" interactions. Corrections for the long range interactions with $r > R\sigma$ are made post hoc using a mean-field approximation. As the interaction becomes longer, variants of the Ewald procedure have been used to approximate the effective pair potential at long range (Hansen, 1973; Jansoone, 1974; Smith and Perram, 1975).

Until 1970 the MC and MD methods were mainly applied to systems of molecules interacting with isotropic potentials. Simulation work before 1970 can be classified under three headings; hard-core systems, square-well and triangular-well systems and short ranged soft potentials. Hard-core systems remain of vital importance in statistical mechanics, in as much as they frequently provide not only the simplest test case for new theoretical approximations but also provide a convenient starting point for treatment of more complicated systems by perturbation theory.

Wood (1975) has given a lengthy review of the equilibrium and dynamical properties of the MC simulation of hard core systems. This review includes discussions of estimating free energy differences of the communual entropy and self diffusion processes in hard sphere fluids. Young and Alder (1974) have reported extensive MD investigations of the moments of the distributions of single particle displacements from the initial lattice positions of hard-disc and hard-sphere solids. MC simulations of mixtures of hard core systems to calculate the equation of state and compressibility (Smith and Lea, 1963) have also been reported.

The attractive square well interaction ($U(r) = \infty$ for $r < \sigma$, $-\varepsilon$ for $\sigma < r < R\sigma$ and zero for $R\sigma > r$, in which ε is the well depth) is one of the simplest models incorporating the character of attractive forces that occur in nature. Extensive MD results in the fluid phase, including the liquid vapour transition are reported by Alder et al., (1972) and in the solid phase by Rosenfeld and Theiberger (1975).

The most frequently studied continuous interaction is the Lennard-Jones potential,

$$U(r) = 4\varepsilon \left[\left(\frac{\sigma}{r}\right)^{12} - \left(\frac{\sigma}{r}\right)^{6} \right] . \qquad (1.1)$$

While the LJ potential is too simple to represent intermolecular interactions between two real atoms accurately, it appears to have considerable value as an effective pair potential for a

variety of substances. The first MC calculation with a continuous LJ potential was made by Wood and Parker (1957) where they calculated the equation of state, compressibility and radial distribution function for an isotherm of argon at 55°C. The thermodynamic properties are in good agreement with experiment. A more systematic investigation of the LJ fluid was reported by Verlet and his colleagues (Verlet, 1967; 1968; Levesque and Verlet, 1970; Levesque et al., 1973). McDonald and Singer (1972) have shown that the good agreement with experiment found for argon is also applicable to other simple liquids when the LJ parameters are appropriately chosen. A recent comprehensive study of the LJ fluid has been made by Nicolas et al., (1979) to complement existing results and produce an equation of state over the wide range of densities and temperatures. This work has primarily been reported because of the usefulness of the LJ fluid as a reference substance in perturbation theories for molecular fluids.

The first MD simulations of molecules with anisotropic potentials were performed by Harp and Berne (1970) who modelled liquid CO using a modified Stockmayer potential; i.e. a LJ 12-6 centre with an additional point dipole and quadrupole. These simulations involve the solution of coupled Newton-Euler equations of motion. Their work contains the first machine calculations of time dependent correlation functions which characterize rotational motion. Since this work, simulations of molecular fluids have moved in two directions; systems of hydrogen bonded

fluids (HF, H_2O) and systems of simple non-dipolar fluids (N_2, CH_4, CS_2).

The most successful simple models accounting for the structure and dynamical behaviour of non-hydrogen bonded fluids have been interaction site models (ISM) (Streett and Gubbins, 1977). These models consist of two or more interaction sites fixed rigidly within a molecule. The sites on different molecules interact through spherically symmetric pairwise additive potentials, and the overall interaction is anisotropic. Barojas et al., (1973) simulated liquid nitrogen using two LJ interaction sites on each molecule. These sites are at positions of the nuclei and ε and σ of each interaction site potential are adjusted to reproduce equilibrium properties of the fluid. MD simulations of N_2 have also been performed by Cheung and Powles (1975, 1976). In the first of two simulations Cheung and Powles used a LJ site-site potential and the thermodynamic properties, structure factors and diffusion coefficients were found to be in essential agreement with experiment, (their parameters are slightly different from those of Barojas et al.). However the reorientation correlation times were produced only qualitatively. In a second simulation an ideal quadrupole-quadrupole interaction was placed at the centre of the bond. The structure factor is closer to experiment and the properties associated with reorientation are also closer to experiment, but the model does not account for all properties especially the correlation times at high temperatures.

Singer et al., (1977) have performed MD calculations on the

halogens F_2, Br_2, $C\ell_2$ and carbon dioxide. The agreement between experimental and computed thermodynamics is very good for F_2, quite good for Br_2, $C\ell_2$ but worse for CO_2. They conclude that the simple site-site potential model cannot be expected to simulate the effects of the long range quadrupole moments of $C\ell_2$, Br_2 and CO_2. Murad et al., (1979) have simulated by MD a system of dense fluid methane using a Williams site-site potential (Williams, 1967). The model gives a good description of the thermodynamic properties, self diffusion coefficients and mean-squared torque. This simulation is also historically important because it first demonstrates the use of the quaternion method (Evans, 1977) for solving the rotational equations of motion. These recent simulations have demostrated that molecular dynamics simulation methods have now advanced to a stage where it is quite feasible to study molecular liquids of moderate complexity.

We note that simulations have also been reported for systems of hard anisotropic molecules. In particular extensive studies have been made on hard "dumbell" fluids using 2 site interaction centres per molecule (Freasier et al., 1976; Tildesley and Streett, 1980). Since the structure of many liquids is strongly affected by short range repulsive forces these simulations were performed to form a basis in the understanding of the structure and thermodynamics of polyatomic liquids and solids. The hard dumbell fluid is also used as a non-spherical reference system for a perturbation theory of diatomic molecules (Tildesley, 1980).

Hydrogen-bonded liquids present more difficulties in simulations because of the long ranged Coulombic forces that occur in these liquids. The first extensive simulation of water was by Rahman and Stillinger (1974) and they used an effective pair potential based on a four-charge model for each molecule, (the ST2 potential). They do not take into account long range forces or three body effects. Structural agreement between theory and experiment is reasonably good, however self diffusion constants were much higher than experimental values. Thermodynamic properties do not agree well with experiment for this model. Probably the most successful model of water is by Clementi and co-workers (Lie et al., 1976). The water-water interaction potential is obtained from self consistent field (SCF) ab initio calculations with configuration interactions (CI) included. This potential predicts a liquid state radial distribution function which is in good agreement with experimental values obtained from X-ray scattering. The simulation indicates that many-body effects contribute little in determining the structure of liquid water, although they seem to be important for an accurate determination of internal energy and related thermodynamic quantities. McDonald and Klein (1978) simulated water by MD, using a potential based on the second virial coefficient of steam. In this simulation they use an Ewald method to sum over periodically replicated systems to account for long range coulombic forces. Their agreement with experiment is somewhat worse than for Clementi water. Simulations have also been performed with reasonable success on ammonia (McDonald and Klein, 1976), hydrogen fluoride (Klein et al., 1978, 1979)

and hydrogen chloride (McDonald et al., 1980).

So far we have reported simulations of homogeneous systems. In view of the success of these simulations a natural extension is to use the Monte Carlo and molecular dynamics methods to study the interfacial region; the gas liquid interface and physical adsorption at a solid surface. The theory of the liquid-vapour interface has been reviewed by Croxton (1980), who discusses much of the simulation work on these systems. In three dimensions the gas-liquid surface has been studied using the MC method by Lee et al., (1974), and Abraham et al., (1975). They use a periodic slab with two free surfaces bounded above and below by a strong external field. The earlier results indicate the presence of density oscillations through the profile. These appear to be an artifact of the MC technique used, and more extensive simulations (Abraham et al., 1975; Chapella et al., 1977) indicate a monatomic interface. Thompson (1976) has performed extensive MD simulations of LJ molecules in the liquid vapour interface and has found that longitudinal oscillations are quite dependent on the size of the periodic box. In this thesis we do not attempt to simulate a "real" gas-liquid surface but use the Monte Carlo method to test a tractable theory of a simple model of the liquid-vapour interface; the penetrable sphere model of Widom and Rowlinson (1970).

A large amount of experimental interest has been generated over the past few years in the area of the gas/solid interface (see Vilches, 1980; Everett, 1977 for excellent review articles). A comprehensive treatise of the theory of physical adsorption

has also been given by Steele (1974), however little work has been done to bridge the gap between theory and experiment using the MC and MD methods. Grand canonical ensemble MC has been performed on systems of liquid Argon adsorbed on a graphite surface (Lane and Spurling, 1976, 1978; Rowley et al., 1975; Hansen et al., 1977). Pressure-isotherms, isosteric heats and distribution functions are reported and agree reasonably well with experimental data. Rowley et al., also compare their results to various simple theories of physical adsorption. Weisemann and Cohen (1980) have used the MD method to study the structure of two dimensional and adsorbed microclusters, concluding that a weak adsorbent-adsorbate potential has little effect on the structure of micro-clusters of rare gas atoms. O'Shea and Klein (1979) have performed MC calculations on a two dimensional array of classical octopoles fixed on their lattice sites. Their work investigates low temperature rotational phase transitions and they discuss the relevance of these models to a registered adsorbed phase of methane adsorbed on graphite. Toxvaerd (1979) has performed an MD simulation in 2-dimensions to study two dimensional diffusion of adsorbed species. To our knowledge little other simulation work has been reported in this field.

Recent experimental results of neutron scattering from methane adsorbed on graphite (Vora et al., 1979; Coulomb et al., 1979; Bomchil et al., 1980) have revealed a rich variety of interesting phase behaviour. It is our aim to use the molecular dynamics

method to give a detailed description of the microscopic properties of methane adsorbed on graphite. In doing so we hope to develop an effective potential model for the methane graphite interaction and help to interpret the experimental work on this system.

1.2 The Gas/Solid Potential

The success of interaction site models in predicting accurate structure factors, pressures and transport properties for bulk liquids (Chandler, 1978; Streett and Gubbins, 1977), and cohesive energies, packing characteristics and barriers to rotation for organic molecular solids (Ramadas and Thomas, 1978) leads us to extend these potential models to the gas/solid interface. (Note the term gas/solid in physical adsorption covers all phases of matter adsorbed on solid surfaces). In this section some of the more general aspects of the pairwise-additive site-site gas/solid potential are discussed.

In a pair of non-bonded atoms, fluctuating multipole moments lead to a quantum mechanical attractive energy known as the attractive London force or the dispersion interaction. The induced dipole-induced dipole dispersion interactions falls off at large distances as $-C_6/r^6$, where r is the inter-atomic distance and C_6 is a constant related to the polarizability and ionization potential of the atom (Steele, 1974). Similar considerations of the induced dipole-induced quadrupole and induced quadrupole interactions lead to additional dispersion terms of the form $- C_8/r^8$ and

$- C_{10}/r^{10}$. These latter terms form a relatively small part of the total dispersion interaction, of the order of a few percent even for nearest neighbours (Kitiagorodsky, 1973).

At shorter distances when the electron clouds of the two non-bonded interacting atoms overlap, a strong repulsive interaction develops. For a spherically symmetric particle quantum theory predicts an exponential increase of the energy of interaction; this can also be approximated by an A/r^n interaction, where $n \geq 12$. Thus for two atoms the energy U_{ij} can be broken up into two terms

$$U_{ij} = \phi_{ij} + \phi_{ij}^{disp} \qquad (1.2)$$

where ϕ_{ij} takes account of the forces of repulsion and ϕ_{ij}^{disp}, the dispersive attraction.

Since molecules are built up from atoms we can represent the the part of the interaction between two molecules (1 and 2) as the sum over all atom pairs in the molecules,

$$U(r_{12},\omega_1,\omega_2) = \sum_{i=1}^{\alpha} \sum_{j=1}^{\beta} U_{ij} \qquad (1.3)$$

where ω_1 and ω_2 represent the relative orientations of the molecules each containing α and β atoms respectively. This equation is the basic ISM potential. $U(r_{12},\omega_1,\omega_2)$ is a reasonable model of the anisotropic repulsion or shape of the molecule.

The attractive part of U, $\phi_{ij}^{disp}(r)$ is an approximation since it assumes the dispersion interaction of an atom in a molecule is isotropic, however CS_2 is more polarizable perpendicular than parallel to the molecular bond (Madden and Tildesley, 1981) and we might expect the dispersion interaction of a sulphur atom to be different parallel and perpendicular to the bond.

In addition to dispersion forces that are always present, the intermolecular potential for a molecule includes interactions between various permanent electric moments when these are present in the molecules of the gas or solid, and the interactions between permanent and induced multipoles. The full pairwise-additive potential can be represented by

$$U(r_{12},\omega_1,\omega_2) = \sum_i^{\alpha}\sum_j^{\beta} U_{ij} + U_{electrostatic} + U_{induced} \qquad (1.4)$$

For a typical molecule, HBr, these terms have the following relative sizes 176 (dispersion), 6.2 (electrostatic) and 4.1 (induced) erg cm^6, or 95%, 3% and 2% of the total interaction energy, (Pryde, 1969). These ideas can be extended to the gas/solid interaction.

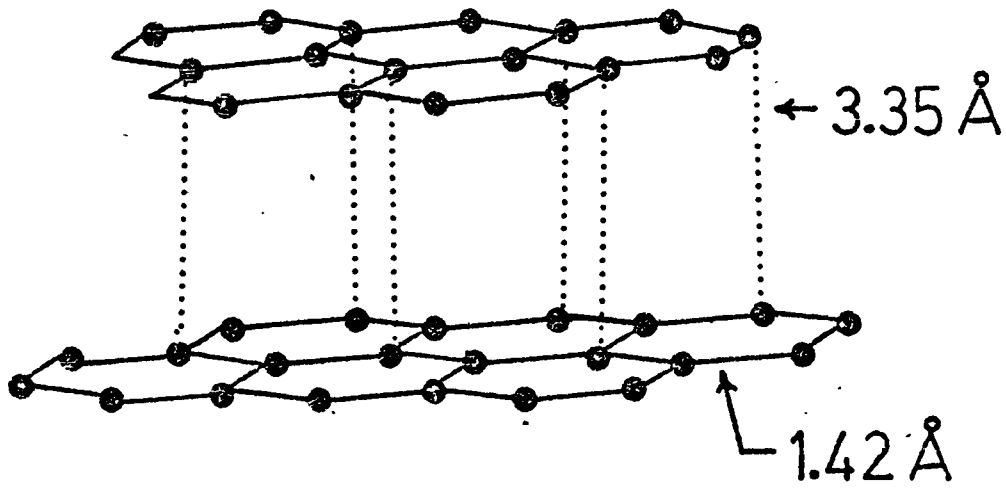
In recent years, a very large number of experimental and theoretical publications have appeared concerning the properties of gases adsorbed on substances known as graphitized carbon blacks (Avgul and Kiselev, 1970). These adsorbents are carbon

blacks of reasonably high specific surface area (10 - 80 m^2/g) that have been graphitized by heat treatment under conditions that produce a nearly uniform surface. The fact that these surfaces are almost uniform means that useful connection can be made between the experimental energies of interaction and the gas surface potential. Graphite is a useful adsorbent since many of its properties such as the crystal structure, thermal expansivity, Debye temperature, binding energy are well known and it is a simple substance both physically and chemically.

A particularly convenient feature of the graphitization process is that the exposed planes are almost entirely basal planes of the graphite lattice, ensuring the absence of heterogeneity due to different adsorptive properties over different lattice planes. The atomic packing and spacing near an exposed basal plane is shown in Figure 1.1. The carbon atoms in the hexagonal array are covalently bonded which accounts for the small separation between atoms in the plane. In contrast the sheets are weakly bound giving rise to nearly free electrons between the planes and the separation of planes is quite large.

Little is known about the electrostatic field and its gradient at a graphite surface caused by these "free" electrons (Steele, 1974). The lowest permanent interaction with the octopole of methane might be the second gradient of the field. At present the only way to account for this effect is to scale the pairwise gas/solid potential parameters to fit experimental data in which this effect

Figure 1.1 Schematic Representation of a Graphite Lattice.



is included.

Although pairwise additivity is assumed, the problem of three body (and higher order) interactions is still important in physical adsorption. First one would like to know whether the effective two body potentials for gas phase atoms interacting near a solid surface are appreciably different from the effective two body potentials interacting in the bulk phase. Secondly it is not unreasonable to assume that gas-gas interactions will have an effect upon the gas-surface interaction. Unfortunately no quantitative estimates of these effects are available at present.

The potential interaction of methane adsorbed on graphite will be represented by the ISM model to account for the repulsion and dispersion forces between methane-graphite and methane-methane interactions. The electrostatic interactions between methane molecules and the effect of the field gradient of the surface are assumed small enough to be ignored. One effective classical pairwise potential will be used that will reproduce measurable experimental quantities of the system including some essentially quantum mechanical properties. This tractable simple model will be seen aposteriori to account for a large number of observed properties of methane adsorbed on graphite.

1.3 Experimental Measurements on the Gas/Solid Surface

The term physical adsorption is associated with the phenomenon of condensed matter binding with a surface due to the attractive interaction between adsorbate and adsorbent. The

adsorbed molecules retain their molecular identity and do not transform into a different species. The activation energy of physical adsorption is small and the heat of adsorption is around 40 KJ $mole^{-1}$ for rare gas atoms. In contrast in chemical adsorption there are large changes in electronic structure and often electron transfer occurs forming new chemical species. The heat of adsorption is around 400 KJ $mole^{-1}$ and the activation energy is correspondingly large ($\simeq$ 80 KJ $mole^{-1}$).

Chemical adsorption is accomplished by an initial physical adsorption and an understanding of this physical process is important in characterizing the mechanism of chemical adsorption which occurs in so many important biological and industrial processes. Physical adsorption itself is also imbedded in seveal major commercial processes. For example, many tonnes of carbon black are used annually in rubber reinforcement and particle size has shown to be an important parameter in determining the rubber properties. Adsorption isotherms have been used for more than 50 years to characterize the surfaces of various charcoals and graphites (Paneth and Radu, 1924). Likewise, silicon gels (amorphous SiO_2) of high surface area are common texturizers and thickeners in many cosmetics and even foodstuffs. For the latter use it is important that surfaces be smooth and rounded. The majority of methods employed in studying three dimensional matter have been modified or adapted for the study of physisorbed films. The experimental techniques for measuring thermodynamic, structural and dynamical properties are summarized in this section.

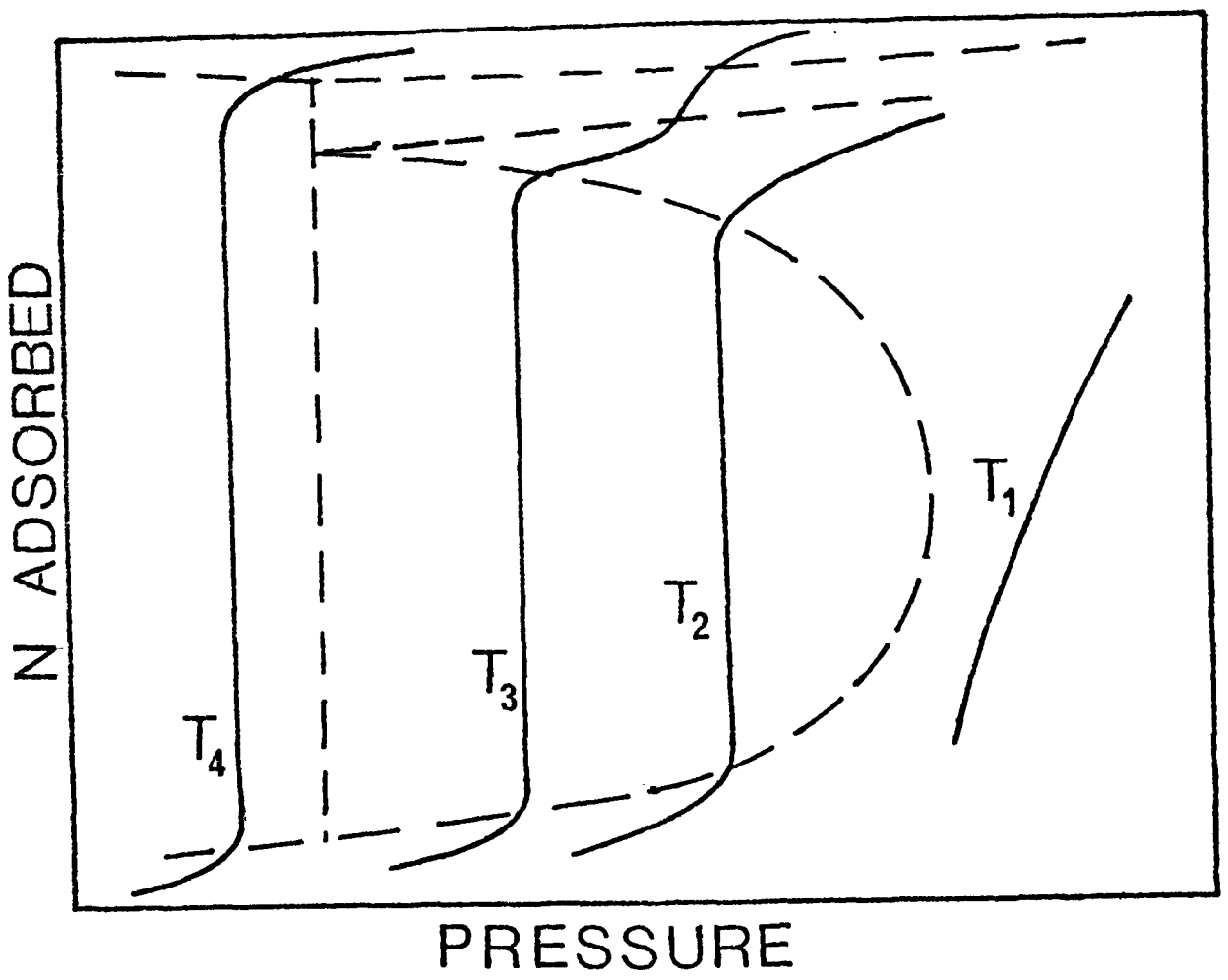
Thermodynamic Measurements

A volumetric adsorption isotherm consists of a measurement in which known amounts of adsorbate (N) are admitted into a cell containing the adsorber at a constant temperature T. When equilibrium is reached the pressure P is measured. A graph of the amount adsorbed v's the equilibrium pressure is the adsorption isotherm. For adsorbers where only a single crystallographic plane is exposed to the adsorbate and for temperatures much lower than the binding energy of the adsorbate to the adsorber, steps are found in the isotherm characteristic of layer by layer adsorption.

Adsorption isotherms exploring the first physisorbed layer have been one of the most revealing experimental tools. Figure 1.2 shows schematically the characteristics seen in many adsorption isotherms. The most striking characteristic in the isotherms is the constant P steps (where P is the pressure normal to the surface). In a pressure-density diagram of a 3-D system these steps represent co-existence between two different phases. A general relationship between film and vapour pressure can be derived (Steele, 1974). If the film spreading pressure is ϕ and the area per particle is $a = A/N^{(s)}_{film}$, then at equilibrium between 2-D film and 3-D vapour (constant T),

$$ad\phi = vdP \qquad 1.5$$

Figure 1.2 Schematic drawing of first layer adsorption isotherm where several phases may coexist. The solid lines represent isotherms at temperatures $T_1 > T_2 > T_3 > T_4$. The dashed lines mark phase boundaries.



where $v = V/N_{vapour}$. Thus if P remains constant, ϕ is also constant and constant steps in the isotherms mean the presence of two co-existing phases in the physisorbed system.

The heat capacity of physisorbed films on a variety of adsorbers has been used as a tool to identify phases and phase transitions (Kiselev and Poshkus, 1976). Heat capacity measurements are done at constant N, and it is possible to find triple points, critical points and co-existence boundaries all of which produce anomalies and discrepancies in the specific heat.

Structural Measurements

An important question which arises when studying the structure of 2-D adsorbed phases, is whether long range ordering will be observed in the 2-D physisorbed solid. Mermin (1968) has shown that spontaneous crystalline order should not exist in one or two dimensions and this has been proved in the special case of a harmonic lattice by Peierls (1935). Long range disorder can be explained in terms of fluctuations U(x,y,z,) about a lattice point (x,y,z). If we represent these fluctuations as a Fourier series in terms of the reciprocal vector k

$$U = \sum_{k} U_k \, e^{i\underset{\sim}{k}\cdot\underset{\sim}{r}} \quad , \qquad 1.6$$

then Landau and Lifshitz (1980) show in three dimensions that the mean square displacement is given by

$$\langle U^2 \rangle = T \int \frac{A}{k^2} \frac{d^3k}{(2\Pi^3)} \qquad (1.7)$$

where T is the temperature and A depends on the direction of the vector k. This integral converges at the lower limit ($k \to 0$) linearly in k; i.e. at large r, the fluctuations in U are finite and small and the crystal has long range order (at low T). For a planar monatomically thick crystal the above integration is taken over 2-D k-space

$$\langle U^2 \rangle = T \int \frac{A}{k^2} \frac{d^2k}{(2\Pi)^2} \qquad (1.8)$$

This integral diverges logarithmically at $k \to 0$, and at large r we do not expect to see any long range order. Physically this means that motions of internally correlated clusters gives rise to long wavelength phonons which cause long range disorder. (Note correlated clusters exist because long wavelength phonons do not affect short and medium ranged correlations (Imry and Gunther, 1971)).

For physisorbed systems substrate inhomogeneities pin down parts of these clusters and long wavelength phonons are destroyed, therefore we do expect to see 2D ordering in experiments on physisorbed systems with finite substrates.

Low energy electron diffraction LEED is the most commonly used tool for the study of molecular crystal structures of chemisorbed systems. It has the important advantage of high

sensitivity; typical scattering cross sections are of order 10 $\mathring{A}^2$ per molecule, so essentially all the incident beam is scattered by the adsorbed monolayer or the first one or two substrate planes. However it has some significant drawbacks for physisorbed systems; poor absolute accuracy (3 - 5%) for lattice parameter determination, the requirement of high vacuum in the experimental chamber and the problem that some electrons have enough energy to dislodge the adsorbate molecules from the surface. However Lander and Morrison (1967) have made quite a successful interpretation of the $\sqrt{3}$ x $\sqrt{3}$ registered structure of Xe physically adsorbed on graphite. LEED has been useful for investigating epitaxy (see Chapter 3) in physisorbed systems.

To date the majority of physisorbed crystal structure studies on graphite, have utilized elastic coherent neutron scattering or neutron diffraction, a technique which at first glance appears ill-suited to monolayer research. Typical neutron scattering cross-sections are of order 10^{-7} $\mathring{A}^2$ per nucleus. Contrasting this cross section with the size of an atom (of order 10 $\mathring{A}^2$) shows that only $\approx 10^{-8}$ of an incident neutron beam is scattered by the first layer of a solid sample. Clearly, neutron scattering cannot be used to study single monolayer samples, (of order 10^5 layers are required). Fortunately, such high surface area graphites (Grafoil, Papyex, UCAR-ZYX etc.,) are commercially available. Although the integrated background scattering from the substrate is orders of magnitude greater than that of the

monolayer, most of it usually occurs in different regions of Q, ω space, making background subtraction possible.

Neutrons are well suited for structural studies where elements with large coherent scattering cross sections are used. Argon and nitrogen are among the best candidates. Other substances for which neutrons are better than any other presently used scattering technique are ^4He, ^3He, H_2, D_2 CH_4 and CD_4 (Vilches, 1980). The first neutron study of 2D-like monolayer Bragg peaks was made by Kjems et al., in 1974. They observed at low coverages and temperatures, N_2 formed a $\sqrt{3}$ x $\sqrt{3}$ registered structure with a nearest neighbour distance of 4.26 Å. On completion of a registered monolayer, addition of more N_2 created a denser triangular phase whose nearest neighbour spacing is temperature and filling dependent. Since this first study a number of systems have been investigated including the structure and phases of methane physisorbed on graphite (Vora et al., 1979; Bomchil et al., 1980), and benzene adsorbed on graphite (Meehan et al., 1980).

Dynamical Measurements

In addition to structural determination, neutron scattering can be used to directly probe the single particle and collective dynamics by energy analysing the scattered beam. Inelastic incoherent scattering is directly related to $G_s(r,t)$ the time-dependent self-correlation function which describes the probability that a given particle moves from its position at t = 0 to a new position

at distance r away in time t , (Van Hove, 1954). For liquids this measures, at long times, the diffusive properties, while for solids it reflects the phonon density of states (McTague et al., 1979). Incoherent inelastic neutron scattering is used as a probe to analyse rotational tunnelling in adsorbed species (Bomchil et al., 1980) and quasi-elastic neutron scattering measures diffusive properties of adsorbed liquids (Coulomb et al., 1979, 1980). Quasi-elastic scattering measures a line broadening associated with translational motion of the adsorbed nucleus, whereas in incoherent inelastic neutron scattering the energy is also adsorbed in the rotational and vibrational modes of the molecules and a second peak in the scattering spectrum occurs at substantial energy shifts from the incident radiation.

Nuclear magnetic resonance (NMR) can also be applied to the study of the dynamical behaviour of physisorbed atoms whose nuclei possess a magnetic moment. It can give information about relaxation times of the magnetization perpendicular, T_1, and parallel, T_2, to the substrate. It is possible to study mobility changes by measurements of the width of the continuous wave resonance line through solid-fluid transitions and to study magnetic behaviour in susceptibility measurements. NMR has been used to examine the melting and orientation of benzene adsorbed on graphite (Tabony et al., to be published 1980). The solid/fluid phase diagram for coverages between 0.4 and 2.0 monolayers is reported.

Direct measurements of diffusion coefficients of methane adsorbed on graphite have been made by the NMR pulsed field gradient method (Tabony and Cosgrove, 1979). Pulsed field gradients dephase the spin on a nucleus. If two field gradients are placed either side of a 180° radio frequency pulse,then the pulse will cancel if the nuclei remain fixed in space. Any net translation of the nuclei will lead to signal attenuation from which the diffusion coefficient can be calculated directly.

Finally X-ray scattering has been a standard structure determination tool in 3-D for many years, but its use in physisorption is very recent. The experimental procedure is analogous to that used in coherent neutron scattering; again large area-to-volume adsorbers are needed and the adsorbates should have large coherent X-ray scattering cross sections. The technique, as applied to Kr adsorbed in graphite (Horn et al., 1978) gives well resolved scattering peaks. Although the X-ray scattering cross section decreases with atomic number, accurate measurements are possible with relatively small molecules like O_2 (Heiney et al., 1980).

1.4 What is to Follow

This thesis is divided into three separate parts, each covering a different topic. In the first part, Chapter 2, we use the Monte Carlo method to simulate the penetrable sphere model of the liquid-vapour interface (Widom and Rowlinson, 1970). A basic outline of the model is given and the computational details of the MC technique are discussed. The Monte Carlo program is tested

for its accuracy by simulating a homogeneous system of hard spheres, and comparing the results to previous simulations. We then proceed to use the program to simulate the penetrable model in the one-phase region and use these results to test the accuracy of virial expansions of the equation of state. The two-phase region is next simulated to obtain density profiles through the gas-liquid interface and to observe the effect of the system near a hard wall. These two results are compared to numerical solutions of the model.

In the second part the molecular dynamics technique is used as a tool to study the physical adsorption of methane on graphite; the microscopic properties of this system are explored in Chapters 3, 4 and 5. In Chapter 3 the molecular dynamics program is developed to enable us to model small rigid molecules adsorbed on a graphite surface. The methane-surface potential is discussed and the parameters are fitted using static calculations to the rotational barrier heights (Bomchil et al., 1980) and using molecular dynamics to the isosteric enthalpy at zero coverage (Kiselev and Poshkus, 1976). We examine the translational and rotational behaviour of a single methane molecule moving across the surface.

The behaviour of solid methane adsorbed on graphite as a function of temperature at constant coverage is reported in Chapter 4. Changes to the MD program are made to incorporate many adsorbate molecules and a program to calculate the time dependent properties is presented. The thermodynamic properties and structure are

given and the translational and rotational dynamics are analysed. The phase transitions of the adsorbed monolayer are discussed and the time-dependent correlation functions are compared to experimental spectra of the system (Bomchil et al., 1980). A qualitative study of a few molecules scattered in the bilayer is made and compared with experiment (Newbery et al., 1978).

A study of methane adsorbed on graphite at submonolayer coverages completes the discussion of this system in Chapter 5. In this chapter we attempt to identify some of the phases predicted by Coulomb et al., (1979, 1980). Diffusion coefficients and spreading pressures are calculated and the diffusion coefficients are compared to experiment (Coulomb, 1980; Tabony and Cosgrove, 1979). The structural and dynamical properties of the adsorbed liquid are also presented.

The third part of the thesis, Chapter 6 differs from the previous work in that the structure of benzene adsorbed on graphite is predicted using numerical solutions to integral equations, rather than employing the brute force simulation technique. The Ornstein-Zernike equation in the Percus-Yevick approximation is solved in two dimensions to obtain 2D radial distribution functions for hard discs. The structure factor of benzene in the free rotor limit is derived. This is a function of the 2d radial distribution function only. The predicted structure factor is compared to experiment (Mathews and Thomas, 1980). Finally we summarize some of the important results of the thesis in Chapter 7 and

discuss future extensions to the work.

CHAPTER 2

Monte-Carlo Simulation of the Gas-Liquid Interface of the Penetrable-Sphere Model

2.1 Introduction

The statistical mechanical theory of surfaces is not so highly developed as that of homogeneous fluids. There are well established equations for the calculation of the thermodynamic properties from distribution functions; however these functions are not readily obtainable for realistic systems. A solution to this difficulty is to introduce a model system that can be handled more rigorously.

Prior to the penetrable sphere model which was proposed in 1970 (Widom and Rowlinson, 1970); the Ising Model (Ising, 1925) was the most successful theoretical model for the study of the gas-liquid surface. This is a model in which the Hamiltonian of a real ferro-magnet is represented by a lattice of 2-state spin systems each of which interacts only with its neighbours. At high temperatures this model forms one phase with an equal number of spins pointing up and down. The result is zero magnetization. At low temperatures, below a critical temperature, two phases form with an unequal number of opposed spins in each phase. A net magnetization in each phase results. An analogy can be drawn between this real ferro-magnet and a lattice gas where a spin

up becomes a lattice site occupied by a molecule and a spin down an empty site. Low energy configurations with an abundance of parallel spins translate into low energy configurations of occupied cells next to occupied cells (Yangand Lee, 1952). Since the partition functions of the two models are isomorphous the lattice gas also has a gas-liquid critical point, and the line of net zero magnetization becomes the isochore through this point.

The symmetry properties that arise from this model make it possible to calculate the partition function exactly in 2 dimensions (Feynman, 1972). The transverse symmetry between spin-up and spin-down becomes a hole-particle symmetry in the lattice gas; from which many analytic results are derived. A serious disadvantage of the model is that the intermolecular potential between a pair of molecules is not a function of distance only. It is also dependent on the relative positions of the molecules in the lattice; or, alternatively, the quantity which effectively measures the distance between molecules is a discrete variable (Widom, 1967). Other disadvantages are that a lattice model is a very artificial description of a fluid; this is especially evident if the structure of the fluid is to be studied. Also strict hole-particle symmetry has an effect on thermodynamic functions which is not found in real fluids (Rowlinson, 1980).

The above disadvantages can be overcome in a continuum model where there is no lattice imposed on the system and the Hamiltonian is a continuous function of particle positions. The

penetrable-sphere model (Widom and Rowlinson, 1970) and later generalizations (Melnyk et al., 1972; Widom and Stillinger, 1973) is a continuum model and not restricted to a particular lattice structure. The transverse symmetry still exists and this is important in the determination of some of the exact results. However this symmetry is not as restrictive as that of the lattice gas. An important consequence is that singularities in the thermodynamic functions at the critical point are permitted where previously they were not due to the transverse symmetry itself.

The introduction of a continuum model increases the complexity of the partition function and some of the tools which facilitate the study of simple liquids, (approximate integral equations, virial expansions, simulations) must be applied to this model to calculate thermodynamic properties and structure. This increase in complexity from the lattice gas is more than outweighed by the more realistic description of the gas-liquid interface. In this chapter we use a Monte Carlo simulation of the penetrable sphere model to calculate density profiles through the interface and compare these results with the solution of the penetrable sphere model in the mean-field approximation (Leng et al., 1976).

In the next section we discuss the fundamentals of the penetrable sphere model, including the phase diagram and the thermodynamic results in the mean-field approximation. In section 3 the Monte Carlo method is described and in section 4 this method is tested for a homogeneous system of hard spheres for which there

is readily available data. We also discuss results of the Monte Carlo simulation of the penetrable sphere model in the one phase region and compare these results to the virial equation of state (Melnyk et al., 1972). Finally in section 5 we report the results and discuss the simulation in the two phase region. An integral equation for the density profile in the mean-field approximation is solved by iteration and compared to the density profiles from the simulation.

2.2 The Models

The continuum models proposed are of two types; a primitive and transcribed form. In both cases we only consider the potential part of the Hamiltonian because the kinetic contribution is simply a function of temperature. First consider the primitive form in which the configurational energy is the sum of pairwise additive intermolecular potentials in an n component system. Let α, β be two components in this system; their intermolecular potential is given by the following relationships,

$$U_{\alpha\alpha}(R) = 0;\ U_{\alpha\beta}(R) \geq 0,\ \alpha \neq \beta \qquad (2.2.1)$$

If the system consisted of one component it would be a perfect gas; likewise if the n component system approached zero density it would also form an ideal gas mixture. Since the potential energy is either zero or positive, at high densities the system will separate into n phases.

The simplest system to consider is that of hard spheres of diameter σ, where

$$U_{\alpha\beta}(R) = \infty \ , \ R < \sigma \ ;$$

$$U_{\alpha\beta}(R) = 0, \ R \geqslant \sigma. \qquad (2.2.2)$$

If all the spheres have the same diameter the symmetry of the model is at maximum and in this case an alternative statement of (2.2.2) is that unlike species are excluded by a co-volume v_o where

$$v_o = \frac{4}{3} \pi \sigma^3 \qquad (2.2.3)$$

Other forms of the same model with different potentials have also been studied (Melnyk et al., 1972; Widom and Stillinger, 1973; Helfand and Stillinger, 1968; Helfand and Wesserman, 1972), but in this work only a 2-component hard sphere potential is considered. We now turn our attention to the transcribed form or the penetrable sphere model.

The grand partition function

In this model the position of molecules of species one are fixed in space and the molecules of the second species are added one by one. The molecule added is permitted the same free space as the first because there is no interaction between like molecules.

Having added all of the molecules of the second component we may now integrate over the co-ordinates of each of these molecules in the grand partition function and hence "remove" the second species from the integral (Rowlinson, 1980). The resulting function has the form of a grand partition function, but the potential and activities are different from the original two species grand canonical partition function. For a system of two components a and b we define the following reduced densities and pressure

$$\rho_a = N_a v_o/V, \ \rho_b = N_b v_o/V, \ \Pi = p v_o/k_B T \qquad (2.2.4)$$

Let λ_a be the dimensionless activity of component a which is normalized to approach ρ_a as Π approaches zero (Rowlinson, 1980).

For a two component system the grand canonical partition function is

$$\Xi_{(2)} = \sum_{N_a=0}^{\infty} \sum_{N_b=0}^{\infty} \left(\frac{z_a}{N_a!}\right)^{N_a} Z_a(V,T) \left(\frac{z_b}{N_b!}\right)^{N_b} Z_b(V,T)$$

$$= \exp\left(\Pi_{(2)} V/v_o\right); \qquad (2.2.5)$$

where z_a and z_b are the activities of each component, $Z_a(V,T)$ and $Z_b(V,T)$ are the configurational integrals and the subscript (2) denotes a two component function. From the above definition of λ, z_a and z_b become λ_a/v_o and λ_b/v_o repectively. Equation (2.2.5)

reduces to

$$\Xi_{(2)} = \sum_{N_a} \sum_{N_b} \frac{(\lambda_a/v_o)^{N_a}}{N_a!} \frac{(\lambda_b/v_o)^{N_b}}{N_b!} \int\int_{vv} d\underset{\sim}{N}_a d\underset{\sim}{N}_b e^{(-\beta U_{ab})} \quad (2.2.6)$$

where $\underset{\sim}{N}_a$ and $\underset{\sim}{N}_b$ denote the position vectors $\underset{\sim}{R}_1 \cdots \underset{\sim}{R}_{N_a}$, $\underset{\sim}{R}_1 \cdots \underset{\sim}{R}_{N_b}$. As we have stated above, for a fixed configuration of a we can integrate over the b molecules. The b molecules are excluded from a volume $W(\underset{\sim}{N}_a)$ which is the volume covered by N_a interpenetrating spheres of radius σ. (Note the a spheres may penetrate since $U_{aa}(R) = 0$ for all R). The integral over the b molecules becomes

$$\int_v dN_b \exp(-\beta U_{ab}) = [(V-W(\underset{\sim}{N}_a)]^{N_b} \quad (2.2.7)$$

Substituting this expression into (2.2.6) the grand partition function is

$$\Xi_{(2)} = \sum_{N_a} \sum_{N_b} \frac{(\lambda_a/v_o)^{N_a}}{N_a!} \frac{(\lambda_b/v_o)^{N_b}}{N_b!} \int_v d\underset{\sim}{N}_a [(V-W(\underset{\sim}{N}_a)]^{N_b} \quad (2.2.8)$$

We can now sum over the N_b molecules using the relation $\sum_{n=0}^{\infty} \frac{x^n}{n!} = \exp x$.

$$\Xi_{(2)} = \sum_{N_a} \frac{(\lambda_a/v_o)^{N_a}}{N_a!} \int_v d\underset{\sim}{N}_a \exp\{[V-W(\underset{\sim}{N}_a)](\lambda_b/v_o)\}$$

$$= \exp \frac{\lambda_b V}{v_o} \sum_{N_a} \frac{(\lambda_a/v_o)^{N_a}}{N_a!} \int_v d\underset{\sim}{N}_a \exp(-W(\underset{\sim}{N}_a)\lambda_b/v_o) \quad (2.2.9)$$

Introducing the term $\exp(-N_a\lambda_b)\exp(N_a\lambda_b)$ into (2.2.9) and taking the part with positive exponent inside the integral gives

$$\Xi_{(2)} = \exp\left(\frac{\lambda_b V}{v_o}\right)\sum_{N_a}\frac{(\lambda_a/v_o \exp(-\lambda_b))^{N_a}}{N_a!}\int d\underset{\sim}{N}_a \exp\left[\frac{(N_a v_o - W(N_a))\lambda_b}{v_o}\right] \tag{2.2.10}$$

This function now has the form of a single component grand canonical partition function,

$$\Xi_{(2)} = \exp\left(\frac{V\ \lambda_b}{v_o}\right)\Xi_{(1)}$$

$$= \exp\left[(\Pi_{(1)} + \lambda_b)V/v_o\right] \tag{2.2.11}$$

where the activity is given by

$$\lambda_{(1)} = \lambda_a \exp(-\lambda_b);$$

the potential by

$$U(\underset{\sim}{N}) = [W(\underset{\sim}{N}_a) - N_a\ v_o]\ \varepsilon/v_o$$

and temperature by

$$\varepsilon/k_B T = \theta = \lambda_b\ . \tag{2.2.12}$$

Comparing (2.2.11) and (2.2.5),

$$\exp\,[\Pi_{(2)}V/v_o] = \exp\,[\Pi_{(1)} + \lambda_b\, V/v_o]$$

we note that

$$\Pi_{(2)}\,(\lambda_a, \lambda_b) = \Pi_{(1)} + \lambda_b$$

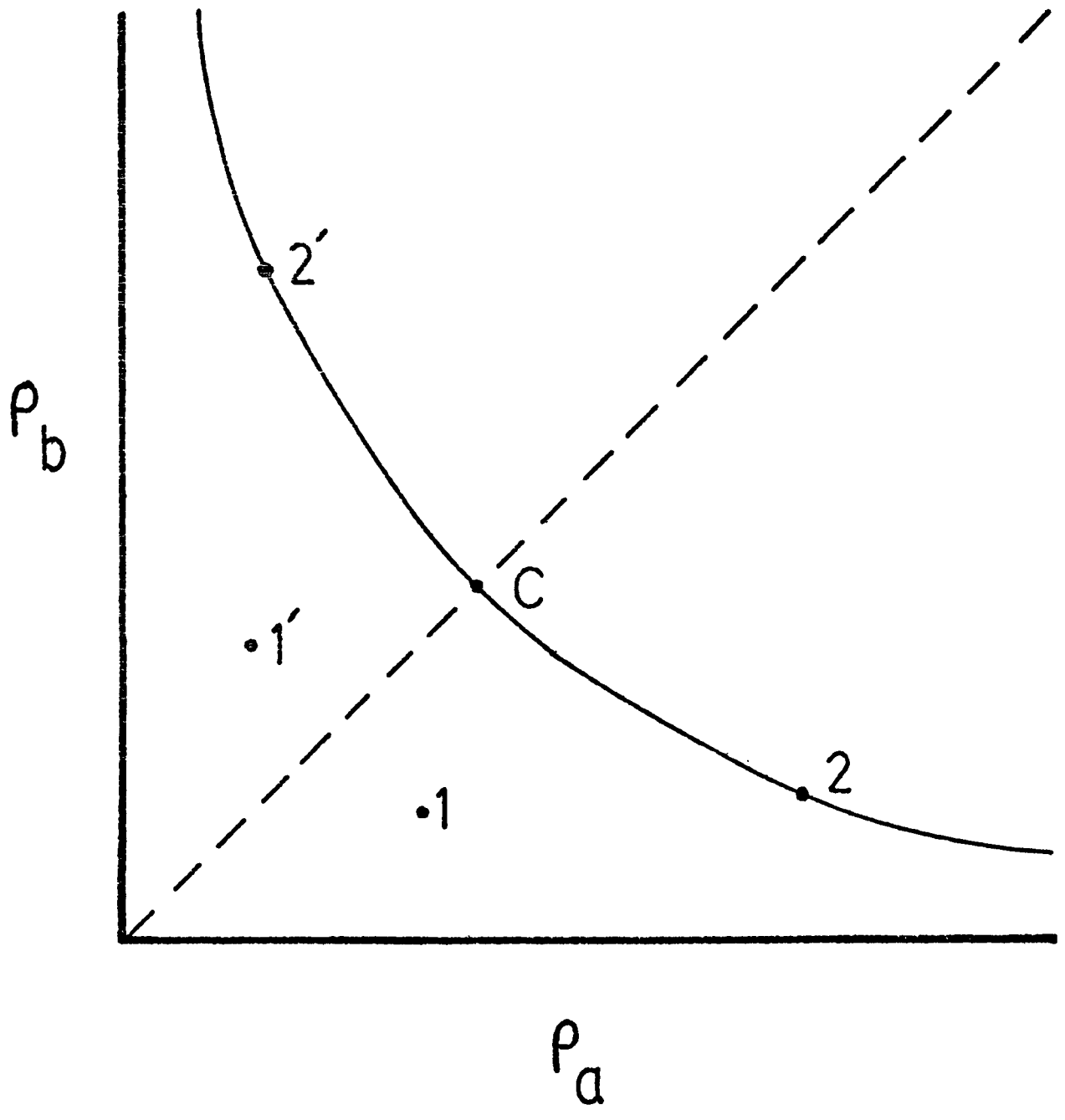
$$= \Pi_{(1)} + \theta \qquad (2.2.13)$$

This is the fundamental connection between the primitive and transcribed versions of the model.

The phase diagram of the two component system

Let us consider the phase diagram of a two component primitive system as function of reduced densities ρ_a and ρ_b. At very low densities the mixture of a and b molecules form a homogeneous single phase and as $\rho \to 0$ the system behaves as an ideal gas. As the relative densities of the components are increased the system forms two phases due to the positive repulsive potential between unlike species. Because of the symmetry of the model, the two-phase boundary is symmetrical about the line $\rho_a = \rho_b$ in Figure 2.1. The critical point, defined when each species occupies the same volume (Rowlinson, 1969), lies on the two phase boundary at $\rho_a = \rho_b$.

Figure 2.1. Sketch of the phase diagram of the binary primitive system. Two pairs of conjugate points, and the critical point are shown. The dashed line is the line of symmetry.



The critical point is at $\rho_a = \rho_b \simeq 1.1$ (Rowlinson, 1980). In the Monte Carlo simulation fluctuations in density are very large around the critical point so we must choose points well into the one-phase and two-phase regions at which to simulate.

Thermodynamic functions in the mean-field approximation

The thermodynamic and structural results from the Monte Carlo simulation gives us an exact set of results to compare with approximate solutions of the penetrable sphere model. Until now we have only considered exact consequences of the model. However to obtain the properties of the model we must introduce some approximations. In this section we discuss the model in the mean-field approximation.

The exact evaluation of the partition function and thermodynamic properties is only possible for dimensionalities, d,of 1 and ∞. For all other systems these functions can only be evaluated with the aid of approximations. If N spheres in our model, each of volume v_o, are randomly distributed in volume V, then the mean covered volume <W> in the thermodynamic limit (Widom and Rowlinson, 1970) is

$$<W>/v = 1 - e^{-\rho} \qquad (2.2.14)$$

This is the equilibrium distribution at infinite temperature ($\theta = 0$), and at non zero values of θ is a mean-field approximation. At $\theta > 0$ the true equilibrium distribution is found by weighting

<W> by the Boltzmann factor, exp (−β U(N)), where U(N) is the potential energy related to W by eqn (2.2.12). The averages $\bar{U}$ and $\bar{W}$ cannot be evaluated directly but may be expressed as a cumulant expansion in θ, where <U> and <W> are the leading terms independent of θ.

We use the property that the thermodynamic results are exact for d = ∞ (Rowlinson, 1980) and use this as an approximation for all d greater than unity. In the primitive version this leads us to the equation of state where all terms with virial coefficients above the second are neglected. The equation of state is given by

$$\Pi_{(2)} = \rho_a + \rho_b + \rho_a\rho_b \qquad (2.2.15)$$

In this solution the mean-field approximation has been used to replace the canonical average <U(θ)>/v by <U(θ = 0)>/v.

If higher terms in the virial expansion are retained the result for the equation of state is more accurate. Coefficients, C_{ij}, of the expansion have been evaluated for the configurational free energy per molecule up to the seventh term (Melnyk et al., 1972). The free energy $A_{non\text{-}ideal}$ differs from that of the perfect gas by

$$k_B T \sum_{i=1} \sum_{j=1} (\rho_a)^i (\rho_b)^j C_{ij} \qquad (2.2.16)$$

and the total free energy of the system is

$$A = -(\rho_a + \rho_b)\, k_B T V - kT \sum_{i=1} \sum_{j=1} (\rho_a)^i\, (\rho_b)^j\, C_{ij} \qquad (2.2.17)$$

The pressure p is given by

$$p = -\left(\frac{\partial A}{\partial V}\right)_{N,T,\mu}$$

$$= (\rho_a+\rho_b)k_B T + Nk_B T\ \frac{d}{dV}\left(\sum_{i=1} \sum_{j=1} \frac{N_a}{v}^{i}\ \frac{N_b}{v}^{j}\ \frac{N_a+N_b}{v}^{-1}\ C_{ij} \right)$$

$$= (\rho_a+\rho_b)k_B T + Nk_B T\ \frac{d}{dV}\left(\sum_{i=1} \sum_{j=1} \frac{N_a^i N_b^j}{N}\, V^{-i-j+1}\, C_{ij} \right)$$

$$= (\rho_a+\rho_b)k_B T + k_B T \left(\sum_{i=1} \sum_{j=1} (-i-j+1)\, N_a^i N_b^i\, V^{-i-j}\, C_{ij} \right)$$

$$= (\rho_a+\rho_b)k_B T - k_B T \sum_{i=1} \sum_{j=1} (i+j-1)\, \rho_a^i\, \rho_b^i\, C_{ij}$$

The usual form of this equation is

$$\frac{p}{k_B T} = \rho_a + \rho_b - \sum_{i=1} \sum_{j=1} (i+j-1)\, \rho_a^i\, \rho_b^i\, C_{ij} \qquad (2.2.18)$$

Values for C_{ij} are given in Table 2.1. In section 4 we compare the results of the simulation in the one-phase region to equations (2.2.15) and (2.2.18). Now that we have considered some of the thermodynamic properties of the penetrable-sphere model we conclude this section

Table 2.1

The coefficients C_{ij} in the density expansion for the equation of state. The evaluation of the integrals is a problem in bichromatic graph theory, that is, graphs in which the nodes have one of two colours, and only nodes of unlike colour are joined (Helfand and Stillinger, 1968; Melnyk et al., 1972).

i	j	C_{ij}
1	1	-1.0
1	2	0
2	2	8.095×10^{-2}
2	3	1.220×10^{-2}
3	3	-8.824×10^{-3}
2	4	1.646×10^{-3}
2	5	1.985×10^{-4}
3	4	-3.687×10^{-3}

with a brief discussion of some of the structural aspects of the model.

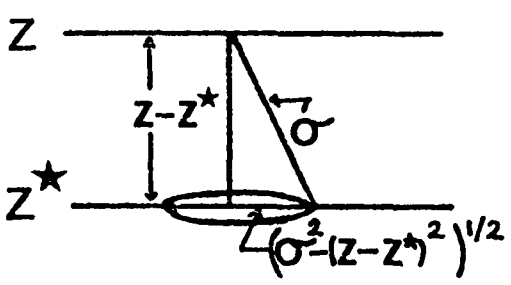
Equations for the density profile in the two phase region of the model in the mean-field approximation have been derived (Leng et al., 1976). An analytic solution is possible for potentials of one dimension, (i.e. a penetrating line). For higher dimensions these equations can be solved by straightforward numerical integration. Let us consider the derivation of the density profile for a system without external constraints (Leng et al., 1976) and extend this to a system bound by hard walls.

The density of molecules $\rho(z)$ on each plane of fixed z is calculated in the mean-field approximation as follows. Consider a slice at height z of thickness δz and area A. The number of molecules with centres in this slice is proportional to the reduced density $\rho(z)$,

$$N(z) = \rho(z)(A/v_o)\ \delta z$$

Let z^* be a plane within distance σ of z. The probability that a point on z^* is covered by a sphere whose centre is in δz is

$$\Pi(\sigma^2 - (z - z^*)^2)/A;|z - z^*|<\sigma \qquad (2.2.19)$$



The probability that a point on z^* is not covered by any of the spheres in the slice is

$$\left(1 - \Pi(\sigma^2 - (z-z^*)^2)\frac{\rho(z)\delta z}{N(z)\ v_o} \right)^{N(z)} \qquad (2.2.20)$$

The limit as A becomes infinite, is denoted by $\rho(z^*, \delta z)$; and

$$\ell n\ \rho(z^*, \delta z) = - \Pi(\sigma^2 - (z-z^*)^2)\ \frac{\rho(z)\delta z}{v_o} \qquad (2.2.21)$$

Hence the probability that a point in z^* is not covered by a sphere is

$$\ell n\ \rho(z^*) = - \int_{z^*-\sigma}^{z^*+\sigma} \frac{\Pi(\sigma^2-(z-z^*)^2)}{v_o}\ \rho(z)dz \qquad (2.2.22)$$

Let $(z - z^*) = x$ and $\sigma = 1$ and (2.2.22) becomes

$$\sigma(z^*) = \frac{3}{4}\int_{-1}^{1} (1-x^2)\ \rho(z^*+x)\ dx\ , \qquad (2.2.23)$$

which is the probability that a point in z^* is not covered by a sphere. The density is related to (2.2.23) by (Leng et al., 1976),

$$\rho(z) = \theta\ e^{-\sigma(z)} \qquad (2.2.24)$$

where θ is given by

$$\theta = \Delta \operatorname{cosech}(\Delta) \exp(\Delta \coth \Delta) \qquad (2.2.25)$$

and

$$\Delta = (\rho_a - \rho_b)/2 \qquad (2.2.26)$$

If we introduce a hard wall into the system we replace the limits of integration in equation (2.2.23) by

$$\sigma(z) = \frac{3}{4} \int_q^r (1-x^2)\, \rho(z+x)\, dx \qquad (2.2.27)$$

The lower limit q is -1 for all $z > z_{min} + \sigma$ and the upper limit r is $+1$ for all $z < z_{max} - \sigma$. In the region $z_{min} + \sigma$ and $z_{max} - \sigma$ the volume not covered $\sigma(z)$ is affected by the vicinity of the hard walls at $z = z_{min}$ and $z = z_{max}$. In this region the limits are $q = -x$, $r = 1$; $z_{min} < z < z_{min} + \sigma$ and $q = -1$, $r = +x$; $z_{max} - \sigma < z < z_{max}$. Physically the hard wall means the volume is not covered, $\rho(z) = 0$ for $z < z_{min}$ and $z > z_{max}$, which implies $\sigma(z)$ will become less as we approach the walls. From equation (2.2.24) we predict the density to increase near the walls.

Equation (2.2.27) can be solved numerically by a trapezoidal rule integration over the range of the density profile. From the estimate of $\sigma(z)$, $\rho(z)$ can be determined via (2.2.21). The new values for $\rho(z)$ then replace the initial estimate of $\rho(z)$ in (2.2.20) and a new value of $\sigma(z)$ is calculated. This cyclic process is repeated until $\rho(z)$ converges to an accuracy of $O(10^{-5})$. The initial value of $\rho(z)$ is the analytic solution for s = 1. The density profile for s = 1 is given by (Leng et al., 1976)

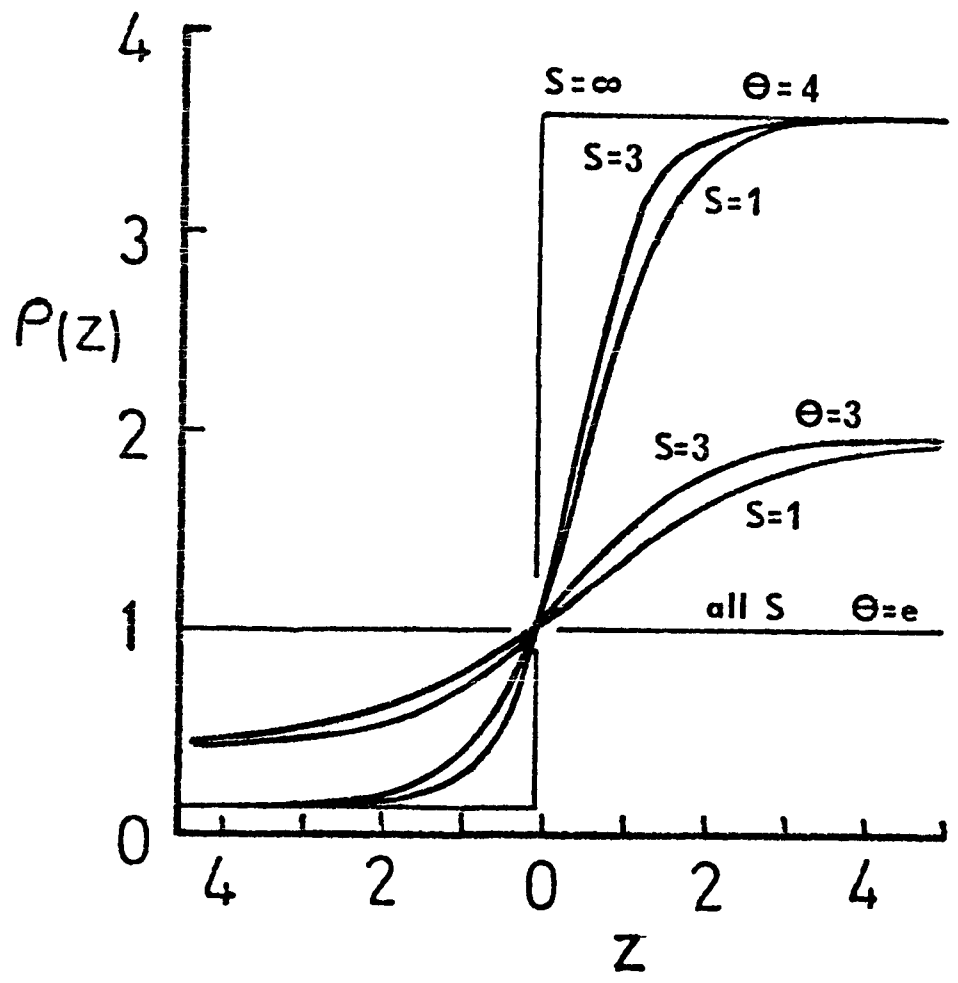
$$\rho(z) = \bar{\rho} + \Delta \tanh\left(\frac{\Delta}{4z} (z - z_o) \right) \qquad (2.2.28)$$

where z_o is the Gibbs surface excess free energy, and $\bar{\rho} = \Delta \coth \Delta$. For all values of $\theta > \theta c$, $z_o = 1/2$. Figure 2.2 shows a plot of the profile for s = 1 at $\theta = 3$. Results for the iterative solution of the density profile are presented in section 5 and are compared to the profiles obtained from the simulation.

2.3 The Monte-Carlo Method

Extensive studies of molecular systems have been made by use of the Monte-Carlo method, these include hard sphere fluids (Metropolis et al., 1953; Wood and Parker 1957); mixtures of hard spheres (Smith and Lea, 1963); Lennard-Jones atoms (Verlet and Levesque, 1967); diatomic hard dumbells (Streett et al., 1975; Freasier, 1975) and the gas-liquid interface (Chapela et al., 1975).

Figure 2.2 The surface profile for different values of the dimensionality S of the potential, at $\theta = \theta_c = e$ and at $\theta = 3$ and 4.



The Monte Carlo process develops a Markov chain of states of the system. The sequence of states is not the same as the time evolution of the system, but if we use the Metropolis (1957) sampling procedure the unweighted average over states in the chain is equivalent to the canonical average if the system is ergodic to the time average.

In this study we adopt the primitive version of the penetrable sphere model to investigate the liquid-vapour interface. This is chosen in preference to the transcribed version because of the potentials involved. In the primitive version there is essentially a mixture of hard spheres which interact via equation (2.2.2). The nature of this potential allows us to use the condition of pairwise additivity i.e.

$$U(\underset{\sim}{r}_1 \cdots \underset{\sim}{r}_N) = \sum_{\substack{\alpha=1 \\ \alpha\neq\beta}}^{N-1} \sum_{\beta=2}^{N} U_{\alpha\beta}(\underset{\sim}{r}_{\alpha\beta}) \qquad (2.3.1)$$

Pairwise additivity not only makes the calculation of the interaction energy in the system simple but it also allows us to relate the thermodynamic state functions via the radial distribution function. For example the pressure equation for a two component system of hard spheres in the canonical ensemble is related to the pair distribution function (Smith and Lea, 1963) by

$$\frac{P}{(\rho k_B T)} = 1 + \frac{2\pi N}{3V}\left(x_\alpha^2 \sigma_{\alpha\alpha}^3 g_{\alpha\alpha}^+(\sigma_{\alpha\alpha}) + 2x_\alpha x_\beta \sigma_{\alpha\beta}^3 g_{\alpha\beta}^+(\sigma_{\alpha\beta}) + x_{\beta\beta}^2 \sigma_{\beta\beta}^3 g_{\beta\beta}^+(\sigma_{\beta\beta})\right), \qquad (2.3.2)$$

where x_α and x_β are the mole fractions of species α and β and $g^+_{\alpha\alpha}(\sigma_{\alpha\alpha})$ is the value of the radial distribution extrapolated to contact. For the penetrable sphere model with a potential of the form of equation (2.2.2) the pressure equation is

$$\frac{p}{\rho k_B T} = 1 + \frac{4\pi N}{3V} x_\alpha x_\beta \sigma^3_{\alpha\beta} g^+_{\alpha\beta}(\sigma_{\alpha\beta}) \qquad (2.3.3)$$

If we considered calculating the potential energy from the transcribed version where

$$U(\underset{\sim}{N}_a) = [W(\underset{\sim}{N}_a) - N_a v_o] \varepsilon / v_o$$

the assumption of pairwise additivity is no longer valid. The calculation of this potential would involve a complicated process to evaluate the co-volume occupied by the inter-penetrating spheres.

As we can see from equation (2.3.3), the pressure only depends on the radial distribution function of unlike species. This correlation function may be defined as the factor that multiplies the bulk density, ρ, of the system to give a local density $\rho^{(1)}(r_{12}) = \rho g(r_{12})$, r_{12} away from some fixed molecule 1 (McQuarrie, 1976). As $r_{12} \to 0$, $g(r_{12}) \to 0$ because the molecules become hard, and as $r_{12} \to \infty$, $g(r_{12}) \to 1$ because the influence of the fixed molecule diminishes. g(r) is numerically calculated by dividing the density

of molecules in a volume element r + dr (from a fixed molecule) by the bulk density of the fluid. The radial distribution function at point of contact, $g^{+}(\sigma)$, is determined by extrapolating g(r + dr) for $r > \sigma$ to $g^{+}(\sigma)$. The number density of molecules in the volume element r + dr about any fixed molecule is the cumulative sum of all molecules in the shell r + dr for the simulation averaged over the number of samples and divided by the number of molecules.

The canonical average of a function of position F(r) is given by,

$$\langle F(r) \rangle = \frac{\int_{v} e^{-\beta U(\underset{\sim}{r}^{N})} F(\underset{\sim}{r}^{N}) \, d\underset{\sim}{r}^{N}}{\int_{v} e^{-\beta U(\underset{\sim}{r}^{N})} d\underset{\sim}{r}^{N}} \qquad (2.3.4)$$

or in the simulation we replace the integral by a sum over many configurations

$$\langle F(r) \rangle = \frac{\sum_{i=1}^{M} \exp\,[-\beta U(i)]\, f(i)}{\sum_{i=1}^{M} \exp\,[-\beta U(i)]} \qquad (2.3.5)$$

Although M is finite it is an extremely large number and it would be impractical to attempt to sample over all of the M configurations. One method is to sample over a subset of configurations (Hammersley and Handscomb, 1964) but the problem with this crude sampling method is that a high proportion of improbable states may be selected. It is therefore necessary to introduce a form of importance

sampling. One solution is that of a Markov-chain process (Wood and Parker, 1957) in which a state is compared to its previous state and is rejected or accepted with a certain probability.

Let the system be in state i at "time" t. We displace a molecule along each axis randomly in the interval of uniform distribution $(-\delta,+\delta)$ to give a trial state i at t + 1. The potentials U(i) and U(j) are compared. If $U(j) < U(i)$ it follows (Hansen and McDonald, 1976) that state j has a higher probability than state i and it is accepted as the new state. If $U(j) > U(i)$ then we accept state j with the probability $\exp [-\beta(U(j) - U(i))]$. This is done by comparing $\exp [-\beta(U(j) - U(i))]$ with random number, R, in the interval (0, 1) and accepting state j if $\exp [-\beta(U(j) - U(i))] > R$.

If the trial state j is rejected then the old state i is retained as the new state and included again in the average.

The choice of δ, the maximum displacement, for dense fluids is usually made so that approximately 60% of states are rejected. It is believed that this value of δ gives rise to the most rapid convergence of the sampling to the canonical average. We note δ is density dependent.

The algorithm used for the simulation of penetrable spheres is based on an efficient procedure presented by Wood (1959). We begin by randomly selecting a molecule β in configuration j(t). This molecule is displaced randomly on the interval $(-\delta, \delta)$ to produce a trial configuration denoted by j'(t). The new configuration

is tested for overlaps, that is the intermolecular distance between pairs of molecules is less than σ. If no overlap occurs we accept the new configuration; i.e. $j(t + 1) = j'(t)$. Likewise if an overlap does occur the old configuration is retained, $j(t + 1) = j(t)$. Averages are then performed and the procedure begins again. Let us consider the algorithm in detail.

The Monte-Carlo Program

To study the properties of a macroscopic system, V ~ 1 cm^3, N is of the order of 10^{22}. However computer capacities and realist run times only allow us to simulate N of order 10^2 ~ 10^3. Just as theories radically reduce the dimensionality of a problem to make it tractable,we must make a similar reduction in the dimensionality of phase space before undertaking numerical work. This is done by applying periodic boundary conditions and using the minimum imaging technique.

Periodic boundary conditions confine the molecules to a unit cube in space. If a molecule leaves through one face of the cube another will enter through the opposite face, i.e. the unit cube is surrounded by an infinite number of image cubes. Because the unit cube is surrounded by images of itself we can only consider interactions with the nearest image of another molecule. The minimum image convention restricts the maximum interaction distance from any molecule to a distance of half the box length (all images of a molecule are separated by the box length).

If the simulation cell is confined to a cube, the choice of N is usually taken to be $4n^3$; n = 1, 2, 3... or N = 4, 32, 108, 256, 500... This number enables us to place the N molecules into a cubic close packed lattice which is a convenient starting configuration.

Selecting a molecule and displacing it in space is straightforward but the procedure to test for overlaps can be done in a number of ways. The immediately obvious method is to construct an r-table that stores the x, y, z co-ordinates of each molecule. The N(N-1)/2 intermolecular distances are calculated at each "time" step and tested for overlaps. This method is extremely time consuming so we must develop a more efficient method for testing the overlaps. Since δ is a small distance relative to the box size only a limited number of molecules within the immediate vicinity of the displaced molecule, β, will possibly come into overlap. For each molecule we associate a nearest neighbour list which contains the labels of molecules that may interact if β is displaced.

We define the nearest neighbour list as follows (Wood, 1959). Let d_4 be a distance from the centre of a molecule, α, inside which volume all molecules will be in the nearest neighbour list of α. The neighbour table is defined as $\mu(\alpha,\gamma)$ where $\alpha = 1,...N$ and $\gamma = 1,2...n$ for which $[r_\alpha - r(\alpha,\gamma)]^2 < d_4^2$. We also define a distance d_3 ($\sigma < d_3 < d_4$) out from the molecular centre to α which we wish to include our statistics. The distance $d_3 - \sigma$ is divided into s segments and is associated with a C-table, C(v); v = 1,2....s.

Two position tables are also defined ; an r-table containing the position co-ordinates at j(t) and an r_o-table containing the position co-ordinates of each molecule at the last time its nearest neighbour table was updated. These tables are identical at t = 0, (the initial configuration). It can be readily shown that as long as a molecule lies within a distance $d = (d_4 - d_3)/2$ of its r_o position, only those molecules in the μ-table ($< d_4$) approach closer than d_3, (i.e. contribute to the statistics or overlap). This implies that the neighbour list is updated for a molecule if it moves a distance d from its r_o position. The advantage of this method of neighbour listing and updating is that when a molecule does move d away from its r_o-position; the only updating required is for the nearest neighbour list of the displaced molecule itself and limited alteration to the lists of nearby molecules. Other methods (Tildesley, 1976) require a larger neighbour list and after a given number of time steps the neighbour list for the whole system is updated.

Since we only wish to evaluate $g^+(\sigma)$ the distance d_3 does not need to be large ($d_3 \sim 1.2 - 1.3\sigma$). The distance $d_3 - \sigma$ ($\sim 0.2 - 0.3\sigma$) can be divided into enough segments to give accurate values from g(r) from which $g^+(\sigma)$ can be extrapolated (Wood, 1959). The choice of d_4 is dependent on two criteria, firstly the maximum step size which will determine the frequency of updating nearest neighbour lists; and secondly the average number of neighbours that would occupy the volume inside d_4 as it is increased. Both of these factors are in competition with each other and experience

has shown that the most efficient runs were made when

$$d_4 = d_3 + 4\delta.$$

A listing of the program, MCPS is given in the appendix at the end of the thesis.

2.4 Simulation of the Penetrable Sphere Model in the One Phase Region

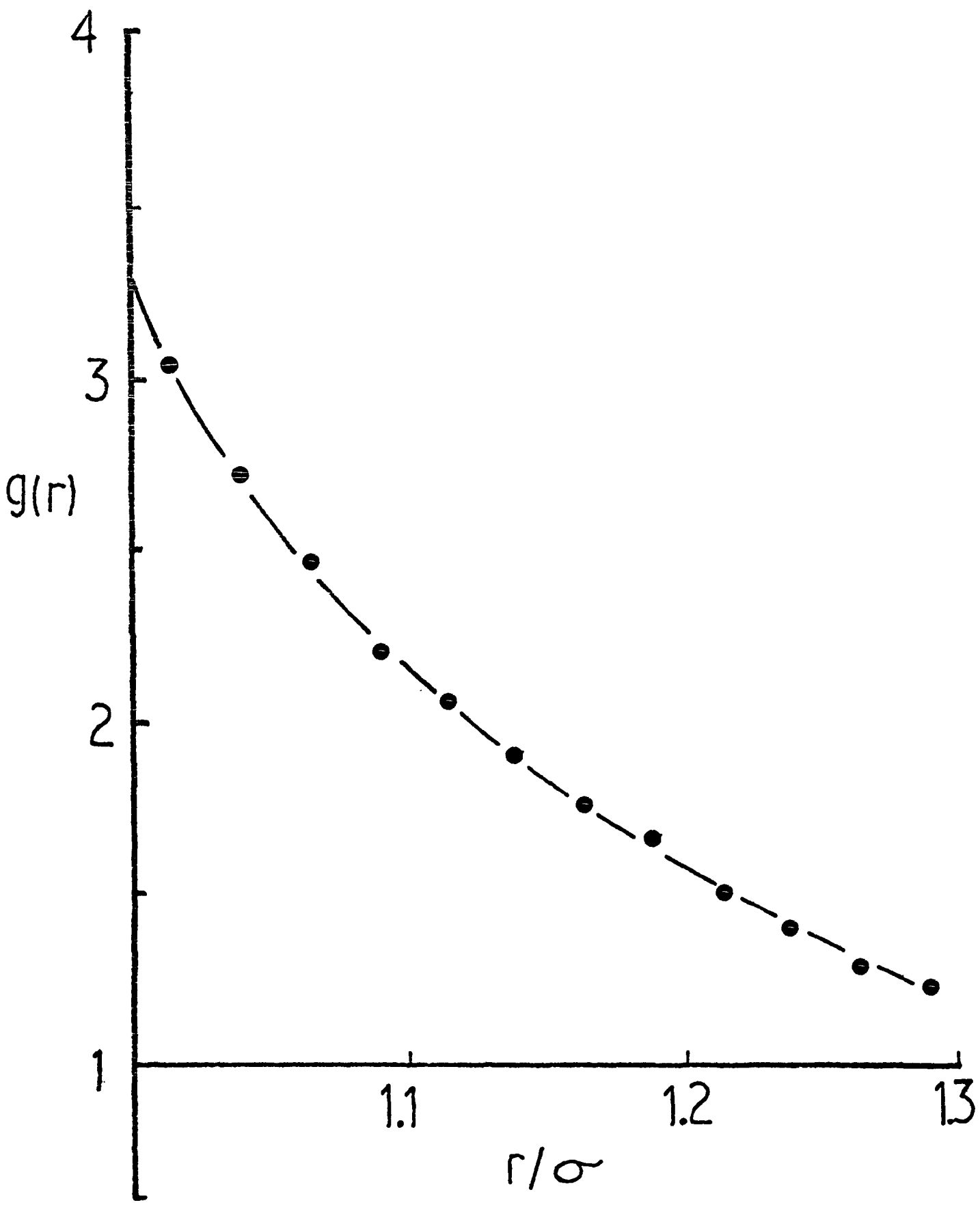
Before proceeding with any simulation we must first check the accuracy and correctness of the algorithm. In this case we make our whole system a one-component fluid of 256 hard spheres for which there are well known results (Temperly et al., 1968). If we define reduced density $\rho^* = N\sigma^3/V$ then a typical liquid density is at $\rho^* = 0.707$. Figure 2.3 shows the radial distribution function at $\rho^* = 0.707$; the extrapolated value at contact is $g^+(\sigma) \simeq 3.29 \pm 0.05$. The pressure for this system is given by

$$\frac{p}{k_B T} = 1 + \frac{2\pi}{3}\rho^* g^+(\sigma) , \qquad (2.4.1)$$

and at $\rho^* = 0.707$, $p/k_B T = 5.87$ Comparing this value to the results of Wood et al., (1959) agreement is exact. We also compare this result to the Carnahan-Starling equation of state for hard spheres,

$$\frac{p}{\rho k_B T} = \frac{1 + \eta + \eta^2 - \eta^3}{(1 - \eta)^3} \qquad (2.4.2)$$

Figure 2.3 The radial distribution function g(r) for a system of hard spheres, $\rho^* = 0.7071$, $g^+(\sigma) = 3.29 \pm 0.05$.



where $\eta = \frac{\pi N\sigma^3}{6V}$. This equation is accurate to within a few percent over the whole liquid range (Hansen and McDonald, 1976). At a density of 0.707 the Carnahan-Starling pressure is 5.83. The simulation result is within close agreement.

The simulation of the hard sphere system was performed on an ICL 2900 series computer, however it is found that to gain good statistics for the penetrable sphere model much longer run times are needed. Consequently the program was transferred to a CDC 7600 computer. Three state points are chosen in the one-phase region. The first two points are at densities of $\rho_a = \rho_b = 0.7$ and 0.8 which are well into the liquid range. The third point at $\rho_a = \rho_b = 0.9$ is much closer to the critical point ($\rho_a = \rho_b \simeq 1.1$).

A system of 250 a-spheres and 250 b-spheres is initialized from a simple cubic lattice where each a-species is surrounded by 6 b-species and vice-versa. The system is allowed to equilibrate over 50,000 configurations before any statistical averages are made. The radial distribution function is than averaged over the next one million configurations. (We note that by simulating along the line of symmetry the averages over the a-species is the same as the averages over the b-species. Consequently we can add the two sets of results to improve our statistics). The standard deviation of the radial distribution function is calculated over intervals of 5000 configurations and is used as a measure of the fluctuations in the system. The deviation is found to be very small for all runs, in the order of 5×10^{-4} of the distribution function values.

Figure 2.4 is an instantaneous plot of configuration one million for $\rho_a = \rho_b = 0.8$. The plot is a slice in x,y plane through the middle of the simulation cell. The radius of each circle is proportional to the amount of each sphere intersecting this particular plane. This figure demonstrates the periodic boundary conditions; the circles at the edges of the box have images on the other side of the box. We also see that like spheres interpenetrate while there is no overlap of unlike spheres.

Figure 2.5 shows the radial distribution functions for the three state points. Table 2.2 compares the values of the equation of state calculated from the Monte-Carlo simulation via equation (2.3.3) to the mean-field approximation (equation 2.2.15) and the virial expansion, equation (2.2.18). Agreement between theory and computer experiment is extremely good for densities of 0.7 and 0.8, however large fluctuations were observed in the radial distribution for $\rho_a = \rho_b = 0.9$. This indicates large fluctuations in density which can be explained by proximity of the critical point.

The simulation in the one phase region has shown the theory for predicting the equation of state to be extremely good at moderately low densities. Since the Monte-Carlo system is subject to large fluctuations near the critical point, the accuracy of the virial expansion could not be determined in this region. We shall now consider the region of space in which phase separation occurs.

Figure 2.4 A "snap-shot" of a slice through the box at configuration 1 million ($\rho_a = \rho_b = 0.8$). Some spheres and their images are marked.

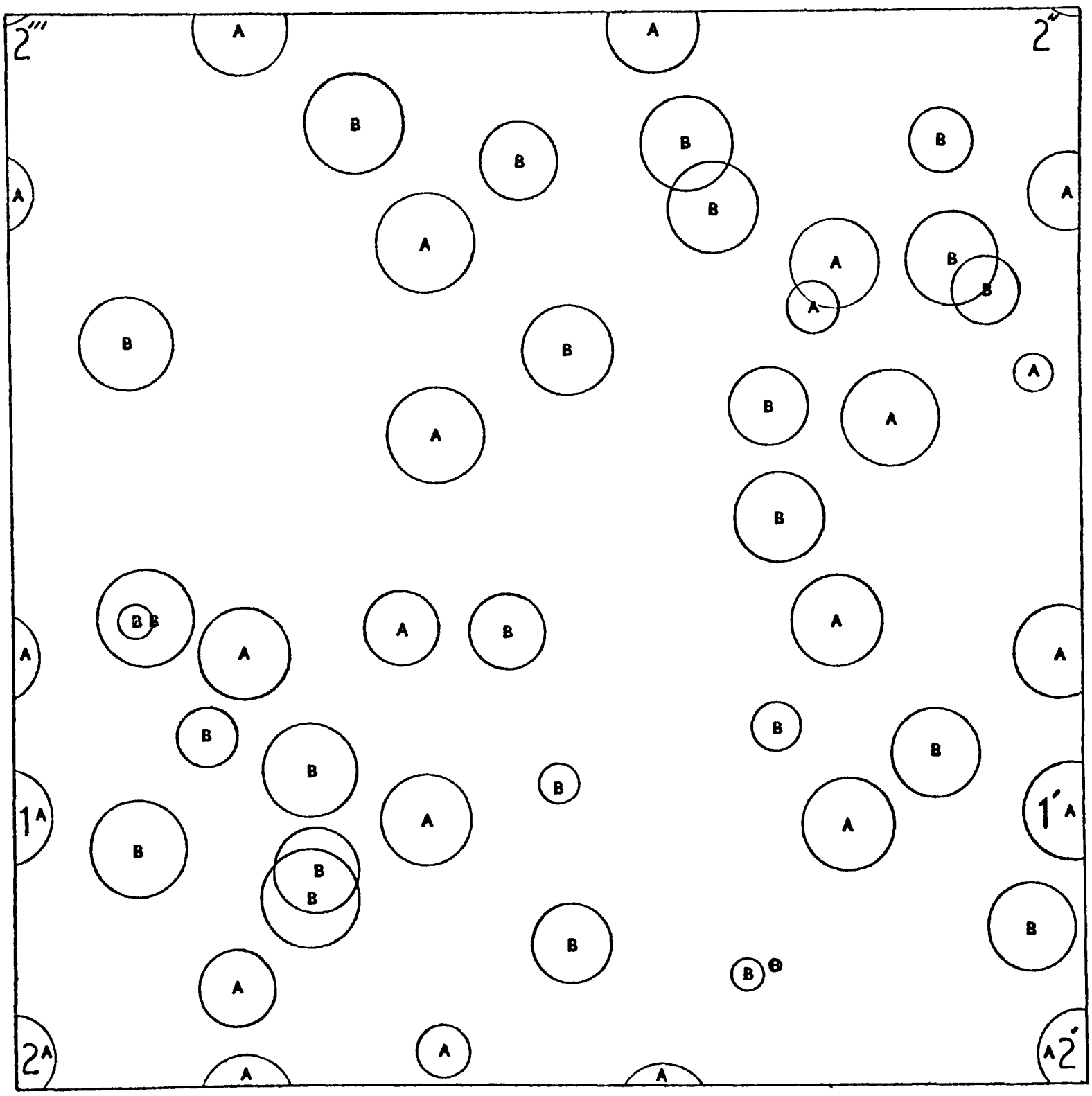


Figure 2.5 $g_{ab}(r)$ extrapolated to $r = \sigma$ at $\rho_a = \rho_b = 0.7$, 0.8 and 0.9. (At a density of 0.9 fluctuations in g(r) are too large to extrapolate to $g = \sigma$).

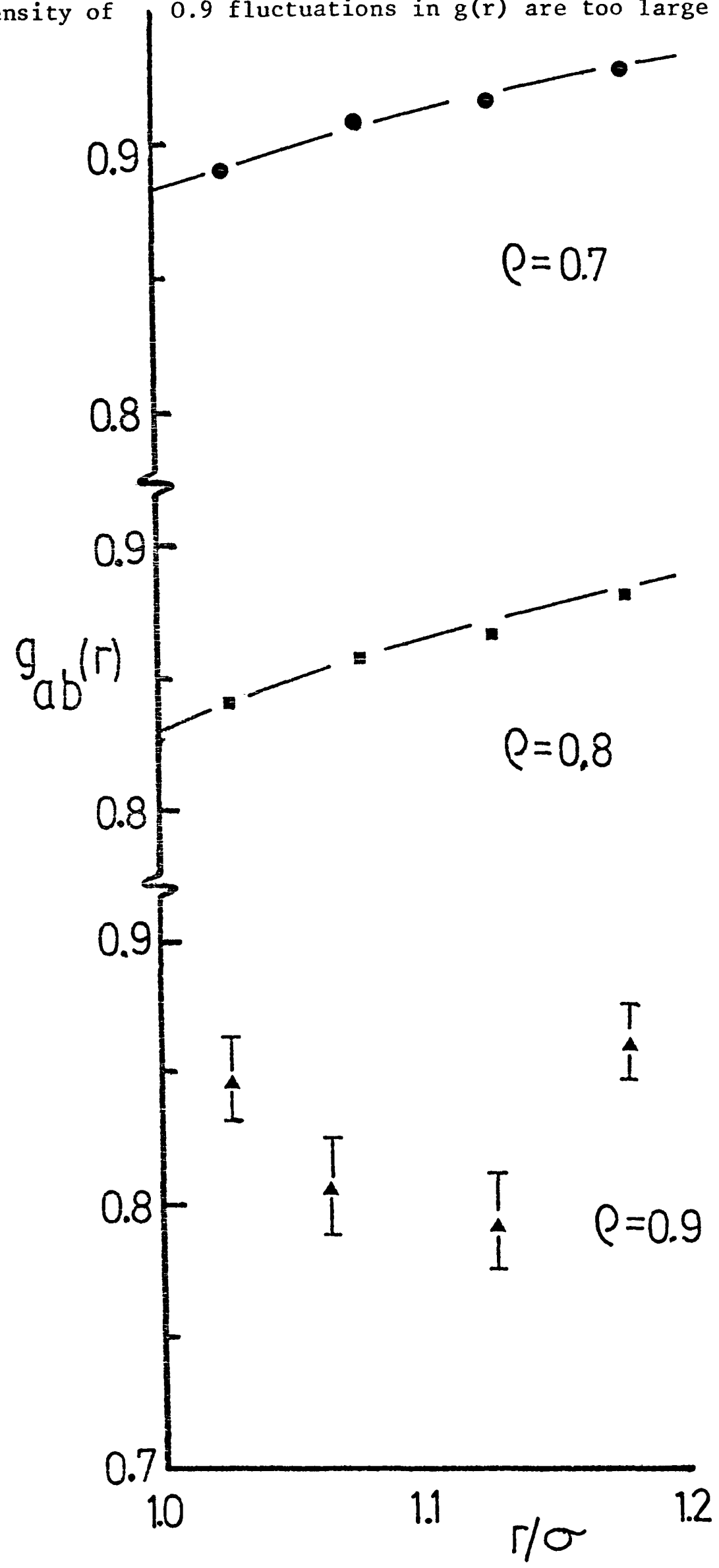


Table 2.2

The equation of state calculated from simulation, the mean field approximation (equation 2.2.15) and the virial expansion (equation 2.2.18).

		pv_o/k_BT		
ρ	$g^+_{\alpha\beta}(\sigma)$	simulation	mean field	virial
0.7	0.883 ± 0.015	1.829	1.89	1.832
0.8	0.833 ± 0.008	2.138	2.24	2.133
0.9	large fluctuations		2.61	

2.5 Simulation in the Two Phase Region

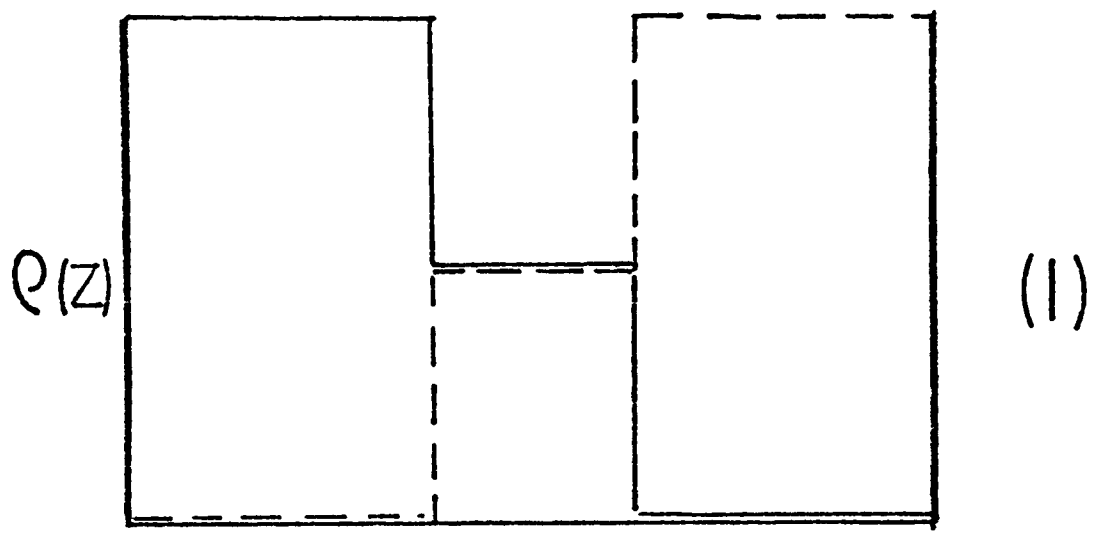
At high densities the penetrable sphere model separates into gas and liquid phases. The separation is observed in the primitive version at densities corresponding to initial mixture densities of $\rho_a = \rho_b = 2.0$ and $\rho_a = \rho_b = 2.4$. Various configurations are tested for initializing the mixture so that the most rapid equilibrium is achieved. These include (1) placing a bulk of each species at opposite ends of the cube and a homogeneous mixture in the middle; (2) placing a bulk liquid of each species at opposite ends of the cube and varying the density from the bulk liquid density to zero across the centre of the cube in a linear way; and (3) butting the two bulk species against each other. These initial profiles are illustrated in Figure 2.6.

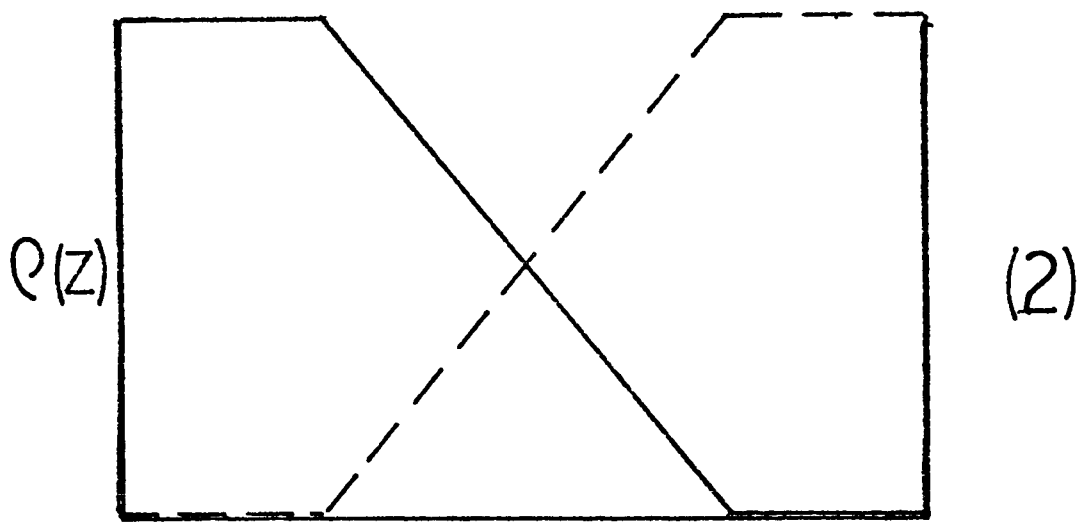
It is found that initializing from configurations (1) and (2), extremely long run times are required for equilibration, whereas initialization from (3) yields an acceptable rate of convergence to equilibrium.

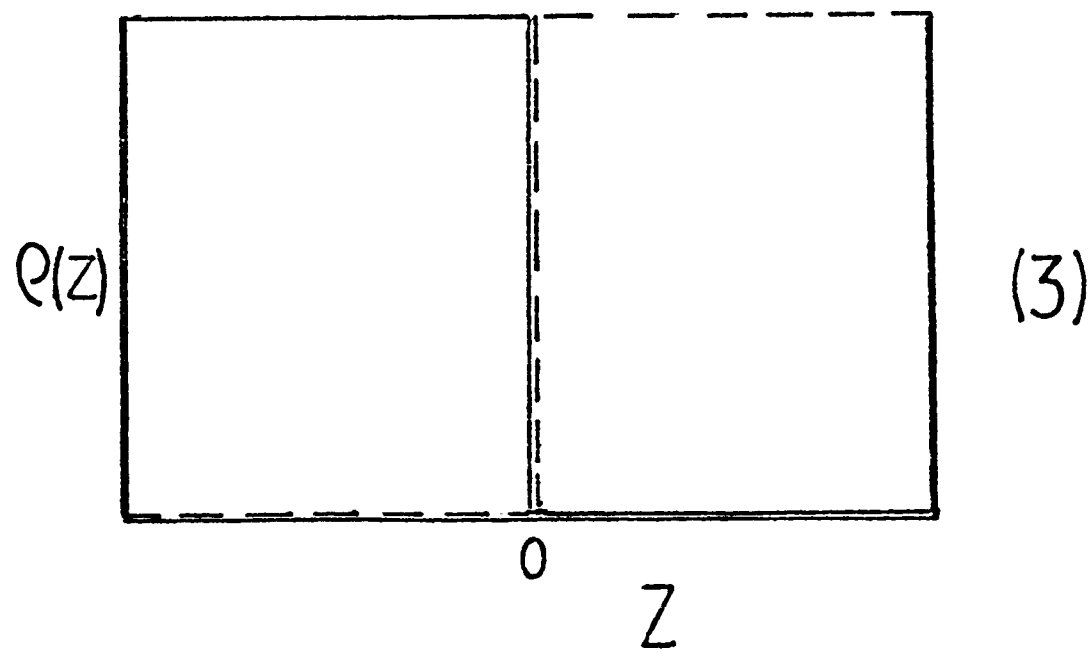
If the periodic boundary conditions are maintained in all directions the phase separation would occur in localized volume elements throughout the cube. To overcome this a hard wall is placed in the x,y plane at z_{min} and z_{max}. The centre of any sphere is not permitted to penetrate these walls while the periodic boundary conditions are still maintained in the x and y directions.

Besides forcing each species into 2 bulk phases (gas and liquid), the hard walls introduce a new and interesting effect

Figure 2.6 Starting configurations for the simulation in the two phase region - ρ_a, ----ρ_b.





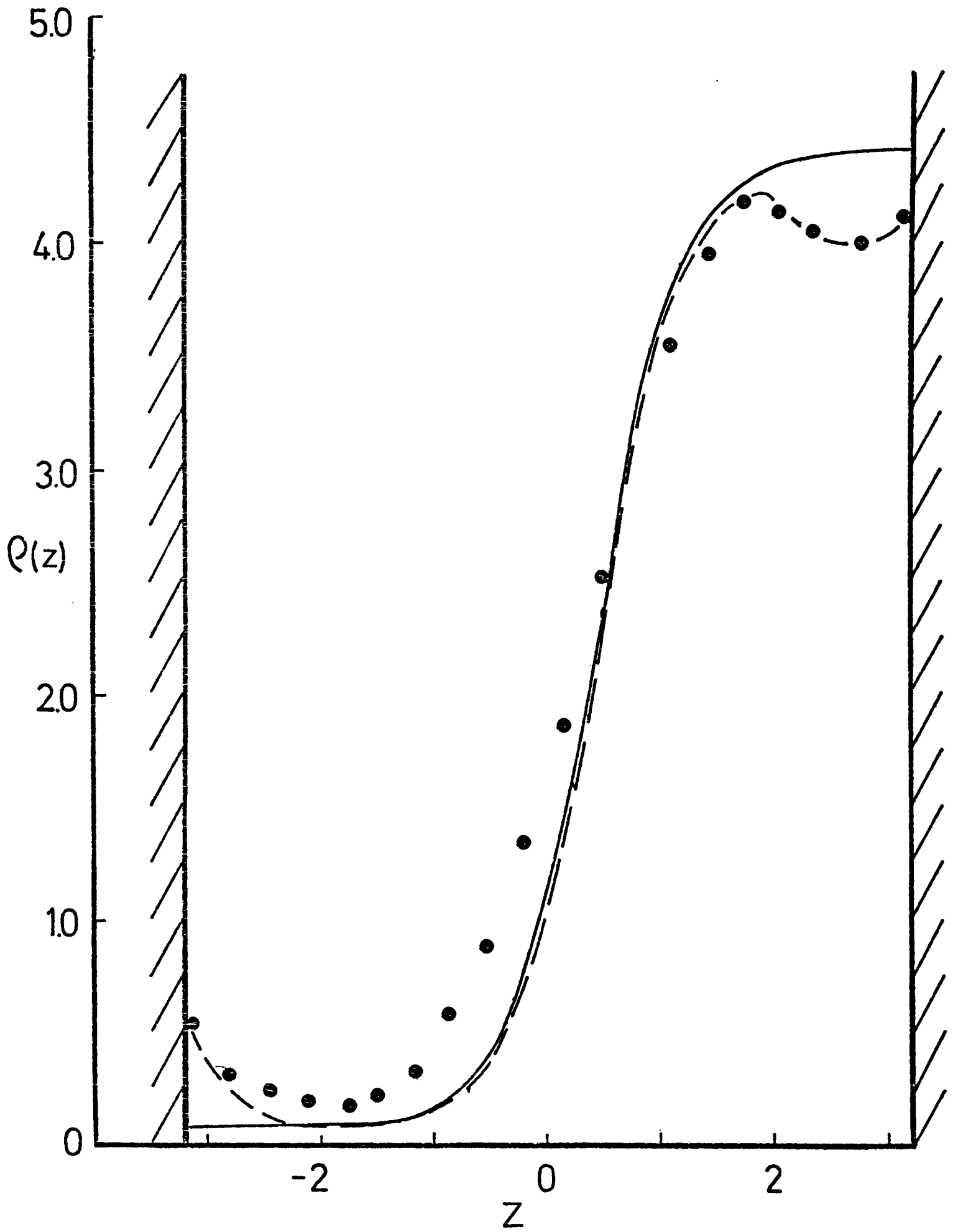


into the system. Not only do we expect to observe a phase separation in the middle of the box but we should expect to see the effects of the penetrable sphere model interacting with a surface. The expression for the density profile near a hard wall is discussed in section 2. However this phenomena was actually discovered from the results of the simulation and the theory realized as a consequence.

The simulations in the one and two-phase regions require many sample points to converge to the canonical ensemble compared to a system of hard spheres. With the computer time available we were only able to run three state points in the one-phase region and two state points in the two-phase region. In the two-phase region 128 a-spheres and b-spheres are simulated. The first simulation in the two-phase region is started at $\rho_a = \rho_b = 2.0$ corresponding to a final value of $\Delta = 2.2$. This system is run for 4 million configurations and the statistical averaging of the density profile is taken over the last 2 million configurations. The second system is initialized at $\rho_a = \rho_b = 2.4$ and corresponds to a final value of $\Delta = 2.75$. This system equilibrates more rapidly as it is further from the critical point and is run for 3 million configurations. The statistics are averaged over the last one million configurations. Figures 2.7 and 2.8 show the density profiles at the two state points.

The results of the simulation are compared with the mean-field integral equation for the density profile (equation 2.2.27), both with and without a constraining wall. Agreement between the

Figure 2.7 Profile $\rho_a(z)$ at an overall density of $\rho_a = 2.0$. The points are the results of the Monte Carlo simulation in a box of hard walls at $z_+ = -z_- = 3.20$, the solid line is the mean-field approximation for a system without hard walls and dashed curve for one with hard walls.



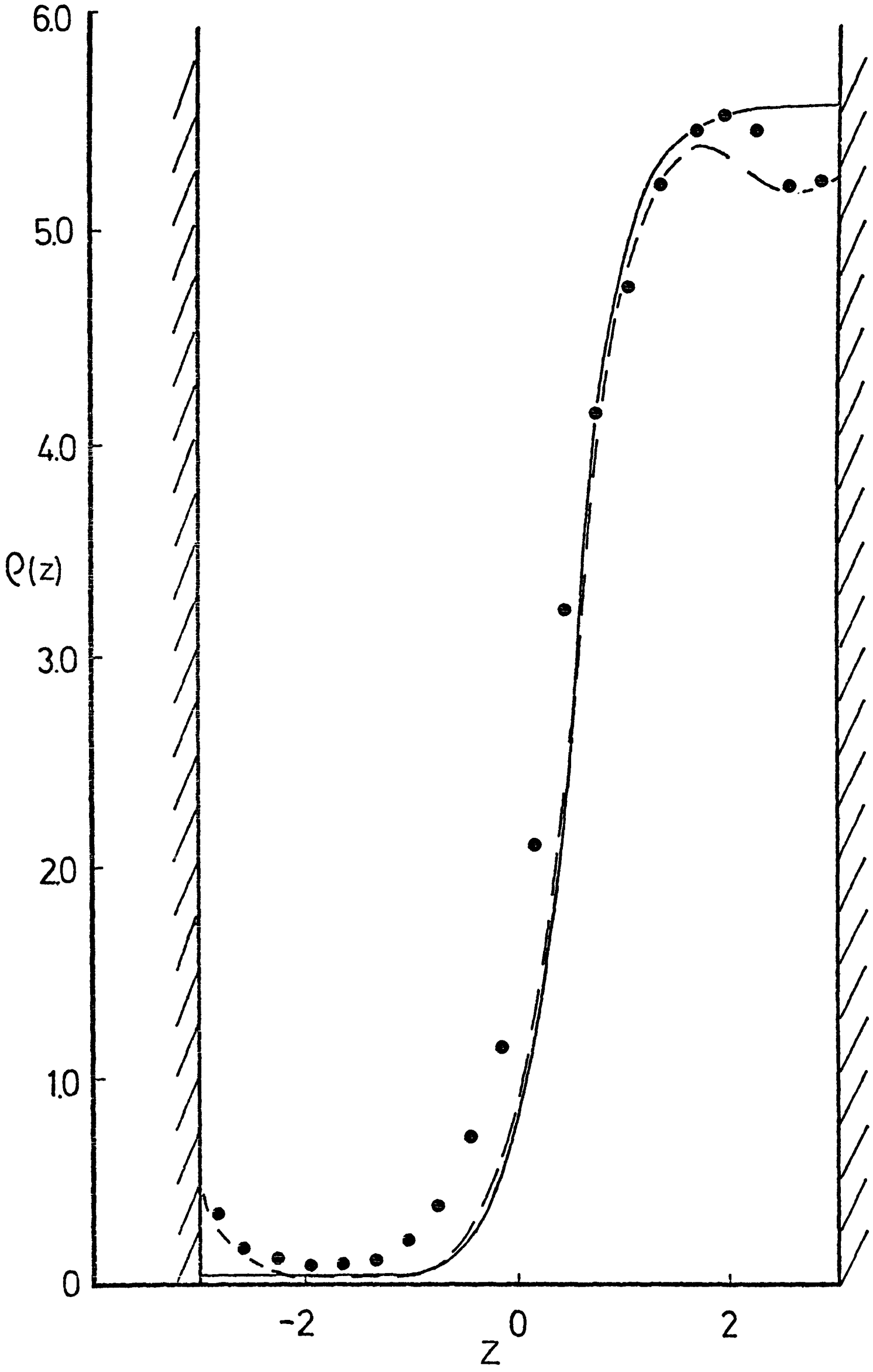


Figure 2.8 Profile $\rho_a(z)$ at an overall density of $\rho_a = 2.4$. Conventions as in Figure 2.7.

simulation and mean-field theory is very good; both sets exhibiting the expected properties near the wall. If the surface thickness is measured by the length $(\rho_a^\alpha - \rho_a^\beta)/\rho_a'$ where ρ_a' is the maximum value of $(d\rho_a/dz)$ and the superscripts α and β are the bulk liquid and gas densities, then it is found that the mean-field interface is too thin by $\simeq$ 30% in each case. Had the computer simulation been made over a larger sample it would probably have led to a thicker surface (Chapela et al., 1979) and so may have increased this discrepancy.

In this chapter we have used the simulation technique to test a theory of the gas-liquid interface. We have been able to show that the theory predicts most of the thermodynamic and structural properties of the model accurately in both the one-phase and two-phase regions, and also predicts the new phenomenon of the structure of the fluid near a hard wall. This last effect may be compared to physical adsorption of a fluid near a solid surface. In the next chapter we apply the simulation technique to a more realistic model of a fluid adsorbed on a solid surface and show how computer results are related to experiments of the real system.

CHAPTER 3

A Methane Molecule Adsorbed on Graphite

3.1 Introduction

Interaction site models have been used to study molecular liquids and solids with considerable success. These models consist of a number of interaction sites fixed rigidly with respect to one another in a molecule. Sites in different molecules interact via some well-known radial potential; Lennard-Jones, hard-sphere, Coulombic, Williams, etc. Generally the interaction sites coincide with the atoms in the molecule and the overall intermolecular potential is anisotropic. Recent reviews have noted that these models predict accurate cohesive energies, packing characteristics and barriers to rotation in molecular solids (Ramadas et al., 1978) and accurate structure factors, pressures and transport properties in molecular liquids (Chandler, 1978; Gubbins, 1977). Since they have proved useful in the homogeneous bulk phase, it is a natural extension to use them to model the interfaces between phases.

In this chapter we examine the behaviour of a single methane molecule adsorbed on a graphite surface using the technique of molecular dynamics. A single, adsorbed methane molecule is of interest because this represents the standard thermodynamic state at zero coverage (Steele, 1974, Chap. 3). The one particle simulation enables us to examine the methane-surface interaction without the additional complication of the methane-methane interaction.

In addition to the molecular dynamics simulation we perform a number of static calculations on adsorbed methane at a coverage of one monolayer to determine the nature of the methane-methane potential.

Our primary aims are to:

1) Determine a methane-surface pairwise potential which will reproduce the available thermodynamic and structural data;

2) develop molecular dynamics programs which will enable us to model small rigid molecules adsorbed on a graphite surface; and

3) use this effective-pairwise potential to examine the behaviour of a single molecule as it diffuses across the surface.

In constructing our model of surface adsorption we are obliged to make a number of simplifying assumptions. The methane molecule consists of five interaction sites (Murad et al., 1979, Murad et al., 1980) and the graphite surface consists of an infinite array of carbon atoms in a rigid two-dimensional hexagonal lattice. The surface is taken to be perfectly smooth and in the simulation we consider an area $\simeq 400$ $\mathring{A}^2$; (this area is surrounded by periodic images of itself). It is possible to obtain experimental samples of graphite with uniform smooth surfaces of these dimensions (Kjems et al., 1976) and our model results can be compared to experiments performed on these carefully prepared samples. The surface is assumed to be perfectly rigid. We ignore the coupling between the phonons of the solid and the adsorbate molecule. It has been shown that coupling can occur between the lattice

vibrations of the solid and the physically adsorbed species (Novaco et al., 1974). This is not a large effect and in our model we have made the simplest possible assumption that the surface atoms have infinite mass. We also assume that the second gradient of the electric field at the surface is small enough to ignore the octopole-field gradient contribution to the adsorption energy. This simplification can be justified a posteriori by a comparison of the interaction energy of the simple site-site model with the heat of adsorption at zero coverage. Finally we assume the methane molecule behaves as a classical particle, i.e. there are no quantum corrections to the free energy and there is no rotational tunnelling. A recent molecular dynamics study of an interaction site model of methane in the dense fluid (Murad et al., 1979) indicates that this classical assumption reproduces the experimental properties of the fluid accurately. The quantum correction to the gas surface second virial coefficient for adsorbed methane contributes approximately 3% at 225K (Sams et al., 1960). However, the quantum correction is more important at lower temperatures and a measure of this effect is discussed in the next chapter. These assumptions have been introduced to produce a tractable model for simulation which contains the essential features of the adsorption problem.

In the following section we discuss the details of the simulation and in Section 3 we propose various gas/surface potential models. In Section 4 the potential parameters for the models are determined and in Section 5 various properties of the model are discussed.

3.2 The Simulation

The molecular dynamics method was first applied to a system with continuous potentials by Rahman (Rahman, 1964). He simulated a system of liquid argon using Lennard-Jones and exp-6 potentials. A more systematic and thorough study of this system was made by Verlet and co-workers (Verlet et al., 1967, 1968, 1970, 1973). Since these first studies were made a large number of simulations of molecular fluids have been performed. A few include; studies of diatomic liquids (Streett and Tildesley, 1978), liquid nitrogen (Cheung and Powles, 1975) and dense fluid methane (Murad et al., 1979). The algorithm for the methane simulation has been modified and extended here to study the gas-solid problem.

This simulation differs from that normally used for a bulk liquid in that the surface atoms are rigid and that the surface has a hexagonal symmetry which can be usefully exploited. The unit cell of graphite is a rhombus of side 2.46 $\mathring{A}$ with an included angle of 120^{o}; (d = 2.46 $\mathring{A}$ is the distance used to reduce all lengths in the simulation). The unit cell contains two carbon atoms and the molecular dynamics cell has a rhombic base of side 12d and contains 288 carbon atoms. The basic structure and underlying hexagonal structure are shown in Figure 3.1 . The methane molecule is free to move in the z- direction out of the x-y plane, but has no mechanism for escaping completely from the surface at the temperatures studied. The basic cell is effectively infinite in the z- direction and is surrounded by periodic images of itself in the x-y plane. Each of the 144 unit

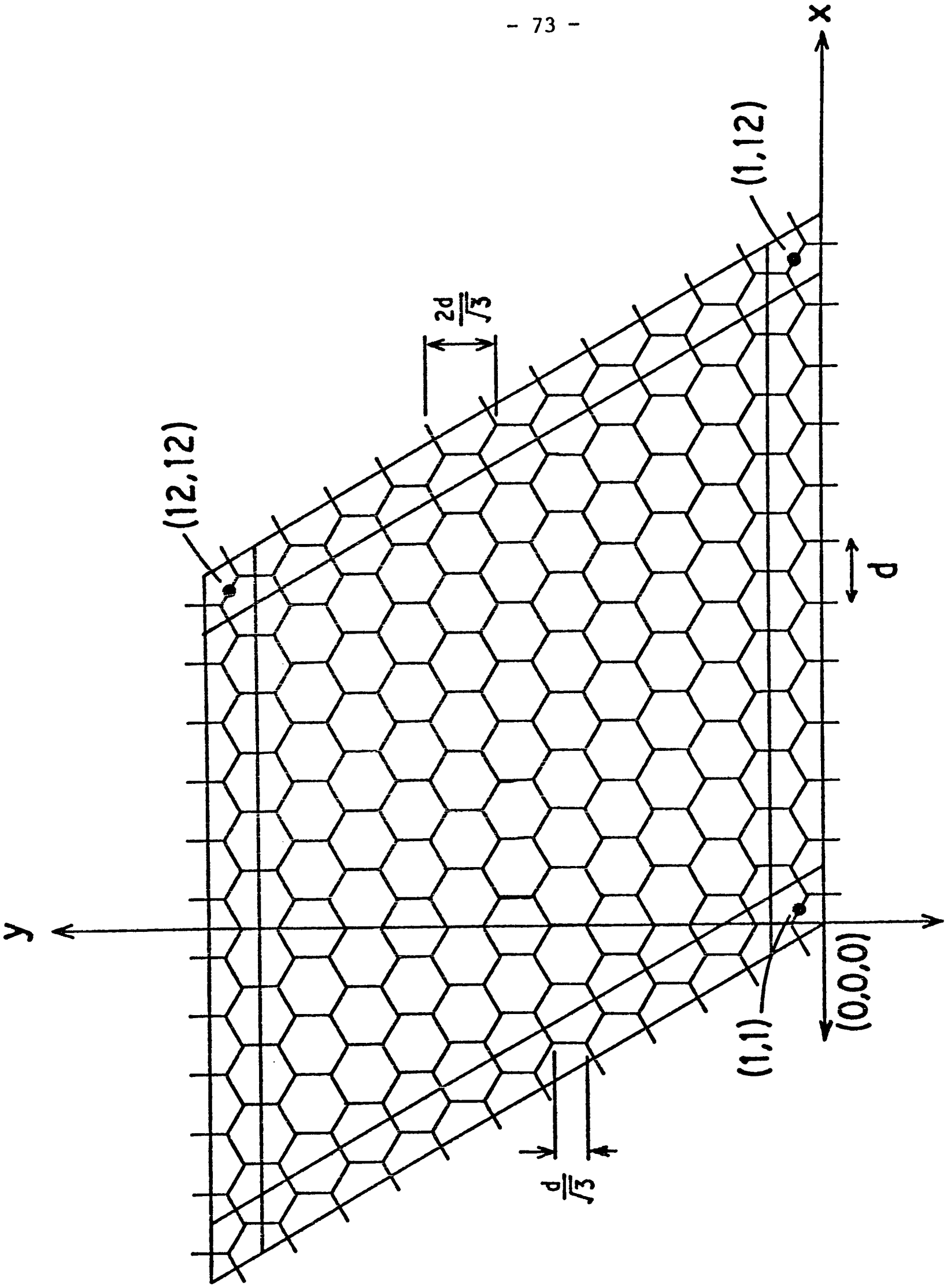


Figure 3.1 A plan of the basic cell used in the molecular dynamics simulation. The basic cell consists of 144 unit cells each containing two carbon atoms. The unit cells are labelled with an index (i,j) as shown. All coordinates are measured in a rectangular cartesian frame based on the origin (0,0,0). The cell is open in the z-direction (out of the page).

cells in the basic cell is surrounded by an identical and symmetrical environment in the surface; this enables us to adopt an efficient method for calculating distances between the atoms of the methane molecule and atoms in the surface. At the beginning of the simulation we calculate and store all the vectors from the centre of one unit rhombus to all the carbon sites of the surface within a specified cutoff distance r_c = 5.0d. Each unit rhombus in the cell is given a label (i,j) and the co-ordinates of the centre of mass (C.O.M.) of that unit rhombus are stored at the beginning of the simulation in an array A(i,j). The unit rhombi, (1,1), (1,12) and (12,12) are shown in Figure 3.1 . The co-ordinates of the centre of mass of the moving adsorbate molecule are measured in a rectangular cartesian frame shown in the same figure.

The site-site distances in the model can be calculated at any timestep using the following sequence of steps.

1) Use the co-ordinates of the C.O.M. of the methane molecule (x_m, y_m, z_m) to compute the index (i,j) of the unit rhombus below the methane

$$i = \text{int} \quad (x_m + y_m/\sqrt{3}) + 1$$

$$j = \text{int} \quad (2\, y_m/\sqrt{3}) + 1$$

2) Look up the C.O.M. of the unit rhombus A(i,j) and calculate the vector from this point to (x_m, y_m, z_m).

3) Use the prepared tables to calculate the vectors from (x_m, y_m, z_m) to all atoms on the surface within the cutoff.

4) Use the orientation and bond length of methane to calculate the vectors from (x_m, y_m, z_m) to each hydrogen atom in the molecule.

5) Calculate all the site-site distances by simple vector addition. This sequence gives all the information to calculate the interaction energy, the forces and torques exerted on the molecule by the surface with minimum computation at each step. We note that the molecule exerts an equal and opposite force on each site on the surface, but that the surface remains stationary. Total energy and angular momentum are conserved in this system.

In the simulation we solve the Newton-Euler coupled equations of translational and rotational motion over a number of timesteps. During the run we measure the microcanonical averages of the system and hence determine the thermodynamic, structural and dynamic properties of the system. In order to solve the equations of motion it is necessary to use an iterative technique that can solve second-order differential equations. The method we have chosen is the well tested predictor-corrector integrating algorithm of Gear (1966).

The Gear Method is based on a Taylor series expansion about a point R, where the new value is calculated from the previous value of R and its first five derivatives for the translational equations and its first four derivatives for the rotational equations.

The predicted values of the acceleration and angular acceleration are compared with the actual values calculated

from the force and torque and these differences are used to correct the trajectories.

The equations for the Gear Method predictors are

$$\underset{\sim}{R}_p^{(0)}(t+\Delta t) = \underset{\sim}{R}^{(0)}t + \Delta t\,\underset{\sim}{R}^{(1)} + \frac{\Delta t^2}{2}\underset{\sim}{R}^{(2)} + \frac{\Delta t^3}{3!}\underset{\sim}{R}^{(3)} + \frac{\Delta t^4}{4!}\underset{\sim}{R}^{(4)} + \frac{\Delta t^5}{5!}\underset{\sim}{R}^{(5)},$$

$$\underset{\sim}{R}_p^{(1)}(t+\Delta t) = \underset{\sim}{R}^{(1)}t + \Delta t\,\underset{\sim}{R}^{(2)} \ldots\ldots\ldots\ldots + \frac{\Delta t^5}{5!}\underset{\sim}{R}^{(5)}$$

$$\vdots$$

$$\underset{\sim}{R}_p^{(4)}(t+\Delta t) = \underset{\sim}{R}^{(4)}\,t + \Delta t\,\underset{\sim}{R}^{(5)}$$

$$\underset{\sim}{R}_p^{(5)}(t+\Delta t) = \underset{\sim}{R}^{(5)}t \qquad (3.2.1)$$

where $\underset{\sim}{R}_p^{(i)}$ is the i-th derivative of the new coordinate and Δt is the time step.

The acceleration of the single molecule $\underset{\sim}{R}^{(2)}(t + \Delta t)$ is calculated via the force which is the gradient of the potential energy function.

The predicted values are corrected according to:

$$\underset{\sim}{R}^{(n)}(t+\Delta t) = \underset{\sim}{R}_p^{(n)}(t+\Delta t) + \alpha n(\Delta A)\,\frac{n!}{\Delta t n} \qquad (3.2.2)$$

where

$$\Delta A = [\underset{\sim}{R}^{(2)}(t+\Delta t) - \underset{\sim}{R}_p^{(2)}(t+\Delta t)]\,\frac{\Delta t^2}{2!} \qquad (3.2.3)$$

The α coefficients are given by:

Fifth Order Expansion

$\alpha_o = 3/16$

$\alpha_1 = 251/360$

$\alpha_2 = 1$

$\alpha_3 = 11/18$

$\alpha_4 = 1/6$

$\alpha_5 = 1/60$

Fourth Order Expansion

$\alpha_o = 251/720$

$\alpha_1 = 1$

$\alpha_2 = 11/12$

$\alpha_3 = 1/3$

$\alpha_4 = 1/24$

The time step Δt is chosen to be small enough to give conservation of total energy to one part in 10^4.

A problem has always arisen when solving the rotational equations of motion. In the Lagrange formulation of the equations the following quantity, $\frac{1}{\sin\theta} \frac{\partial U}{\partial \theta}$, is well defined in the limit as $\theta \to 0$, but machine accuracy cannot handle this limit. We can overcome the problem by coupling the Euler angles and the rotational velocities by introducing quaternions (Evans, 1977) into the system. The quaternion parameters χ, η, ξ, ζ are related to the Euler angles by the following equations

$$\chi = \cos(\theta/2)\cos(\psi + \phi)/2,$$

$$\eta = \sin(\theta/2)\cos(\psi - \phi)/2,$$

$$\xi = \sin(\theta/2)\sin(\psi - \phi)/2,$$

$$\zeta = \cos(\theta/2)\sin(\psi + \phi)/2, \qquad (3.2.4)$$

and it is readily seen that

$$\chi^2 + \eta^2 + \xi^2 + \zeta^2 = 1 \ .$$

The rotation matrix A (Goldstein Ch. 4) defined by

$$\underset{\sim}{V}_{body} = \underset{\approx}{A} \cdot \underset{\sim}{V}_{space}$$

is given by

$$\underset{\approx}{A} = \begin{Bmatrix} -\xi^2 + \eta^2 - \zeta + \chi^2 & 2(\zeta\chi - \xi\eta) & 2(\eta\zeta + \xi\chi) \\ -2(\xi\eta + \zeta\chi) & \xi^2 - \eta^2 - \zeta^2 + \chi^2 & 2(\eta\chi - \xi\zeta) \\ 2(\eta\zeta - \xi\chi) & -2(\xi\zeta + \eta\chi) & -\xi^2 - \eta^2 + \zeta^2 + \chi^2 \end{Bmatrix}$$

(3.2.5)

This matrix gives the trasformation of coordinates from a space fixed or laboratory system to internal body fixed coordinates.

The principal angular velocity ω_p is related to the quaternions by the matrix equation

$$\begin{Bmatrix} \dot{\xi} \\ \dot{\eta} \\ \dot{\zeta} \\ \dot{\chi} \end{Bmatrix} = \frac{1}{2} \begin{Bmatrix} -\zeta & -\chi & \eta & \xi \\ \chi & -\zeta & \xi & \eta \\ \xi & \eta & \chi & \zeta \\ -\eta & \xi & -\zeta & \chi \end{Bmatrix} \begin{Bmatrix} \omega_{px} \\ \omega_{py} \\ \omega_{pz} \\ \omega_0 \end{Bmatrix} \qquad (3.2.6)$$

The inverse of (3.2.5) is easy to find because the 4 x 4 matrix is orthogonal. The equations of motion for these parameters are thus free of singularities. The force and torque on the methane molecule are calculated in the space-fixed coordinate system. The torques are then converted to the body-fixed system using the rotation matrix (3.2.5). Body-fixed torques $\underset{\sim}{T}_p$ and forces $\underset{\sim}{F}$ are then used to evaluate the time derivatives of the body-fixed angular velocities and the accelerations $\ddot{\underset{\sim}{r}}$ of the molecules using

$$R^{(2)}(t + \Delta t) = \frac{d^2 r}{dt^2} = F/m$$

and

$$\omega^{(2)}(t + \Delta t) = \frac{d\omega_{p\alpha}}{dt} = T_{p\alpha}/I \ , \ (\alpha = x,y,z).$$

(3.2.7)

These values are then substituted into (3.2.3) to give the corrector.

We now give a description of the whole prodecure for the molecular dynamics program. It is useful to follow the flow chart in Figure 3.2 during the discussion.

1) The first step is to read in initial data which includes the time step, cutoff distance (r_c), the total number of timesteps, temperature and information relating to the state of the system; i.e. if it is a new run, the system is still equilibrating

or the system has equilibrated and it is a continuation run. All constants of the system are initialized, for example ε's, σ's etc. If it is not a new run we jump to step 3.

2) The initial coordinates for the methane molecule are chosen. The molecule is placed over a hexagon centre (of the surface) at a height of 1.3d and in its minimum rotational energy configuration. Random centre of mass and angular velocities are generated. We give each degree of freedom $\frac{1}{2}k_BT$ of kinetic energy so the translational kinetic energy is given $\frac{3}{2}k_BT$ and the rotational kinetic energy is given $\frac{3}{2}k_BT$. If there is more than one molecule we must also correct for any overall drift and rotation the system may attain.

The force routine is next called to determine the initial translational and angular velocities using the rotation matrix (3.2.5) and equations (3.2.7). The first derivative of the quaternions is calculated from (3.2.6). Set all higher derivatives to zero.

3) If it is a continuation run the restart data is read from tape. This includes translational and rotational positions, velocities and accelerations and all higher derivatives.

4) All new positions and derivatives are predicted for the cartesian coordinates, angular velocity and quaternions.

5) Call the force routine to calculate the force and

and torques. From the rotation matrix (3.2.5), the transform (3.2.6) and equation (3.2.7) determine accelerations, angular velocities and first derivatives of the quaternions. Next calculate the correctors according to (3.2.3) and correct all the predicted cartesian, angular and quaternion values.

6) If the system has equilibrated go to step 7. During equilibration the translational and rotational kinetic energies must be continually scaled to the correct temperature ~~via equations (3.2.11) and (3.2.13)~~. This is because kinetic energy is continually being converted to potential energy and vice-versa. The system is considered equilibrated once the average temperature remains constant at the desired value. Experience has shown that the system requires about 2000 timesteps before the linear and angular velocities have the correct values to maintain a constant temperature.

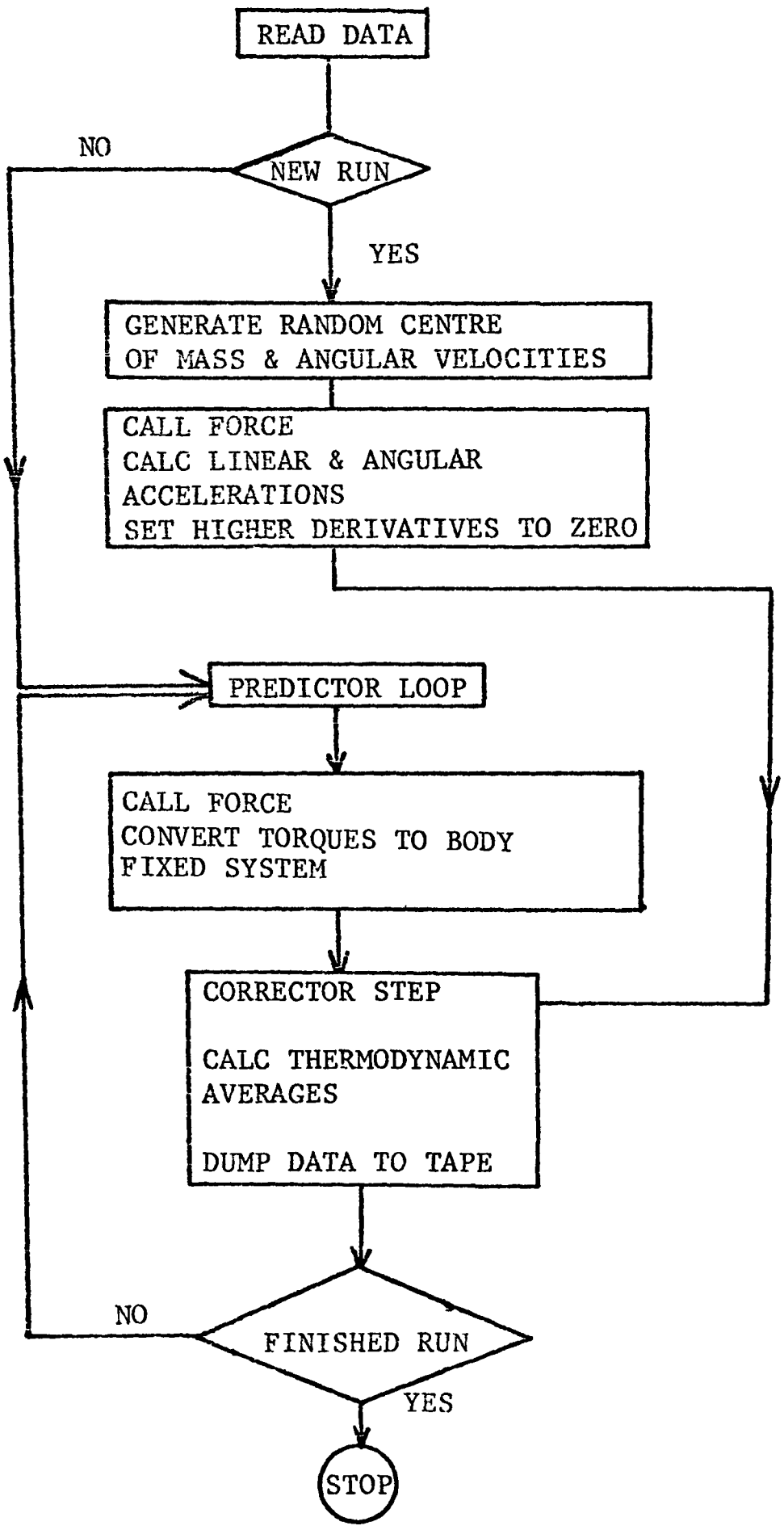
7) Energies, temperatures and any other quantity of interest are summed to arrays and periodically averaged for output to tape or line printer.

8) If the maximum number of timesteps is not reached go to step 4, otherwise stop the run.

A listing of the molecular dynamics program SURFACEONE is in the program appendix at the end of the thesis.

The motion of the particle is monitored over 100,000 timesteps of 1.25×10^{-15}s. The total energy is conserved to one part in 10^4 over 10^3 timesteps. Small changes in total energy occur as methane molecules move across the boundary of a unit rhombus.

Figure 3.2


READ DATA
NO
NEW RUN
YES
GENERATE RANDOM CENTRE
OF MASS & ANGULAR VELOCITIES
CALL FORCE
CALC LINEAR & ANGULAR
ACCELERATIONS
SET HIGHER DERIVATIVES TO ZERO
PREDICTOR LOOP
CALL FORCE
CONVERT TORQUES TO BODY
FIXED SYSTEM
CORRECTOR STEP
CALC THERMODYNAMIC
AVERAGES
DUMP DATA TO TAPE
NO
FINISHED RUN
YES
STOP

This occurs because the cutoff in the surface is based on the centre of the unit rhombus which is below the methane and not on the molecule itself. These changes are of order 1 part in 10^4 and vary in sign. There is no overall drift in energy. Sites in the surface which are more than 5.0d from the centre of the unit rhombus below the centre of the methane molecule do not contribute to the force and torque on the molecule. A test has been made in which the cutoff distance is centred around the C.O.M. of the methane molecule. No improvement in energy conservation is achieved because there is a bias in the distribution of surface atoms for any circle (of radius r_c) drawn on the surface except when the C.O.M. lies above the centre of a unit rhombus, a hexagon centre or a surface atom.

During the simulation the average temperature and configurational energy are monitored after an initial equilibration period of approximately 2×10^3 timesteps. The long range correction to the internal energy is calculated at every timestep since it is a function of the height of the molecule above the surface, (see section 3.3). The position and orientation of the molecule are stored on tape at every tenth timestep.

3.3 The Potential Model

Two potential models will be developed and compared in this section before we discuss the fitting of the adjustable parameters in the model. In the first model (1) a methane molecule

interacts specifically with all the atoms on the basal plane of the graphite out to a cutoff r_c and which includes two long range corrections to the configurational energy. The first, due to the surface atoms beyond r_c and the second from the solid below the basal plane. Model (1) is shown schematically in Figure 3.3a . The total pairwise potential $U(\underset{\sim}{r}_m \underset{\sim}{\omega}_m)$, between the methane and the surface can be divided into three contributions for model (1); the direct interaction, $U_{\alpha s}$, the long range surface correction, $U_{surface}$ and the long range bulk correction U_{bulk}.

$$U(\underset{\sim}{r}_m \underset{\sim}{\omega}_m) = U_{\alpha s} + U_{surface} + U_{bulk} \qquad (3.3.1)$$

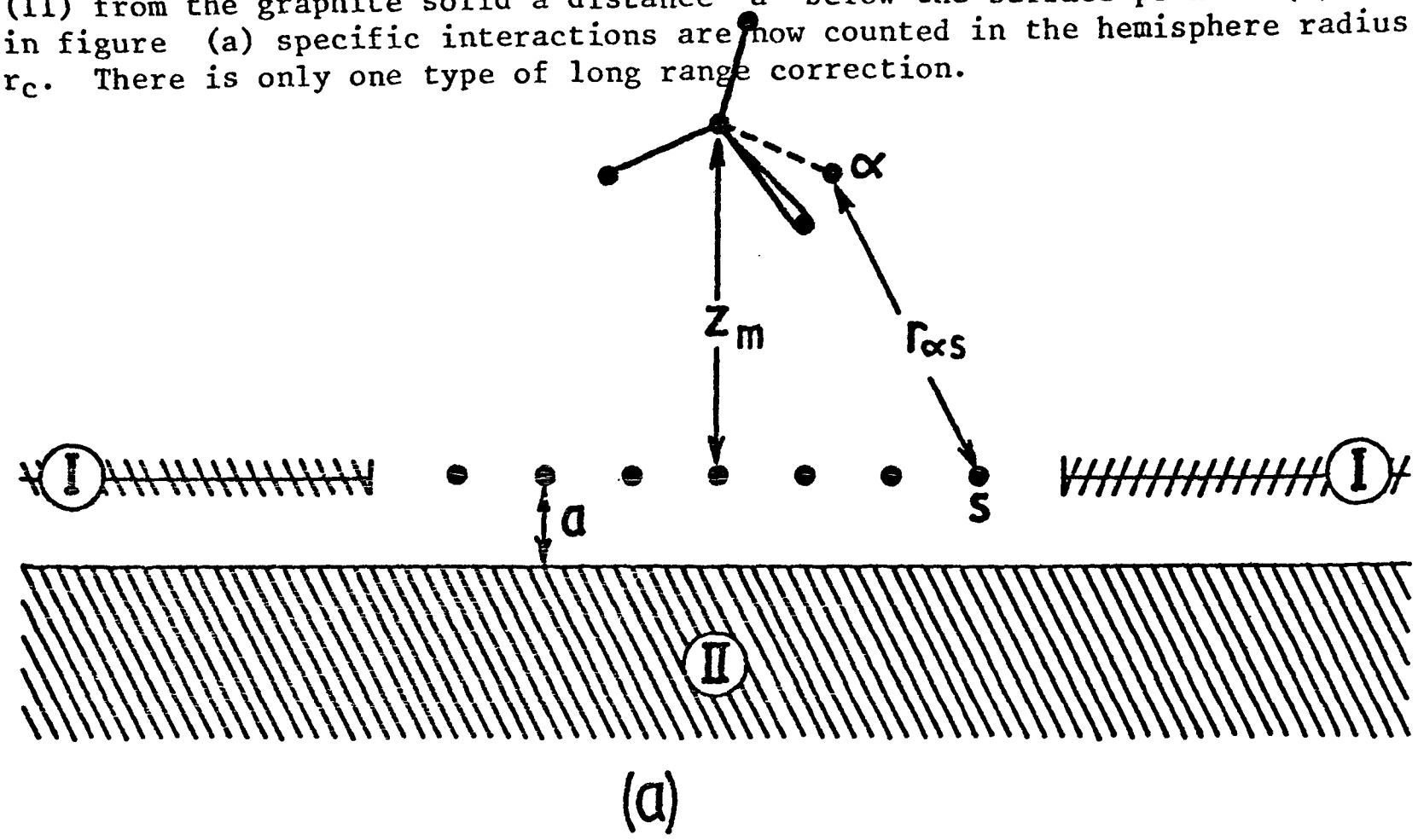
We follow the method of Steele (Steele, 1974) to derive $U_{surface}$ and U_{bulk}. Let us first consider $U_{\alpha s}$ the direct interaction. The direct contribution is an interaction site potential of the Lennard-Jones 12-6 form, i.e.

$$U_{\alpha s} = \sum_{s} \sum_{\alpha=1}^{5} 4\, \epsilon_{\alpha s} \left[\left(\frac{\sigma_{\alpha s}}{r_{\alpha s}}\right)^{12} - \left(\frac{\sigma_{\alpha s}}{r_{\alpha s}}\right)^{6}\right] \qquad (3.3.2)$$

The summation α is over the five independent interaction sites in the methane molecule and the summation s is over the atoms on the basal plane of graphite inside the cutoff distance. $\epsilon_{\alpha s}$ and $\sigma_{\alpha s}$ are the energy and length parameters in the Lennard-Jones potential and $r_{\alpha s}$ is the site-site distance.

Now consider $U_{surface}$, the long range correction due to the basal plane beyond r_c. We assume the methane molecule

Figure 3.3 (a) Potential model (i). The c.o.m of the methane molecule is z_m, above the surface. Specific interactions between sites $r_{\alpha s}$ are calculated explicitly in a circle of radius r_c centred on the unit rhombus below the methane and extending on the basal plane of the graphite. Long range corrections are of two types; (1) from the atoms on the surface beyond r_c, (II) from the graphite solid a distance 'a' below the surface plane. (b) As in figure (a) specific interactions are now counted in the hemisphere radius r_c. There is only one type of long range correction.



appears as a point at height z above the surface and the surface atoms have a uniform continuous distribution of n_A, n_A = 0.378 atoms/Å^2. Let r_{is} be the molecule-surface distance; then the long range correction to the potential is

$$U_{surface} = \sum_{\substack{s \\ r>r_c}} U_{\alpha s}(r_{is}) \quad . \qquad (3.3.3)$$

Since the surface atoms are continuously distributed we can replace the sum by an integral over the surface. Let (x,y) be the coordinates of a surface element in dA; r_{is} is then given by

$$r_{is} = (z^2 + x^2 + y^2)^{\frac{1}{2}}$$

and eqn. (3.3.3) becomes

$$U_{surface} = \int U_{\alpha s}(r_{is})\ n_A\ dxdy, \qquad (3.3.4)$$

where the integration is over the surface beyond r_c. The assumption here is that the x and y coordinates of all the sites are taken to be equal to the x,y coordinates of the centre of the rhombus above which the methane molecule lies. This is a reasonable approximation since r_c is chosen to be large enough; that is

$$[(x_\alpha^2 + y_\alpha^2) - (x_{rhom}^2 + y_{rhom}^2)]^{-6} \simeq 0$$

for r_c large. Since the potential is very rapidly varying with z we must include z_α explicitly. Substituting (3.3.2) into (3.3.4) gives

$$U_{surface} = \int_x \int_y \sum_{\alpha=1}^{5} 4\,\varepsilon_{\alpha s}\left[\frac{\sigma_{\alpha s}^{12}}{(z_\alpha^2+x^2+y^2)^6} - \frac{\sigma_{\alpha s}^{6}}{(z_\alpha^2+x^2+y^2)^3}\right] n_A\, dxdy \tag{3.3.5}$$

Changing from cartesian to polar coordinates, $U_{surface}$ becomes,

$$U_{surface} = \sum_{\alpha=1}^{5} 4\, n_A\, \varepsilon_{\alpha s} \int_0^{2\pi} \int_{r_c}^{\infty} \left[\frac{\sigma_{\alpha s}^{12}}{(z_\alpha^2+r^2)^6} - \frac{\sigma_{\alpha s}^{6}}{(z_\alpha^2+r^2)^3}\right] r\,dr\,d\theta \tag{3.3.6}$$

Straightforward integration yields the desired result,

$$U_{surface} = \sum_{\alpha=1}^{5} 4\pi\, n_A\, \varepsilon_{\alpha s}\left[\frac{\sigma_{\alpha s}^{12}}{5(z_\alpha^2+r_c^2)^5} - \frac{\sigma_{\alpha s}^{6}}{2(z_\alpha^2+r_c^2)^2}\right] \tag{3.3.7}$$

The second correction to the energy is from the bulk graphite below the basal plane. We make the same assumptions as above except the atoms are now smeared with density distribution,

n_v, n_v = 0.113 atoms $\mathring{A}^{-3}$. Let r_{cs} be the molecule-(graphite) atom distance and the bulk correction is

$$U_{bulk} = \sum U_{\alpha s}(r_{is}) , \qquad (3.3.8)$$

where the sum is over all atoms below the graphite surface. Let atom i, in the bulk, be at (x,y,z_s) in a volume element dV and replace the sum by an integral. The molecule-atom distance is

$$r_{is} = ((z_s + a + z_\alpha)^2 + x^2 + y^2)^{\frac{1}{2}} \qquad (3.3.9)$$

where a is the distance between the basal plane and the first layer in the surface, a = 3.35 $\mathring{A}$ (Steele, 1974); z_s the perpendicular distance from the first layer to the volume element dV and z_α is the height of the molecule above the surface. Substituting (3.3.9) and (3.3.2) into the integral form of (3.3.8) gives

$$U_{bulk}(z_\alpha) = \int_x \int_y \int_{z_s} \sum_{\alpha=1}^{5} 4\,\varepsilon_{\alpha s}\left[\frac{\sigma_{\alpha s}^{12}}{((z_s+a+z_\alpha)^2+x^2+y^2)^6} - \frac{\sigma_{\alpha s}^{6}}{((z_s+a+z_\alpha)^2+x^2+y^2)^3}\right] n_v\, dxdydz_s$$

$$= \int_{\theta=0}^{2\pi} \int_{s=0}^{\infty} \int_{z_s=0}^{\infty} \sum_{\alpha=1}^{5} 4\,\varepsilon_{\alpha s}\left[\frac{\sigma_{\alpha s}^{12}}{((z_s+a+z_\alpha)^2+s)^6} - \frac{\sigma_{\alpha s}^{6}}{((z_s+a+z_\alpha)^2+s)^3}\right]\frac{n_v}{2}\, d\theta ds dz_s \qquad (3.3.10)$$

where $s = x^2 + y^2$ and the Jacobian of the coordinate transform is 1/2.

Integrating the above gives

$$U_{bulk} = \frac{2}{3} \pi n_v \sum_{\alpha=1}^{\Gamma} \varepsilon_{\alpha s} \sigma_{\alpha s}^3 \left[\frac{2}{15} \left(\frac{\sigma_{\alpha s}}{z_\alpha + a} \right)^9 - \left(\frac{\sigma_{\alpha s}}{z_\alpha + a} \right)^3 \right] \quad (3.3.11)$$

The expression for the total potential energy is the sum of (3.3.2), (3.3.7) and (3.3.11);

$$U(r_m \omega_m) = U_{\alpha s} + U_{surface} + U_{bulk}$$

$$= \sum_{\substack{s \\ r<r_c}} \sum_{\alpha=1}^{5} 4 \varepsilon_{\alpha s} \left[\frac{\sigma_{\alpha s}}{r_s}^{12} - \frac{\sigma_{\alpha s}}{r_s}^{6} \right]$$

$$+ 4 \pi n_A \sum_{\alpha=1} \varepsilon_{\alpha s} \left[\frac{\sigma_{\alpha s}^{12}}{5(z_\alpha^2 + r_c^2)^5} - \frac{\sigma_{\alpha s}^6}{2(z_\alpha + r_c)^2} \right]$$

$$+ \frac{2}{3} \pi n_v \sum_{\alpha=1} \varepsilon_{\alpha s} \sigma_{\alpha s}^3 \left[\frac{2}{15} \left(\frac{\sigma_{\alpha s}}{z_\alpha + a} \right)^9 - \left(\frac{\sigma_{\alpha s}}{z_\alpha + a} \right)^3 \right] . \quad (3.3.12)$$

Model (1) suffers from inconsistency in that we have specifically counted interactions out to r_c on the surface but have ignored specific interactions from sites within a distance r_c which are below the surface. Model (II), shown schematically

in Figure 3.3b, counts sites out to r_c in the solid specifically and averages the effect of the remainder of the solid. The potential has two terms

$$U(\underset{\sim}{r}_m, \underset{\sim}{\omega}_m) = U_{\alpha s} + U_{bulk} \tag{3.3.13}$$

Let r_{is} be the surface -molecule distance and r_{min} be defined by

$$r_{min} = (z_\alpha^2 + r_c^2 - 2\, z_\alpha\, r_c \cos\theta)^{1/2} \tag{3.3.14}$$

which is the distance from the molecule to the edge of the hemisphere in Figure 3.3b. θ is the angle between r_c and z_α. The bulk correction to the energy is given by

$$U_{bulk} = \sum U_{\alpha s}(r_{is}), \tag{3.3.15}$$

and using the same assumptions as in model (1) we can express this as an integral over the volume element dV namely

$$U_{bulk} = \int_0^{2\pi} \int_{\frac{\pi}{2}}^{\pi} \int_{r_{min}}^{\infty} n_v\, U_{\alpha s}\,(r_{is})\, r^2 \sin\theta\, d\theta d\phi dr. \tag{3.3.16}$$

Now substituting

$\int_{\frac{\pi}{2}}^{\pi} \sin\theta \, d\theta = -\int_{0}^{1} d\cos\theta = \int_{-1}^{0} dq$, where $q = \cos\theta$, and

for $U_{\alpha s}(r_{is})$ into (3.3.16),

$$U_{bulk} = \int_{-1}^{0}\int_{0}^{2\pi}\int_{r_{min}}^{\infty} \sum_{\alpha=1}^{5} 4\, n_v\, \varepsilon_{\alpha s}\left[\left(\frac{\sigma_{\alpha s}}{r_{\alpha s}}\right)^{12} - \left(\frac{\sigma_{\alpha s}}{r_{\alpha s}}\right)^{6}\right] r^2\, dr d\phi dq$$

$$= 8\pi n_v \sum_{\alpha=1}^{5} \varepsilon_{\alpha s} \int_{-1}^{0}\left[\frac{\sigma_{\alpha s}^{12}}{9(z_\alpha^2 + r_c^2 - 2z_\alpha r_c q)^{9/2}} - \frac{\sigma_{\alpha s}^{6}}{3(z_\alpha^2 + r_c^2 - 2z_\alpha r_c q)^{3/2}}\right] dq$$

$$= 8\pi n_v \sum_{\alpha=1}^{5} \varepsilon_{\alpha s}\left[\frac{\sigma_{\alpha s}^{12}}{63 z_\alpha r_c}\left(\frac{1}{(z_\alpha^2 + r_c^2)^{7/2}} - \frac{1}{(z_{\alpha s} + r_c)^{7}}\right)\right.$$

$$\left. - \frac{\sigma_{\alpha s}^{6}}{3 z_\alpha r_c}\left(\frac{1}{(z_\alpha^2 + r_c^2)^{1/2}} - \frac{1}{(z_\alpha + r_c)}\right)\right] \qquad (3.3.17)$$

The expression for the total potential energy for model (ii) becomes

$$U(r_m, \omega_m) = \sum_{s}\sum_{\alpha=1} 4\, \varepsilon_{\alpha s}\left[\left(\frac{\sigma_{\alpha s}}{r_{\alpha s}}\right)^{12} - \left(\frac{\sigma_{\alpha s}}{r_{\alpha s}}\right)^{6}\right]$$

$$+ \frac{8\pi n_v}{z_\alpha r_c} \sum_{\alpha=1}^{5}\left[\frac{\sigma_{\alpha s}^{12}}{63}\left(\frac{1}{(z_\alpha^2 + r_c^2)^{7/2}} - \frac{1}{(z_\alpha + r_c)^{7}}\right)\right.$$

$$\left. - \frac{\sigma_{\alpha s}^{6}}{3}\left(\frac{1}{(z_\alpha^2 + r_c^2)^{1/2}} - \frac{1}{(z_\alpha + r_c)}\right)\right] \varepsilon_{\alpha s} \qquad (3.3.18)$$

We note that in both models (I) and (II) the long-range corrections can alter the well depth by as much as 10% for a variety of methane orientations. Figure 3.4 shows a comparison of the potential models (I) and (II) for the most stable methane orientation, the tripod, with the molecule directly above the centre of a hexagon, ($\varepsilon_{\alpha s}$ and $\sigma_{\alpha s}$ are taken from table 3.1) and a cutoff distance r_c = 12.3 Å. Increasing the cutoff to distances greater than 12 Å has little effect on the potential functions in either equations (3.3.12) and (3.3.18).

As we might expect, the two potentials are close to one another although certainly distinguishable at the bottom of the well. For computational convenience we have decided to work with model (I); this form of the potential enables us to use the simulation techniques described in section 3.2. Finally we note the effect on the potential of changing the methane orientation and translating the molecule across surface sites. The methane is orientated at a particular angle of tilt away from the perpendicular to the surface and is moved along the perpendicular. (Again the methane is situated above the centre of a hexagon.) The potential curves are shown in Figure 3.5 . It is evident that rotating through an angle of 60^{o} decreases the well depth by 20% and increases the height of the methane at the potential minimum by 5%. We can expect some substantial effects from the structure of the methane molecule. We next translate the methane molecule across the surface at a fixed height of 1.3d and fixed orientation,

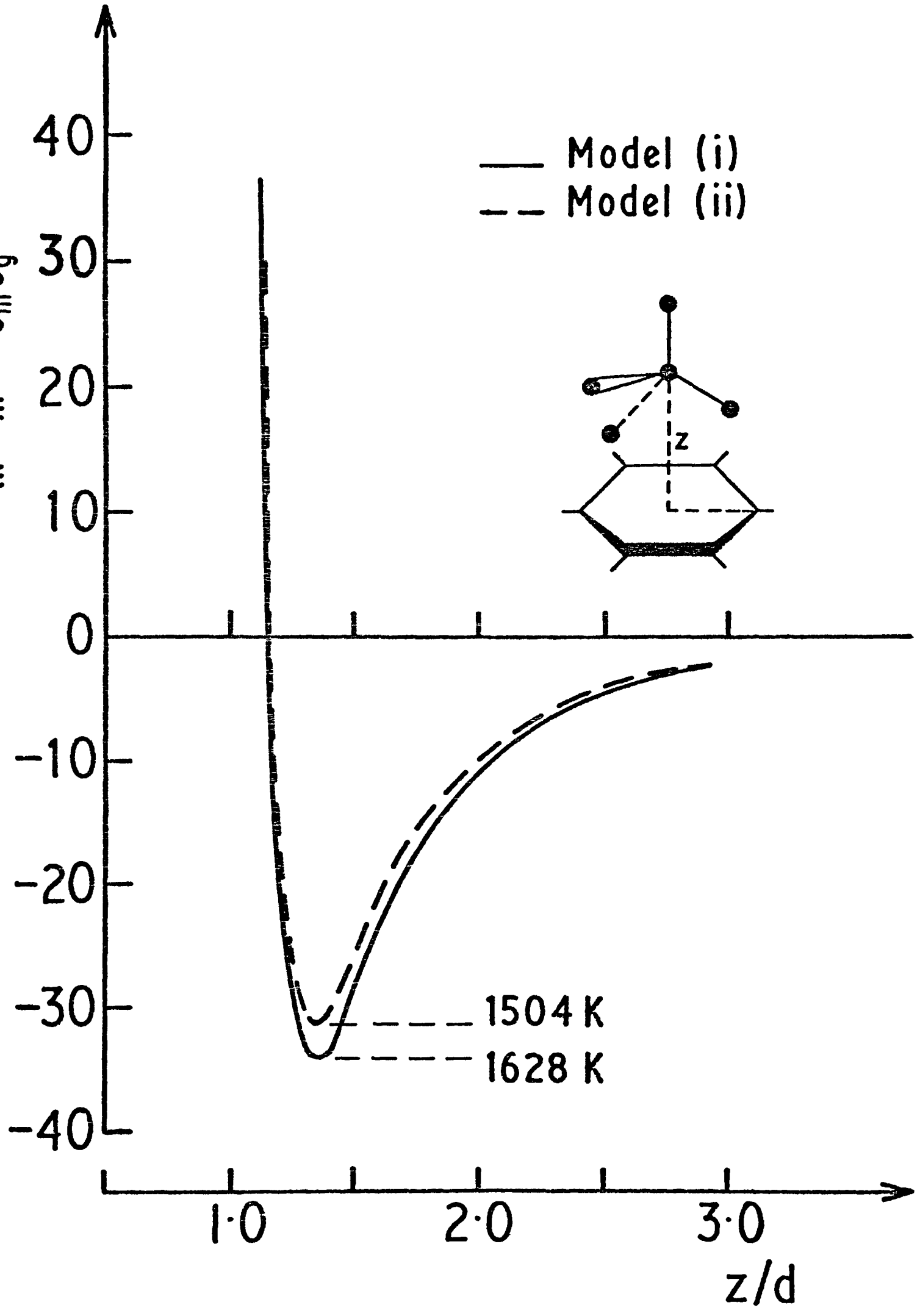
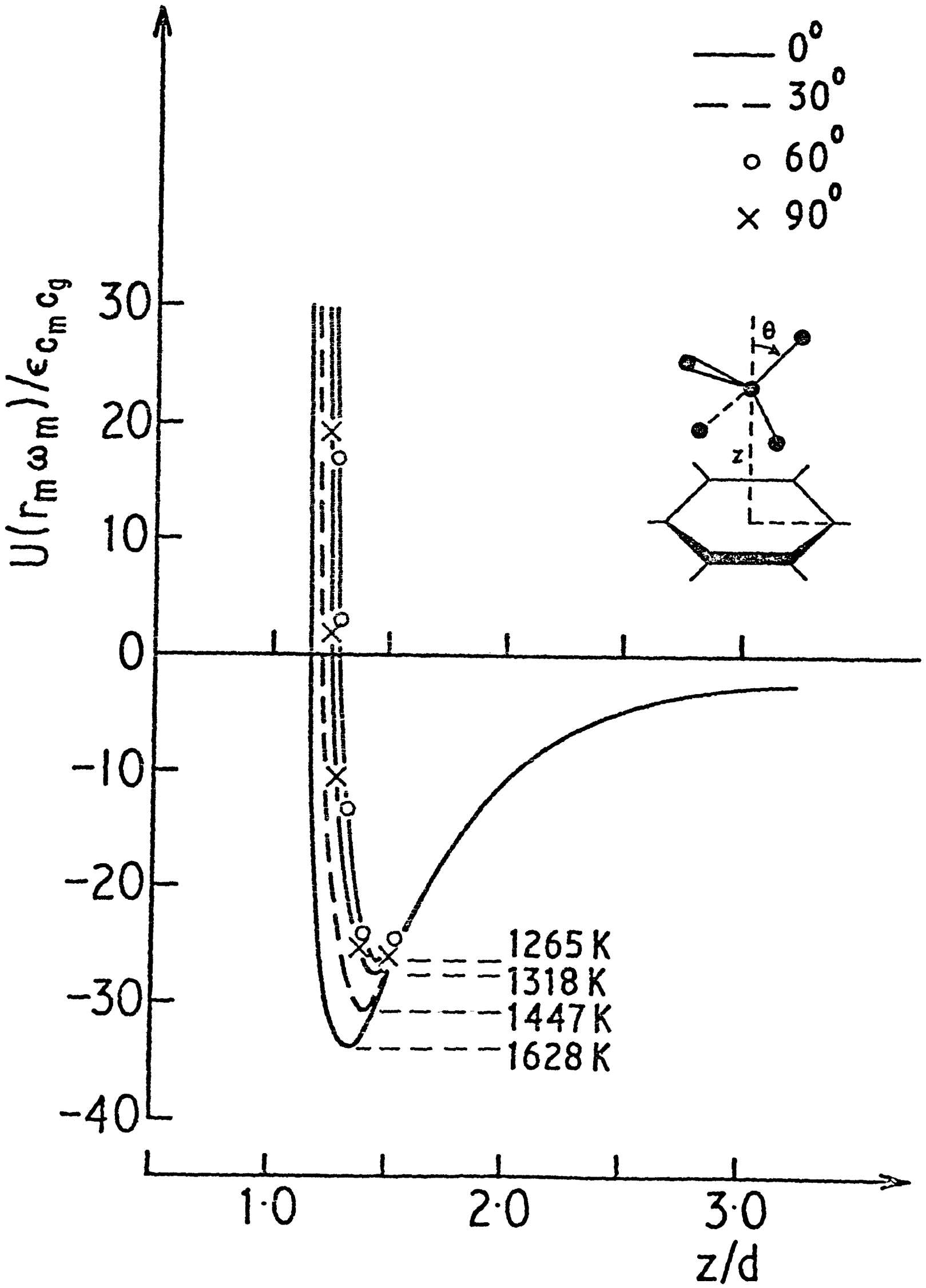


Figure 3.4 A comparison of potential models (I) and (II). The relative orientation of the methane with respect to the surface is shown in the figure. The height of the molecule above the surface, z, is varied while the orientation of the molecule with respect to the surface is fixed. The potential energy curves differ by 7 per cent at their well depths. It is interesting to note that potential well for methane against a graphite surface is an order of magnitude deeper than well depth between two methane particles.

Figure 3.5 The methane-surface potential is shown as a function of the angle of tilt of a carbon-hydrogen bond. $\theta = 0^{o}$ corresponds to the most stable methane-surface orientation we have found.



(the tripod). The potential curves for three translations are show in Figure 3.6 . It can be seen these curves are periodic, coinciding with the surface periodicity in all directions. The minimum energy is over a hexagon centre while the most unstable configuration is when the C.O.M. is above a surface carbon atom. The maximum variation in the potential is only 17K, which, compared to the well depth, is very small. We do not expect the surface structure to have substantial effects on the dynamics except at very low temperatures less than 30K. Other aspects of the potential surface will be discussed as they are required. Let us now consider the adjustment of the potential parameters $\varepsilon_{\alpha s}$, $\sigma_{\alpha s}$.

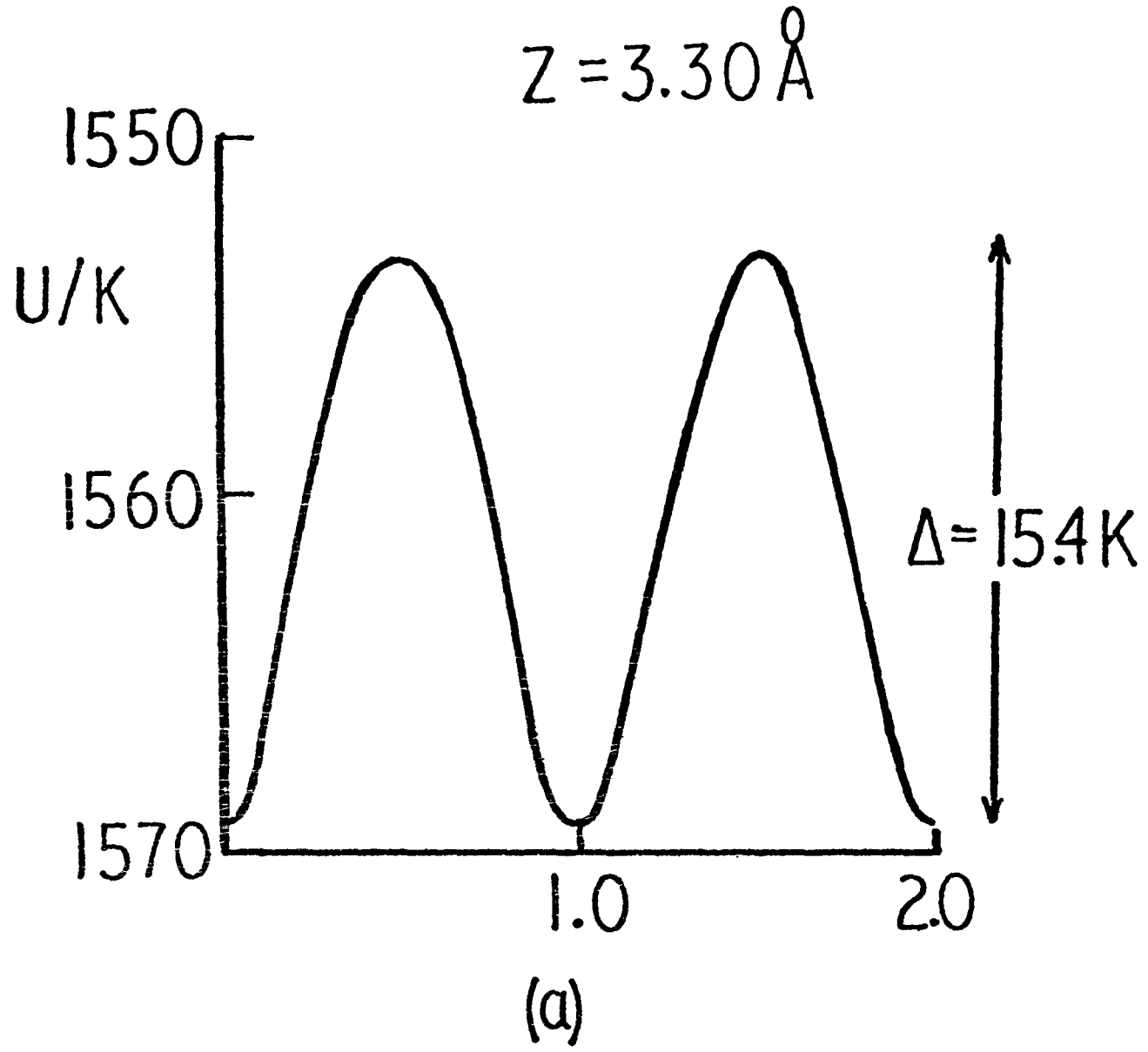
3.4 The Potential Parameters of the Methane-Surface Interaction

The Initial Guesses

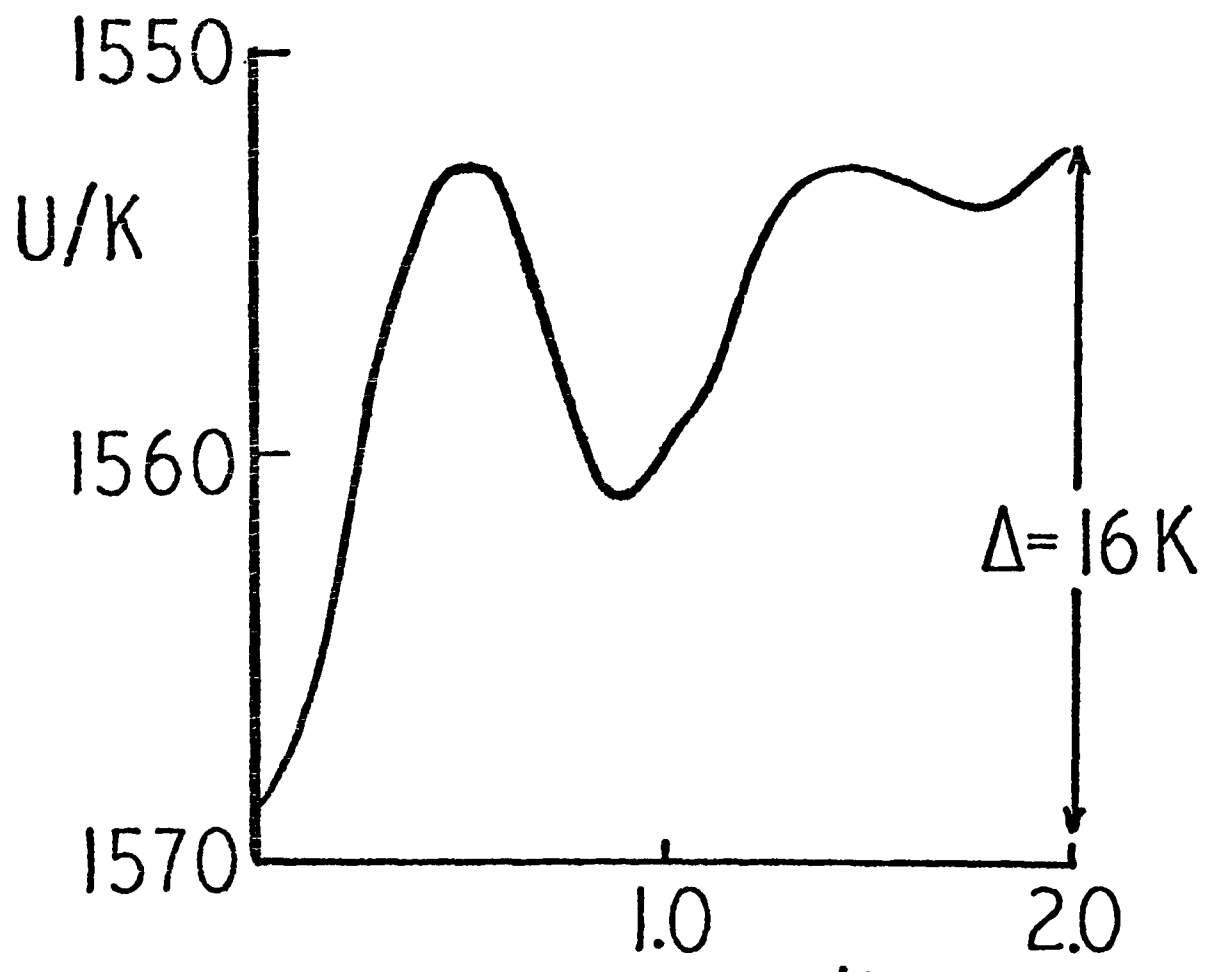
There are five adjustable parameters in the surface-methane potential; the carbon hydrogen bond length in methane (ℓ) and the two Lennard-Jones parameters for each of the two independent site interactions between the methane atoms, (C_m,H_m), and the carbon atom in the surface, (C_g). In addition in the adsorbed monolayer, we have to consider the potential parameters governing the methane-methane interaction.

Our strategy has been to take two initial guesses for the interactions. The first set, A, is taken from a study of dense fluid methane (Murad et al., 1979). The second set B is from a study of non-bonded potential solid potentials in crystals of aliphatic hydrocarbons (Williams, 1966).

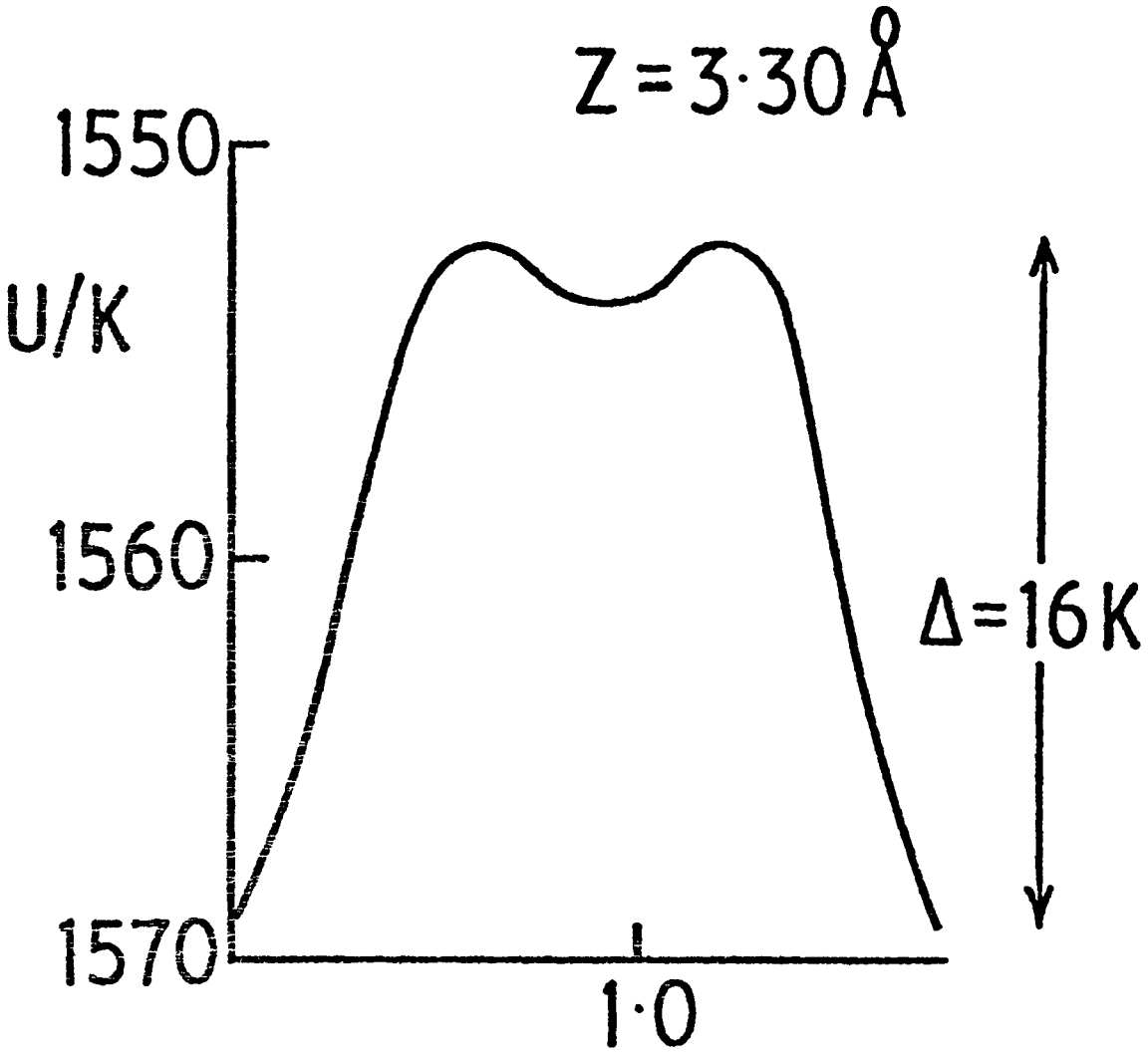
Figure 3.6 The potential energy curves resulting from the translation of one methane molecule at fixed height 3.3 Å in the tripod configuration. (a) is a translation parallel to the x axis and across the centres of the hexagons. The period of the curve is 1d. (b) is a translation at - 45^{o} to the y-axis; there is no period in the curve. (c) is a translation at - 60^{o} to the y-axis and the period is $\sqrt{3}$d. (d) is a translation in the same direction as (c) but the height of the c.o.m of methane is raised to 3.44 Å to demonstrate the rapid fall off in the barrier to translation as the methane moves away from the surface.


Z = 3.30 Å
1550
U/K
1560
1570
Δ = 15.4 K
1.0
2.0

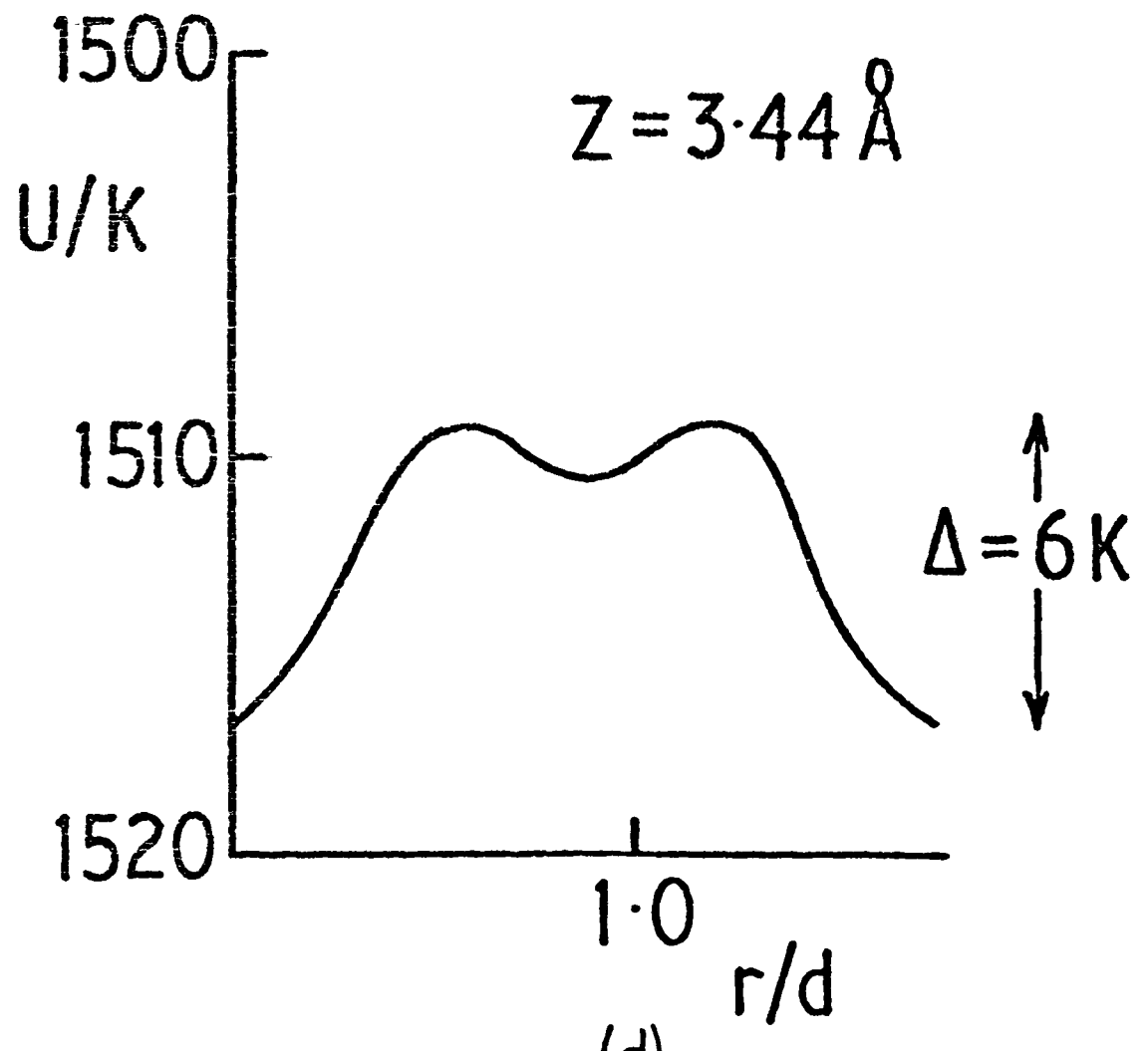
(a)


1550
U/K
1560
1570
Δ = 16 K
1.0
2.0
r/d

(b)


Z = 3·30 Å
1550
U/K
1560
1570
Δ = 16 K
1·0

(c)


1500
Z = 3·44 Å
U/K
1510
Δ = 6 K
1520
1·0
r/d

(d)

In parameter set A, the methane is assumed to be a rigid tetrahedron, with sites at the positions of the nuclei and ℓ is fixed at the spectroscopic bond length of 1.10 Å. The Lennard-Jones parameters for the methane-methane interaction are taken from the fluid study. The graphite-graphite Lennard-Jones parameters are determined from compressibility measurements on graphite (Crowell, 1958) and the studies of rare gas energies (Giamano et al., 1975). Finally the methane-surface interaction is obtained using the Lorentz-Berthelot mixing rules.

$$\sigma_{C_g C_m} = (\sigma_{C_g C_g} + \sigma_{C_m C_m})/2$$

$$\sigma_{C_g H_m} = (\sigma_{C_g C_g} + \sigma_{H_m H_m})/2$$

$$\varepsilon_{C_g C_m} = (\varepsilon_{C_g C_g}\ \varepsilon_{C_m C_m})^{1/2}$$

$$\varepsilon_{C_g H_m} = (\varepsilon_{C_g C_g}\ \varepsilon_{H_m H_m})^{1/2}$$

The parameter set A is given in table (3.1).

In the parameter set B the methane is again assumed to be a rigid tetrahedron with ℓ = 1.10 Å. The potential parameters are taken from set IV of a paper by Williams (1966). The potentials originally computed by Williams have an exponential repulsion.

Table 3.1

	Initial guesses A	Initial guesses B	Final values
CH_4			
$\varepsilon_{C_mC_m}/\kappa$	51.198 K	47.68 K	51.198 K
$\varepsilon_{C_mC_m}/\kappa$	23.798 K	24.46 K	23.789 K
$\varepsilon_{H_mH_m}/\kappa$	8.631 K	4.87 K	4.87 K
$\sigma_{C_mC_m}$	3.35 Å	3.35 Å	3.35 Å
$\sigma_{C_mH_m}$	2.995 Å	2.99 Å	2.99 Å
$\sigma_{H_mH_m}$	2.813 Å	3.12 Å	2.61 Å
Graphite			
$\varepsilon_{C_gC_g}/\kappa$	28.00 K		
$\sigma_{C_gC_g}$	3.40 Å		
CH_4/graphite			
$\varepsilon_{C_gC_m}/\kappa$	37.862 K	47.68 K	47.68 K
$\varepsilon_{C_gH_m}/\kappa$	15.54 K	24.46 K	17.00 K
$\sigma_{C_gC_m}$	3.375 Å	3.35 K Å	3.30 Å
$\sigma_{C_gH_m}$	3.107 Å	2.99 K Å	2.98 Å

ℓ = 1.10 Å and r_c = 11.0 Å

The potential parameters used with model (i). Sets A and B are the initial guesses. The origins of these two parameter sets are described in the text. The final column represents the best fit to all the available experimental data on adsorbed methane.

We have plotted these potentials in Figure 3.7 and simply taken the well-depths and collision diameters (ε, σ) from these Williams potentials to use in our Lennard-Jones 12-6 site-site potential. The parameter set B is also given in Table 3.1. We note that in this set of site-site potentials the methane-methane and methane-surface interactions are identical.

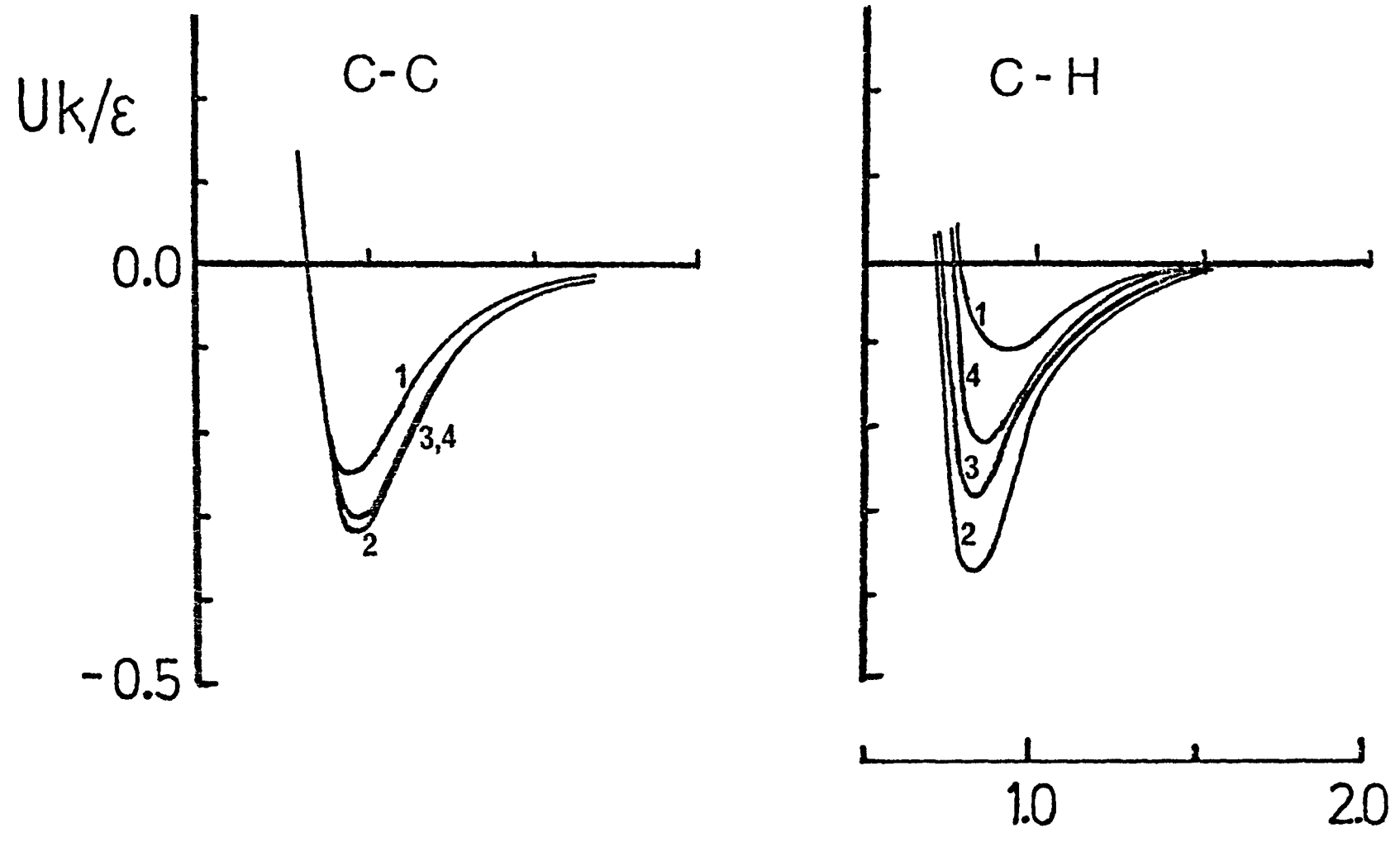
Using sets A and B as an initial guess we have adjusted the potentials to obtain the best fit to several different experiments performed on the adsorbate.

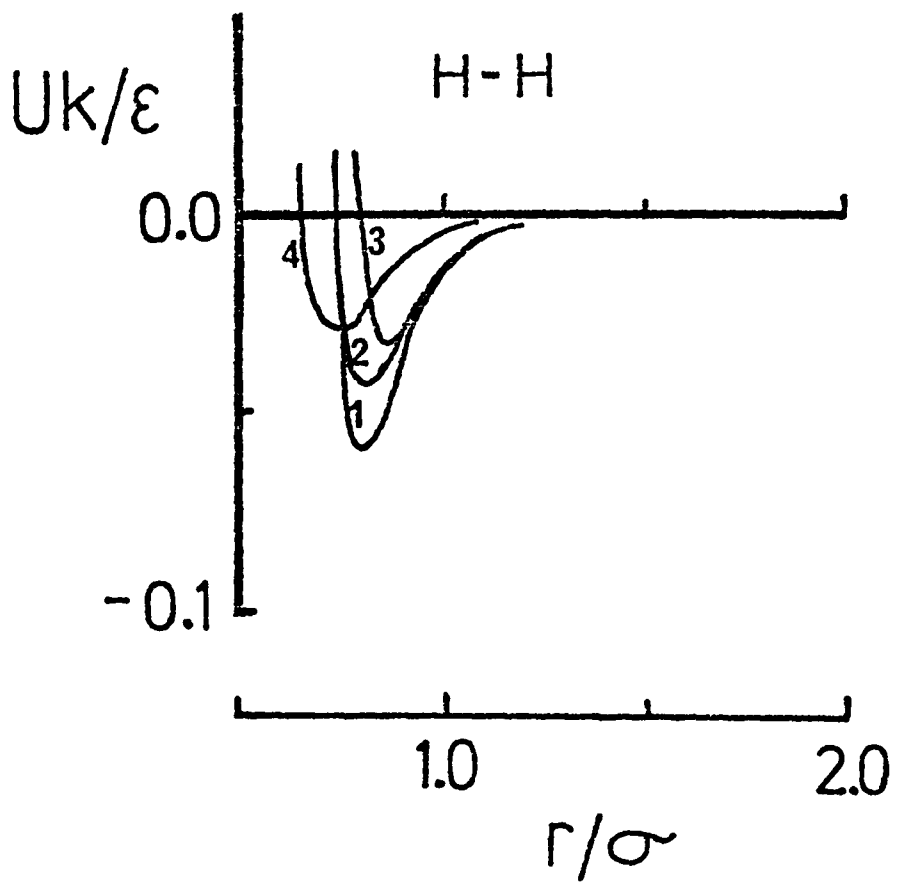
The Rotational Barriers

Neutron scattering studies have allowed the analysis of the rotational tunnelling of the hydrogen atoms in methane adsorbed on graphite (Bomchil et al., 1980). This is a quantum mechanical effect and the general procedure for calculating the tunnelling levels from the spectra is well understood (Huller et al., 1975) The classical analogy to this quantum tunnelling is the potential energy barrier to rotation about the axis of the methane molecule when it is adsorbed at a monolayer coverage. At a monolayer coverage the methane exists in the $\sqrt{3}$ x $\sqrt{3}$ epitaxial structure (Marlow et al., 1977) as a solid adsorbed on the surface. The structure is shown in Figure 3.8. Two barriers to rotation can be obtained from the neutron-scattering data. The first, the h_4-barrier, is obtained by rotating the methane molecule, in the monolayer, about an axis perpendicular to the graphite surface and through the methane

Figure 3.7 A comparison of the Lennard-Jones and Williams potentials. The table below lists the potential parameter. ε/k = 142.87K and σ = 4.10 Å

Interaction	1:L-J from dense fluid CH_4	2:Williams from dense fluid CH_4	3:Williams IV	4:LJ from Williams IV
C-C	ε/k = 37.862K σ = 3.375 Å	A^* = 0.42779 B^* = 218024 C^* = 14.436	A^* = 0.45331 B^* = 262372 C^* = 14.436	ε/k = 47.68K σ = 3.35 Å
C-H	ε/k = 15.54K σ = 3.107 Å	A^* = 0.18043 B^* = 38744 C^* = 14.717	A^* = 0.11780 B^* = 33161 C^* = 14.717	ε/k = 24.86K σ = 3.1 Å
H-H	ε/k = 8.631K σ = 2.831 Å	A^* = 0.02736 B^* = 9260 C^* = 14.997	A^* = 0.03050 B^* = 13791 C^* = 14.997	ε/k = 4.87K σ = 2.62 Å


C-C
C-H
Uk/ε
0.0
-0.5
1
2
3,4
4
3
1.0
2.0


H-H
Uk/ε
0.0
-0.1
4
3
2
1
1.0
2.0
r/σ

carbon atom. This rotation and the resulting barrier are also shown in Figure 3.8. This barrier is particularly sensitive to $\epsilon_{H_mH_m}$ and $\sigma_{H_mH_m}$ and is almost unaffected by surface structure. We have adjusted these barriers to the final values shown in table 1. The height of the h_4-barrier obtained using our fitted potential is 212 cm^{-1}; the experimental height is 205 ± 5 cm^{-1} (Bomchil et al., 1980). An adjustment of only 0.01 Å in $\sigma_{H_mH_m}$ alters this barrier by as much as 10%. In addition our potential predicts that the $\sqrt{3}$ x $\sqrt{3}$ epitaxial structure shown, is the minimum energy configuration in the monolayer; (we note small changes in $\epsilon_{H_mH_m}$ can cause other relative orientations of the adsorbate to become more stable).

The second barrier, the h-rotation (Huller et al., 1975) is the rotation about one of the three carbon-hydrogen bonds pointing towards the surface. This rotation is performed in the registered solid structure, with the rest of the monolayer remaining fixed in the stable tripod. The rotation and the barrier obtained are shown in Figure 3.9. This barrier depends primarily on the methane-surface interaction, but has to be calculated in the presence of the rest of the monolayer. The barrier is affected by the $\epsilon_{C_gH_m}$ and $\sigma_{C_gH_m}$ parameters as these determine the strength of the interaction as the hydrogen atom ploughs into the surface. In addition the barrier height depends on $\sigma_{C_gC_m}$ since this parameter primarily determines the average height of the monolayer above the surface. These three parameters were adjusted to give the best agreement between the model and experiment. The parameters shown

Figure 3.8 The figure shows a plan of the $\sqrt{3}$ x $\sqrt{3}$ epitaxial structure of solid methane adsorbed at monolayer coverage. One of the four carbon hydrogen bonds is perpendicular to the surface. The h_4-rotation is a rotation around this perpendicular bond with the other molecules in the monolayer remaining fixed. The barrier to this rotation is shown in the right-hand side of this figure.

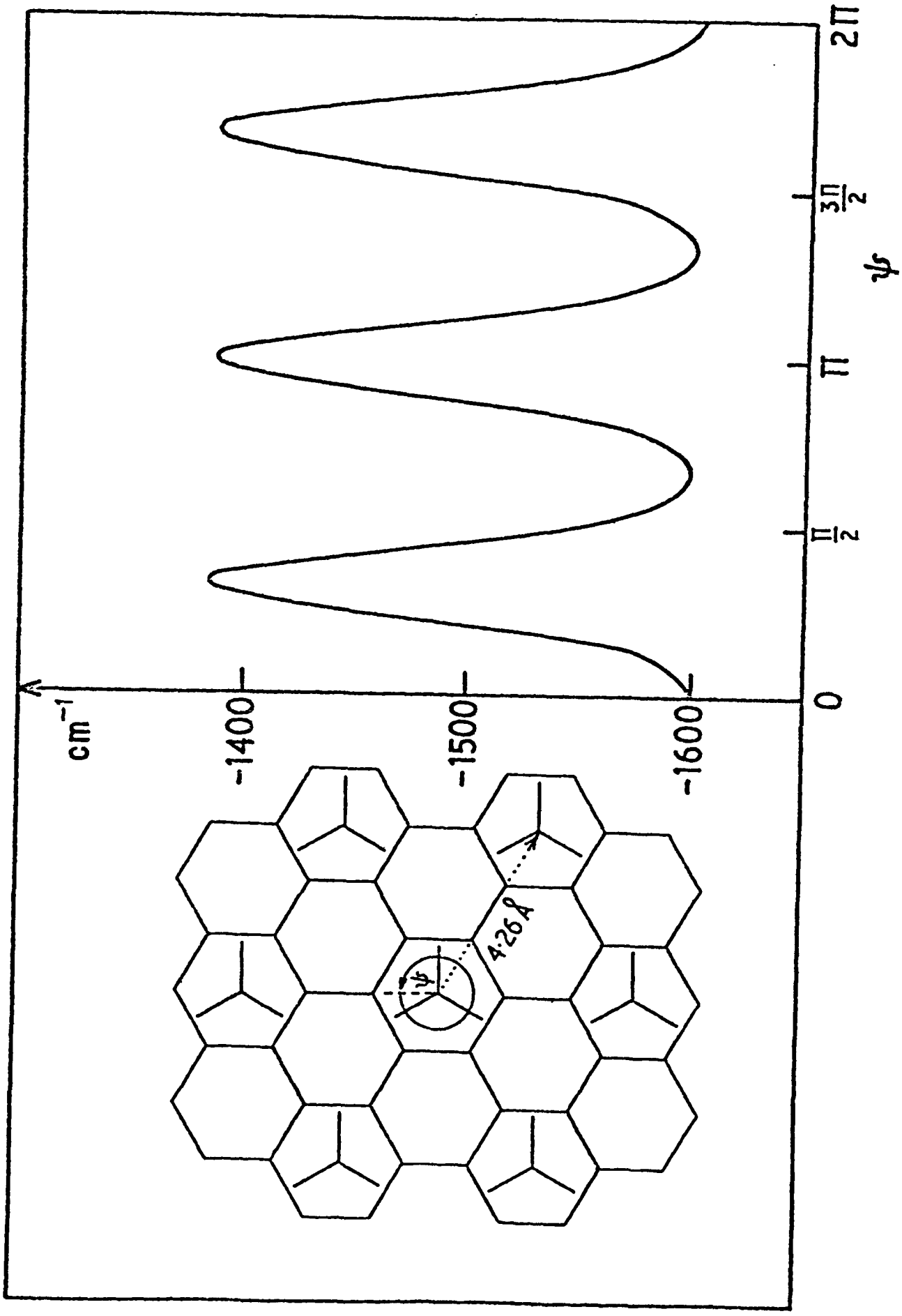
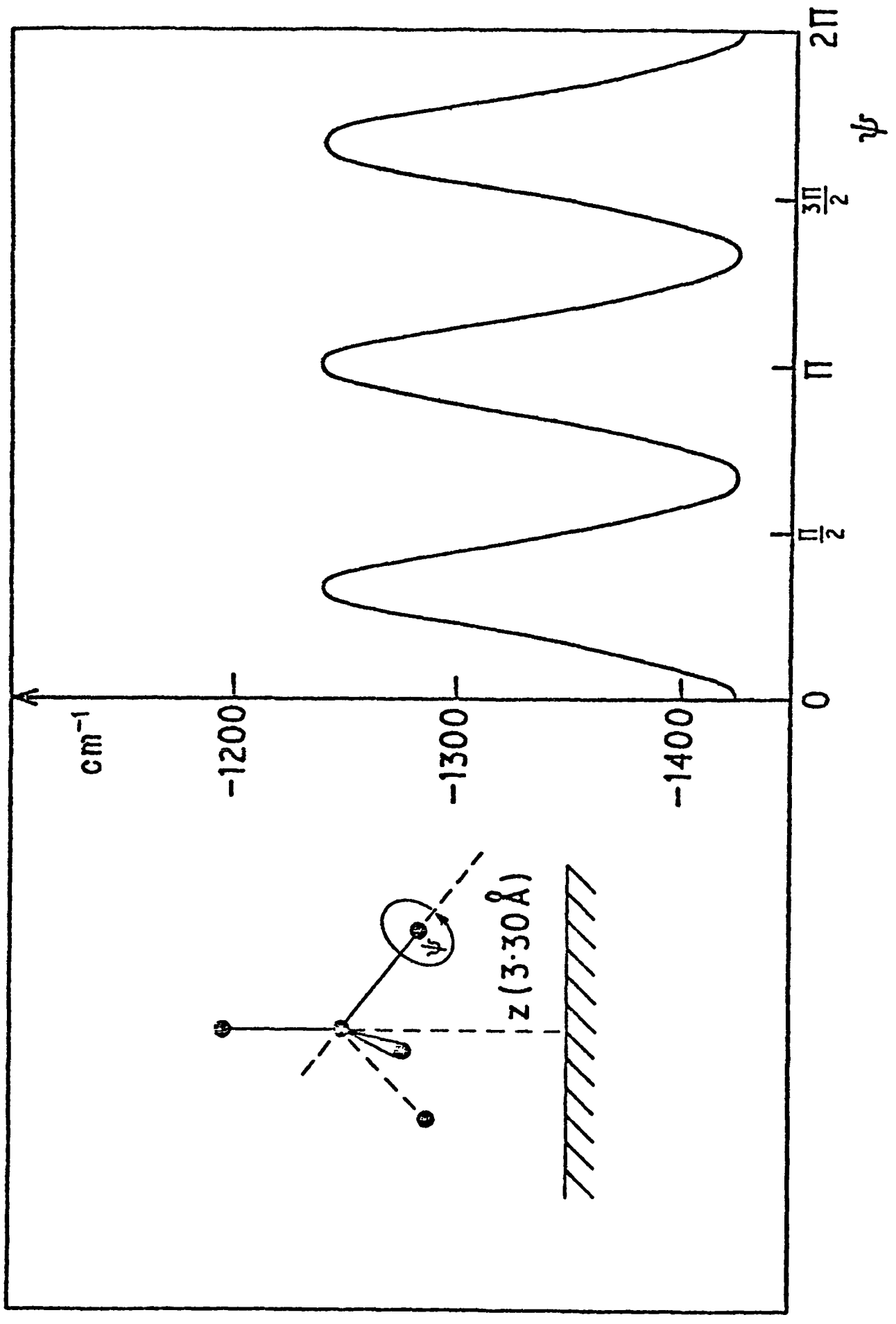


Figure 3.9 The rotation which gives rise to the h barrier. The molecule is fixed at its minimum potential energy with respect to the surface and rotated around one of the bonds pointing into the surface. The remaining molecules in the monolayer remain fixed. The barrier to this rotation is shown in the right-hand side of this figure.



in table 3.1 give a barrier height of 180 cm^{-1}; the experimental height is 175 ± 5 cm^{-1} (Bomchil et al., 1980).

The average height of the monolayer above the surface, (that is the potential minimum in the tripod orientation), is predicted by the model to be 3.3 Å which is the same as the experimental value determined by neutron scattering. Again very fine adjustments in ε and σ in the order of < 5% alters the barrier height by up to 15%. The program ROTBAR used to calculate these barriers is listed in the program appendix at the end of the thesis.

3.4.3 Isosteric Enthalpy at Zero Coverage

In contrast to the static calculation used to determine the rotational barriers, the molecular dynamics simulation of a single molecule on the surface gives a value of the isosteric enthalpy at zero coverage, $q_{st}^{\ominus}$. Steele (1974) has shown that

$$q_{st}^{\ominus} = RT - L < U (\underset{\sim}{r}_m \underset{\sim}{\omega}_m) > \qquad (3.4.1)$$

where L is Avogadro's constant and < > represents a time-average over all the configurations generated in the molecular dynamics simulation. Simulations were performed at a number of points between 0 and 150K. The results are summarized in Figure 3.10.

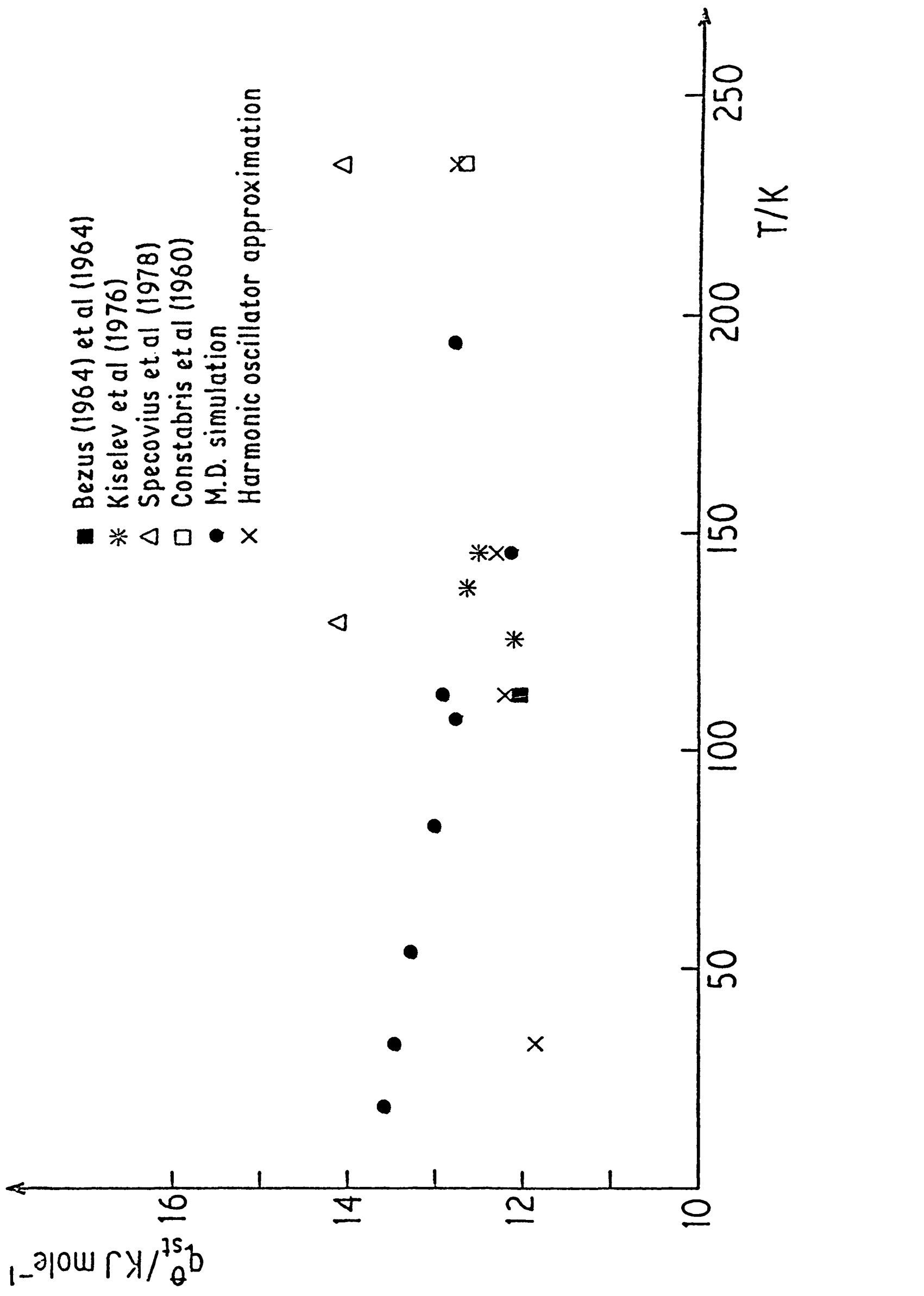


Figure 3.10 The isosteric enthalpy at zero coverage is plotted as a function of temperature. The points represent the computer simulation results using the model described in the text. The crosses are the results obtained by applying the harmonic oscillator approximation to the same model.

The isosteric enthalpy at zero coverage can be measured from experiment in two ways; low pressure measurements of the adsorption of methane on graphitized carbon black (Bezus et al., 1964; Sams 1965), and the slope of $\ell n\ K_H$ versus 1/T (Kiselev et al., 1976) where K_H is Henry's law constant governing adsorption at low pressures (Steele, 1974). Both these experimental techniques involve an extrapolation of experimental results to zero-coverage and the spread of experimental results shown in Figure 3.10 is indicative of the difficulty in performing these experiments. The simulation results between 100 and 150K are in reasonable agreement with experiment, although the experimentalists offer no estimate of the error in their results. This property is most sensitive to $\varepsilon_{C_gH_m}$ and to a less extent $\varepsilon_{C_gC_m}$, that is the two independent well depths of the surface-methane interaction. Fine adjustment was made on $\varepsilon_{C_gH_m}$, (while $\varepsilon_{C_gC_m}$ was held fixed at the Williams IV value of 47.68K) to give the best agreement with experiment. Anytime adjustment is made to the simulation parameters, the rotational barriers are recalculated to ensure they remain consistent with experiment. The values already quoted for the barriers are those calculated after the final adjustment to all parameters.

These results enable us to test an approximation for the isosteric enthalpy at zero coverage. If we assume the rigid methane molecule behaves as an harmonic oscillator in the z direction (Steele, 1974, pp 116-118) we can derive a simple

expression for $q_{st}^{\ominus}$. The gas solid potential for a uniform surface with no barriers to free translation is a function of z and the single particle configuration energy can be written as (Steele, 1974),

$$Z_1^{(s)} = \int_A dxdy \int_{z(s)} \exp\left(- U_s(z)/k_B T\right) dz \qquad (3.4.2)$$

The harmonic oscillator approximation is used to evaluate this integral. The potential energy is,

$$U_s(z) = \varepsilon_{min} + \frac{k_z}{2} (\bar{z} - \bar{z}_{min})^2 \qquad (3.4.3)$$

where k_z is the vibrational force constant defined in the usual way as

$$k_z = \left(\frac{\partial^2 U}{\partial z^2}\right)_{z=z_{min}} \qquad (3.4.4)$$

Equation (3.4.2) becomes

$$Z_1^{(s)} = A \exp\left(-\varepsilon_{min}/k_B T\right) \int \exp\left(- \frac{k_z}{2k_B T} \zeta^2\right) d\zeta \qquad (3.4.5)$$

where $\zeta = z - z_{min}$. Since the integrand decreases rapidly with increasing ζ, we can extend the integration from $+\infty$ to $-\infty$ with negligible error, to obtain

$$Z_1^{(s)} = A\, e^{-\varepsilon_{min}/k_B T} \left(\frac{2\pi\, k_B T}{k_z} \right)^{\frac{1}{2}} \qquad (3.4.6)$$

Substituting this into the equation for $q_{st}^{\ominus}$,

$$q_{st}^{\ominus} = RT + R\, \frac{\partial\, \ell n\, Z_1^{(s)}}{\partial(1/T)} \qquad (3.4.7)$$

we get

$$q_{st}^{\ominus} = \tfrac{1}{2}RT - L\, \varepsilon_{min} \quad . \qquad (3.4.8)$$

If we average the surface-methane potential over all orientations of the methane molecule and over all positions of the surface we obtain the spherical potential U(z),

$$U(z) = \frac{1}{8\pi^2} \int_{x=-\infty}^{+\infty} \int_{y=-\infty}^{+\infty} \int_{\psi=0}^{2\pi} \int_{\theta=0}^{2\pi} \int_{\phi=0}^{\pi} U(\underset{\sim}{r}_m, \underset{\sim}{\omega}_m)\, \sin\theta\, d\psi d\phi d\theta dx dy$$

(3.4.9)

The limits of integration can be simplified to give a tractable numerical solution; (the method is discussed in the next section). We measure ε_{min} from equation (3.4.9) and compare the results of $q_{st}^{\ominus}$ (harmonic oscillator) in Figure 3.10 with experiment and

simulation. The agreement at 150K with the exact model result is impressive. However, because ε_{min} is independent of temperature, the harmonic oscillator result has the opposite trend with temperature to the exact result. The slope of $q_{st}^{\ominus}$ vs T depends on the temperature dependence of $< U(\underset{\sim}{r}_m, \omega_m)>$ at zero-coverage.

The Surface Second Virial Coefficient

A knowledge of $q_{st}^{\ominus}$ and the rotational barriers enables us to adjust the potential parameters of the methane-surface potential. We can check the final parameterization given in table 3.1 by calculating the surface second virial coefficient. The number of molecules in the adsorbed phase, N_s, can be written as a series expansion in powers of the pressure normal to the surface (P).

$$N_s = B_{as} \frac{P}{k_B T} + C_{aas} \left(\frac{P}{k_B T}\right)^2 + D_{aas} \left(\frac{P}{k_B T}\right)^3 \ldots\ldots, \qquad (3.4.10)$$

where k_B is Boltzmann's constant and B_{as}, C_{aas} and D_{aas} are the surface virial coefficients (Steele, 1974). B_{as} can be shown to be (Steele 1974)

$$B_{as} = \int_v \exp\left(-U_s(\underset{\sim}{r}_{\alpha s})/k_B T\right) - 1 \; d\underset{\sim}{r}_{\alpha s} \; . \qquad (3.4.11)$$

The calculation of B_{as} for our model will involve integrating over all configurations of one molecule at all heights over the surface. The symmetry of the surface allows us to simplify this integral to evaluating the integrand over one unit cell of the surface. To sample uniformly over a rhombus a change from normal cartesian x,y variables is necessary. We change from x,y to a_x, a_y where $a_x = x$ and $a_y = y/\cos 30^o$. The Jacobian for this transform is $\cos 30^o$ and the second virial coefficient can be written as

$$B_{as} = \frac{\cos 30^o}{8\pi^2} \int_{a_x=0}^{d} \int_{a_y=0}^{d} \int_{z=0}^{\infty} \int_{\cos\theta=-1}^{+1} \int_{\phi=0}^{2\pi} \int_{\phi=0}^{2\pi} [\exp(-U_s(r_{\sim\alpha s})/k_B T) - 1] \, d\phi d\psi d\cos\theta \, dz da_y da_x \tag{3.4.12}$$

It is not possible to evaluate this integral numerically in the range $z = 0$ to ∞. For small z, U_s is very large and the exponential is too small to be handled by the computer. To overcome this problem we assume the exponential is zero in the range $z = 0$ to r_{min}. The analytic solution to this integral is

$$B_{as}^{0 \to r_{min}} = \frac{\cos 30^o}{8\pi^2} \int_0^d \int_0^d \int_0^{r_{min}} \int_{-1}^{1} \int_0^{2\pi} \int_0^{2\pi} -1 \, da_x da_y dz d\cos\theta \, d\phi d\psi$$

$$= -1 \frac{\cos 30}{8\pi^2} \, d.d. \, r_{min} . 2.2\pi . 2\pi$$

$$= - \frac{\sqrt{3}}{2} \, r_{min} \, d^2 \, . \qquad (3.4.13)$$

At large z the potential approaches zero rapidly and we set the integrand to zero. We chose an upper limit of z that will satisfy the above condition. A value of z = 50 Å is sufficiently large. The total integral for B_{as} now becomes

$$B_{as} = - \frac{\sqrt{3}}{2} \, r_{min} \, d^2$$

$$+ \int_0^d \int_0^d \int_{r_{min}}^{50\text{Å}} \int_{-1}^{1} \int_0^{2\pi} \int_0^{2\pi} [\exp(-U_s/k_B T) - 1] \, da_x da_y dz d \cos\theta \, d\phi d\psi .$$

(3.4.14)

This integral does not have a simple numerical solution and we must adopt a non-product integration method (Stroud, p. 224) to solve (3.4.14). This method divides the n-dimensional phase space into many small regions and evaluates the integrand for a given number of points in each sub-region. Convergence is tested by increasing the number of regions in the interval of integration until a further increase does not affect the result by a predetermined amount.

The algorithm for evaluating an integrand in a small region of phase space is now described. For an n-dimensional integral (in our case n = 6), we select 2n points in the region

to be evaluated. The interval of integration for each dimension is scaled to -1 to +1, and the values of these points distributed "evenly" over each region is given by

$$r_{i,2k-1} = \sqrt{\frac{2}{3}} \cos \frac{(2k-1)}{n} i\pi,$$

and

$$r_{i,2k} = \sqrt{\frac{2}{3}} \sin \frac{(2k-1)}{n} i\pi, \qquad (3.4.15)$$

where $k = 1,2,\ldots\frac{n}{2}$ and $i = 1,2\ldots2n$ for n even.

$$\text{If n is odd} \quad r_{in} = \left(-\frac{1}{\sqrt{3}}\right)^{i} \qquad (3.4.16)$$

where $i = 1,2\ldots2n$.

The k index represents each variable of integration and the n index gives the 12 values for each variable. The value of the integral I is equal to the sum

$$I = \sum_{j} \frac{V_j}{2n} \sum_{i=1} f(r_{in}), \qquad (3.4.17)$$

where the sum i is over the 2n points in each n-dimensional region, j is the sum over all regions in space, and V_j is the

volume of one region. When applying this technique to the 6-dimension integral (eqn. (3.4.14), we must divide the interval of integration for each variable into a number of smaller intervals. V_j will be the product of the values of each of the small intervals. It can be seen by the way we have represented equation (3.4.17) that V_j need not be constant for the whole range of integration, i.e. we can reduce the volume of the region where the value of the function is large or rapidly changing.

We use this technique to calculate the spherically averaged potential $U_s(\bar{z})$ in the previous section. A listing of the program VIRIAL is shown in the appendix at the end of the thesis.

Before proceeding to calculate B_{as}, the integrating algorithm was tested using a function with an analytic result. The function chosen is

$$\int_0^1 \int_0^1 \int_0^1 \int_0^1 \int_0^1 \int_0^1 e^{-(a+b+c+d+e+f)}\, dadbdcdddedf$$

$$= (1 - \frac{1}{e})^6 = 0.063797 \qquad (3.4.18)$$

Not only does this function have a simple analytic expression but it is also similar in characteristic to the integral we wish to evaluate. Each of the intervals of integration are divided into 4 sub-intervals giving a total of 4096 regions and 49152 points. The numerical value of the integral for this number of points is 0.063795, which is sufficiently accurate for our requirements.

The intervals of integration for equation (3.4.14) are divided as follows; a_x, a_y, $\cos\theta$ into 2; ϕ, ψ into 3; z from 2.88 to 7.87 Å into 10 intervals and from 7.87 to 47.23 Å into 8 intervals. These give results within machine error.

Experimental values for the second virial coefficient of methane adsorbed on graphite were determined calorimetrically by Sams in 1965 over a temperature range of 220 to 300K. In comparing these experimental values with the calculated values, eqn. (3.4.14), we require the surface area per gram of graphite used in the experiment. The surface area per gram, A, as determined from the experimental measurements of Sams is 11.3 $m^2\ g^{-1}$, but this estimate is certainly model dependent. Our results using a number of values of A are shown in Table 3.2. Excellent agreement is obtained with experiment using a surface area of 10.5 $m^2\ g^{-1}$. The model reproduces the temperature dependence of the surface second virial coefficient between 224 and 297K almost exactly. This agreement between model and experiment using a realistic surface area helps to confirm the parameterisation given in Table 3.1.

The final values of the potential parameters are close to the initial guesses. The potential produces the correct rotational barriers in the monolayer and gives the $\sqrt{3}$ x $\sqrt{3}$ registered epitaxial structure as the most stable monolayer structure. The potential predicts the observable height of the monolayer above the surface. It also predicts the experimental value of the isosteric enthalpy

Table 3.2

T/K	$B_2(T)$exp/$cm^3\ g^{-1}$	$B_2(T)$ eq(3.4.14)/$cm^3\ g^{-1}$		
		10.5 $m^2\ g^{-1}$	10.6 $m^2\ g^{-1}$	11 $m^2\ g^{-1}$
224.1	0.419	0.417	0.425	0.441
230.2	0.359	0.359	0.363	0.376
235.0	0.320	0.319	0.322	0.334
242.3	0.273	0.269	0.271	0.282
250.5	0.228	0.225	0.227	0.235
263.3	0.179	0.174	0.175	0.182
277.2	0.137	0.135	0.136	0.141
287.3	0.118	0.114	0.115	0.120
297.2	0.099	0.098	0.099	0.103

The second virial coefficient of methane adsorbed on graphite. The model results depend on the value of A, the surface area per gram, of the carbon used in the experiment. Comparison with the experimental results are shown using three difference values of A.

at zero coverage and gives good estimates of the surface second virial coefficients.

The collision diameters, $\sigma_{C_gC_m}$ and $\sigma_{C_gH_m}$, for the methane surface interaction are in reasonable agreement with three previous estimates (Kiselev and Poshkus 1963); (Battezzati et al., 1975) (Lal and Spencer, 1974). However our value for $\varepsilon_{C_mC_g}$ is higher than estimated by two other workers (Battezzati et al., 1975); (Kiselev et al., 1963) and comparable with the value of (Lal and Spencer, 1974).

3.5 Some Properties of the Model

In the last section we showed how the potential function describing the methane surface interaction could be parameterised. In this section we use this parameterised potential to examine some aspects of the behaviour of a single methane molecule as it translates and rotates across the surface and vibrates against the surface.

Figures 3.11 - 3.13 show the translation of a methane molecule across the surface at three different temperatures. At the lowest temperature of 18.6K, the methane sits as a tripod above the surface. The molecule translates across the surface in the tripod orientation and rotates with some degree of freedom around the C-H bond perpendicular to the surface. The methane molecule contains only a small amount of translational energy and its

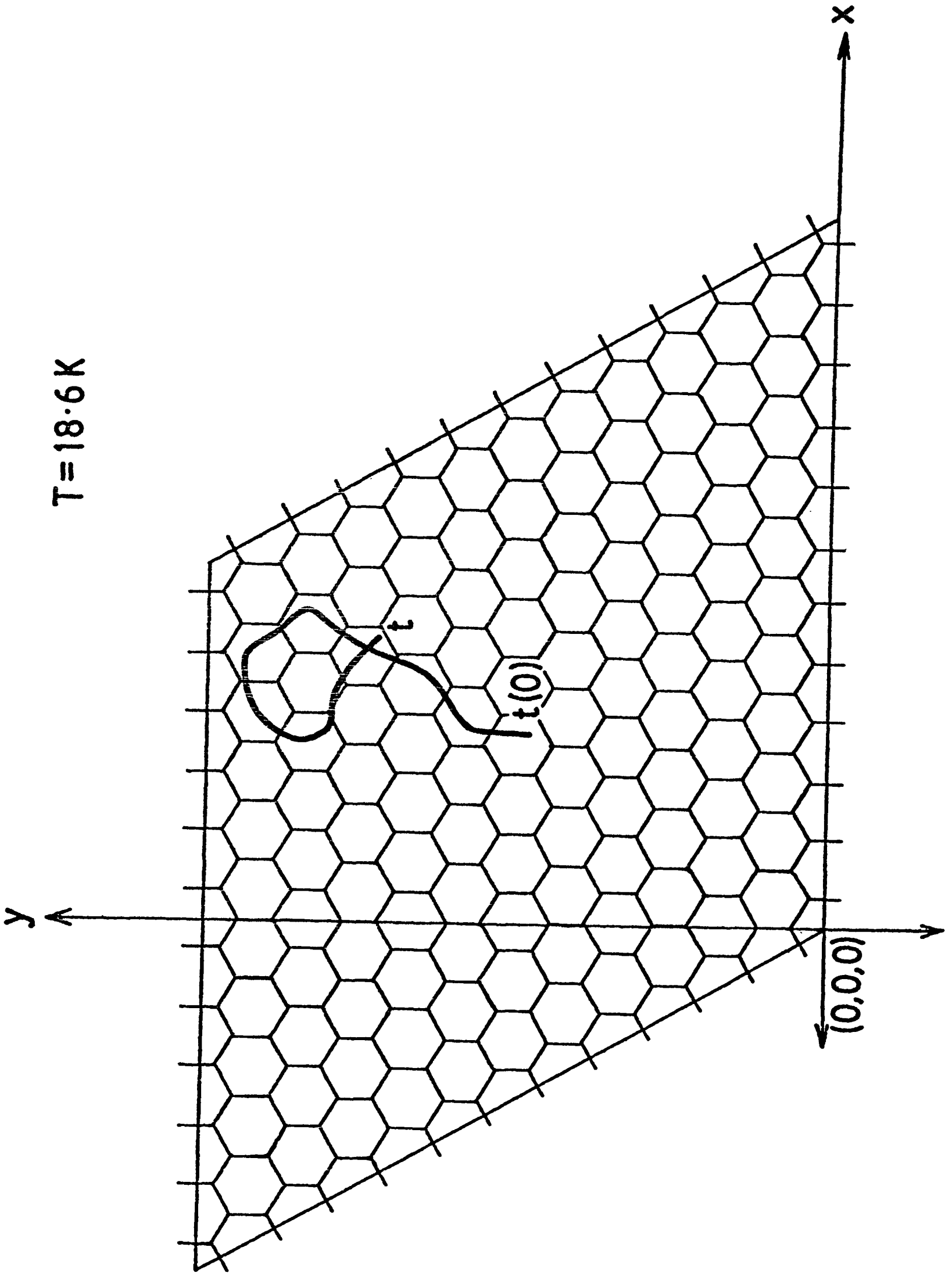
motion is influenced by the surface structure. The molecule remains close to the equilibrium height of 3.3 Å.

At the higher temperature of 53.4K (Fig. 3.12) the molecule still translates in the tripod orientation, now rotating freely about the C-H bond perpendicular to the surface. The molecule has substantial kinetic energy and moves in essentially straight lines across the surface, scarcely noticing the surface structure. During the simulations in the microcanonical ensemble there are fluctuations in the temperature and during this run the temperature obtained an instantaneous value at which tumbling took place. This is marked with a star in Figure 3.12. At this point the molecule loses translational kinetic energy and begins to feel the structure of the surface.

Finally, Figure 3.13 shows the behaviour at a high temperature of 108K. The molecule now tumbles and collides with the surface, however it is not a free rotor. It contains enough kinetic energy to translate in straight lines across the surface, unaffected by surface structure. Each of these figures constitutes a run of 20,000 timesteps, or a real time period of 25 picoseconds.

As the molecule translates and rotates, it vibrates against the surface. Figure 3.14 shows this vibrational behaviour at two temperatures. At the lower temperature of 18.6K the vibrations are of small amplitude and are regular. An abscica is drawn at the average height of the molecule above the surface which is

Figure 3.11 The translation of a methane molecule across the surface. t(0) and t represent the initial and final positions of the projection of the c.o.m of the methane molecule on the surface. The molecule leaves the basic cell at x and re-enters at x'.



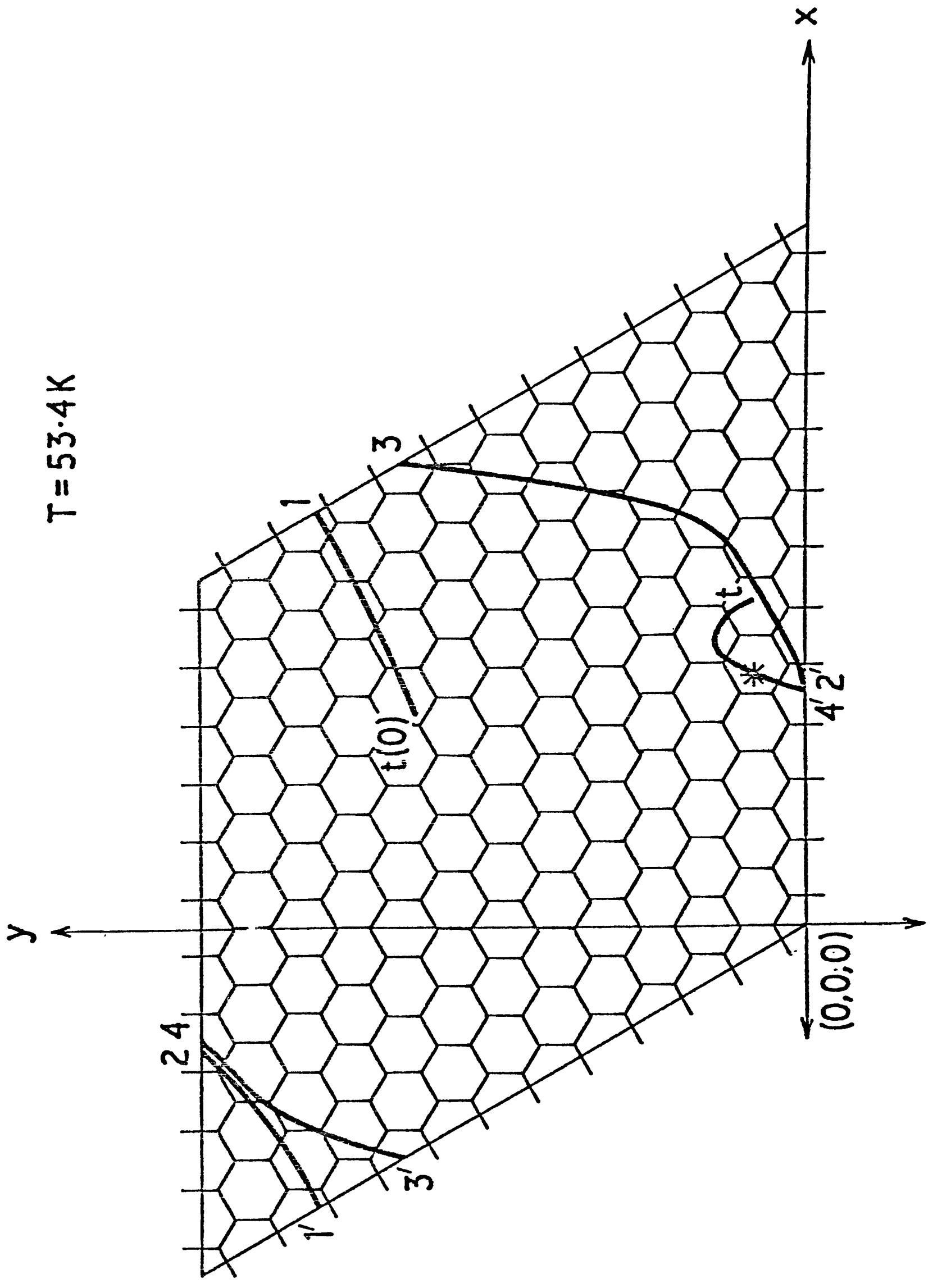


Figure 3.12 Translation of a methane molecule across the surface of the basic cell. Conventions are the same as Figure 3.11. The star represents the onset of tumbling (see text).

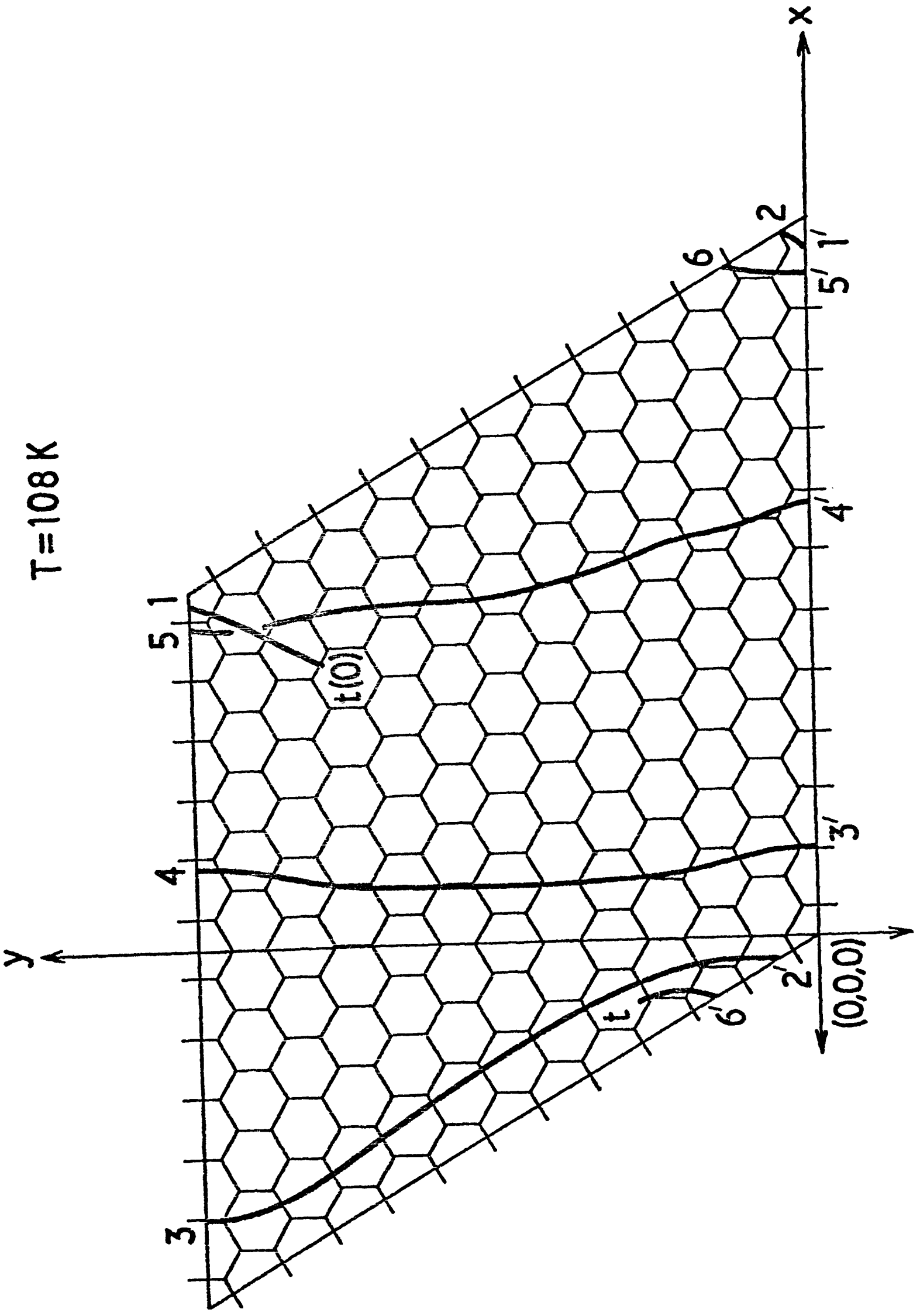


Figure 3.13 The translation of a methane molecule across the surface of the unit cell. Conventions are the same as Figure 3.11.

3.35 Å. At the higher temperature the amplitude of the vibration is larger and the methane molecule makes a number of collisions with the surface. These collisons help to randomise the orientation of the molecule. The fact that the molecule is tumbling diminishes the periodicity of the vibrational motion. The average distance of the molecule from the surface increases with temperature.

We can extract the vibrational frequency directly from Figure 3.14. These frequencies, as a function of temperature, are given in Table 3.3. The vibrational frequency appears to vary almost linearly with temperature and we can predict that the vibrational frequency close to absolute zero would be 98 ± 2 cm^{-1}. It is encouraging that neutron scattering on the adsorbed monolayer against the surface is approximately 100 cm^{-1} (Bomchil et al., 1980).

We can examine the rotational behaviour of the molecule by calculating the single particle reorientational correlation functions,

$$C_\ell(t) = \langle P_\ell (\underset{\sim}{u}(o) \cdot \underset{\sim}{u}(t)) \rangle \quad . \qquad (3.5.1)$$

$P_\ell(x)$ is the ℓ^{th} order Legendre polynomial, $\underset{\sim}{u}(t)$ is a unit vector describing the orientation of a molecule at a time t and the brackets indicate an ensemble average. For convenience $\underset{\sim}{u}(t)$ is taken to point along the C-H bond perpendicular to the surface, and $C_1^{\perp}(t)$ as a function of temperature is shown in Figure 3.15. $C_1^{\perp}(t)$ is more commonly recognised as $\langle \cos\theta \rangle$,

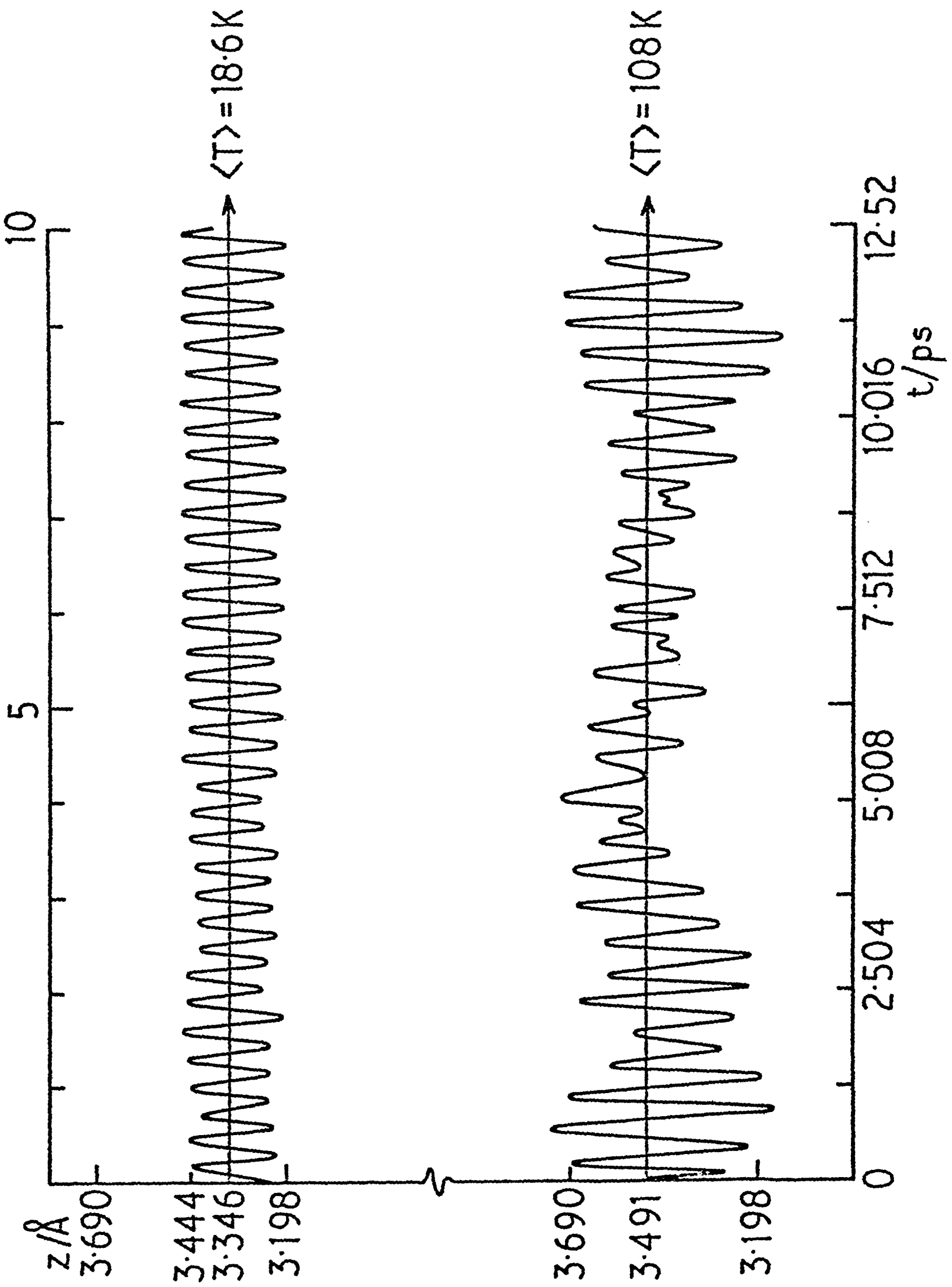


Figure 3.14 The height of the c.o.m of the methane molecule above the surface is shown as functions of time for two temperatures. The amount of real time covered, 12.52 pico-seconds, is 10^4 molecular dynamics timesteps in the total simulation. The average height of the methane increases with increasing temperature and the frequency of the vibration decreases with increasing temperature.

Table 3.3

T/K	No. cycles/10^4 timesteps	ν/cm^{-1}
170	28	74.5 ± 2
117	31	82.5 ± 2
97	32	85.1 ± 2
61	34	90.4 ± 2
32	35	93.1 ± 2
18	36	95.8 ± 2
0	extrapolated	98 ± 2

The vibrational frequency of the methane molecule for the vibration against the graphite surface. One timestep is 1.252 x 10^{-15} s, and x cycles/10^4 timesteps is equivalent to 2.66 x cm^{-1}.

and is known as the auto-reorientational correlation function. The angle θ is the angle between the C-H bond initially perpendicular to the surface and the z axis.

At low temperatures the molecule librates around the tripod orientation as its C.O.M. moves across the surface and $C_1^{\perp}(t)$ hardly deviates from its t = 0 value of unity. At higher temperatures the molecule tumbles and its position at a time t becomes uncorrelated with its position at time zero. The free rotor correlation function for a tetrahedral molecule is known exactly (Berne and Pecora 1976)

$$C_\ell^o(t) = \frac{1}{2\ell+1} \sum_{m=-\ell}^{\ell} (1-m^2\tau^2) \exp(-m^2\tau^2/2) \qquad (3.5.2)$$

where the superscript o implies free rotation and $\tau = (k_B T/I)^{\frac{1}{2}} t$. I is the moment of inertia of the molecule. The $C_1^o(t)$ correlation function at 130K shown in Figure 3.15; the limit as $t \to \infty$ of $C_1^o(t)$ is 1/3 for all values of t. It is evident that at high temperatures the molecule is not rotating freely on the surface. The strong interactions or collisions with the surface cause rapid changes in the torques which tend to randomise the orientation of the methane.

Finally at low temperatures we can also consider the rotation of a unit vector $\underset{\sim}{u}''(t)$ parallel to the surface and perpendicular to $\underset{\sim}{u}(t)$. If the molecule rotates around its epitaxial C-H bond

the correlation function $C_1^{''}(t)$ describing the memory of $\underset{\sim}{u}^{''}(t)$ is given by

$$C_1^{''}(t) = \langle P_1(\underset{\sim}{u}^{''}(o) \cdot \underset{\sim}{u}^{''}(t))\rangle \quad . \tag{3.5.3}$$

If the rotation is free, then the probability the molecule is rotating about its epitaxial bond with an angular velocity ω_Z is,

$$f(\omega_Z)\, d\omega_Z = (2\pi\, k_B T/I)^{-\frac{1}{2}} \exp\,(-I\omega_Z^2\,/2k_B T) \tag{3.5.4}$$

and

$$C_1^{''^{,O}}(t) = (2\pi\, k_B T/I)^{-\frac{1}{2}} \int_{-\infty}^{+\infty} \cos\,(\omega_Z t) \exp\,(-I\omega_Z^2/2k_B T)\, d\omega_Z$$

(3.5.5)

This standard integral (Gradshteyn and Ryzhik, 1965) gives

$$C_1^{''^{,O}}(t) = \exp\,(-\tau^2/2) \quad . \tag{3.5.6}$$

Figure 3.16 shows a comparison of $C_1^{''}(t)$ and $C_1^{''^{,O}}(t)$ which indicates that at low temperatures the methane particle behaves like a free rotor around its epitaxial axis. At higher

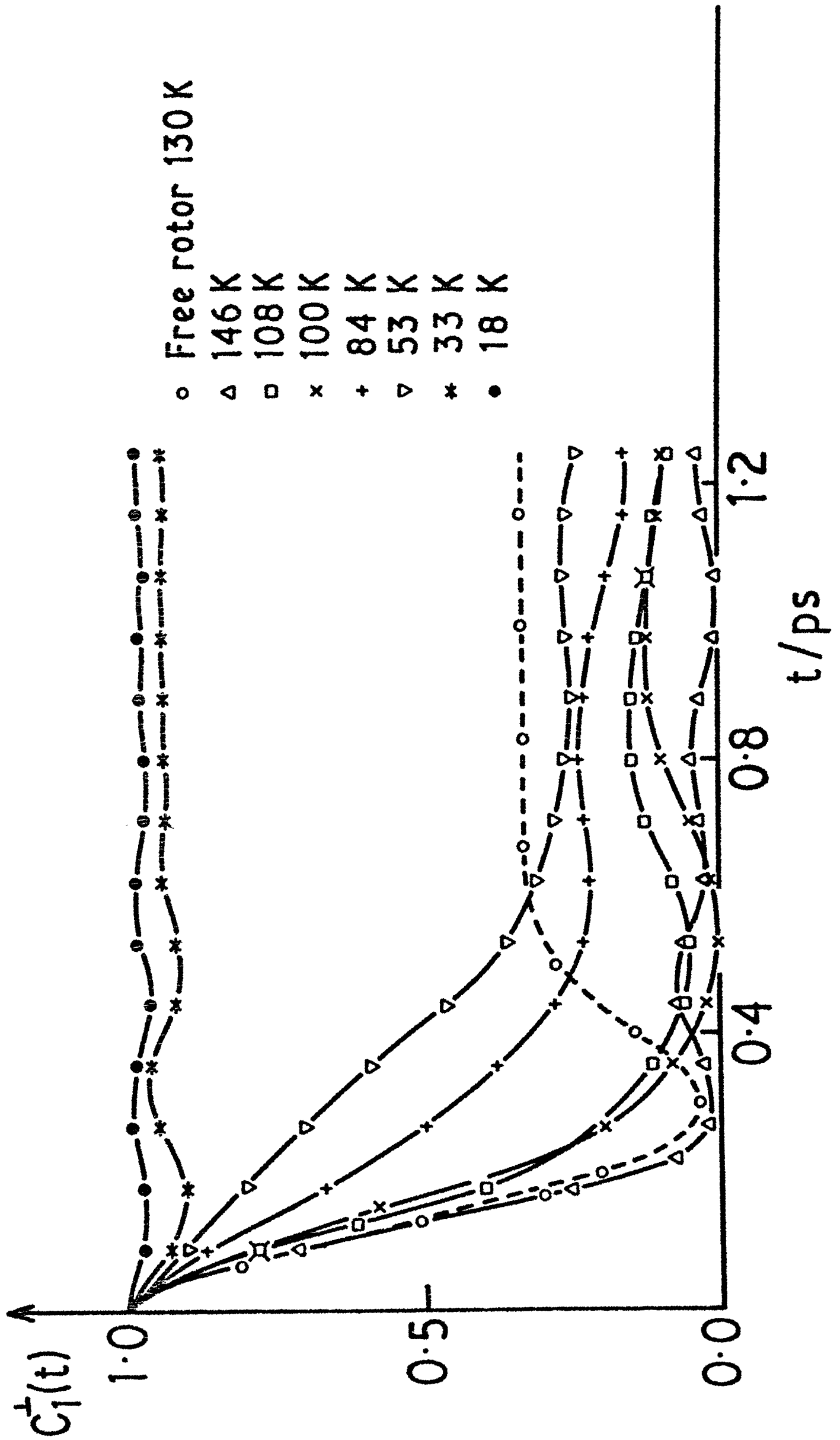


Figure 3.15 The single particle reorientational correlation function for a methane particle adsorbed on a graphite surface. These correlation functions were obtained by averaging over runs of 10^5 timesteps. The free rotor correlation function at 130K is included for comparison.

temperatures $C_1^{\parallel}(t)$ should be equivalent to $C_1^{\perp}(t)$.

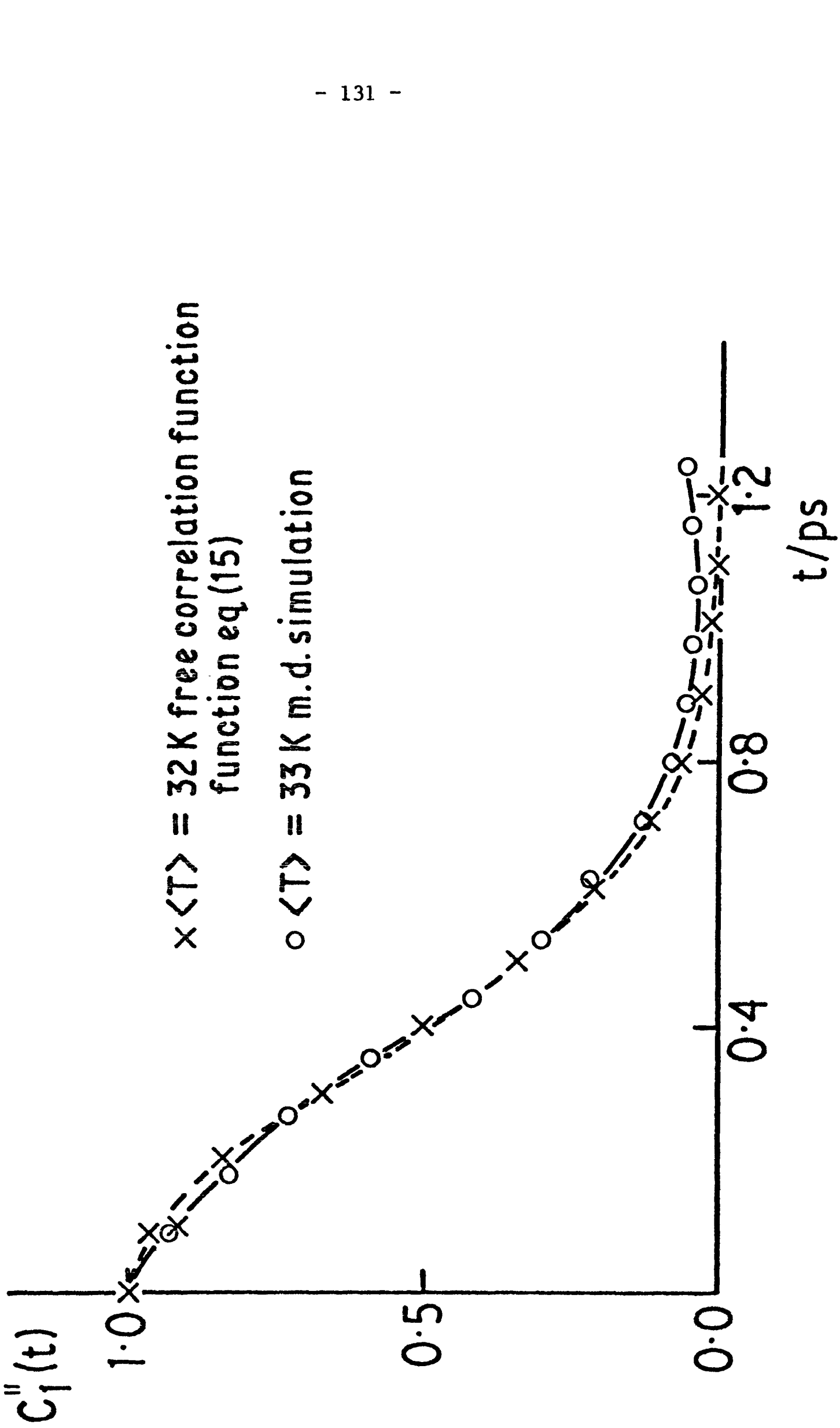


Figure 3.16 The single particle reorientational correlation function for a unit vector $\underset{\sim}{u}$ (t) perpendicular to the epitaxial axis. This is almost identical to free rotor correlation function given by equation (3.5.6) indicating that rotation around the epitaxial bond at low temperatures is hardly affected by the surface structure.

CHAPTER 4

Solid Methane Adsorbed on Graphite

4.1 Introduction - The Phase Diagram

At temperatures below 100K methane adsorbed on a basal plane of graphite exhibits a rich variety of phase behaviour. The experimental information on this system comes from three principal sources, the thermodynamic measurements of the adsorption isotherm (Thomy and Duval, 1970), the coherent and incoherent scattering of neutrons by the adsorbate (Vora et al., 1979; Bomchil et al., 1980; Coulomb et al., 1979), and pulsed field gradient measurements in N.M.R (Tabony and Cosgrove, 1979).

Measurements by Thomy and Duval (1970) indicate methane is an adsorbate which wets the underlying surface forming a monolayer at suitable temperatures and pressures. The discontinuities in the adsorption isotherm indicates the presence of different phases in the monolayer when the methane is adsorbed on particularly homogeneous graphite.

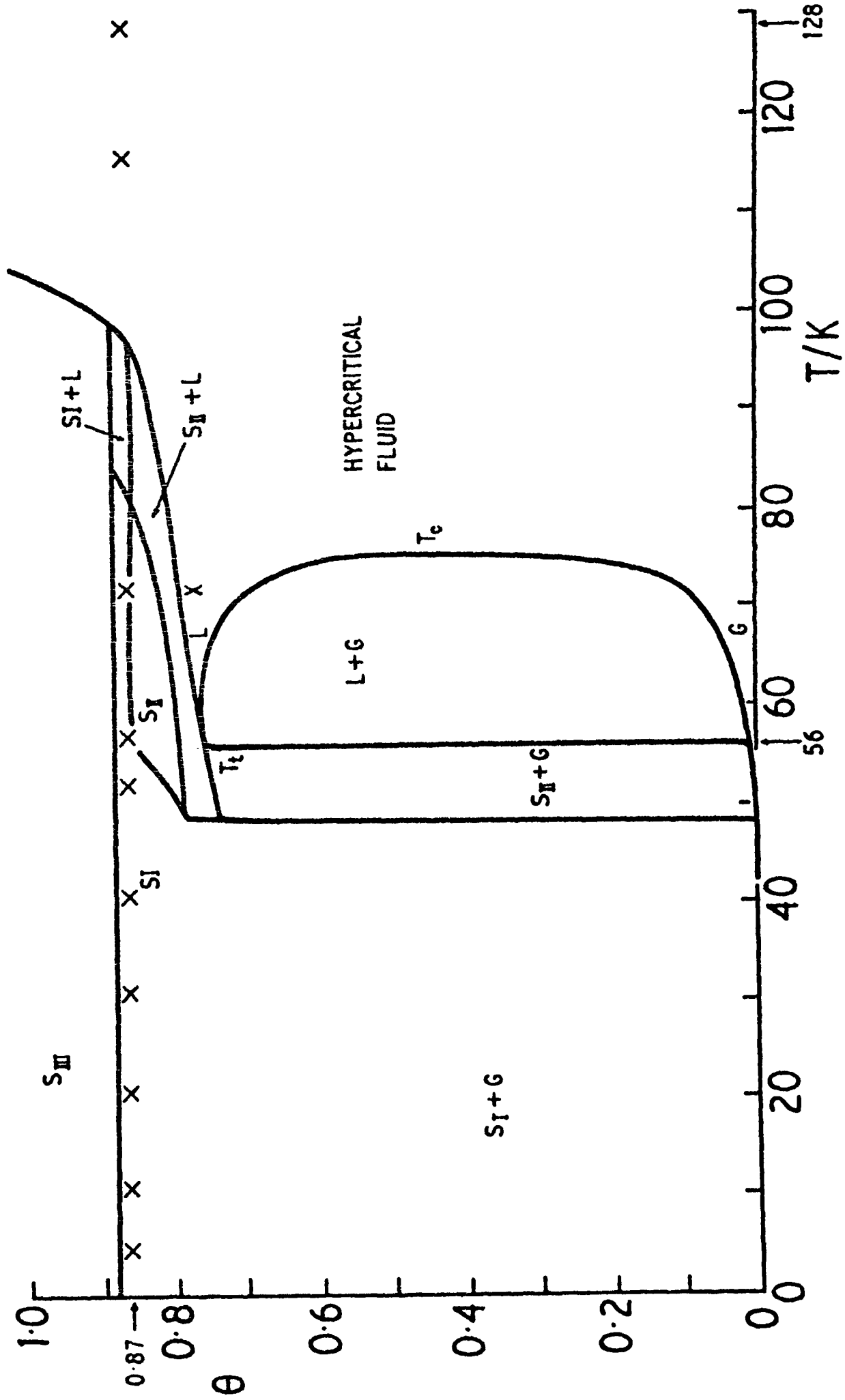
Neutron diffraction studies on adsorbed deuteromethane (see references above) measure the lattice spacing of the methane molecules and the correlation length of the phase on the surface. This information is very useful in characterising the structure of the solid phases. Incoherent inelastic neutron scattering from the protons in methane (Bomchil et al., 1980; Newbery et al., 1978)

provides insight into the rotational motion of the molecule in the solid. The quasi-elastic scattering (Coulomb et al., 1979) and pulsed gradient N.M.R (Tabony and Cosgrove, 1979) can be used to determine the self-diffusion coefficient in the adsorbed liquid.

The combination of all the available experimental data has enabled the construction of a tentative phase diagram for methane adsorbed on graphite (Vora et al., 1979; Coulomb et al., 1979). This diagram is shown in Figure 4.1. It should be noted that the exact loci of the two phase lines are not known, but the triple point marked T_t has been carefully measured (Coulomb et al., 1979). The phase S_{III} is believed to be a two-dimensional close-packed solid which is incommensurate with the underlying lattice. It is often referred to as the compressed solid phase and occurs at coverages above 0.88. A coverage of one is defined by the completed compressed monolayer; at coverages higher than one, the molecules will be added to the second and subsequent layers.

The phase S_I has been identified as a $\sqrt{3} \times \sqrt{3}$ hexagonal lattice (Vora et al., 1979; Marlow et al., 1978) and is thought to be in registry with the basal plane of graphite. The lattice spacing of the adsorbate (4.26 Å) is a factor of $\sqrt{3}$ larger than the lattice spacing in the graphite (2.46 Å). There is likely to be a small range below 0.88 where the phase S_I coexists with the liquid (Vora et al., 1979). S_{II} has been characterized by diffraction as an expanded solid phase. Its nature is not yet well understood, but it has been suggested that it is associated with some localized

Figure 4.1 A phase diagram of methane adsorbed on graphite at submonolayer coverages. This diagram has been constructed from experimental information and a number of previously published diagrams. T_t the triple point temperature is thought to be at 56K and T_c the gas-liquid critical temperature between 70K and 80K. The exact loci of the two phase lines are not known. The simulations reported in this work are marked with the symbol 'X'.


SI+L
SII+L
HYPERCRITICAL
FLUID
Tc
L+G
G
L
SI
Tt
SII+G
SIII
SI+G
1·0
0·8
0·6
0·4
0·2
0
θ
0·87
0
20
40
56
60
80
100
120
128
T/K

rotational freedom in the solid (Newbery et al., 1978).

In addition to these three solid phases, two liquid phases have been proposed (Coulomb et al., 1979). The first is a region of liquid-gas coexistence where the molecules form patches of liquid surrounded by gas, and the second is a hypercritical region where the fluid methane spreads over the entire graphite surface. Although this phase diagram is tentative it demonstrates the rich variety of phase behaviour that can be expected for the adsorbed methane.

In this chapter we examine the behaviour of the adsorbed solid as a function of temperature at constant coverage, $\theta = 0.87$. This surface density corresponds to 0.0636 molecules Å^{-2}, (the completed compressed monolayer has a surface density of 0.073 molecules Å^{-2}). The simulations performed are marked by crosses in Figure 4.1. The S_I solid structure has been partially characterized (see Figure 3.8), although it is not certain whether the methane sits over the centre of a hexagon or over one of the carbon sites. This knowledge of the structure enables the use of realistic starting configurations.

In section 2 we describe the changes to the molecular dynamics program to incorporate many adsorbate molecules and a program to analyse the time dependent properties of the system. We report the configurational energies and specific heats which give a clear indication of the phase transitions at this coverage. The mean squared forces and torques are used to determine the

quantum corrections to the system. In section 3 we present a discussion of the solid structure of the adsorbate as a function of temperature. This structure can be characterized by the translational order parameter of the adsorbate molecules, and the order parameter characterizing the correlation between the adsorbate molecules and the underlying surface, (Vieillard-Baron, 1972; Freasier et al., 1976). The velocity auto-correlation functions parallel and perpendicular to the surface are calculated and these can be related to the phonon density of states obtained by incoherent neutron scattering (Bomchil et al., 1980). Similarly the angular velocity auto-correlation function can be used to characterize the librational motion of the methane.

In section 4 we examine the rotational behaviour of the methane molecules on the surface. 3-dimensional solid methane exhibits a number of rotational phases (Parsonage and Staveley, 1978) which have been interpreted using the classical James-Keenan model (James and Keenan, 1959). The 2-dimensional analogue of this model has been studied by a Monte Carlo simulation (O'Shea and Klein, 1979) which predicts three rotational phases. The onset of rotational diffusion between 20 and 30K has been observed experimentally by incoherent neutron scattering from the monolayer (Newbery et al., 1978). We monitor the orientational order in the monolayer by calculating the reorientational correlation functions of the methane parallel and perpendicular to the surface.

Finally Newbery et al., (1978) have examined the behaviour of methane molecules in the second layer above the basal plane.

This neutron scattering experiment has been complemented by a theoretical treatment of the bilayer by Maki and O'Shea (1980). To simulate this situation we place three additonal methane molecules on top of the S_I solid structure at a temperature corresponding to 30K. The results of this simulation are discussed in section 5, and are compared to the single particle simulation. The particles in the second layer behave similarly to a free methane molecule on the surface with the strong surface-methane potential attenuated by the intervening monolayer.

4.2 The Simulation and Thermodynamic Properties

In section 3.2 we describe the details of the simulation of one methane molecule adsorbed on graphite. This program is extended to simulate many molecules adsorbed on the surface in the following way.

Seventy five methane molecules are used in the basic cell to simulate the completed S_I solid at $\theta = 0.87$. To accommodate seventy five molecules the graphite surface contains 15 x 15 unit cells corresponding to 450 surface atoms with a total area of 1179 $\mathring{A}^2$. The surface described in section 3.2 contains only 288 atoms and we have increased the size of the basic cell to increase the statistical information available on the adsorbed methane molecules and to increase the cut-off distance for the methane surface interaction. This cut-off distance is now 15.9 $\mathring{A}$ and each methane molecule interacts specifically with approximately 300 surface atoms. The large cut-off distance

means a larger proportion of the energy acting on a methane molecule comes directly from the site-site potential and a smaller amount from the approximate long range potential. The interaction between the methane molecule and the surface is given by eqn. (3.3.12) using the parameters in Table (3.1). The methane-methane interaction, $U_{CH_4-CH_4}$ is,

$$U_{CH_4-CH_4}(r_{12}\omega_1\omega_2) = \sum_{\alpha=1}^{5}\sum_{\beta=1}^{5} U_{\alpha\beta}(r_{\alpha\beta}) \quad , r_{12} < 9.8 \text{ Å};$$

$$= U_{\text{Long Range}}, \; r_{12} > 9.8 \text{ Å} \qquad (4.2.1)$$

where

$$U_{\alpha\beta}(r_{\alpha\beta}) = 4\,\varepsilon_{\alpha\beta}\left[\left(\frac{\sigma_{\alpha\beta}}{r_{\alpha\beta}}\right)^{12} - \left(\frac{\sigma_{\alpha\beta}}{r_{\alpha\beta}}\right)^{6}\right]. \qquad (4.2.2)$$

Twenty five site-site interactions, $U_{\alpha\beta}$, between two methane molecules are characterized by the usual Lennard-Jones energy and length parameters, $\varepsilon_{\alpha\beta}$ and $\sigma_{\alpha\beta}$, which are also given in Table (3.1). The cut-off, r_c, for the methane-methane interaction is based on the centre of mass separation of the molecules. At separations greater than 9.8 Å we add a correction. This long-range correction is derived in a similar way to the long range correction to the methane-surface interaction. We assume any

methane above the monolayer is sufficiently dilute to behave like an ideal gas and the z dependence of $r_{12} > 9.8$ Å is negligible. Beyond r_c the bulk methane is smeared with a density N_{CH_4}/A where N is the number of methane molecules in the basic cell of area A. Let r_i be the methane-fluid distance to area element dA(x,y). Following the steps of equations (3.3.3) through (3.3.7) the potential is given by,

$$U_{\text{Long Range}} = \sum_{\alpha=1}^{5} 4\pi N_A \varepsilon_{\alpha\beta} \int_{r_c}^{\infty} \left(\frac{\sigma_{\alpha\beta}}{r}\right)^{12} - \left(\frac{\sigma_{\alpha\beta}}{r}\right)^{6} r dr$$

$$= \sum_{\alpha=1}^{5} 4\pi N_A \varepsilon_{\alpha\beta} \left[\frac{\sigma_{\alpha\beta}^{12}}{10 r_c^{10}} - \frac{\sigma_{\alpha\beta}^{6}}{4 r_c^{4}}\right]. \qquad (4.2.3)$$

The term which contains $1/r_c^{10}$ is negligible and we approximate the long range potential by

$$U_{\text{Long Range}} \simeq \sum_{\alpha=1}^{5} - \pi N_A \varepsilon_{\alpha\beta} \frac{\sigma_{\alpha\beta}^{6}}{r_c^{4}}. \qquad (4.2.4)$$

The site-site potential on the molecules is calculated by counting over the N(N-1)/2 interactions of the N molecules, where there are twenty five site-site interactions per pair of molecular interactions. A neighbour list which stores the labels of molecules within a certain distance of any molecule is included in the program. In a bulk fluid simulation we only count over the molecules in the neighbour list which is associated with each molecule, and the neighbour list is updated approximately

every 10 timesteps. This method of calculating the forces and torques on the molecules improves the efficiency of the algorithm considerably, and we can even extend this type of summing procedure to a two tier multiple timestep algorithm (Streett et al., 1978). At coverages of less than $\theta = 0.87$ the molecules have a large amount of 2-dimensional mobility and experience has shown a neighbour list needs to be updated every two timesteps. The majority of the simulations have been performed without a neighbour list and we count over $N(N-1)/2$ molecular interactions at each timestep. The potential and forces of the methane-methane interaction are summed with the methane-surface potential and forces to give the total potential and forces on each molecule. The algorithm to calculate the methane-methane interaction is subroutine FORCEG in the listing of the many particle program MONOLAYER.

A difficulty with the monolayer simulation, which did not occur in the single particle work, is that at temperatures higher than 90K some methane molecules leave the surface. This problem is overcome by including a reflecting wall at a height of 19.7 Å above the basal plane of the graphite. When the z- component of the molecular position exceeds 19.7 Å the sign of the z- component of each of the odd derivatives of the motion is changed (Thompson, 1980). The particle then moves back towards the surface. The angular velocity and its derivatives remain unaltered during the reflection.

Each simulation reported in this chapter comprises of 5000 timesteps of 1.252×10^{-15} s. Equilibration takesplace over an

additional 1000 - 1500 timesteps at the beginning of the simulation.

The length of the runs in real time is 6.26 picoseconds. Each timestep requires 1.2 seconds of CDC 7600 c.p.u. time.

The results for the thermodynamic properties of the ten runs performed on the S_I solid are shown in table 4.1. The coverage is fixed at 0.87 of the compressed completed monolayer and the temperature is increased from OK to 128K. These results are also plotted in Figure 4.2. The residual part of the specific heat at constant volume, C_v^r is calculated using (Lebowitz et al., 1967; Cheung, 1977)

$$\frac{C_v^r}{Nk} = \frac{3}{[1-<(\delta U)^2>/3Nk_B^2T^2]} - 3 \quad , \qquad (4.2.5)$$

where $\delta U = U - <U>$ and U is the instantaneous configurational energy. At temperatures below 30K C_v^r does not settle down to an average value but fluctuates during the course of the simulation; (it is still possible to calculate an accurate value of the configurational energy in this region). At temperatures between 85K and 100K both C_v^r and U fluctuate.

This behaviour is characteristic of two phase transitions at a coverage of $\theta = 0.87$; one below 30K and the other at about 90K. The change in slope of $<U/N\varepsilon>$ as a function of T at 30K and 90K supports this conclusion. The phase diagram, Figure 4.1, suggests

T^*	T/K	θ	-U/NkT	C_V^r/Nk	$F^2\sigma^2/\epsilon^2$	Γ^2/ϵ^2
0.079	3.5	0.87	42.65	-	100.2	38.71
0.236	11.3	0.87	42.30	-	245.1	14.56
0.416	19.8	0.87	41.65	-	505.0	25.00
0.635	31.2	0.87	41.02	8.2	808.66	38.62
0.847	40.4	0.87	40.56	2.7	1071.1	49.45
1.087	51.8	0.87	39.99	2.0	1433.5	62.73
1.510	72.0	0.87	39.12	1.7	2035.9	86.29
1.764	84.1	0.87	38.41	8.6	2487.8	108.04
2.443	116.5	0.87	34.96	5.0	3514.4	143.90
2.680	127.8	0.87	32.33	3.3	2990.4	124.64
0.597^*	28.4	0.92	39.80	2.7	738.0	34.28
$1.512^{\neq}$	72.1	0.77	37.59	1.1	1779.6	86.51

Table 4.1 The thermodynamic properties of methane adsorbed on graphite at a coverage, θ, corresponding to the registered monolayer (S_I). U is the configurational energy, C_v the specific heat at constant volume, F^2 and Γ^2 are the mean squared force and the mean squared torque per particle. * corresponds to the S_I solid with three additional particles in the second layer. ≠ corresponds to a state in which the surface density is reduced by 10% bringing the methane molecules into a 2-d liquid phase. The reducing parameters used in the simulation are σ = 2.46 Å and ϵ = 51.198K.

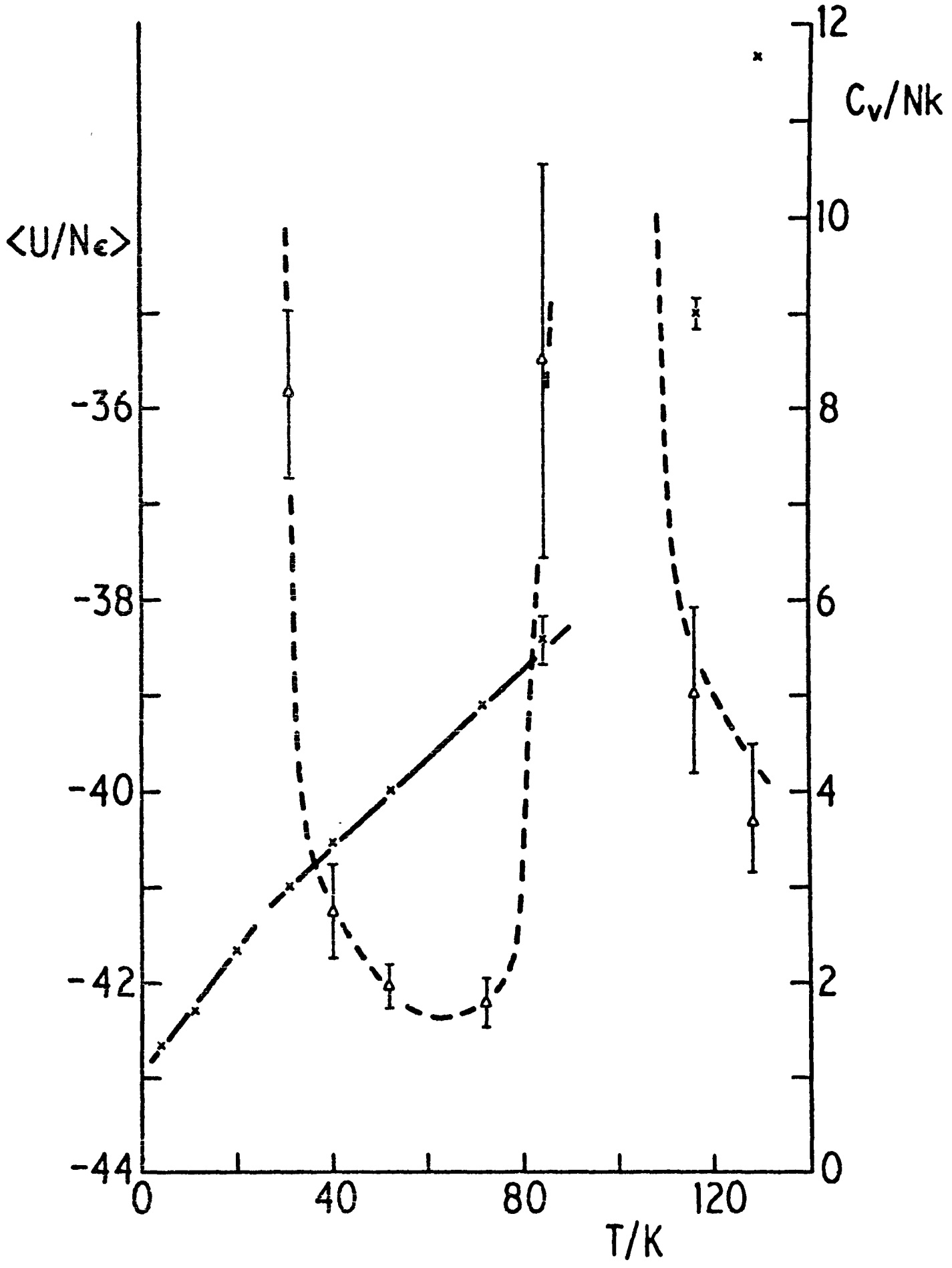


Figure 4.2 The configurational energy, X, and the specific heat at constant volume, Δ, as a function of temperature at a coverage of 0.87. The dashed line through the specific heat is drawn as a guide to the eye. All error bars show the maximum deviation from the average over the final 1000 timesteps of the simulation. The errors in the configurational energy are negligible on this scale except at 84K which appears to be close to a solid/fluid phase transition.

that the higher temperature phase transition is from solid to fluid. The nature of the lower temperature phase transition is not yet understood. These transitions are discussed more fully in sections 3 and 4. In addition to the solid methane simulations we report one simulation at a coverage of $\theta = 0.77$ and a temperature of 72.1K where the adsorbate forms a 2-d liquid (see Figure 4.1), and a simulation of the S_I solid at 28.4K where three additional methane molecules and added to the second layer. The thermodynamic properties of the methane under these conditions are included in table 4.1 for completeness.

We also report the mean squared forces $\langle F^{*2} \rangle$ and torques $\langle \Gamma^{*2} \rangle$ from which we can calculate the difference in free energy between a quantum and classical treatment of the system. The difference in free energy for a symmetric top molecule is (Powles and Rickayzen, 1979),

$$A - A_{classical} = \frac{\hbar^2}{24(kT)^2}\left[\frac{\langle F^2 \rangle}{m} + \frac{\langle \Gamma^2 \rangle}{I}\right] - \frac{\hbar^2}{8I} + O(h^4) . \qquad (4.2.6)$$

We simplify this equation by substituting the reduced quantities

$$F^* = \frac{F\sigma}{\epsilon} , \quad \Gamma^* = \frac{\Gamma}{\epsilon} \quad \text{and} \quad I^* = \frac{I}{m\sigma^2} ,$$

to give

$$A^*_{correction} = \frac{h^2}{(96\pi^2\sigma^2 m\varepsilon)} \frac{1}{T^{*2}} \left[\langle F^{*2} \rangle + \frac{\langle \Gamma^{*2} \rangle}{I^*} \right] - \frac{h^2}{32\pi m\sigma^2 I^*} \qquad (4.2.7)$$

The average energy <E> of a system is (McQuarrie, 1976),

$$\langle E \rangle = kT^2 \frac{\partial \ell n\, Q}{\partial T}$$

$$= - T^2 \frac{\partial}{\partial T} \left(\frac{A}{T} \right) \qquad (4.2.8)$$

The total energy is the sum of kinetic and potential terms. If ~~the kinetic terms have quantum fluctuations we introduce relativistic co-efficients~~ via the uncertainty principal. ~~These effects are very small~~ (Powles and Rickayzen, 1979) and We assume the correction is due to the potential energy only i.e.

$$\Delta \langle U_{cor} \rangle = - T^2 \frac{\partial}{\partial T} \left(\frac{A_{cor}}{T} \right) \qquad (4.2.9)$$

A plot of (A_{corr}/T) gives the slope, $\frac{\partial}{\partial T}(A_{corr}/T)$ and multiplying by $- T^2$ we obtain the correction to the average potential energy. The quantum correction is less than 5% for all simulations above 19K. Below 19K the correction is approximately 10%, however we justify simulations below this temperature because the effective pair potential is scaled to the quantum rotational tunnelling barriers at 0 kelvin (see section 3.4).

During each simulation we store the particle positions, velocities, angular velocities forces and torques at intervals of ten timesteps on magnetic tape. After a simulation we return to this tape and analyse some time dependent properties of the simulation. Before proceeding with the next section we briefly discuss the program to analyse the data. A program is written to calculate some or all of the following auto-correlation functions; the total velocity, x, y and z components of the velocity, the force, torque and angular velocity, the P_1 - P_4 Legendre polynomials (P_1 is the reorientational auto-correlation function) and the mean displacement $\langle r(t)^2 - r(o)^2 \rangle$.

The program reads the time dependent properties from tape and reformats the angular velocities and site positions into the space fixed system. This data is written to a temporary file on disc. We then start at the first record on the disc and correlate the next J records, where J multiplied by the time between successive records is the maximum correlation time. The disc file is then rewound and we begin at record 2 and compare the next J records. We continue with this process until we have compared all of the records on tape. The advantage of this type of program is that it requires little use of store; (a necessary requirement of the CDC 7600). Only two records are stored at any one time. However rewinding and reading from the disc is a slow process, so we must include the code to write the up to date averages to a permanent file and restart the program at any point during the averaging process. This is similar to the restart procedure for the simulation

program which requires about 5 restarts for a complete simulation. The program TPANALYSIS is listed at the end of the thesis.

4.3 Translational Order and Structure of the Adsorbed Methane

The structure of the adsorbed fluid where the molecules interact with pair potentials can be completely described by the pair distribution function, $g(\underset{\sim}{R}_1, \underset{\sim}{R}_2, \omega_1, \omega_2)$ where R_i is the position of the centre of mass of molecule, i and ω_i are the three Euler angles which describe its orientation in space. In this section we are interested in the distribution of molecular centres,

$$g_{cc}(\underset{\sim}{R}_1,\underset{\sim}{R}_2) = \langle g(\underset{\sim}{R}_i,\underset{\sim}{R}_j,\omega_i,\omega_j)\ \delta(\underset{\sim}{R}_1-\underset{\sim}{R}_i)\delta(\underset{\sim}{R}_2-\underset{\sim}{R}_j)\rangle, \qquad (4.3.1)$$

where < > represents an ensemble average, $\delta(\underset{\sim}{R}_1 - \underset{\sim}{R}_i)$ is the Dirac delta function and is equal to one when $\underset{\sim}{R}_i$ is at $\underset{\sim}{R}_1$ and zero otherwise. $g_{cc}(\underset{\sim}{R}_1\underset{\sim}{R}_2)$ is not considered a function of the scalar $|\underset{\sim}{R}_1 - \underset{\sim}{R}_2|$. It depends on the relative heights of the molecules above the surface, z_1 and z_2 and in the case of a surface with transverse structure it also depends on x_1, y_1 and x_2, y_2. For monolayer adsorption on graphite we make two plausible assumptions;

(i) The heights of the molecules are confined to a small range, $z_1 - z_2 < 1$ Å.

(ii) The fluid structure around molecule 1 is not strongly affected by the position of 1 on the surface. (The potential interaction between molecules and the surface varies by only 8K from its average

value as the molecule translates across the surface, see section 3.3).

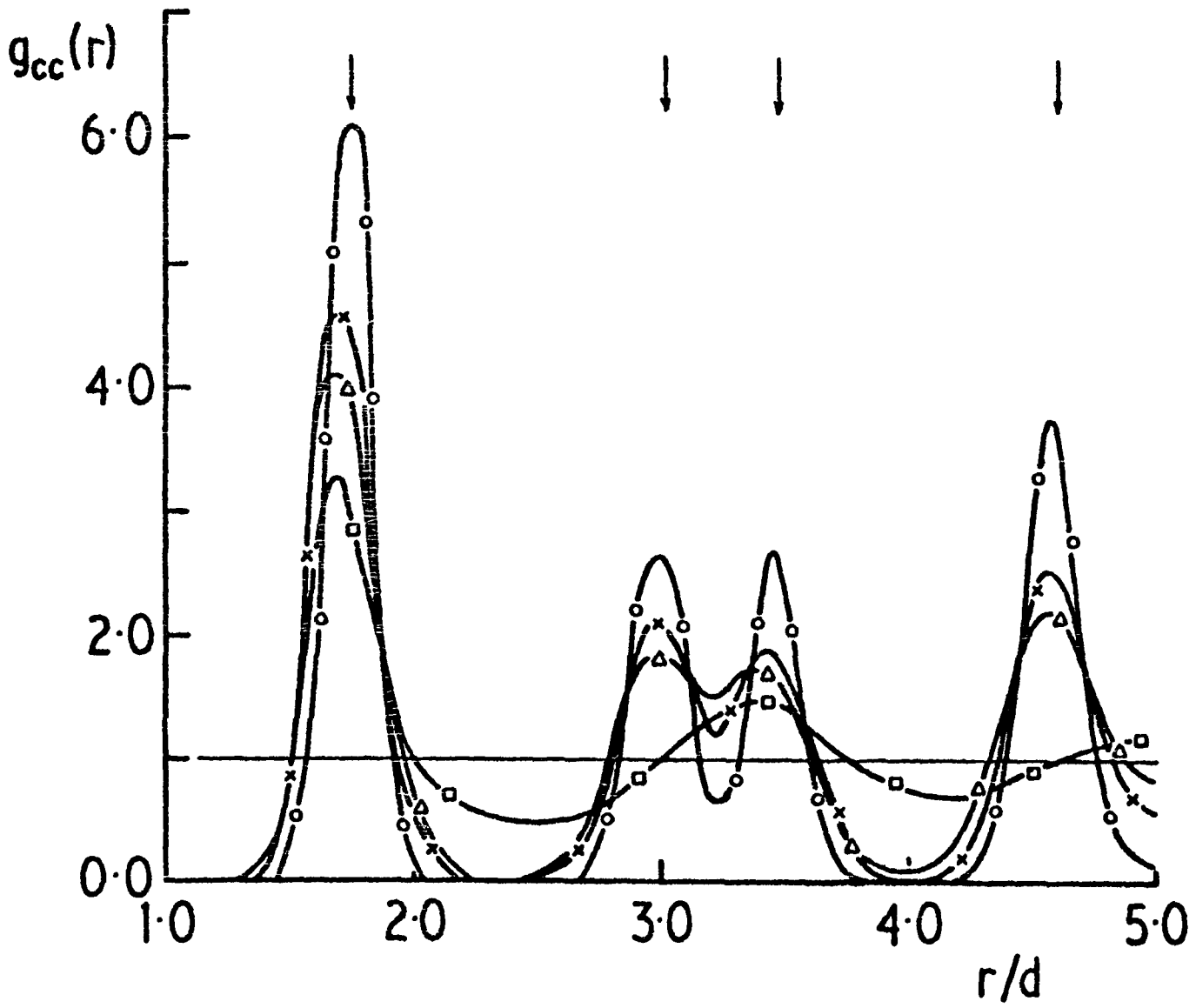
In this case it is sensible to discuss a '2-d' distribution independent of z, and depends only on $r^* = [(x_1-x_2)^2+(y_1-y_2)^2]^{\frac{1}{2}}$. Then

$$N_A^2\, g_{cc}(r^*) = \left\langle \sum_{i=j} \delta(r_i^*)\, \delta(r_j^*-r) \right\rangle \qquad (4.3.2)$$

where N_A is the surface density of the adsorbate and $\delta(r)$ is the 2 dimensional Dirac delta function. A typical $g_{cc}(r^*)$ is shown for adsorbed liquid methane (θ = 0.77, T = 72K). The distribution is similar to that of carbon atoms in '3-d' liquid methane close to the triple point (Murad et al., 1979). The '2-d' $g_{cc}(r^*)$ has a sharper first peak and a more pronounced structure at intermediate separations than its '3-d' analogue. In the case of an adsorbed solid the periodicity of the adsorbate destroys the translational invariance of $g_{cc}(r^*)$. This invariance is lost even if the underlying lattice has no structure. $g_{cc}(r^*)$ describes the normalized probability of finding a molecule in a shell of thickness dr^*, at a distance r^* from a lattice point. In the solid molecules are not distributed isotropically in any shell.

Several distributions for adsorbed solids, θ = 0.87, are shown in Figure 4.3. The arrows indicate the position of the first four nearest neighbour distances in the solid S_I structure. This is the zero kelvin solid structure determined by neutron scattering

Figure 4.3 The distribution function of molecular centres in an adsorbed monolayer. The function $g_{cc}(r)$ is the 2-dimensional, translationally invarient, distribution function discussed in the text. There are three solid points $\theta = 0.87$ T = 19.8K,o; $\theta = 0.87$ T = 51.8K,X;$\theta = 0.87$ T = 72K,Δ and one liquid point $\theta = 0.77$ T = 72.0K,□ d, the graphite lattice spacing is 2.46 Å. The arrows mark the four nearest neighbour distances in the S_I structure.



(Vora et al., 1979) and is the starting configuration used in the simulation. It is clear that the S_I solid structure persists up to temperatures of 70K, while the nearest neighbour distance is shifted to slightly smaller separations with increasing temperature. There is no fundamental change in the solid structure between 19.8K and 51.8K, which cannot explain the anomalous behaviour of C_v at low temperatures. A 10% reduction in coverage at 70K brings the adsobate into the liquid phase, with a typical short ranged $g_{cc}(r^*)$.

A more quantitative description of ordering in the adsorbed solid can be obtained by calculating two order parameters. We define an adsorbate-adsorbate parameter (Vieillard-Baron, 1972)

$$O_1 = \frac{1}{N} \sum_{i=1}^{N} \sum_{j=1}^{N} \cos (\underset{\sim}{k}^*_\ell \cdot \underset{\sim}{r}^*_{ij}) \quad , \qquad (4.3.3)$$

where $\underset{\sim}{k}^*_\ell$ are the reciprocal lattice vectors of the S_I solid, $\underset{\sim}{k}^*_1 = 2\pi\ (-d, -d/\sqrt{3})$ and $\underset{\sim}{k}^*_2 = 2\pi\ (0, 2d\sqrt{3})$, and d is the graphite lattice spacing. If the methane particles are at their lattice positions $O_1 = N$ and if the particles are randomly distributed only the self terms contribute to the sum and $O_1 = 1$. In addition we can define an adsorbate-adsorbent order parameter, O_2 given by

$$O_2 = \sum_{i=1}^{N} \cos (\underset{\sim}{k}^*_\ell \cdot \underset{\sim}{r}^*_i) \qquad (4.3.4)$$

where the vector $\underset{\sim}{r}_i^*$, the position of molecule i, is defined relative to the corner of the simulation box which is the origin of the graphite lattice. The reciprocal lattice vectors $\underset{\sim}{k}_\ell^*$ are the same as above. If the methane molecules remain in registry with the underlying graphite lattice (see Figure 3.8) O_2 has a value of N; if the molecule positions are random with respect to the underlying lattice $O_2 = 0$. The order parameters calculated over 5000 timesteps are shown in table 4.2.

O_1 exhibits the behaviour we would normally expect for a solid lattice. The value is high for the low temperature solid and decreases with increasing temperature. At $\theta = 0.87$ and $T = 127.2K$ the O_1 order parameter has fallen to a typically liquid value. This confirms the idea that the phase transition around 90K is from the adsorbed solid to liquid. At 127.2K, 12 of the 75 methane particles have a height greater than 4 Å, (1.55 d). The 65 particles which remain firmly on the surface relax to a liquid structure. An instantaneous configuration for the $\theta = 0.87$, $T = 127.2K$ simulation is shown in Figure 4.4. The shaded particles have $z_i > 1.55$ d.

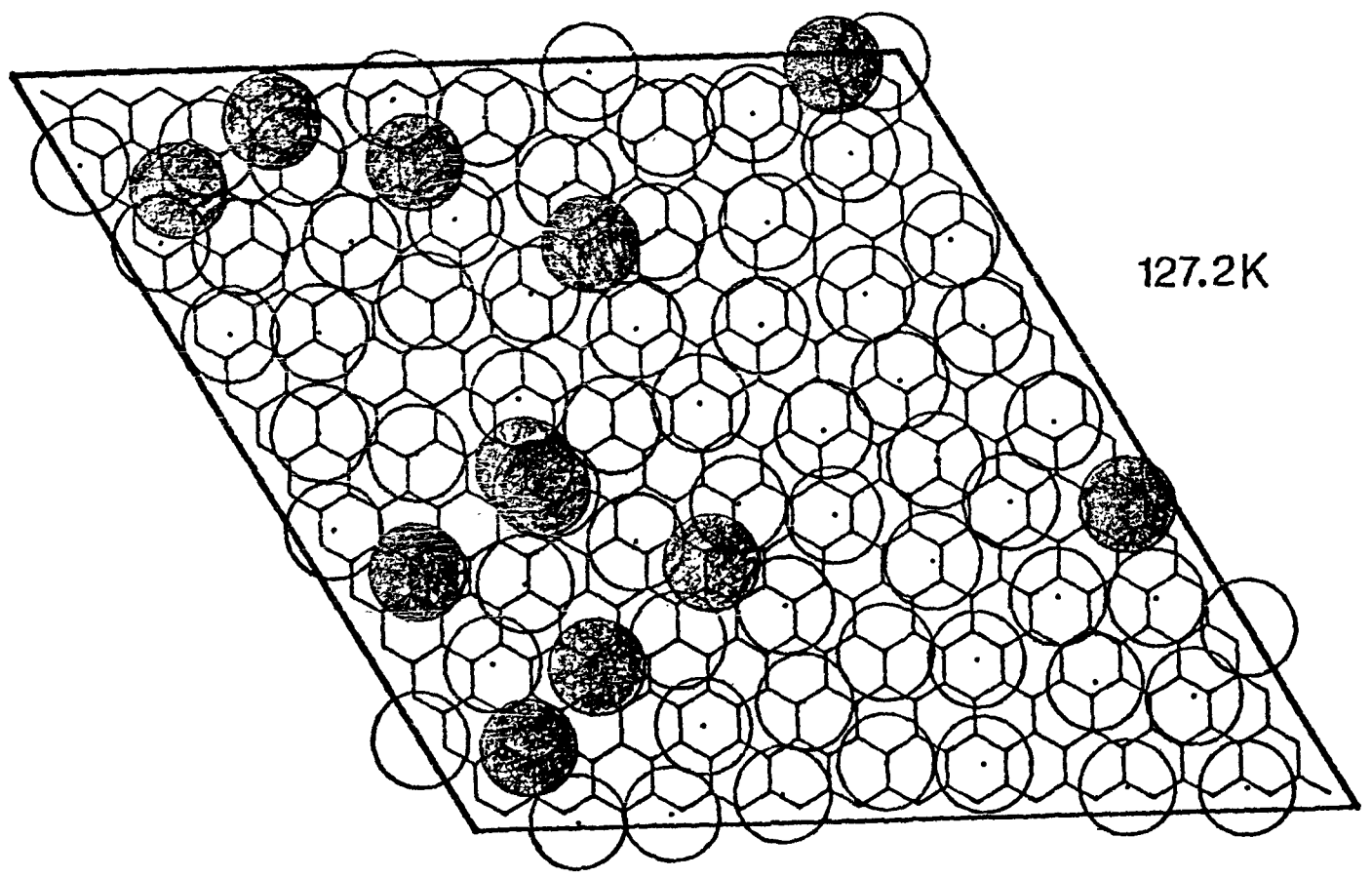
The O_2 order parameter is small for the low temperature solid and considerably smaller than O_1. This means the methane-methane solid structure is retained although the methane particles do not remain in strong registry with the underlying lattice. The current evidence from neutron diffraction is that the nearest neighbour distance is close to the estimated S_I spacing of 4.26 Å (Vora et al., 1979; Coulomb et al., 1979; Newbery et al., 1978)

Table 4.2

The order parameters O_1 and O_2 for adsorbed methane. The value in brackets is the expectation of O_1 and O_2 if methane molecules remain in their registered lattice positions. The liquid point $\theta = 0.77$, 72K is included for comparison with $\theta = 0.87$, 127.2K.

T/K	θ	O_1	O_2	
11.3	0.87	52.6	11.4	(75)
19.8	0.87	52.1	8.2	(75)
51.8	0.87	36.8	24.3	(75)
127.2	0.87	1.2	4.3	(75)
72.1	0.77	0.9	1.4	(67)

Figure 4.4 An instantaneous configuration from a high temperature monolayer simulation, $\theta = 0.87$, $T = 127.2K$. The methane particles are represented by discs of diameter 4.0 Å. The shaded particles have a height greater than 4.0 Å. The remaining 65 particles form a liquid structure on surface.

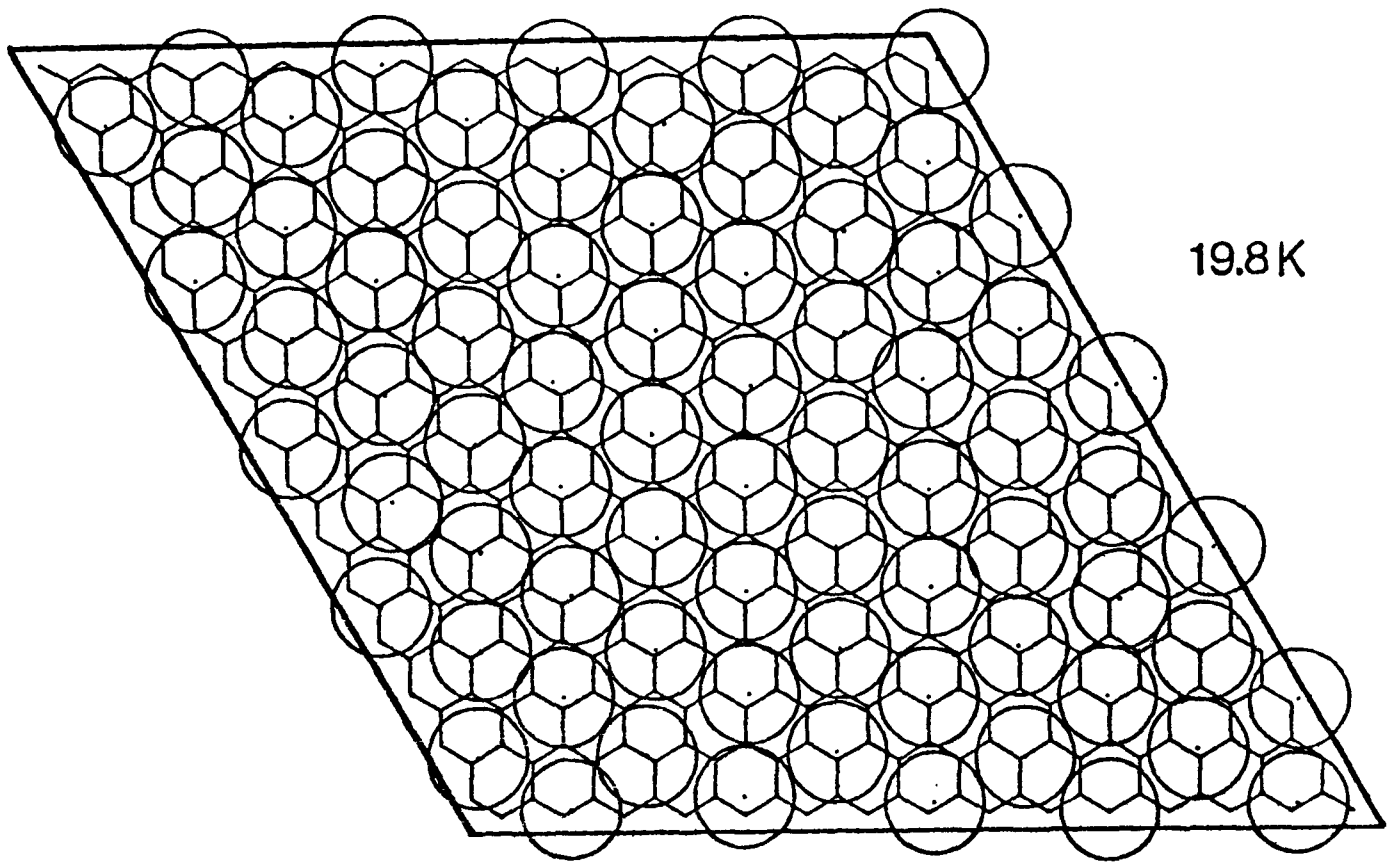


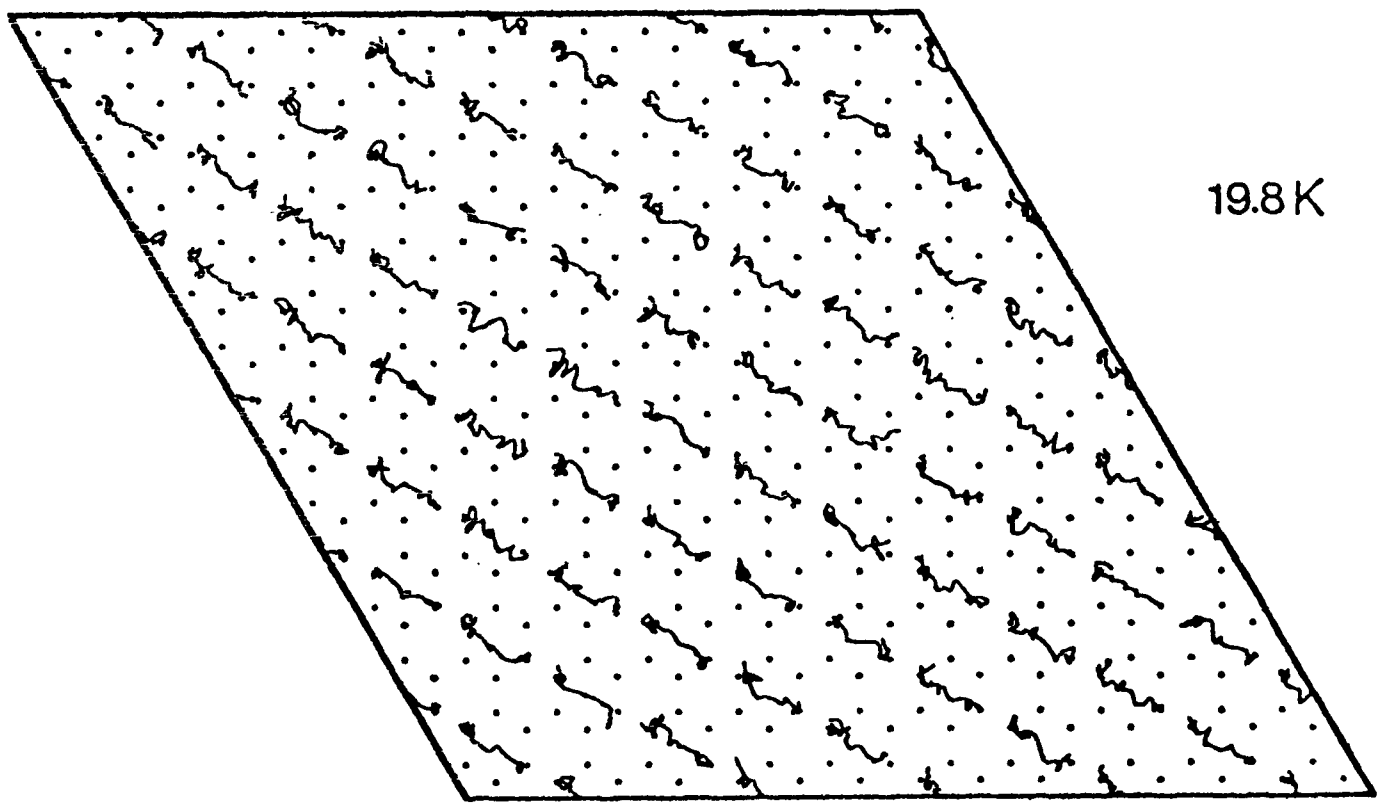
which is consistent with a high value of O_1. To our knowledge there has been no measurement of O_2 and it remains an open question as to whether the methane is commensurate with the underlying lattice and sits over the centre of a hexagon or over a carbon atom.

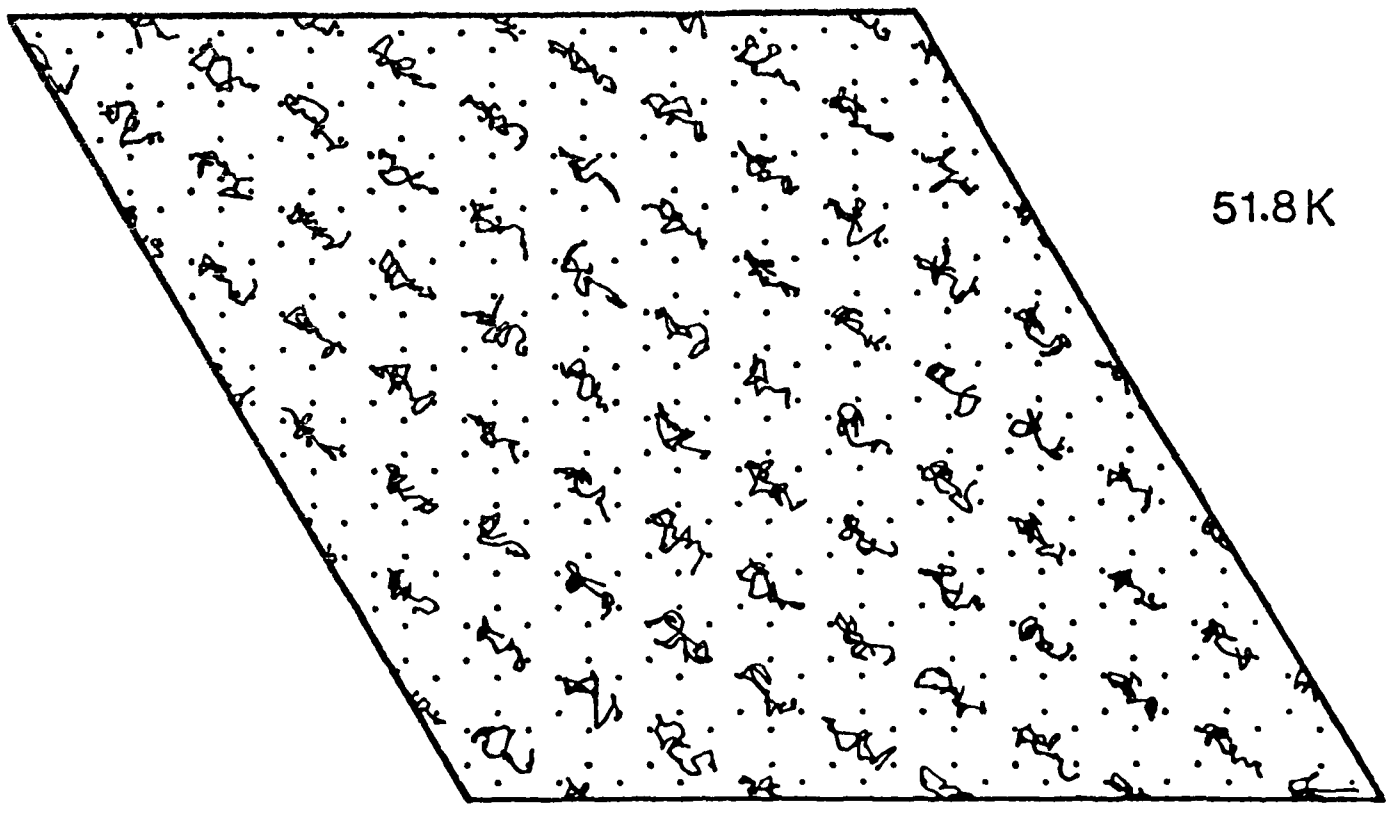
The O_2 order parameter for our model increases with increasing temperature. This result can be explained with reference to the particle trajectories shown in Figure 4.5. The trajectories show the projection of the C.O.M. of the methane molecules on the surface over a period of approximately 6 picoseconds. In Figure 4.5 at a temperature of 51.8K the methane molecules oscillate around their initial positions, (in the centre of the hexagons). The solid remains registered because of collisions with other methane molecules. At 19.8K the solid floats across the underlying surface. The motion appears to be collective, that is the methane molecules nudge one another in an ordered fashion, and the solid moves in a particular direction. O_2 at 51.8K is three times larger than O_2 at 19.8K.

It is important to establish whether this behaviour is an observable property of the adsorbate or an artifact of the simulation. We have repeated the simulation for three different initial velocity distributions and removed the net momentum in any direction during equilibration. Although the initial velocities are quite different the adsorbate moves in the same direction in each case, (twice right/left and once left/right). The particles are moving

4.5 Trajectories of the centres of mass of the methane molecules projected onto the graphite surface. These trajectories are taken over 5000 timesteps corresponding to times of approximately six picoseconds. The dots represent the positions of the centres of mass of the carbon atoms in the underlying graphite lattice. The central box is surrounded by images in the plane, (a) an instantaneous configuration from the trajectory shown in (b), (b) $\theta = 0.87$, T = 19.8K. (c) $\theta = 0.87$, T = 51.8K.


19.8K


19.8K


51.8K

in the constant external field, $\phi(x,y,z)$, of the surface and there is no momentum exchanged when they collide with the graphite lattice. In this model momentum is not conserved parallel to the surface and it is possible for the whole solid to translate, if the initial configuration is not in symmetric registry with the substrate.

The simulation result is reproducible, but the question still remains as to whether the assumptions in the model cause the collective motion. In nature the adsorbate might exchange energy with the graphite. The methane surface vibration, coupling with the phonons in the solid could randomize the translational motion of the methane. In addition real surfaces are not homogeneous and defects would destroy the collective nature of this motion. Finally the real adsorbate is not continuous and different rafts of methane floating in different directions would cause the molecules to rebound across the surface. The O_2 order parameter might increase for times substantially greater than six picoseconds. If deutero-methane is adsorbed on prepared Papyex graphite at $\theta = 0.87$ and the solid is rapidly cooled from 50K to 20K the floating might be induced. The O_2 order parameter could be measured by X-ray or neutron diffraction by monitoring reflections parallel to the surface (Thomas, 1981).

A question which remains unexplained is why molecules translate along the direction at 30^{o} to the base of the cell. In our model the potential energy is a minimum for a molecule over the centre of a hexagon. The barrier to translation is practically isotropic

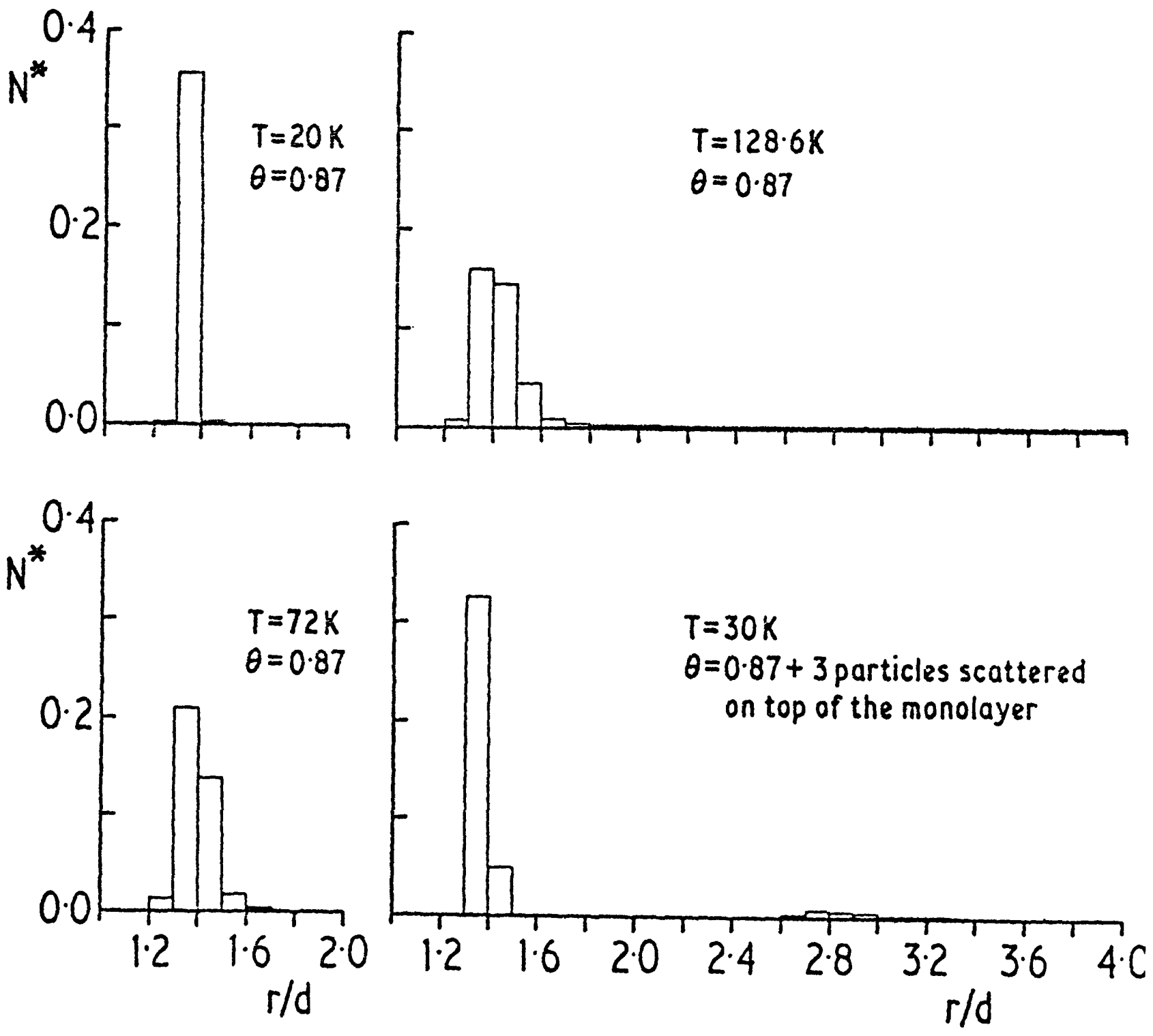
with a height of approximately 16K (at z = 3.30 Å) which varies by 2K in any direction (see Figure 3.6). This barrier depends on the height of the methane and the orientation of the molecule with respect to the surface. We finally note floating also occurs for the model at 10K. At this temperature the molecules can only translate across the surface at the point during their vibration when they are a maximum height above the surface.

We conclude the discussion of the structural properties of the system by comparing the distribution of molecule heights above the surface as a function of temperature. Each of the histogram blocks in Figure 4.6 is equivalent to 0.25 Å and at $\theta = 0.87$, T = 20K the deviation from the average height is very small, ± 0.015 Å. As the temperature is increased to 70K the molecules remain bound but the distribution of heights becomes broader. At 128K thirteen molecules leave the surface and are distributed at random above the adsorbate; they do not form a bilayer. The remaining molecules relax to form an adsorbed liquid. In the fourth diagram three particles are scattered above the S_I, $\theta = 0.87$, monolayer and at 30K it is evident the three molecules remain in a bilayer at an average height of 2.3d (6.9 Å) above the surface.

The dynamical behaviour of the monolayer

The dynamics of the adsorbed monolayer can be studied by incoherent inelastic neutron scattering (White et al., 1978).

Figure 4.6. The distribution of molecular centres above the surface averaged over 5000 time steps. Each histogram block is equivalent to 0.25 Å. At $\theta = 0.87$, T = 126K the thirteen molecules are randomly distributed from r/d = 1.8 to r/d = 8.0.



This scattering comes predominantly from motions involving displacement of the hydrogen atoms in the monolayer. The phonon spectra of adsorbed methane on Vulcan and Papyex, two forms of graphite, have recently been measured by Bomchil et al. (1980). For comparison with the molecular dynamics simulation the results on Papyex are most interesting. This form of exfoliated graphite is oriented principally in one plane, and neutrons can be inelastically scattered parallel and perpendicular to the surface. In a homogeneous monatomic fluid the Fourier transform of the velocity auto-correlation function, $Z(\omega)$, can be related to the incoherent structure factor (Hansen and McDonald, 1976) by

$$Z(\omega) = \omega^2 \lim_{k \to 0} \frac{S_S(k,\omega)}{k^2} \qquad (4.3.5)$$

This relationship cannot be simply extended to molecular fluids because the phonon density of states $Z(\omega)$ is affected by the coupling between translational and rotational motion (Quentrec, 1974). In the case of an anisotropic molecule the exact contributions to the density of states is not yet understood but we would expect the principal peaks in $S_s(0,\omega)$ to correspond to the peaks in $Z^v_{\alpha\alpha}(\omega)$ where

$$Z^v_{\alpha\alpha}(\omega) = \int_{-\infty}^{\infty} e^{i\omega t} < \underset{\sim}{V}_\alpha(0) \; . \; \underset{\sim}{V}_\alpha(t) > dt \; , \qquad (4.3.6)$$

and

$$Z^{\Omega}_{\alpha\alpha}(\omega) = \int_{-\infty}^{\infty} e^{i\omega t} \langle \underset{\sim}{\omega}_{\alpha}(0) \cdot \underset{\sim}{\omega}_{\alpha}(t) \rangle \, dt \qquad (4.3.7)$$

$V_{\alpha}(t)$ and $\omega_{\alpha}(t)$ are the α components of the linear and angular velocities of the adsorbed methane molecule. In the m.d. simulation we calculate the normalized correlation functions

$$C_{\alpha\alpha}(t) = \frac{\langle \underset{\sim}{V}_{\alpha}(t) \; \underset{\sim}{V}_{\alpha}(0) \rangle}{\langle \underset{\sim}{V}_{\alpha}(0) \; \underset{\sim}{V}_{\alpha}(0) \rangle} \qquad (4.3.8)$$

by choosing every tenth timestep as an origin and correlating the velocities over 1670 timesteps (2 picoseconds). The experimental incoherent structure factors, parallel and perpendicular to the surface have been determined (Bomchil et al., 1980). These are measured at 10K and a coverage of 0.7, that is with the methane in the S_I solid structure. The peak positions in these vibrational spectra are insensitive to momentum transfer, q, and we can think of these spectra as $S_S(0,\omega)$.

The total velocity auto-correlation function $C^{v}(t)$ is shown in Figure 4.7(a).

Where

$$C^{v}(t) = \frac{\langle \underset{\sim}{V}(t) \cdot \underset{\sim}{V}(0) \rangle}{\langle \underset{\sim}{V}(0) \cdot \underset{\sim}{V}(0) \rangle}$$

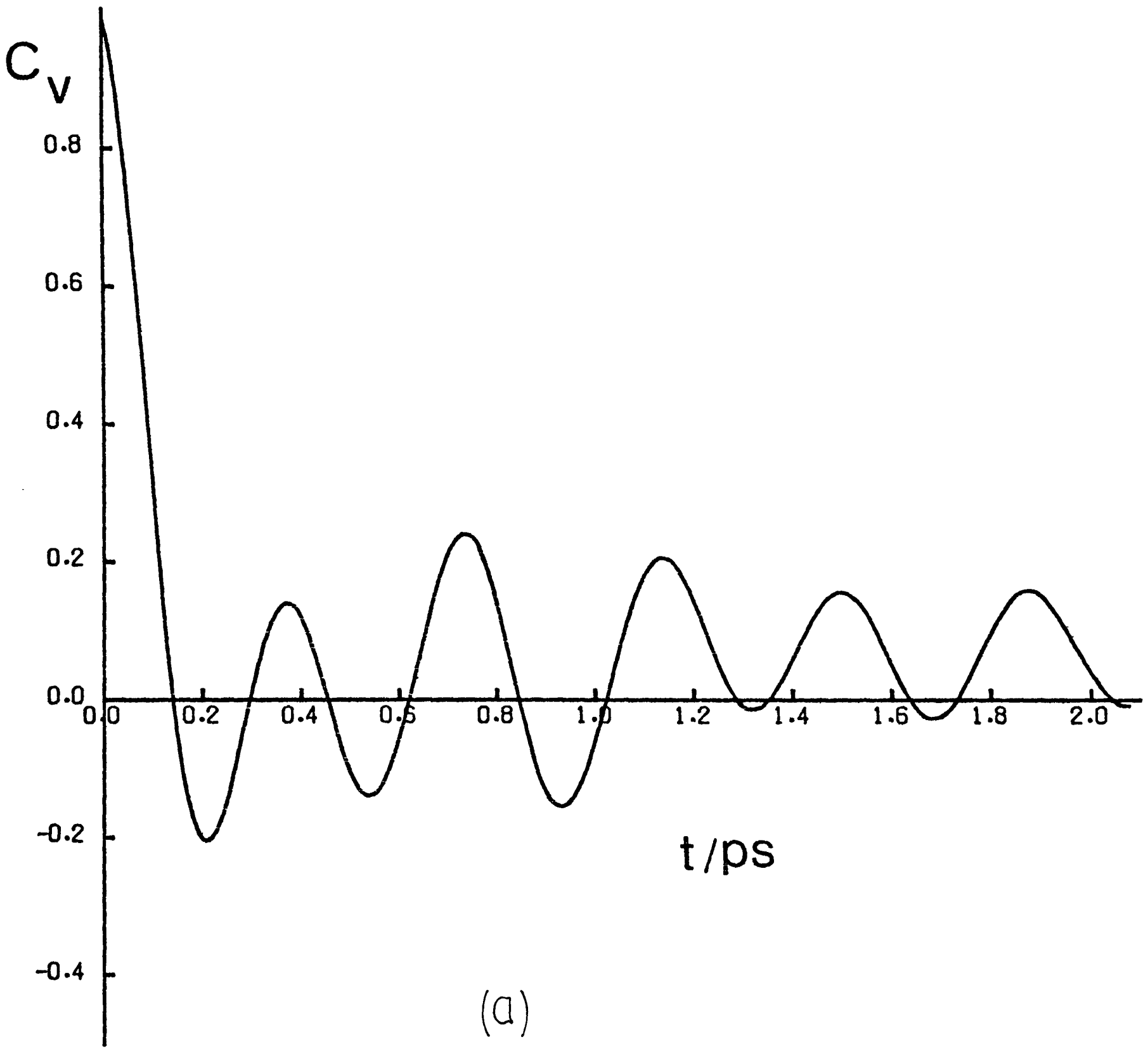
and

$$C^{v}(t) = C^{v}_{xx}(t) + C^{v}_{yy}(t) + C^{v}_{zz}(t) \qquad (4.3.9)$$

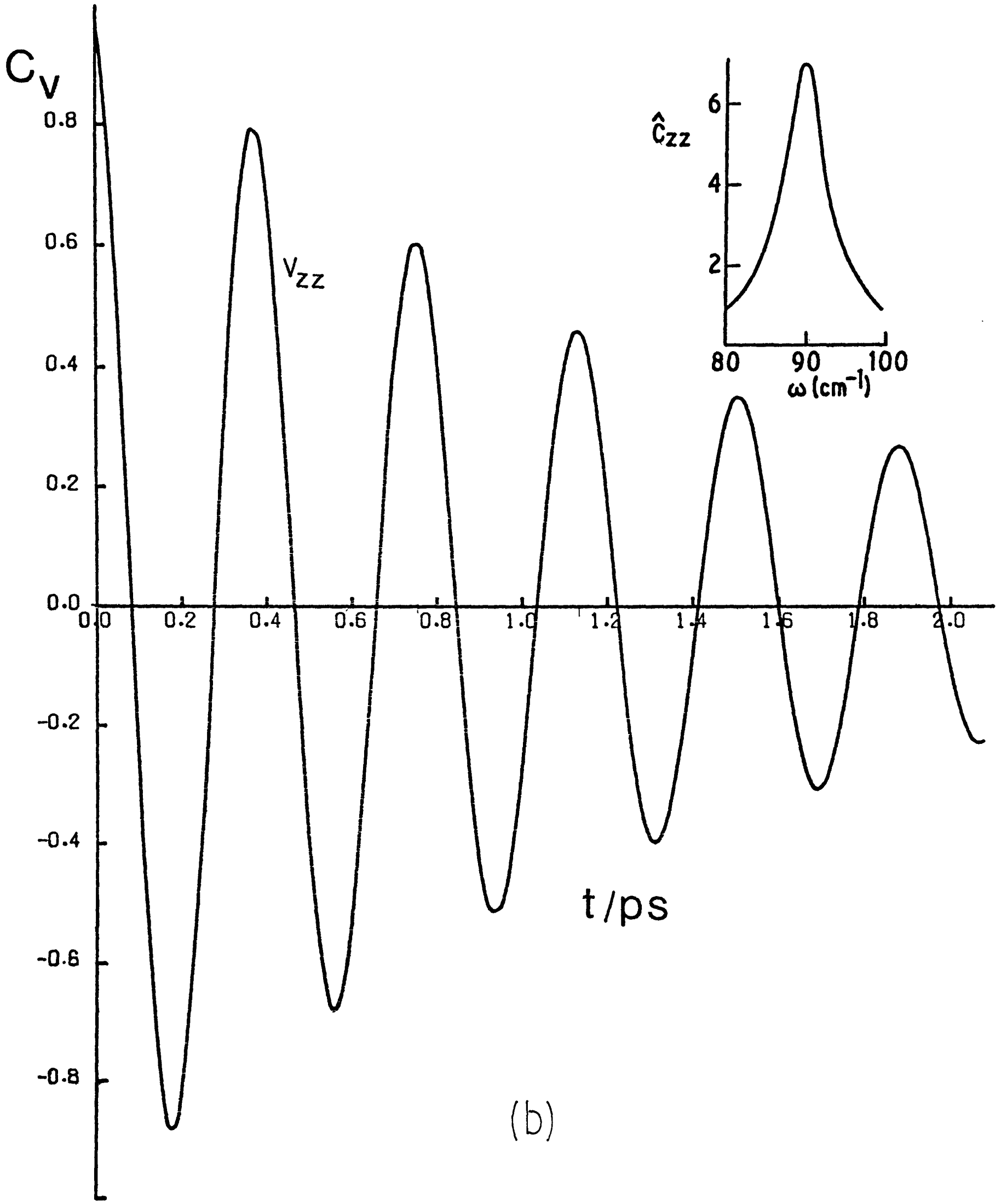
This function is calculated from a run of 5000 timesteps for $\theta = 0.87$, T = 19.8K. The function does not decay rapidly with time and the self motions are strongly correlated over periods in excess of 2 picoseconds. This oscillatory behaviour is typical of the velocity auto-correlation function of a solid; in this case the lattice vibrations are strongly anisotropic. This behaviour is best illustrated by examining the components of $C^{v}(t)$. $C^{v}_{zz}(t)$, shown in Figure 4.7(b), is an exponentially damped cosine function. The Fourier transform of $C^{v}_{zz}(t)$ is a Lorentzian centred at 89 cm^{-1} with a width at half height of 7 cm^{-1}. This curve corresponds most closely to the peak in $S^{\perp}_{s}(0,\omega)$ at 100 cm^{-1}, (neutron energy loss of 12 meV). As expected this peak is considerably weaker in the experimental $S^{\parallel}_{s}(0,\omega)$ and the simulation confirms the assignment of this peak to the strong vibrational motion perpendicular to the surface.

The behaviour of $C^{v}_{xx}(t)$ and $C^{v}_{yy}(t)$, describing the motion parallel to the surface is different. It should be remembered that the axes are arbitrary orthogonal directions in the surface, see Figure 3.1, and there is no reason to suppose that at low temperatures the in-plane velocity auto-correlation functions should be isotropic. However there are strong similarities between $C^{v}_{xx}(t)$ and $C^{v}_{yy}(t)$, both functions oscillate with a similar period at times greater than 0.2 picoseconds and neither function has decayed to zero within 2 picoseconds, see Figure 4.7(c). This long-time correlation is consistent with particle trajectories

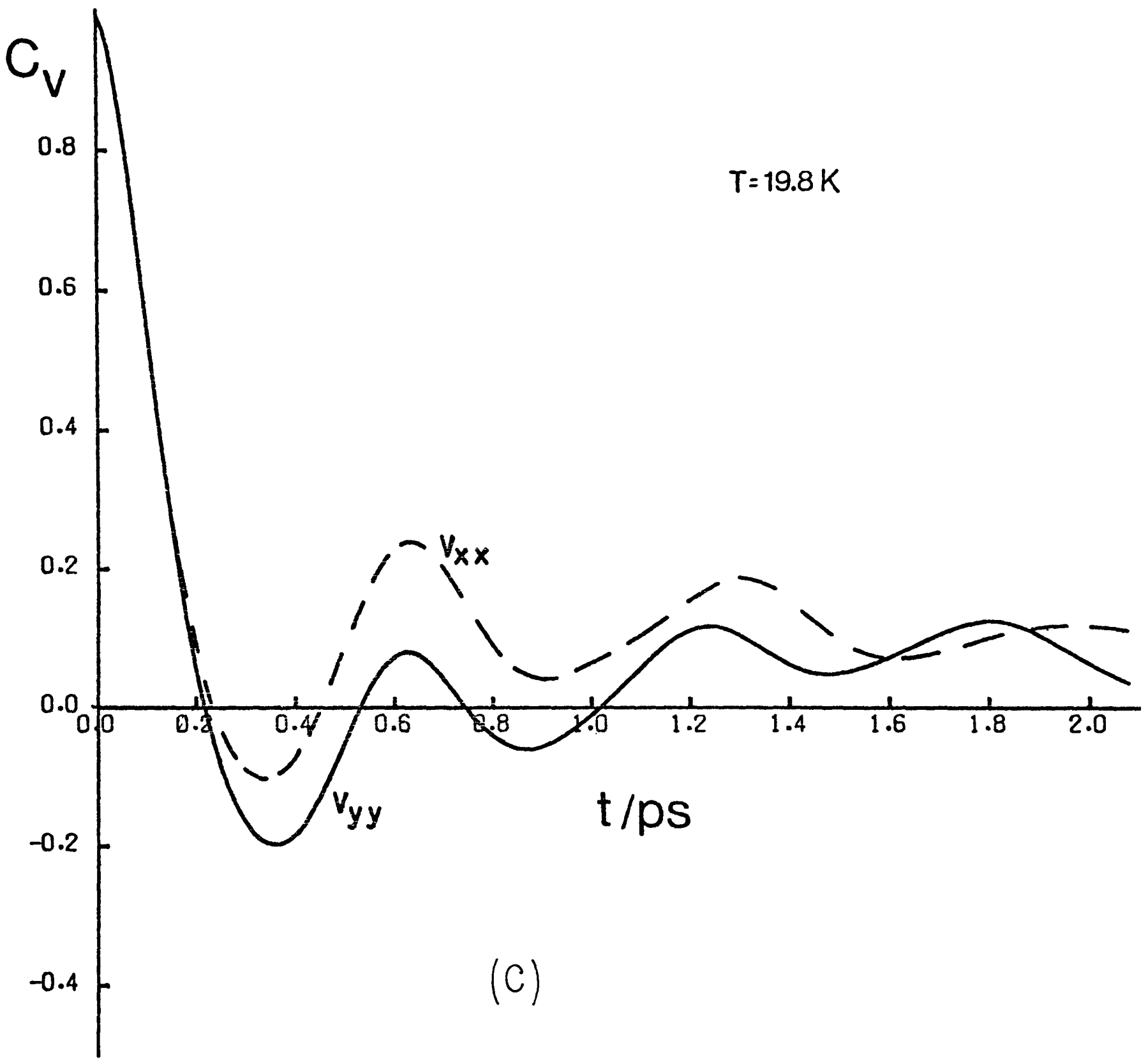
Figure 4.7 The velocity auto-correlation functions of the centre of mass of the methane molecules in an adsorbed solid, $\theta = 0.87$, $T = 19.8K$. Figure (a) shows the total velocity a.c.f. and figures (b) and (c) show the three independent components. The spectra of (b) is shown as an inset.



(a)


C_V
0.8
0.6
0.4
0.2
0.0
-0.2
-0.4
-0.6
-0.8
V_{zz}
0.0
0.2
0.4
0.6
0.8
1.0
1.2
1.4
1.6
1.8
2.0
t/ps
$\hat{C}_{zz}$
6
4
2
80
90
100
$\omega\,(cm^{-1})$

(b)


C_V
0.8
0.6
0.4
0.2
0.0
-0.2
-0.4
0.0
0.2
0.4
0.6
0.8
1.0
1.2
1.4
1.6
1.8
2.0
v_{xx}
v_{yy}
t/ps
T=19.8 K

(C)

shown in Figure 4.5(a) and results from the adsorbed solid floating over the surface. It is clearly not possible to Fourier transform the functions $C^{v}_{xx}(t)$ and $C^{v}_{yy}(t)$ since they have not decayed to zero and have no clear functional form. These functions have long correlation times, t_c, and the relative error in the auto-correlation functions goes as $(t_c/NT)^{\frac{1}{2}}$, where N is the number of particles and T the time of the run (Zwanzig and Ailawadi, 1969; Frenkel, 1980). Attempts to extend $C^{v}_{xx}(t)$ and $C^{v}_{yy}(t)$ to longer times without running longer simulations results in statistical noise. However the oscillations in $C^{v}_{xx}(t)$ and $C^{v}_{yy}(t)$ have a characteristic frequency of 50 ± 10 cm^{-1}. This may correspond to the peaks between 35 and 50 cm^{-1} in $S_s(0,\omega)$, (a neutron loss of 4-6 meV). This peak in the density of states would be associated with translational motion parallel to the surface.

At 51.8K the frequency of the vibrational motion perpendicular to the surface has decreased to 52 cm^{-1}. This decrease in frequency with temperature is also observed for the single methane particle. The decrease can be associated with a larger amplitude of vibration and hence a longer mean time between oscillations. The spectrum associated with $C^{v}_{zz}(t)$ is no longer Lorentzian and is broader than the spectrum at 19.8K, see Figure 4.8(a). A typical in-plane velocity auto-correlation function at 51.8K is shown in Figure 4.8(b) with the spectrum shown as an inset. The function oscillates

Figure 4.8(a) The velocity auto-correlation function orthogonal to the plane at 51.8K. The function is no longer Lorentzian and no simple analytic form for the Fourier transform is available.

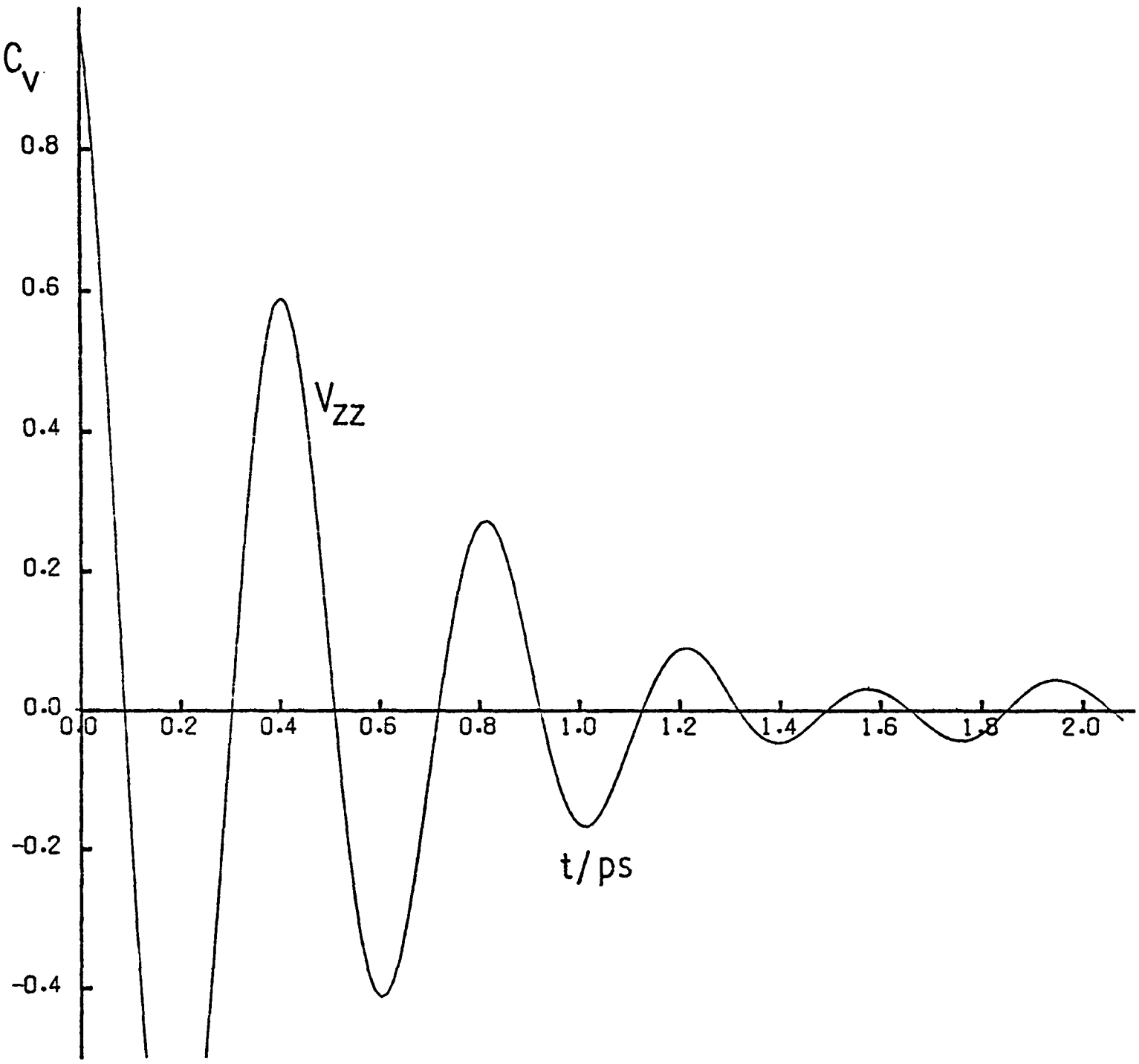
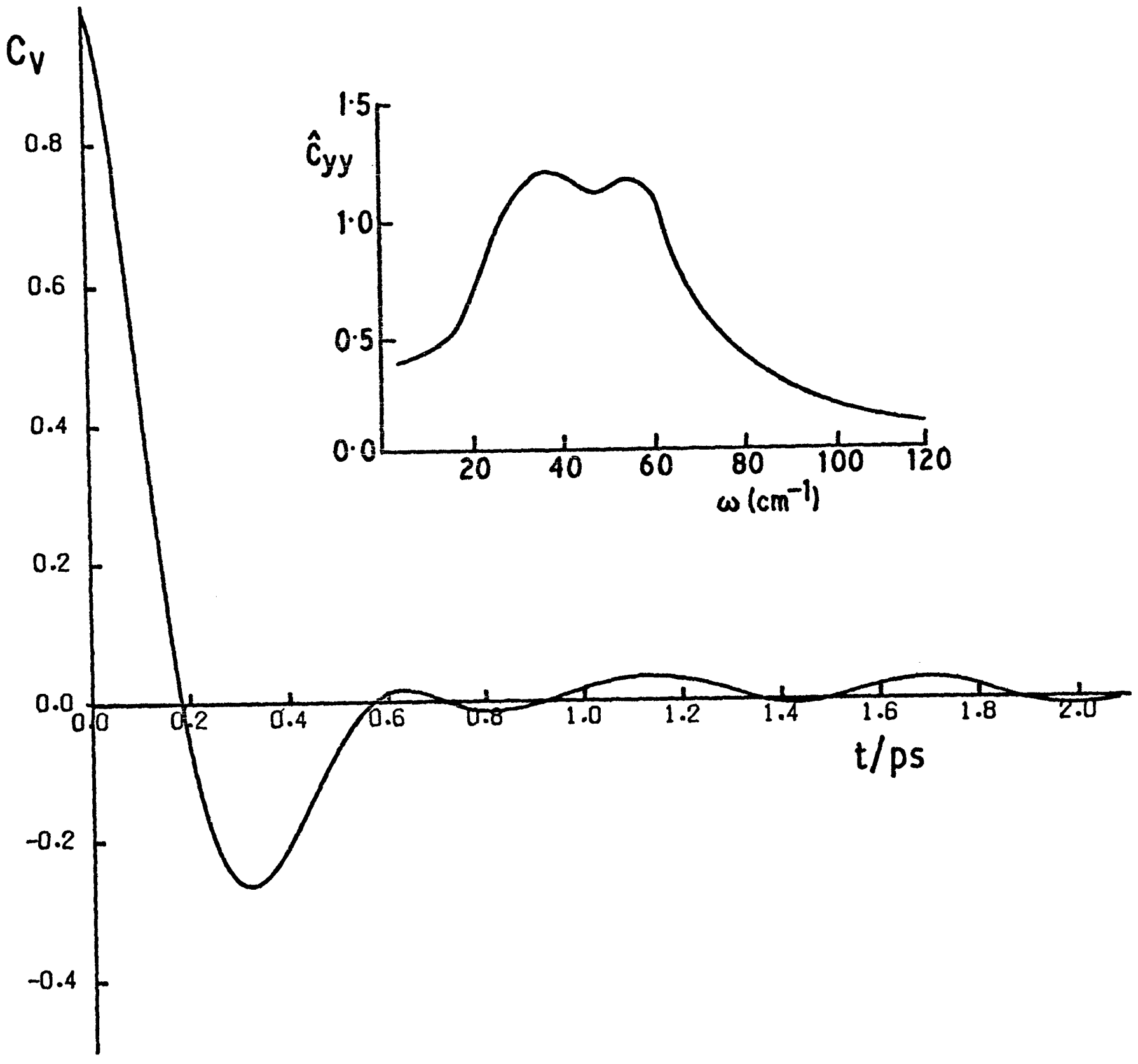


Figure 4.8(b) The in-plane velocity a.c.f for the adsorbed solid at 51.8K. The function decays more rapidly at the higher temperature and has a spectrum with a characteristic frequency around 50 cm^{-1}.



around zero indicating the y component of the in-plane velocity is frequently reversed and that on average particles remain registered in their lattice positions.

4.4 Orientational Behaviour of the Adsorbed Methane

An advantage of using an interaction site model to represent the methane molecules is that it is possible to monitor the reorientational behaviour of the adsorbate. In a previous Monte-Carlo simulation O'Shea and Klein (1979) found three rotational phases. The high temperature phase (corresponding to temperatures in excess of 140K) is rotationally disordered. The low temperature phase, (below 26K), has the methane molecules in the tripod configuration. The intermediate phase is not specifically characterized but is "partially" ordered. In their model the molecules are fixed in a 2-d plane and interact with an octopole-octopole interaction. Although this potential has the same symmetry as our methane-methane interaction, the model does not include specific interactions of the surface.

The orientational behaviour of the adsorbate can be explained by two orientational correlation functions. The first $C_1^{\perp}(t)$ describes the orientation of the bond perpendicular to the surface, through the C_z axis of methane when it is in the tripod orientation.

$$C_1^{\perp}(t) = \langle P_1(\underset{\sim}{h}(t) \cdot \underset{\sim}{h}(0)\rangle \qquad (4.4.1)$$

where $\underset{\sim}{h}(t)$ is the unit vector along the bond at time t. The

second $C_1^{\parallel}(t)$ is defined with the unit vector $\underset{\sim}{h}$ parallel to the surface when the molecule is in the tripod configuration. This vector is not pointing along a C-H bond, but along the S_4 symmetry axis. There are some limiting results for these correlation functions. If the molecule is rotating freely, since it is a spherical top, $C_1^{\perp}(t) = C_1^{\parallel}(t)$. If the molecule is fixed rigidly in its lattice position on the surface then $C_1^{\perp}(t) = C_1^{\parallel}(t) = 1$ for all t. If $C_1^{\perp}(t) = 1$ for all t and $C_1^{\parallel}(t)$ decays towards zero, then the molecule remains in the tripod orientation but there is some rotation around the C_z axis perpendicular to the surface. Finally if $C_1^{\perp}(t) = 1$ for all t and $C_1^{\parallel}(t)$ decays, the molecule is flipping from the tripod orientation to a structure in which the C-H bond points towards the graphite. It is unlikely that any of these rules will be obeyed precisely by the adsorbed methane, but the functions $C_1^{\perp}(t)$ and $C_1^{\parallel}(t)$ should fit one of the four limits discussed here.

$C_1^{\perp}(t)$ and $C_1^{\parallel}(t)$ are calculated over runs of 5000 timesteps using time origins at every ten timesteps and correlating the orientation vectors $\underset{\sim}{h}$ over 1670 timesteps (2 picoseconds). The results for three temperatures, T = 11.3K, 19.8K and 51.8K at $\theta = 0.87$ are shown in Figures 4.9(a) and 4.9(b). At the lowest temperature studied, 11.3K, both $C_1^{\perp}(t)$ and $C_1^{\parallel}(t)$ are close to one for all times less than two picoseconds. There is the beginning of a slight loss of memory around the S_4 axis parallel to the surface but the molecules are rotationally ordered in their minimum energy configuration (see Figure 3.8). At 19.8K

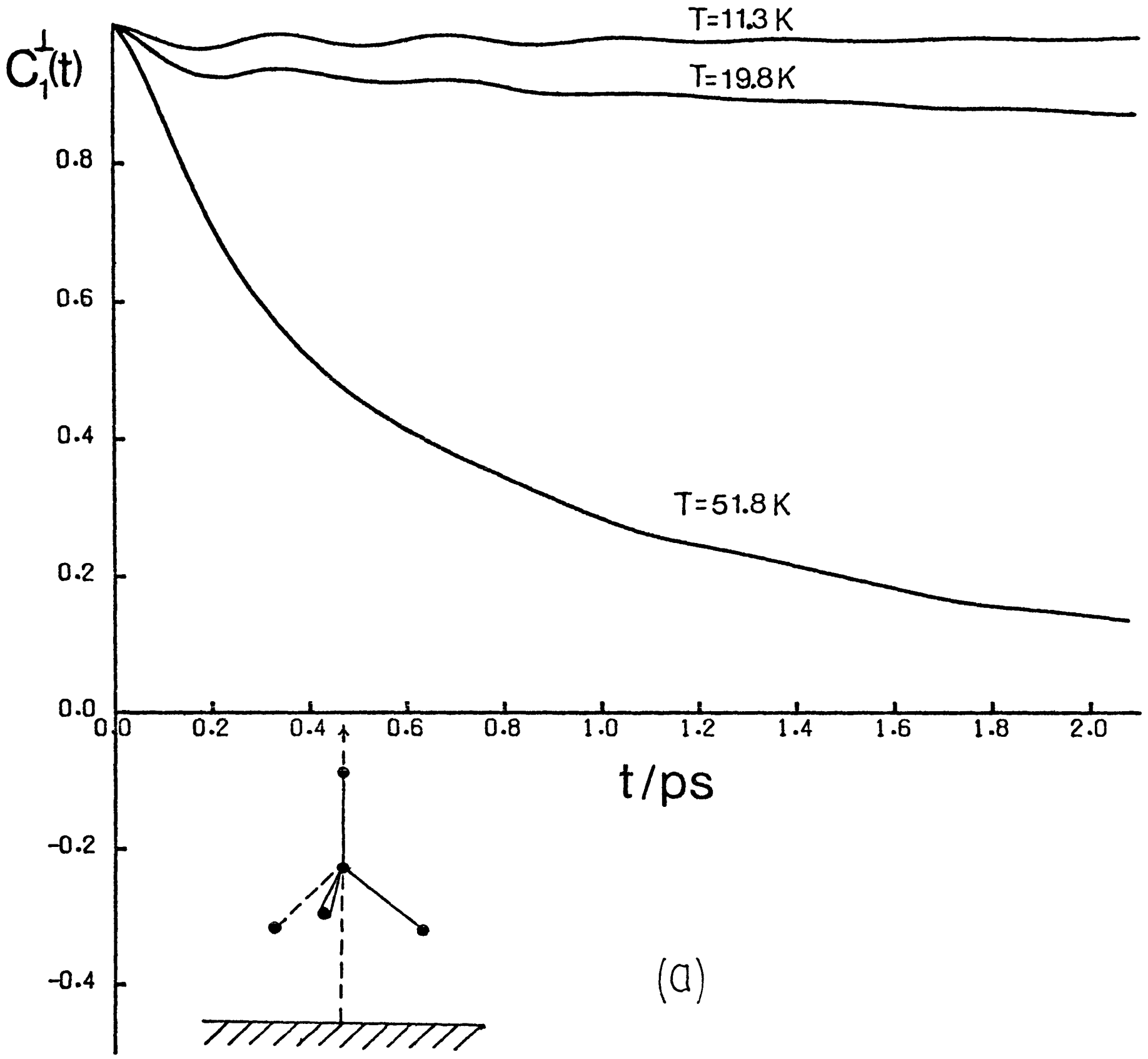
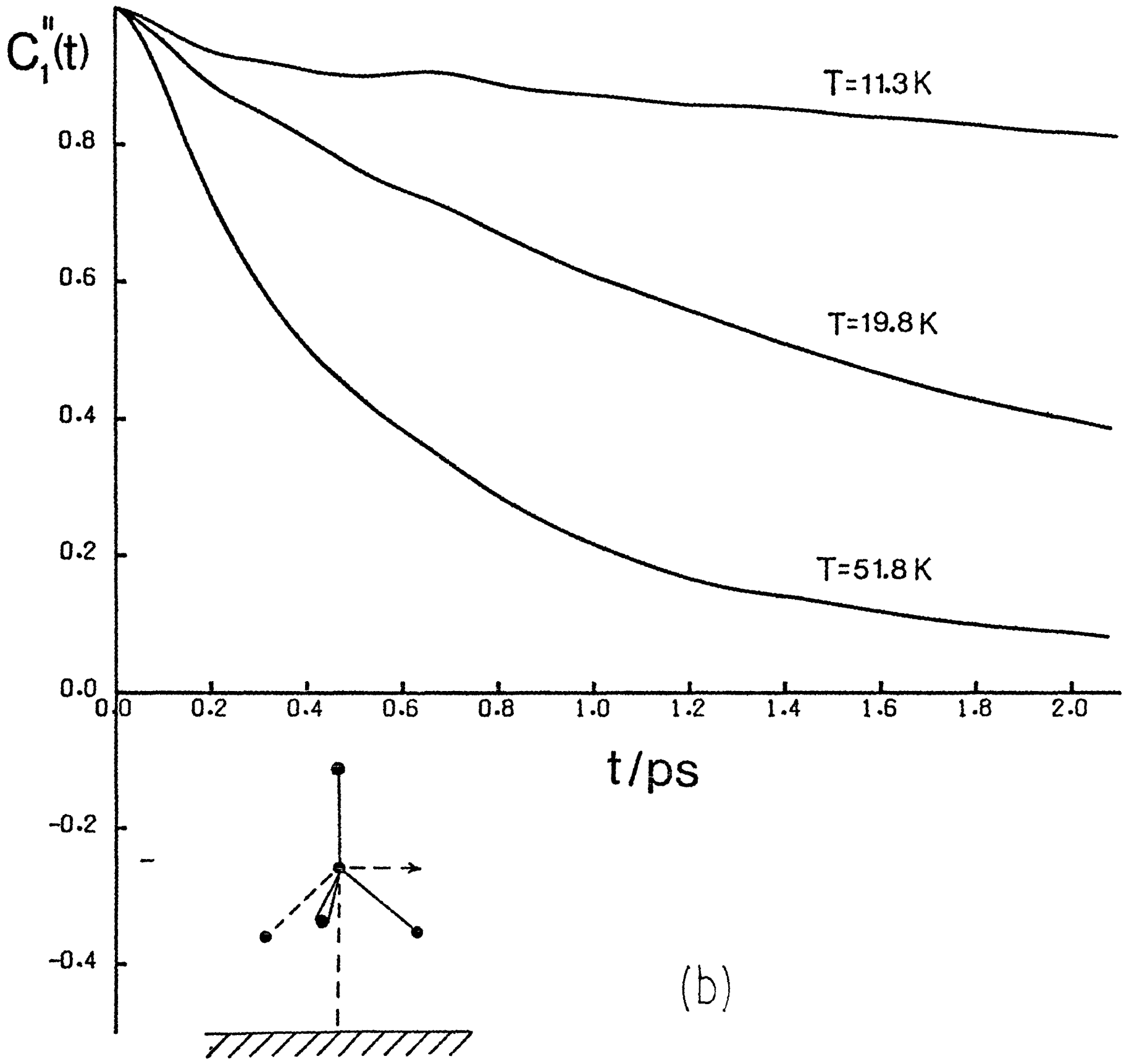


Figure 4.9 The reorientational a.c.f's in the adsorbed solid as a function of temperature. These a.c.f's determine rotational properties of the monolayer. Figure 4.9(a) shows the reorientation of an axis perpendicular to the surface, $C_1^{\perp}(t)$ and 4.9(b) the reorientation of an axis parallel to the surface, $C_1^{\parallel}(t)$.


$C_1''(t)$
T=11.3 K
T=19.8 K
T=51.8 K
0.8
0.6
0.4
0.2
0.0
-0.2
-0.4
0.0
0.2
0.4
0.6
0.8
1.0
1.2
1.4
1.6
1.8
2.0
t/ps

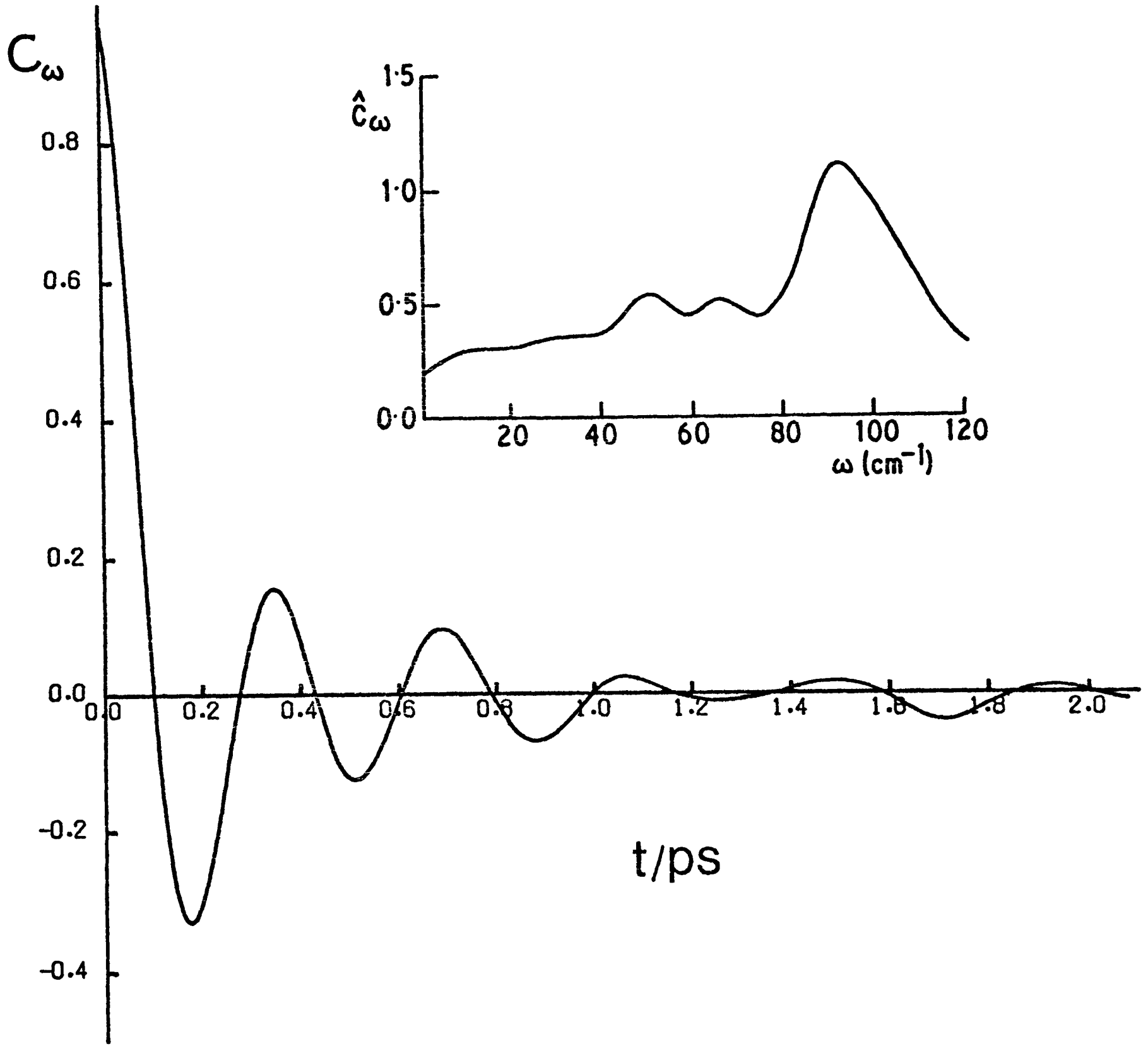
(b)

$C_1^{\perp}(t)$ stays close to one but $C_1^{\parallel}(t)$ decays indicating some rotational disorder around the bond perpendicular to the surface. At 51.8K $C_1^{\perp}(t)$ and $C_1^{\parallel}(t)$ are similar particularly at short times indicating that vectors from the centre of mass of the molecules are equivalent. This corresponds to rotational diffusion. It is important to stress that the molecules are not rotating freely in the disordered phase since the free rotor spectrum of a symmetric top has a plateau of 0.33 (see Figure 3.15).

The angular velocity auto-correlation function for the intermediate rotational phase, 19.8K is shown in Figure 4.10, with its spectrum shown in the inset. This function measures the memory of the angular velocity, which since $C_1^{\perp}(t) \simeq 1$ must be, principally around the C_z axis perpendicular to the surface. The rapid decay of the function indicates there is rotational motion around this bond and the regular reversal of the sign of $C^{\omega}(t) = \langle\omega(t) \cdot \omega(0)/\omega(0) \cdot \omega(0)\rangle$ indicates some kind of librational motion. This motion would expect to contribute peaks at 48, 68 and 91 cm^{-1} in $S_s(0,\omega)$. We note that the spectra $C^{v}_{\alpha\alpha}(t)$ and $C^{\omega}(t)$ have a number of peaks in common, but that the peak at 68 cm^{-1} only appears in the librational motion and corresponds to the peak at 72 cm^{-1} in $S^{\perp}(0,\omega)$ and $S^{\parallel}(0,\omega)$.

These results are in reasonable qualitative agreement with those of O'Shea and Klein (1979). There are however two principal differences in our results. At low temperatures our model predicts that the methane molecules sit as stable tripods, whereas the

Figure 4.10 The angular velocity a.c.f. for the adsorbed solid at 19.8K. This function shows the rapid librational motion of the methane around the bond perpendicular to the surface. The spectrum of this motion contains frequencies at 48, 68 and 91 cm^{-1}.



low temperature phase in O'Shea and Klein consists of alternating stable and unstable tripods. Secondly, rotational disorder occurs at 30K in our model but does not set in until higher temperatures (> 100K) in O'Shea and Klein's model. In both areas our model appears to be in closer agreement with experiment (Newbery et al., 1978) than the much simpler model of O'Shea and Klein.

At low temperature below 10K we see an ordered phase and at 20K some rotational motion around one of the C-H bonds. We cannot identify three distinct phases from the simulation and it is possible that the change from rotationally ordered to disordered solid takes place gradually from 0 to 30K. A number of the phase transitions in 3-d solid methane have a gradual second-order component and a sudden first-order component at a particular temperature (Parsonage and Staveley, 1978; Bloom and Morrison, 1973). These simulation results can also be compared with the experimental neutron scattering spectroscopy (Newbery et al., 1978). At 30K the tunnelling spectrum has a smooth contour which is characteristic of rotational diffusion. Both the simulation and the scattering experiment are consistent with the picture of an adsorbed plastic crystal between 30K and 70K at a completed $\sqrt{3} \times \sqrt{3}$ coverage. At 20K the tunnelling peaks can be distinguished and it is clear from the peak broadening in the spectrum that there is some rotational diffusion in the adsorbate. The simulation result is consistent with this observation. At 12K there is a sharp spectrum with two distinct peaks either side of zero energy transfer.

Tunnelling is, of course, a quantum mechanical phenomenon

which could not be expected to appear in a purely classical simulation. The simulation enables us to infer there is little classical rotation at 10K and the spectra are the result of proton tunnelling, however it is extremely difficult to distinguish between these two phenomena for methane below 40K.

4.5 Orientational Behaviour in the Bilayer

In addition to studying the orientational behaviour of the adsorbed solid a few molecules are scattered on top of the $\sqrt{3}$ x $\sqrt{3}$ monolayer at 30K. We monitor the behaviour of adsorbed molecules in the bilayer where the strong surface-methane potential is attenuated by the intervening monolayer. A simulation is performed over 5000 timesteps and the reorientational correlation function of three particles is calculated over 1000 timesteps (1.2 picoseconds). Since the average is over a few molecules and the relative error goes as $(t_c/NT)^{\frac{1}{2}}$ we can only make some qualitative conclusions about the behaviour in the bilayer.

The reorientational correlation function of the three molecules decays to zero in 1.1 picoseconds for both $C_1^{\perp}(t)$ and $C_1^{\parallel}(t)$. This correlation length of 1.1 picoseconds is similar to that of the rotationally disordered phase at 127.2K where the correlation function decays to zero in 1.2 picoseconds. The three molecules in the bilayer appear to be rotationally disordered.

The S_I solid monolayer at 30K shows signs of partial disorder comparable to the solid at 51.8K and the oscillatory behaviour of C^{ω} around zero indicates that the motion is mainly librational,

although we know by monitoring the spatial co-ordinates of one of the C-H bonds of the molecules that some molecules do occasionally flip. Figure 4.11 shows the reorientational auto-correlation functions of the S_I solid, the three molecules in the bilayer and the single methane molecule adsorbed on graphite at 30K.

The large methane-surface interaction holds the single methane molecule in the tripod position with little degree of librational freedom and its orientation remains highly correlated. The addition of a surrounding solid reduces the barrier to rotation by approximately 100% to 200 cm^{-1} (see section 3.3) and rotation sets in. The dramatic reduction in the rotational barrier is caused by the competition between the most stable methane-surface configuration and the most stable methane-methane configuration. The most stable methane-surface configuration is the tripod orientation while an alternate array of molecule up (tripod), and molecule down (anti-tripod) is the most stable 2-d methane-methane orientation. The competition between these two configurations allows rotational diffusion to set in at much lower temperatures in the solid than for a single adsorbed molecule. The correlation function of the solid decays more rapidly than the single particle correlation function at the same temperature. The shielding effect of the monolayer in turn reduces the barrier to rotation in the bilayer, and the reorientational correlation function of the bilayer decays more rapidly than for the monolayer, and the single particle.

Figure 4.11 The reorientational a.c.f's for three molecules in the second layer of adsorbed methane. The a.c.f for molecules in the first layer and for a single molecule adsorbed directly on the graphite surface are included for comparison. The three a.c.f's are calculated from simulations performed at 30K.

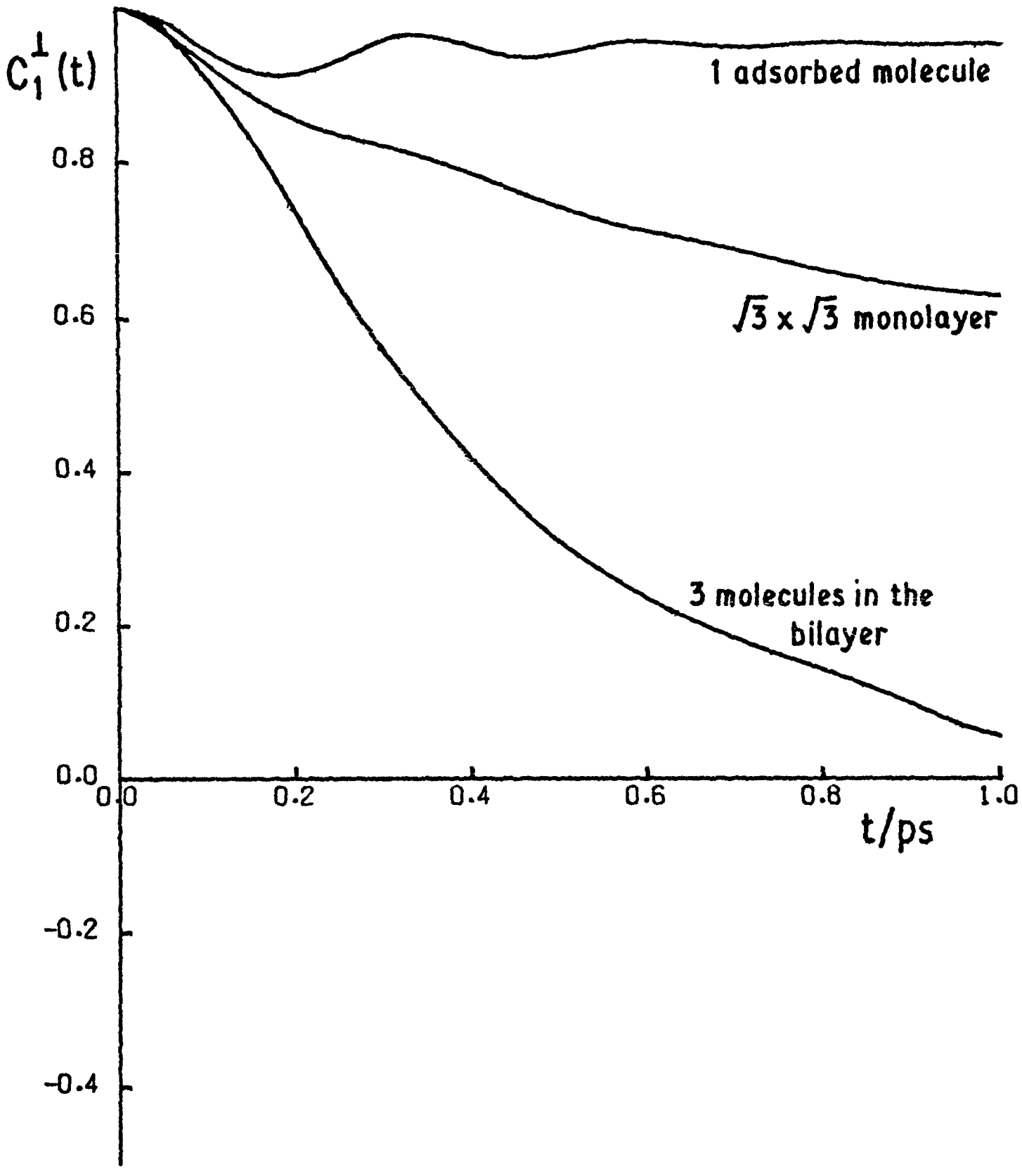
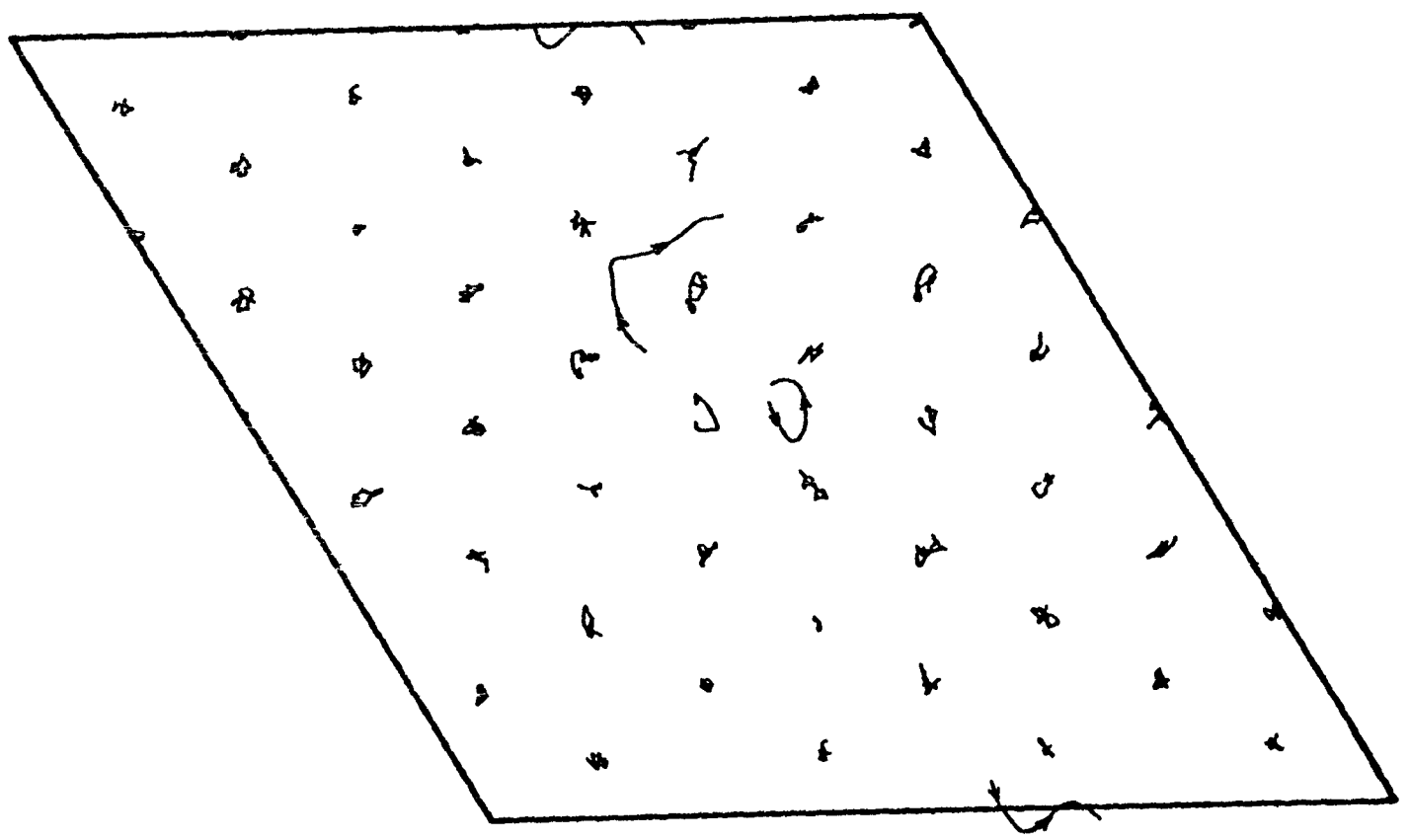


Figure 4.12 shows the trajectory of the S_I monolayer and the three molecules in the bilayer over 5000 timesteps at 30K. We first note the effect of the floating solid has disappeared, i.e. the methane-methane interactions randomize the translational motion of the solid at T = 30K. Secondly the three adsorbed molecules in the bilayer do not diffuse very far from their initial positions. The small amount of translational diffusion compared to the single adsorbed molecule (see Figure 3.10) may be caused by large potential barriers in the adsorbed monolayer and by mutual attraction of the three molecules in the bilayer.

Newbery et al., (1978) have measured the rotational tunnelling of methane in the monolayer and bilayer at 6K. The underlying monolayer is complete and the sharp peaks in the spectrum indicate quantum rotational tunnelling only. When a bilayer is added to the system the spectrum becomes broad and this indicates the molecules in the bilayer have only slightly hindered rotation. Our results above are in qualitative agreement with this observation, i.e. rotation is strongly hindered in the monolayer but quite free in the bilayer at low temperatures.

Figure 4.12 Trajectory of $\sqrt{3}$ x $\sqrt{3}$ solid methane plus three molecules scattered in the bilayer at 30K. Note the floating solid has disappeared at this temperature.



CHAPTER 5

Liquid Methane Adsorbed on Graphite

5.1 Introduction

The two extremes in coverage in single layer adsorption are examined in Chapters 3 and 4. The model predicts a large number of properties of the real system at these two coverages and it should be useful in examining the sub-monolayer region where a number of different solid and fluid phases are thought to exist.

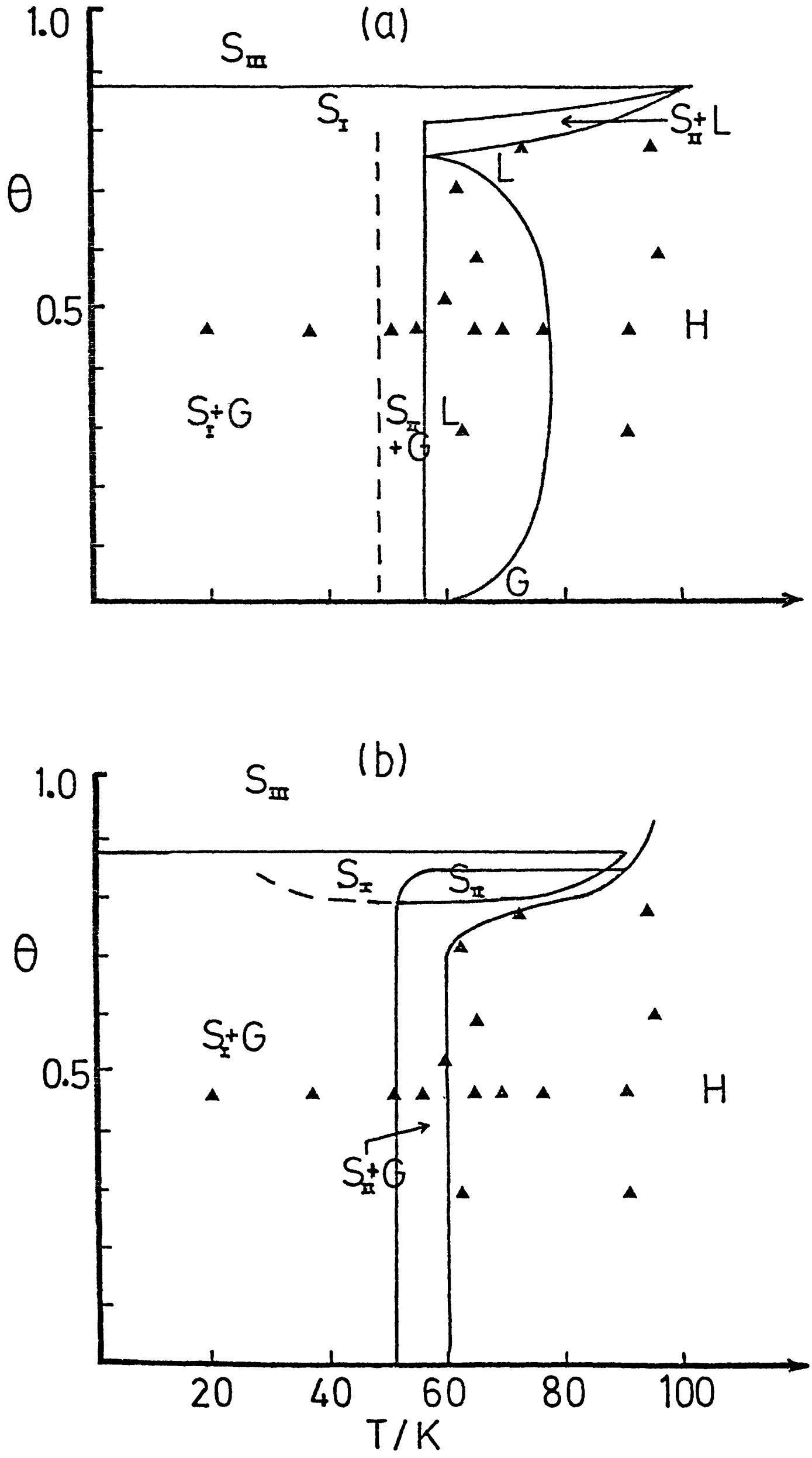
A tentative phase diagram proposed by Coulomb et al., (1980) is shown in Figure 5.1(a) and its solid monolayer phases are discussed in detail in Chapter 4. At temperatures below 50K patches of S_I ($\sqrt{3}$ x $\sqrt{3}$) solid plus gas are observed. As the temperature is increased from 50K to 60K (at coverages of less than $\theta = 0.8$) an expanded solid S_{II}/gas phase is proposed and the triple point is predicted at T = 56K, $\theta = 0.75$. A solid/fluid transition occurs at 56K and from the measurement of the diffusion coefficient of methane on graphite, Coulomb et al., (1980) have postulated that a liquid/gas phase exists from 56K up to a critical temperature $\simeq$ 75K. Beyond the critical temperature a hypercritical fluid is observed. Other phases S_I, S_{II}, S_{II} + liquid are all expected to exist in a small region between $\theta = 0.75$ and 0.87, and T = 56 to $\simeq$ 100K.

Vora et al., (1979) have also constructed a phase diagram by observing the line broadening of neutron diffraction peaks over

a large range of temperature and coverage. This experiment predicts the same solid phases as Coulomb et al., (1980). However, there is a difference between the two phase diagrams in the liquid region; Vora et al., see no evidence for a coexisting phase of liquid and gas. They observe a transition ($\theta < 0.8$) from S_I solid/fluid to a expanded S_{II} solid/fluid at 50K, and then to a hypercritical fluid at temperatures beyond a critical point at $\simeq$ 60K. This phase diagram is shown in Figure 5.1(b). In both diagrams triangles are marked to indicate the simulation points.

In this chapter we attempt to unravel some of the inconsistencies in the phase diagrams constructed from different experiments. The structure of the submonolayer phases is discussed in Section 2 and particular attention is paid to an isochore at $\theta = 0.46$, along which we expect to observe most of the fluid phases. Distribution functions, order parameters and specific heats are calculated in order to characterize the phases along this isochore. Liquid phase site-site distribution functions at $\theta = 0.77$ are compared to the dense fluid correlation functions (Murad et al., 1979) and the feasibility of calculating a neutron structure factor from these site-site distribution functions is discussed. Another route to characterizing the phase diagram is by observing the change in the translational self diffusion coefficients of the adsorbate as a function of temperature and coverage. In Section 3 the translational behaviour of methane is examined and compared to experiment (Coulomb et al., 1980; Tabony and Cosgrove, 1979). Finally, in Section 4,

Figure 5.1 Phase diagrams of methane adsorbed on graphite, (a) is from Coulomb et al., (1980) and (b) is from Vora et al., (1979). L is liquid, G is gas and H is a hypercritical fluid.



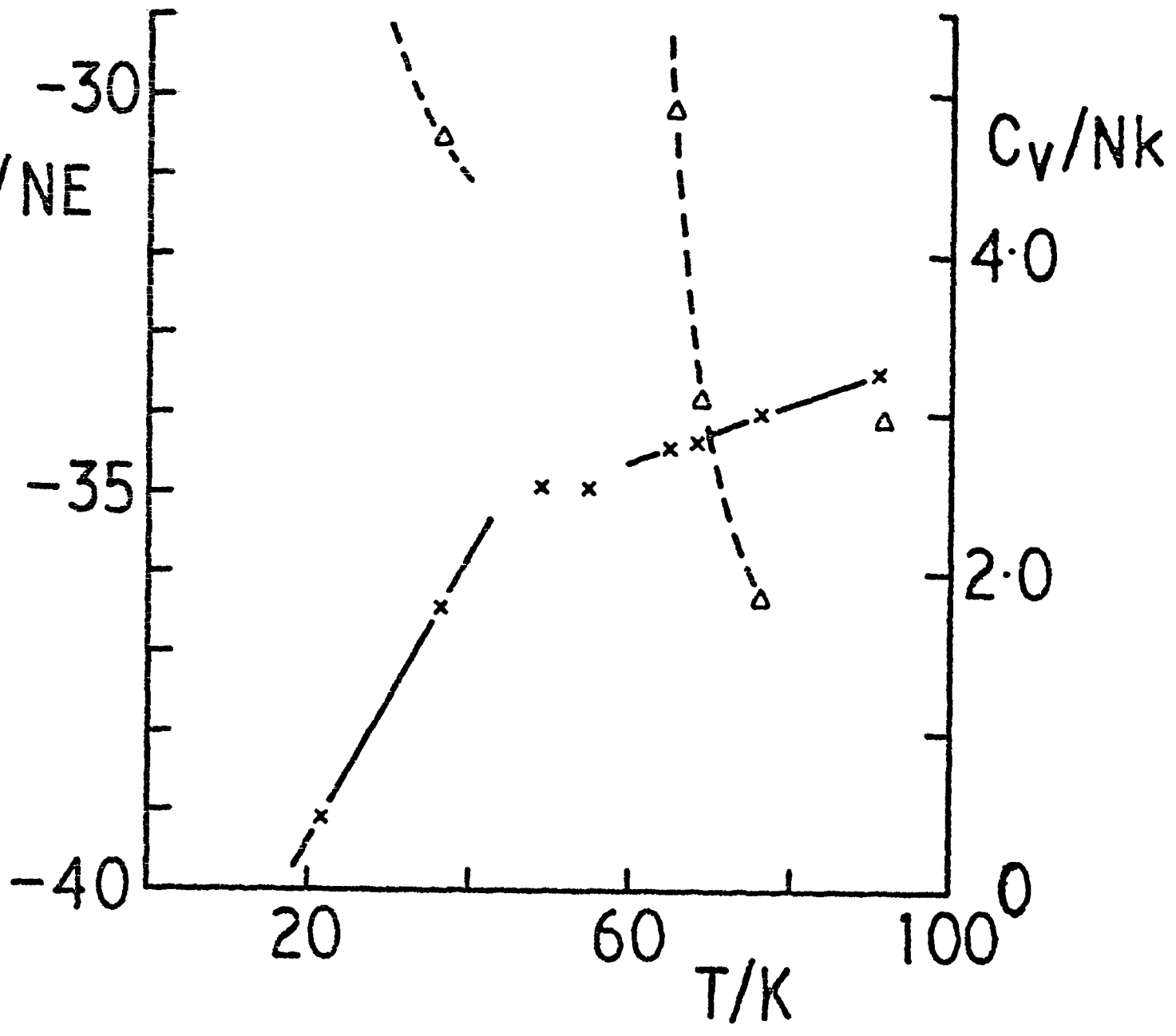
the statistical mechanical expression of the spreading pressure for an adsorbed molecular fluid is derived and values of the spreading pressure are reported over a wide range of the phase diagram. Comparison is made with experiment where possible.

5.2 Thermodynamics and Structure

The first route to characterizing the existence of different phases along an isochore is by observing changes in the slope of the internal energy and discontinnuities in the specific heat as a function of temperature. A change in slope or a discontinuity is associated with a phase transition. The internal energy and specific heat averaged over 5000 timesteps of 1.25×10^{-15} s at $\theta = 0.46$ are shown in Figure 5.2. The behaviour of these quantities indicates that a phase transition occurs in the simulation between 50K and 60K. The specific heat is very large at temperatures below 50K and this indicates that a slow rotational or translational transition may be occurring over quite a broad range of temperature. Neither the internal energy nor the specific heat indicates that a transition occurs around 75K.

The structure of the adsorbed fluid can be described by the molecular centres pair distribution function $g_{cc}(\underset{\sim}{R}_1\underset{\sim}{R}_2)$ defined by equation (4.3.2). Several distribution functions at $\theta = 0.46$ over the temperature range T = 20K to 90K are shown in Figure 5.3. The arrows indicate the first four nearest neighbour distances

Figure 5.2 The configurational energy, X, and the specific heat, Δ, as a function of temperature at constant coverage of θ = 0.46. The dashed line through the specific heat is drawn as a guide to the eye. The error in the specific heat is ≃ ± 0.5 while the errors in the configurational energy are negligible.



in the solid S_I structure. Unlike the isochore at $\theta = 0.87$ (see Figure 4.3) the S_I solid structure does not persist beyond 30K and even at T = 36.6K the second peak in the distribution function has disappeared. At higher temperatures T > 50K the distribution of molecular centres resembles that of a bulk fluid (see Figure 1 of Murad et al., 1979, for $g_{cc}(r)$ of dense fluid methane).

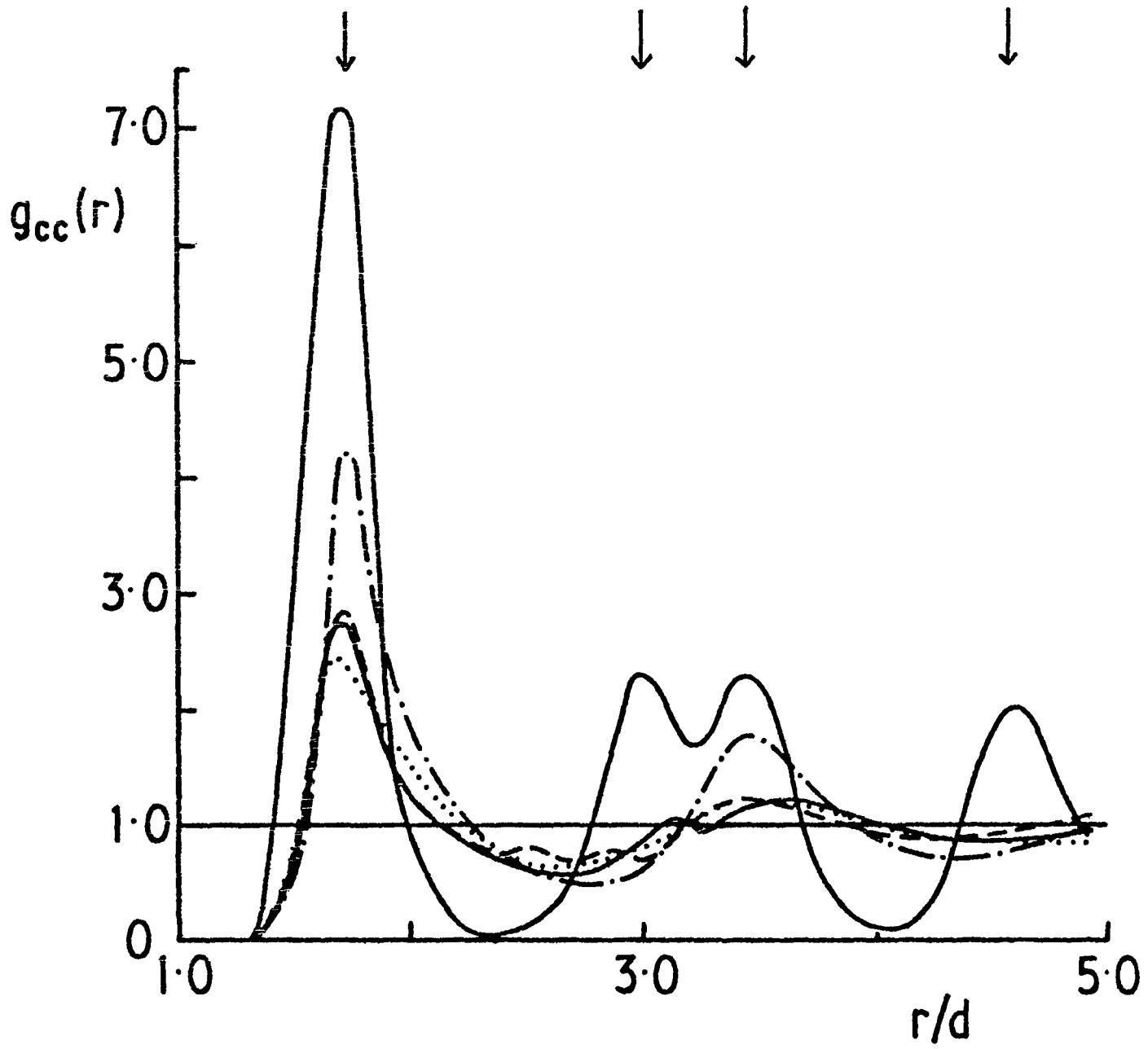
A more quantitative description of the ordering is given by the adsorbate-adsorbate order parameter O_1 (defined by equation (4.3.3)) and the adsorbate-adsorbent order parameter O_2 (defined by equation (4.3.4)). These order parameters calculated over 5000 simulation timesteps at $\theta = 0.46$ are listed in Table 5.1. At a coverage of $\theta = 0.46$, 40 particles are simulated and a registered solid at 0K would have a value of 40 for O_1 and O_2. At T = 21.7K O_1 is relatively smaller than the value at T = 19.8K, $\theta = 0.87$ and this may be due to the onset of melting even at this low temperature. Figure 5.4a is a trajectory of the 40 molecules at T = 21.7K. The molecules have longer trajectories than at $\theta = 0.87$, T = 19.8K (see Figure 4.5) but the adsorbate still appears to float across the surface and this is confirmed by the relatively large value of $O_2 \simeq 11$. As the temperature is increased the order parameters decay towards zero indicating the transition to a liquid phase. Figures 5.4b - 5.4d show the trajectories at T = 36.6, 49.9 and 90.6K. These trajectories confirm that melting begins below 36.6K and that the transition from solid to liquid

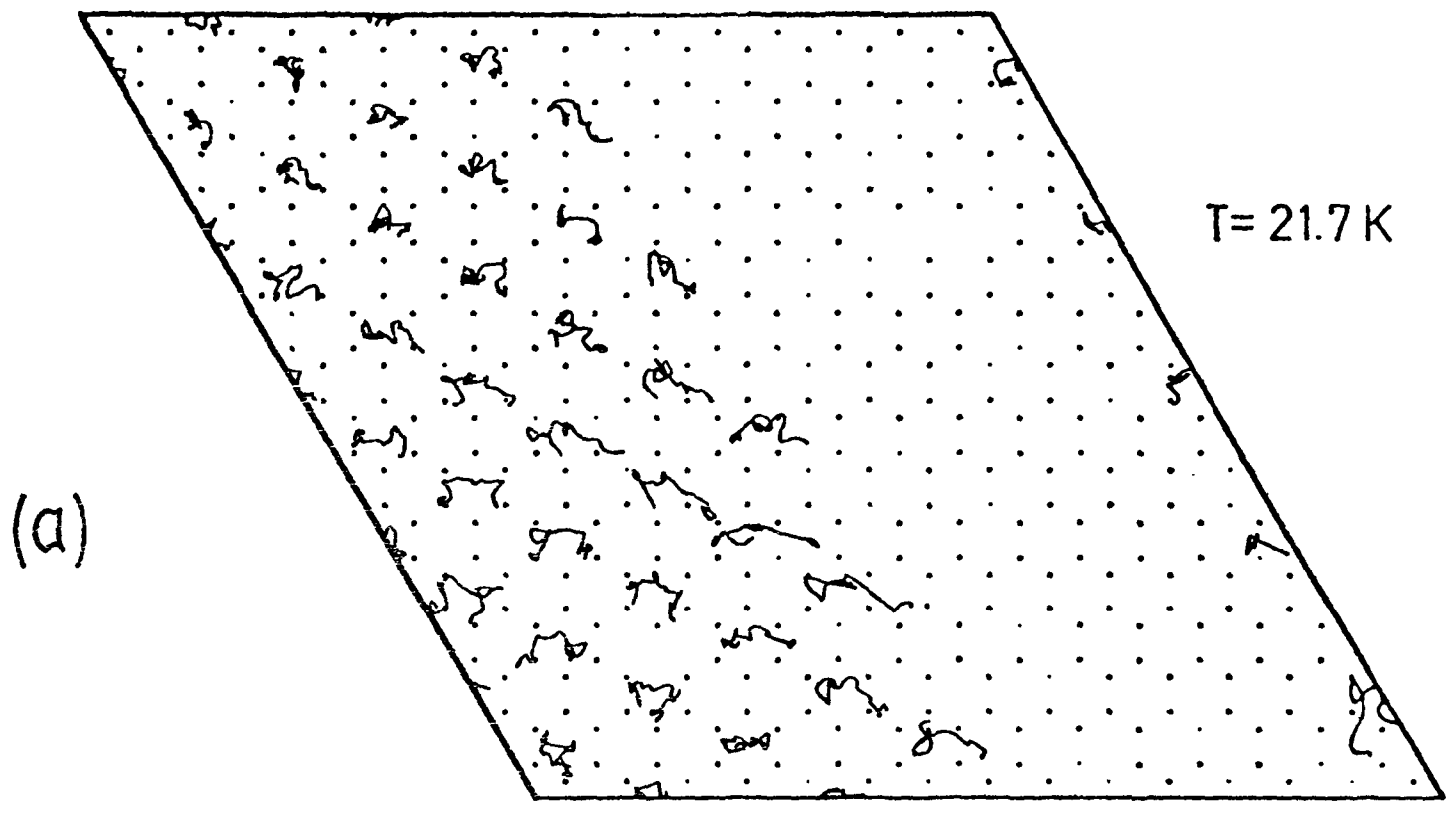
Table 5.1

θ = 0.46, number of methane molecules is 40

T/k	U/Nε	C_V/Nk	O_1	O_2	nearest neighbour	D x $10^{-5}cm^2s^{-1}$	Comments
21.7	-39.12	-	12.2	11.0	4.429 Å	1.8	floating solid -- see trajectory
36.4	-36.45	4.73	2.3	4.1			
49.9	-34.91		1.5	2.4	8.656 Å	13.2	- see trajectory " " $g_{cc}(r)$ v. liquid like.
54.4	-35.03	-				17.7	
64.4	-34.38	4.91	1.2	0.6	8.153 Å		
68.6	-34.98	3.12					
76	-33.94	1.82					
90.6	-33.54	2.95	1.20	0.56		22.0	

Figure 5.3 The distribution of molecular centres at $\theta = 0.46$.
The functions correspond to temperatures of: ———21.7K (solid like g(r));
·-·-·36.6K; ------49.9K; —— 64.4K; .....90.6K.





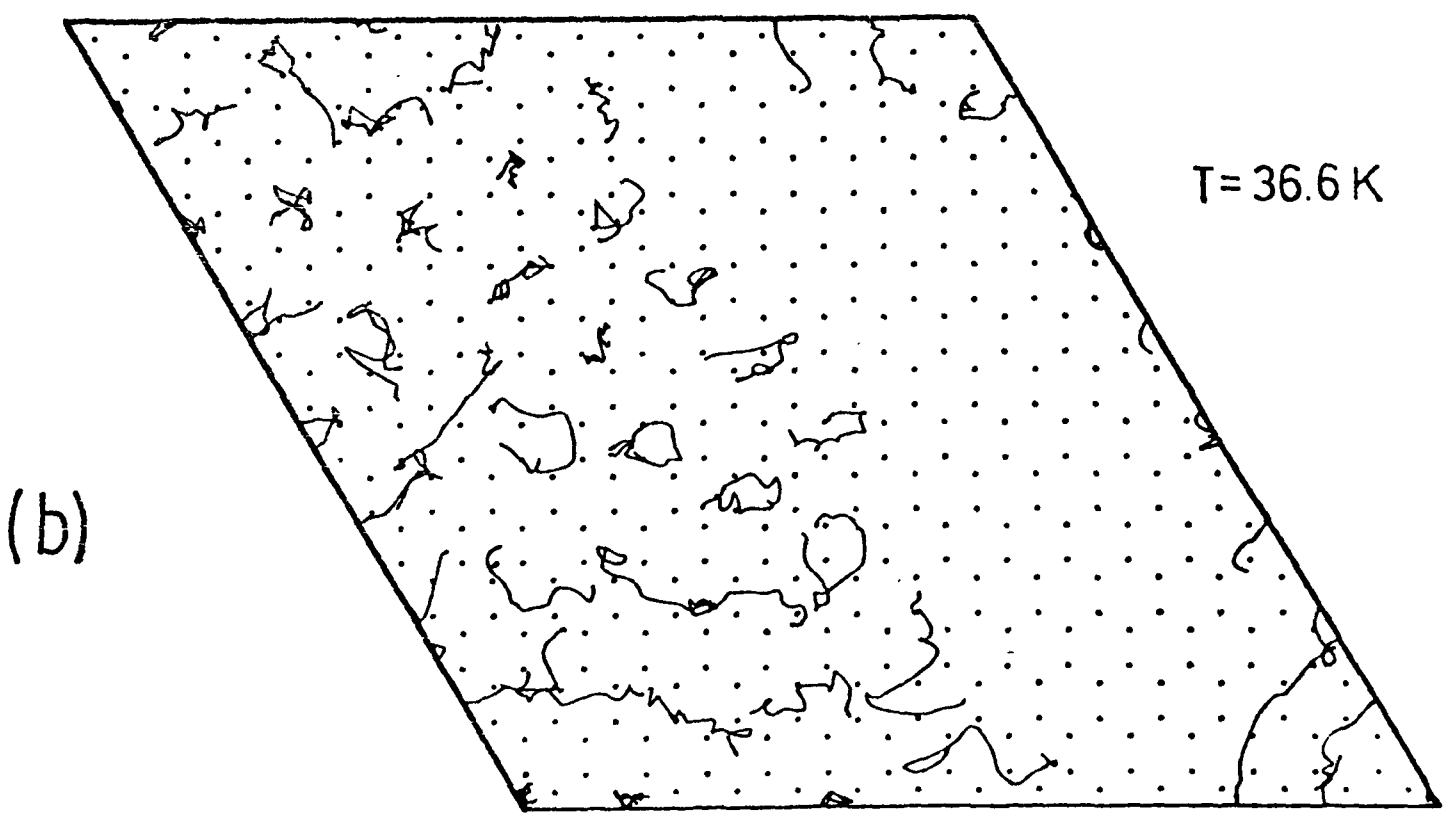
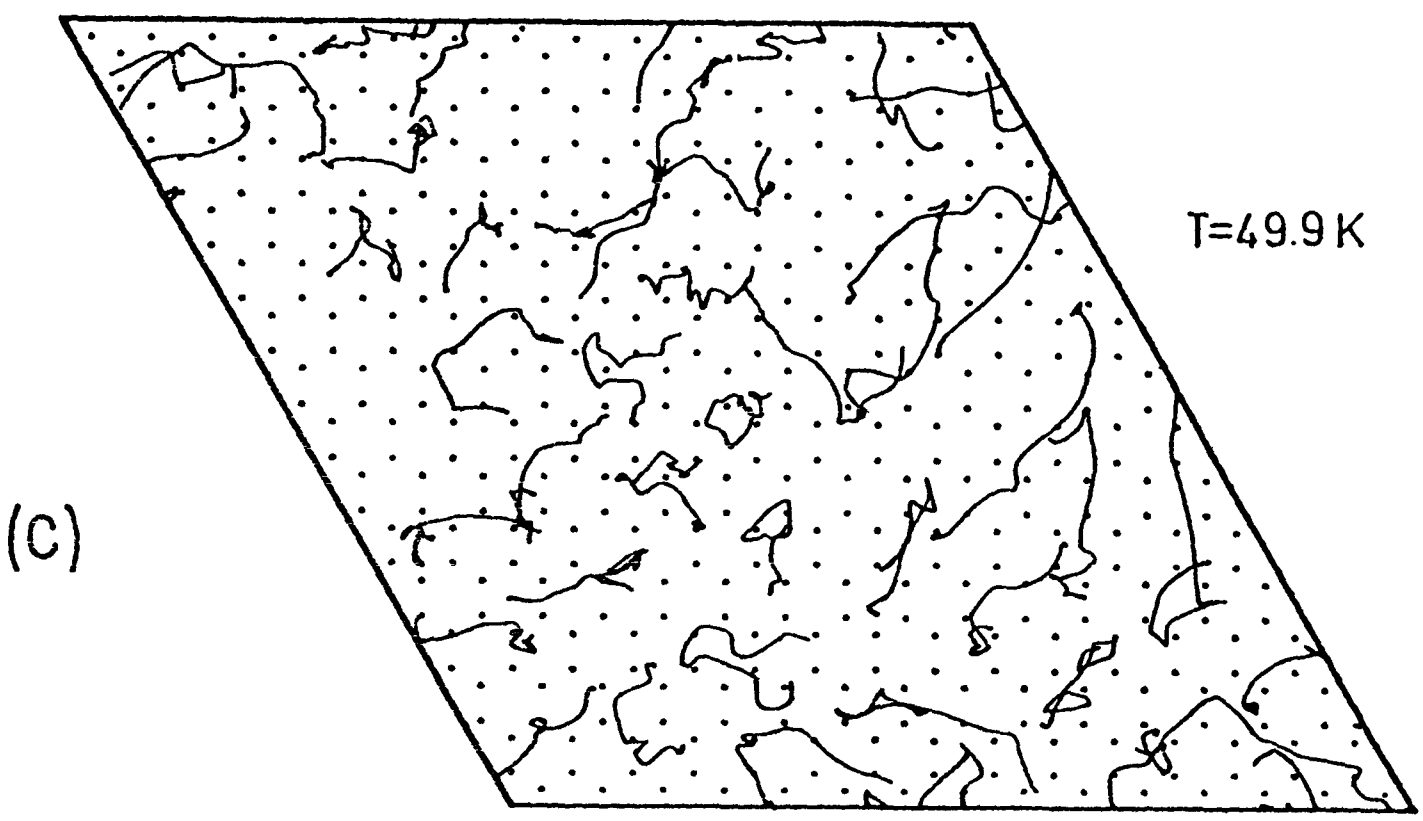
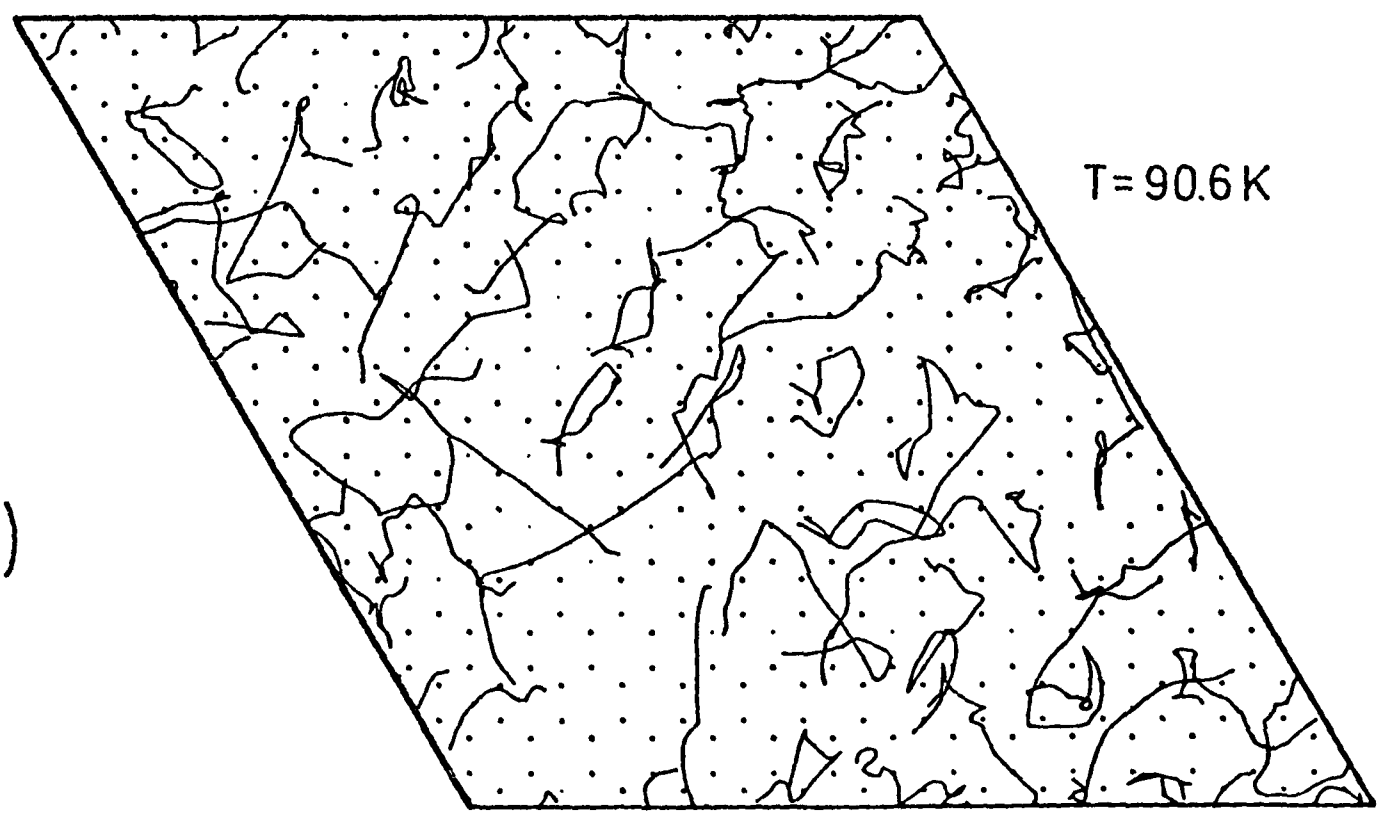


Figure 5.4 Trajectories of the centre of mass of the methane molecules projected onto the graphite surface. These trajectories are taken over 5000 timesteps corresponding to times of approximately 6 picoseconds. At 21.7K it appears that melting has begun and at 36.6K the solid $\sqrt{3} \times \sqrt{3}$ structure has disappeared. A liquid like phase is observed at higher temperatures, 49.9K and 90.6K.



(C)



(d)

is a gradual process for our model.

The site-site distribution functions $g_{CC}(r)$, $g_{CH}(r)$, $g_{HH}(r)$ at a liquid point $\theta = 0.77$, $T = 72.1K$ are shown in Figure 5.5. The peaks in these distribution functions are all within 2% of the peaks in the bulk fluid site-site correlation functions at $T = 130K$, (Figure 1, Murad et al., 1979) and the assignment of the cusps in the distribution functions is most likely the same in two-dimensions as in three dimensions. Murad et al., have also calculated a neutron scattering structure factor for liquid methane using site-site correlation functions.

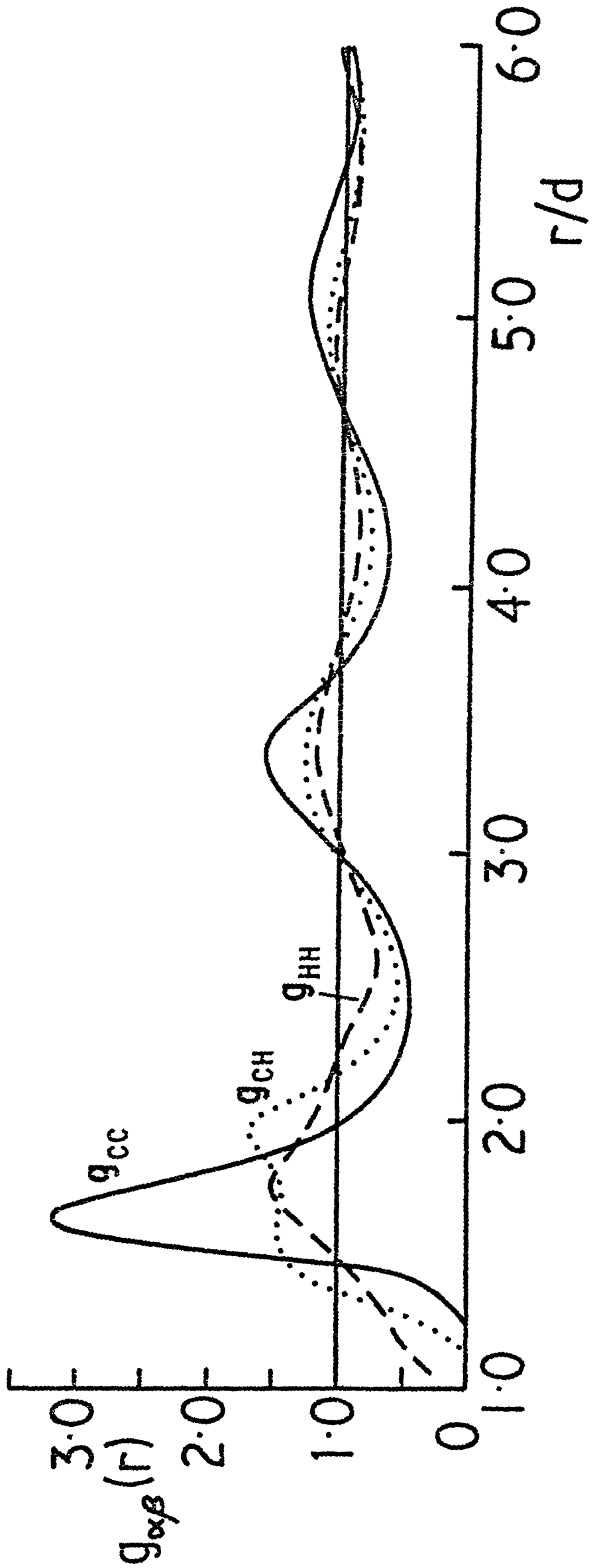
The neutron structure factor for a molecular fluid is given by (Gubbins et al., 1973)

$$S(k) = \frac{1}{N(\sum_{\alpha} b_{\alpha})^2} \sum_{ij} \sum_{\alpha\beta} \bar{b}_{\alpha}\bar{b}_{\beta} < \exp [i \underset{\sim}{k}.(\underset{\sim}{r}_{i\alpha} - \underset{\sim}{r}_{j\beta})]> \qquad (5.2.1)$$

where N is the number of molecules in the system, $\bar{b}_{\alpha}$ is the coherent scattering length of nucleus α and $\underset{\sim}{r}_{i\alpha}$ is the position of nucleus α in molecule i. The structure factor may be divided into two parts, an intra-molecular part (i = j terms) and an inter molecular part ($i \neq j$ terms). In the case of bulk liquid methane we write (Murad et al., 1979)

$$S(k) = S_{intra}(k) + S_{inter}(k) \qquad (5.2.2)$$

Figure 5.5 Site-Site distribution functions at θ = 0.77, T = 72.1K.



where

$$S_{intra}(k) = (b_C+4\bar{b}_H)^{-2}\left[b_C^{\,2}+4\bar{b}_H^{\,2}+8\bar{b}_H\bar{b}_C\frac{\sin(k\,L_{CH})}{(k\,L_{CH})} + 12\bar{b}_H^{\,2}\frac{\sin(k\,L_{HH})}{(k\,L_{HH})}\right], \quad (5.2.3)$$

and

$$S_{inter}(k) = (b_C+4\bar{b}_H)^{-2}(b_C^{\,2}S_{CC}(k) + 8\bar{b}_C\bar{b}_H S_{CH}(k) + 16\bar{b}_H^{\,2}S_{HH}(k)) \quad (5.2.4)$$

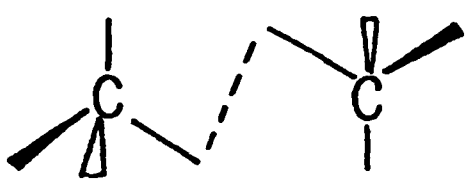
$S_{\alpha\beta}(k)$, the $\alpha\beta$ partial structure factor, is the Fourier transform of the internuclear total correlation function $h_{\alpha\beta}(r) = g_{\alpha\beta}(r) - 1$, i.e.

$$S_{\alpha\beta}(k) = \frac{4\pi\rho}{k}\int_0^\infty h_{\alpha\beta}(r)\sin(k\,r)\,r\,dr \quad (5.2.5)$$

The diffraction of methane adsorbed on graphite using Paypex, a partially oriented adsorbent with a mozaic spread of $\pm 30^o$ (Coulomb et al., 1980), has been measured experimentally (Bomchil et al., 1980). This experiment cannot be compared to the model three dimensional structure factor above because the methane has essentially a two dimensional distribution on these partially

oriented planes. (It is probable that diffraction patterns from methane adsorbed on a powdered substrate, where the basal planes are randomly oriented, will give a 3-d structure factor). A two-dimensional model of diffraction cannot be compared to the experiment using Papyex either because the substrate planes are only partially oriented with respect to the incident neutron beam. It may be possible to obtain good agreement between two-dimensional models and adsorption experiments using a more highly oriented substrate in the future such, as XY graphite. However it is still not a simple task to construct a model to account for the structure factor of methane adsorbed on a 2-dimensionally ordered adsorbent.

At intra-molecular distances the scattering from the nuclei is determined by the 3-d shape of the methane molecule. The first possible approach to calculating the structure factor is to use a 3-d model at small r to calculate S_{intra}, and a 2-d model at large r to calculate S_{inter}. This approach is not consistent since at high density the intermolecular scattering from nearest neighbours might have a 3-d element. This is particularly true for S_{HH} in the orientation



Another approach is to adapt a planar model for methane and derive a purely 2-d structure factor. This model is represented by the projection of the nuclei of the methane molecule in the plane of the incident neutron beam. The in-plane inter-nuclear distance within a molecule is given by

$$L_{\alpha\beta} = \frac{1}{8\pi^2} \int_{-1}^{+1} \int_{\phi}^{2\pi} \int_{\psi}^{2\pi} g^{(1)}(\theta,\psi,\pi,T,N/A)\ \ell_{\alpha\beta}(\theta,\phi,\psi)\ d\cos\theta d\phi\ d\psi \qquad (5.2.6)$$

where θ, ψ, ϕ, are the Euler angles, T the temperature, N the amount adsorbed. $g^{(1)}(\theta,\psi,\pi,T,N/A)$ is the probability that the methane molecule is in space fixed orientation θ, ϕ, ψ at coverage N/A and temperature T. $\ell_{\alpha\beta}(\theta,\phi,\psi)$ is a projection of the inter-nuclear distance $r_{\alpha\beta}$ in the plane parallel to the substrate. The intra part of the structure factor in terms of $L_{\alpha\beta}$ is

$$S_{intra} = (b_C + 4b_H)^{-2} [b_C^2 + 4b_H^2 + 8b_C b_H\ J_0(k\ L_{CH}) + 12b_H^2\ J_0(k\ L_{HH})] \qquad (5.2.7)$$

where J_0 is a Bessel function of the first kind; (see Chapter 6 for a detailed derivation of structure factors in 2-dimensions). The inter term of the structure factor is given by

$$S_{inter}(k) = (b_C + 4b_H)^{-2}[b_C^2 S_{CC}(k) + 8b_C b_H\ S_{CH}(k) + 16b_H^2\ S_{HH}(k)] \qquad (5.2.8)$$

where

$$S_{\alpha\beta}(k) = 2\pi \rho \int_0^\infty g_{\alpha\beta}(r)\, J_0(k\, r) r dr \qquad (5.2.9)$$

and $g_{\alpha\beta}(r)$ is the angle-averaged site-site distribution function. $g_{\alpha\beta}(r)$ would be a two dimensional distribution function (or the projection of the distribution of sites on the surface). This approximation is only valid if the z- dependence of the distribution is small. For two liquids (θ = 0.77, T = 72K and 94K) the distributions of molecular heights above the surface are shown in Figure 5.6. In the simulation we have not calculated the singlet distribution function $g^{(1)}(\theta,\phi,\psi,T,N/A)$ so it is not possible to obtain the intra term in the structure factor which contributes significantly at small r or large k. Figure 5.7 shows the inter terms of the 2-d structure factor for a liquid at θ = 0.77 and T = 72.1K. The three curves exhibit the same qualitative behaviour as the partial structure factors in the dense fluid (see Figure 3 of Murad et al., 1979).

5.3 Translation Across the Surface - the Diffusion Coefficient

A property of particular interest in the characterization of 2 dimensional phases is the translational self diffusion coefficient, D (Dorfman and Van Beijeren, 1977). In a hypercritical fluid phase the adsorbate molecules spread out to cover the surface and at a constant temperature, D should increase with decreasing coverage. The possible existence of a sub-critical fluid phase has been suggested (Coulomb et al., 1979, 1980). In this phase the liquid molecules form puddles surrounded by gas and D should

Figure 5.6 Distribution of molecular centres above the surface. Each histogram block is 0.25 Å. As the coverage and temperature are increased the distribution becomes broader. See also Figure 4.6 for more examples.

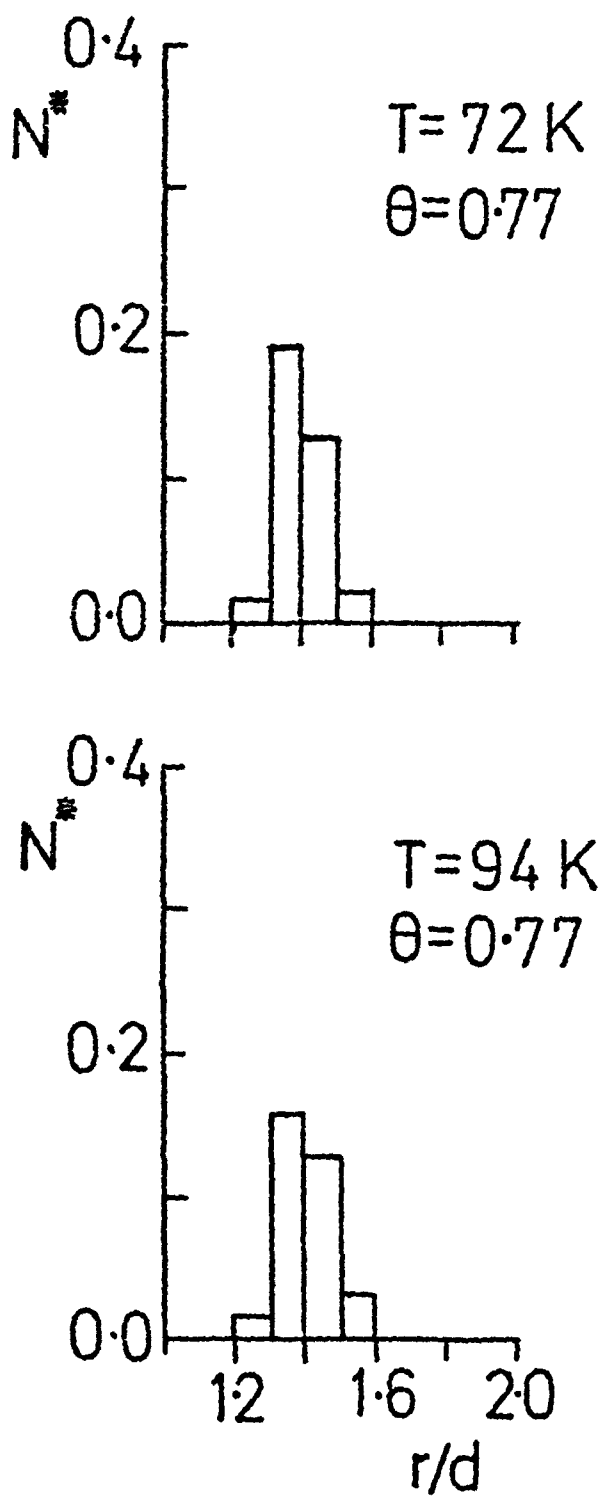
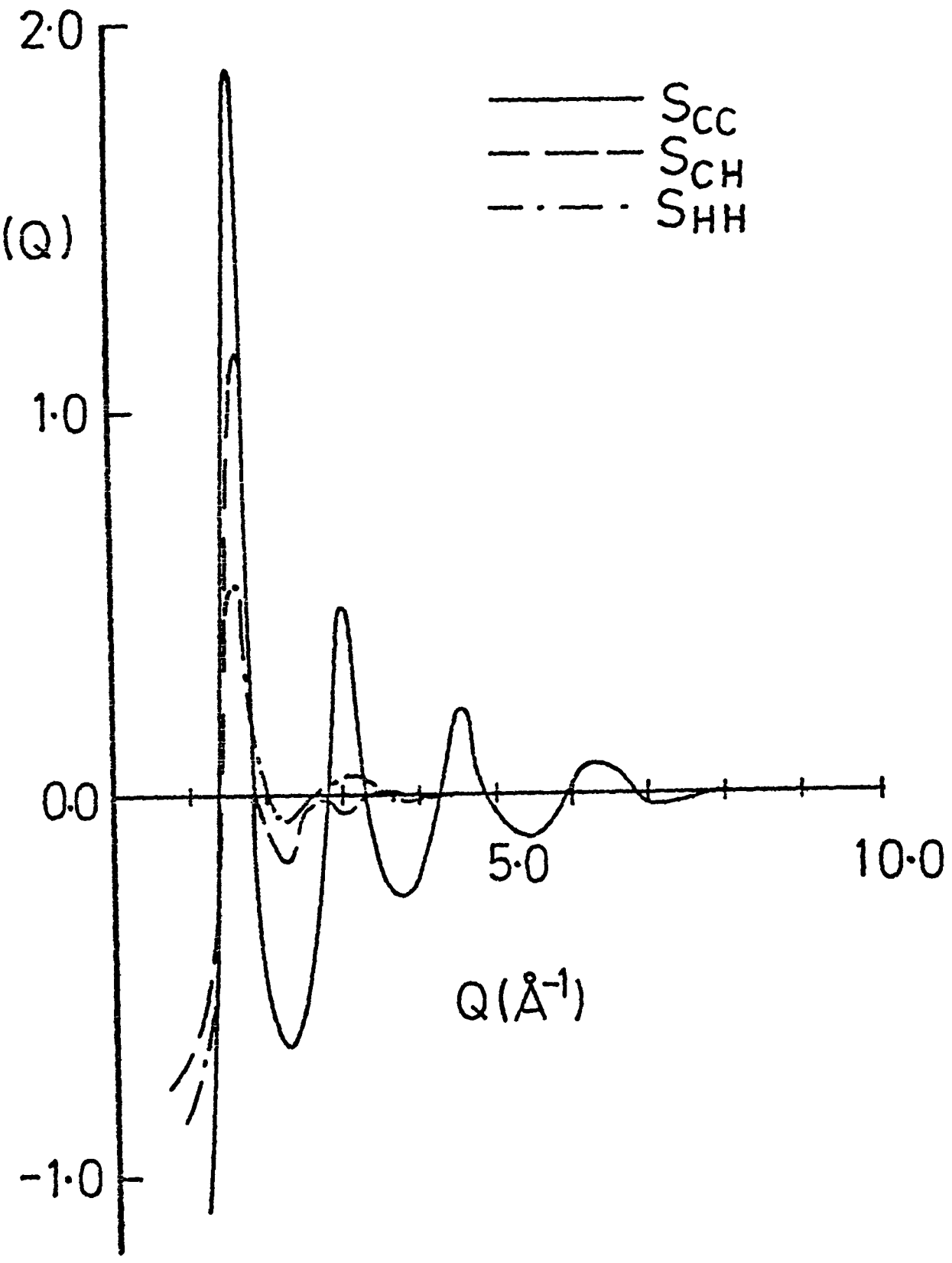


Figure 5.7 The "inter" site-site structure factors at $\theta = 0.77$, $T = 72.1K$ for the model described in the text. The carbon-hydrogen and hydrogen-hydrogen rapidly converge to zero while the carbon-carbon structure factor persists beyond 7 $\AA$



remain constant with decreasing coverage.

Two sets of experimental translational self-diffusion coefficients have been published for methane adsorbed on the basal plane of graphite; quasi-elastic neutron scattering of liquid methane on Papyex, (a partially oriented, recompressed, exfoliated graphite) (Coulomb et al., 1980), and pulsed field gradient NMR from methane adsorbed on Vulcan III, (a graphitized carbon black powder) (Tabony and Cosgrove, 1979). The results of each experiment are outside the experimental errors of one another, and the differences are probably due to the different homogeneities of the two surfaces studied and the time-scales of the experiments. The small differences in temperature would not account for the discrepancy. As expected at a high temperature (> 80K), in the hypercritical region, D increases with decreasing coverage. However, only neutron scattering results are reported at a lower temperature, 61.7K, and D is constant with decreasing coverage. Coulomb et al., postulate a coexisting liquid and gas at this temperature.

Two dimensional diffusion has previously been examined by Toxvaerd (1979) using a molecular dynamics simulation. He studied a system of 2-d Lennard-Jones particles, with and without a 2-d external field. The calculated diffusion coefficients from this model fluid at 90K and $\theta = 0.848$ are in good agreement with the experimental result (Coulomb et al., 1979) but the variation in D with temperature and coverage has not been examined. In this section we explore the variation of the translational diffusion coefficient over the relevant part of the phase diagram.

The diffusion coefficient is generally calculated in the simulation by one of two equivalent routes. The first involves the monitoring of the particle positions, $\underset{\sim}{r}_i$, as a function of time;

$$D_{2-d} = \lim_{t\to\infty} \frac{1}{4t} < \sum_{i=1}^{N} [\underset{\sim}{r}_i(t) - \underset{\sim}{r}_i(0)]^2 > \qquad (5.3.1)$$

A plot of the mean squared displacement against time should be linear at long times with a slope of 4D. The second method involves monitoring the particle velocities, v_i;

$$C^v(t) = \frac{<\underset{\sim}{v}_i(t) \cdot \underset{\sim}{v}_i(0)>}{<\underset{\sim}{v}_i^2(0)>} \qquad (5.3.2)$$

$$D = \lim_{t\to\infty} \int_0^t C^v(t)\, dt \qquad (5.3.3)$$

The diffusion coefficient is the Fourier transform of the velocity auto-correlation function, $C^v(t)$, at zero frequency. (5.3.3) is derived from (5.3.1) and (5.3.1) can be derived assuming the single particle probability function is Gaussian at all times (Hansen and McDonald, 1976). Equations (5.3.1) and (5.3.3) are applicable to a strictly 2-d system. Our system is not strictly 2 dimensional but the distribution of molecular heights for two liquids, (θ = 0.77, T = 72K and 90K), shown in Figure 5.6 indicates the motion is quite small, and (5.3.1) and (5.3.3) should be applicable.

An extensive study of the two dimensional diffusion coefficient (Alder and Wainwright, 1970) shows that D has a weak logarithmic dependence of N, the number of particles in the system. In a strictly 2-d system equation (5.3.3), $C^v(t)$, goes as t^{-1} at large t and the diffusion coefficient is infinite. The two studies of the LJ systems (Toxvaerd, 1979; Fehder et al., 1971) shows that the velocity auto-correlation function goes to zero in approximately 2 picoseconds and that the diffusion coefficients calculated from (5.3.1) and (5.3.3) agree within 3%. The anomalous behaviour of the velocity auto-correlation function does not seem to have a large effect in the region t < 10 ps at high densities.

In this study D is calculated using equation (5.3.1) and in a number of cases (5.3.3). Each of the simulations are run for 5,000 timesteps of 1.252×10^{-15} s. The velocity auto-correlation functions are calculated using every tenth timestep as a time origin and correlating the velocities over 1670 timesteps (2 ps). C^v_{xx}, C^v_{yy} and C^v_{zz} are calculated independently and are shown in Figure 5.8. The following prescriptions are used to calculate D,

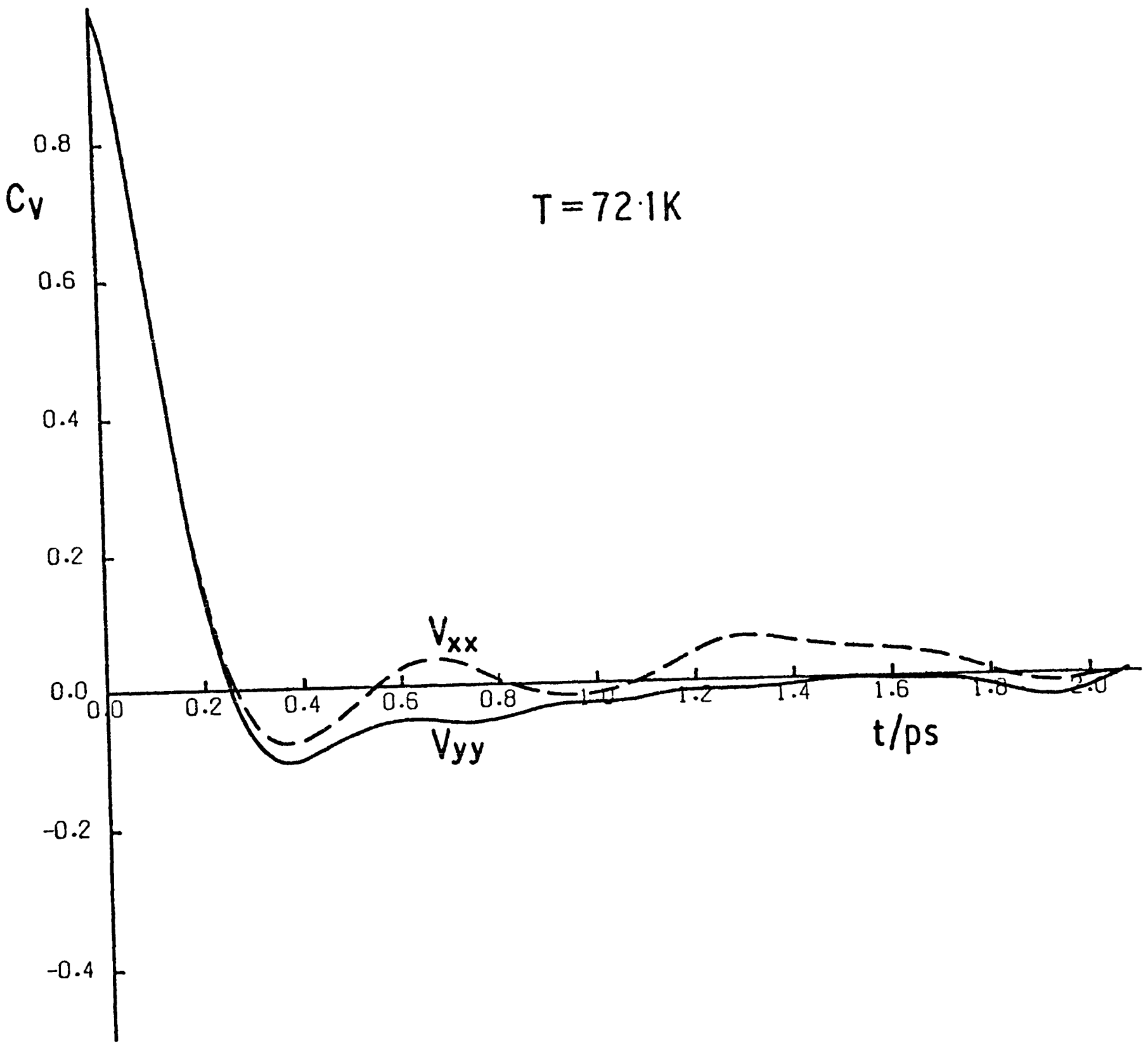
$$D^{\parallel} = \tfrac{1}{2} \int_0^\infty C_{xx}(t) + C_{yy}(t)\, dt \qquad (5.3.4)$$

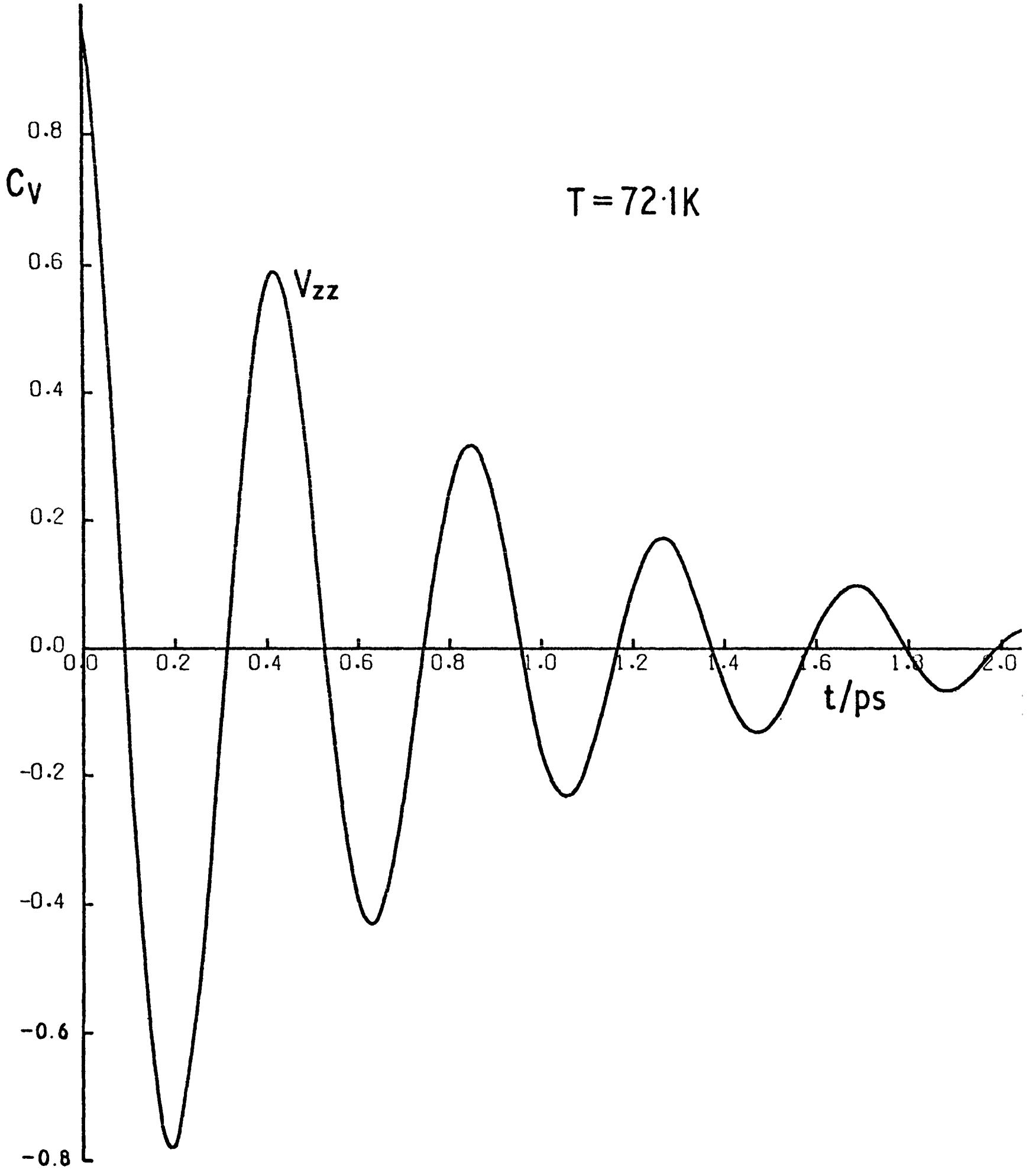
and

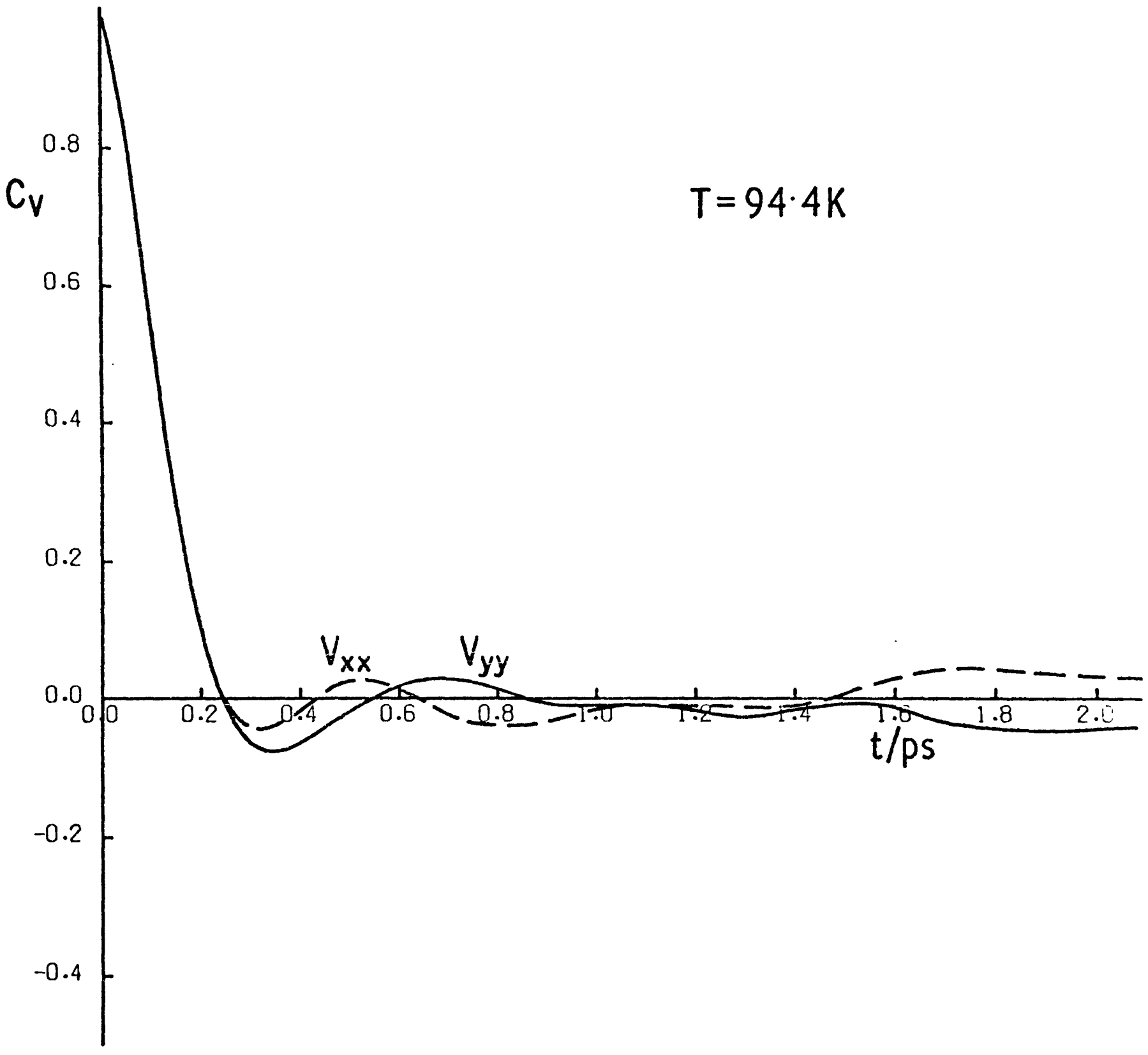
$$D^{\perp} = \int_0^\infty C_{zz}(t)\, dt \qquad (5.3.5)$$

For this system $D^{\perp}$ is approximately zero and $D^{\parallel}$ is equivalent to the 2-d diffusion coefficient.

Figure 5.8 The velocity auto-correlation functions of the centre of mass of the methane molecules at θ = 0.77, T = 72.1K and 94.4K.




C_V
T = 72·1K
V_{zz}
0.8
0.6
0.4
0.2
0.0
-0.2
-0.4
-0.6
-0.8
0.0
0.2
0.4
0.6
0.8
1.0
1.2
1.4
1.6
1.8
2.0
t/ps


0.8
C_V
0.6
0.4
0.2
0.0
-0.2
-0.4
0.0
0.2
0.4
0.6
0.8
1.0
1.2
1.4
1.6
1.8
2.0
t/ps
V_{xx}
V_{yy}
T=94·4K

During the simulation the particle positions are calculated using the rhombic boundary conditions. At the same time the real path of each particle, ignoring boundary conditions, is stored on tape. These real trajectories are used in (5.3.1) to calculate D. In Figure 5.9 the root-mean-squared displacement is plotted as a function of time and the slope of the line at large t is used to determine the diffusion coefficients given in table 5.2. The two techniques are compared in table 5.3. It is clear from table 5.3 that an error estimate of $\pm$ 1 x 10^{-5} cm^2 s^{-1} in our results should bracket the possible errors.

The calculated diffusion coefficients increase with increasing temperature and decreasing coverage. The temperature dependence is more marked at lower coverage. A comparison with experimental values at two temperatures is shown in Figure 5.10. It is clear that the simulation is in excellent agreement with neutron scattering results at 90K, but the simulation does not yield constant diffusion coefficients at 65K. The simulation is started from a small cluster surrounded by space and we can find no evidence for two phase behaviour.

A criticism which is often justifiably levelled against simulation studies of phase transitions (Frenkel and McTague, 1980) is that the system size is too small to study these effects without introducing artifacts. However the nature of the adsorption problem is different. For Vulcan and Papyex electron microscopy (Dash, 1975) reveals patches of exposed basal planes of graphite of length 50 Å and 200 Å respectively. A useful way of describing

Figure 5.9 The mean squared displacement $[r(t) - r(0)]^2$ v's time. At times > 1 ps the displacement is linearly proportional to time and the diffusion coefficient is measured from the slope of the curves at long time.

	θ	T/K
A	0.46	90.6
B	0.52	59.7
C	0.46	59.5
D	0.46	49.9
E	0.77	94.4
F	0.70	61.2
G	0.77	72.1
H	0.46	21.7

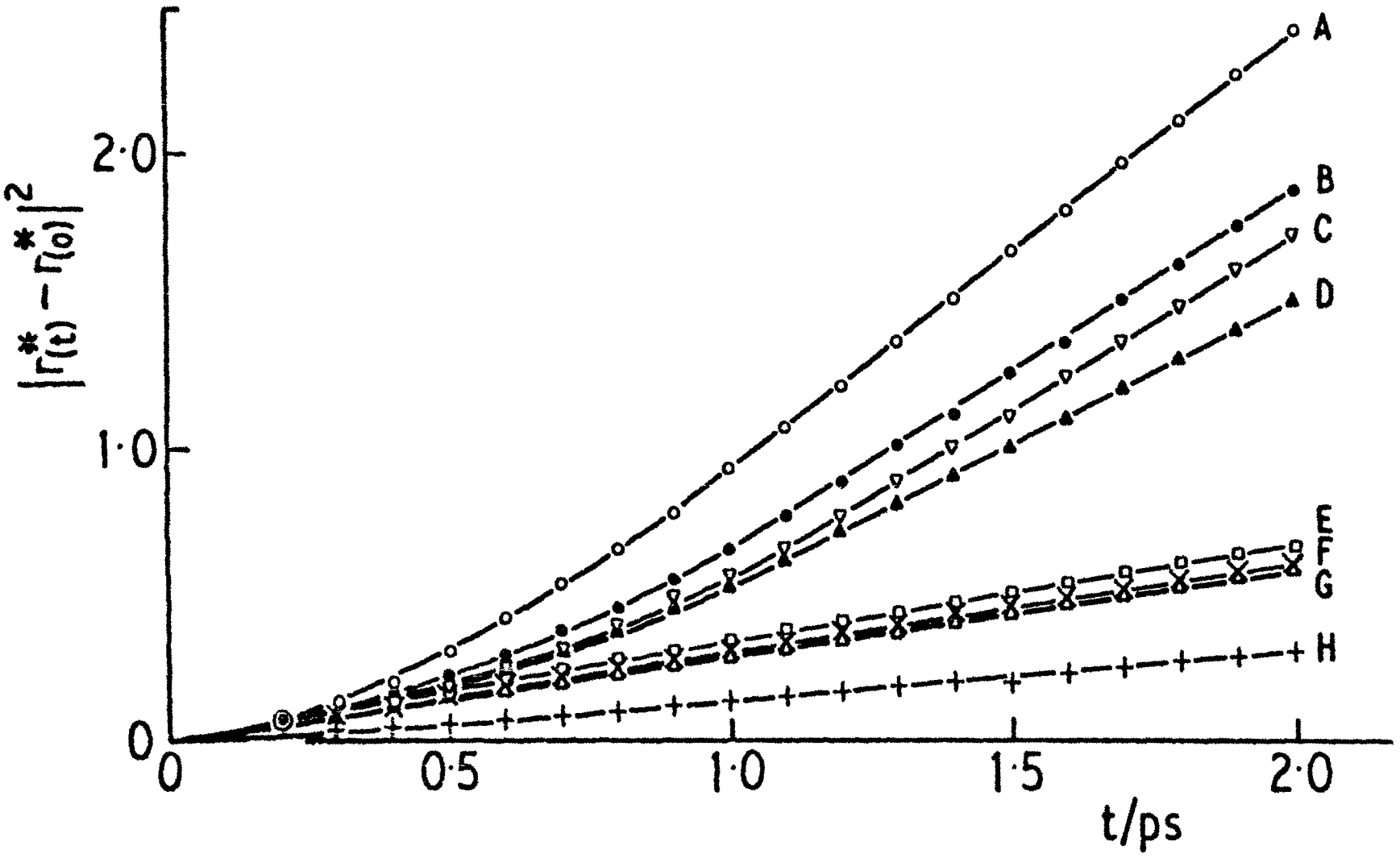

$|r^*_{(t)} - r^*_{(0)}|^2$
2·0
1·0
0
0
0·5
1·0
1·5
2·0
t/ps
A
B
C
D
E
F
G
H

Table 5.2

The diffusion coefficient as a function of temperature and coverage for adsorbed liquid methane above 56K.

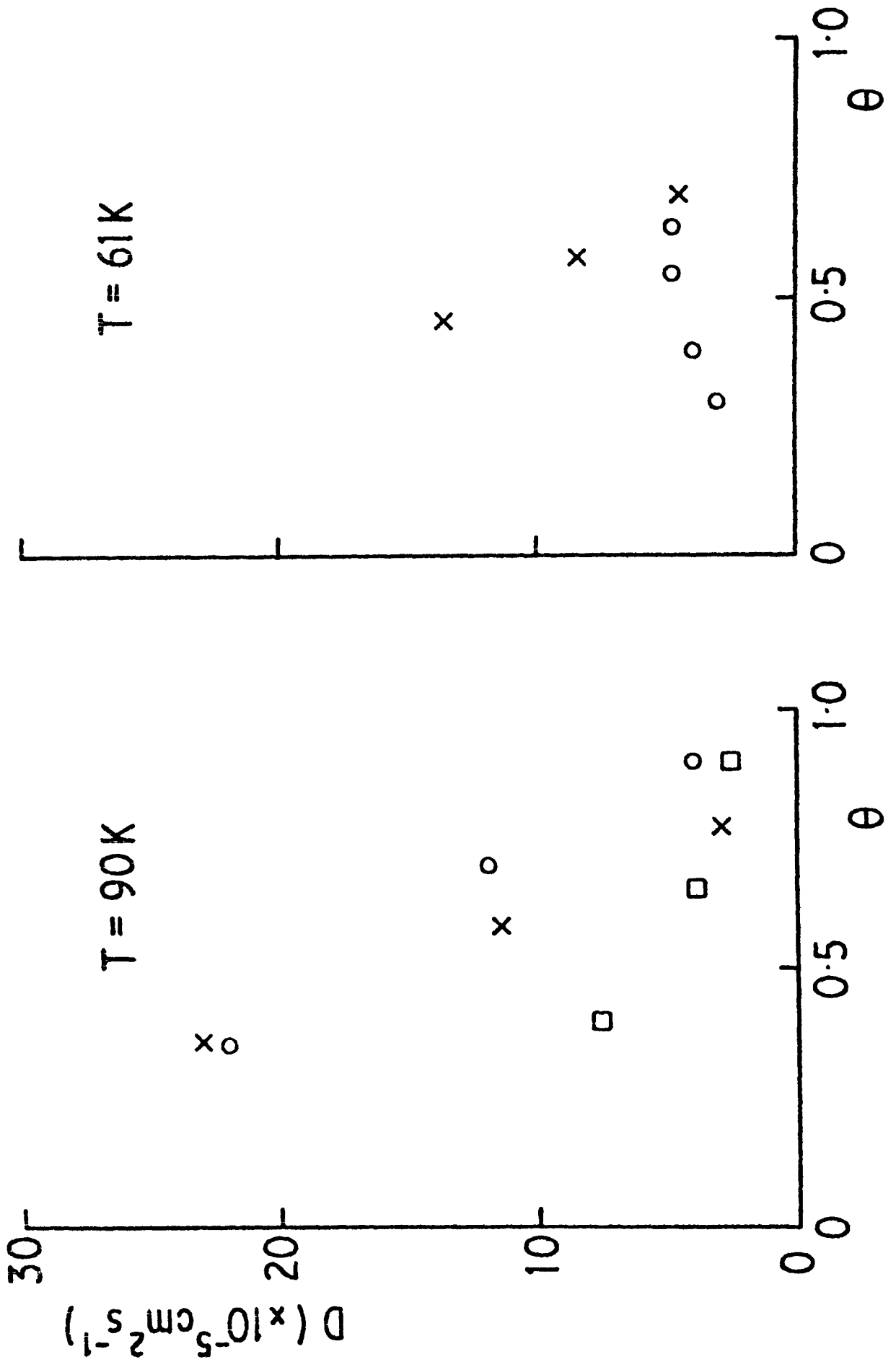
NP	θ	T/K	D x 10^{+9} $m^2 s^{-1}$
67	0.77	94.9	4.9
50	0.58	95.3	11.4
40	0.46	90.6	22.6
60	0.70	61.2	4.5
50	0.58	64.5	8.5
40	0.46	64.5	13.5
60	0.70	61.2	4.5
67	0.77	72.1	4.8
67	0.77	94.4	4.9
75	0.87	1.28	12.5

Table 5.3

A comparison of the in plane diffusion coefficient, D , calculated from equation (5.3.1) and equation (5.3.3) for a fluid $\theta = 0.77$.

T/K	D x $10^9/m^2s^{-1}$ eq. (3)	D x $10^9/m^2s^{-1}$ eq. (1)
72	3.7	4.4
90	4.7	4.8

Figure 5.10 The diffusion coefficients from the simulation, x, compared to experiment, Coulomb et al., O; Tabony and Cosgrove, □ . The experiment gives no indication of the magnitude of the errors. The errors in the values from the simulation are less than ± 1 x 10^{-5} cm^2 s^{-1}.



this system is to imagine a flat surface of about 2000 $\mathring{A}^2$ with an edge which could be a crystal defect or a second plane of graphite at some angle to the surface under consideration. Additional evidence for this picture comes from the coherence length of the methane on the surface, calculated from the leading edge of the diffraction peak. This quantity can be interpreted as the cluster size and for CD_4 on Graphoil it is below 200 $\mathring{A}$ (See Figure 1 of Vora et al., 1979). Adsorbed liquids are not infinite 2-d fluids and the system sizes under consideration are comparable to the system studied here; (the area of the box is approximately 1200 $\mathring{A}^2$, with additional periodic boxes).

The finite system size can explain the difference between N.M.R. and neutron scattering results. The neutrons measure D over times of picoseconds and distances less than 5 $\mathring{A}$, and this is clearly the diffusion of the liquid in the plane of the graphite. The N.M.R. measures D over distance of 10,000 $\mathring{A}$ and this diffusion must be associated with the crossing of zone boundaries.

The difference between the simulation and neutron scattering measurements at lower temperatures is more difficult to explain. The good agreement at high temperatures indicates that the diffusion coefficients are accurate down to coverages of 0.4. There are a number of possible explanations for the difference in the results. The real graphite surface unlike the simulation surface is not ideal and at low temperature the defects and inhomogeneities in the surface, within the zone boundary, may slow the diffusion of the methane molecules. The real graphite unlike the model is

not rigid and coupling of the surface phonons with the motion of the graphite may well influence in-plane diffusion. The analysis of neutron results assumes there is no broadening in the quasi-elastic neutron scattering due to rotational diffusion and that the diffusion is Fickian.

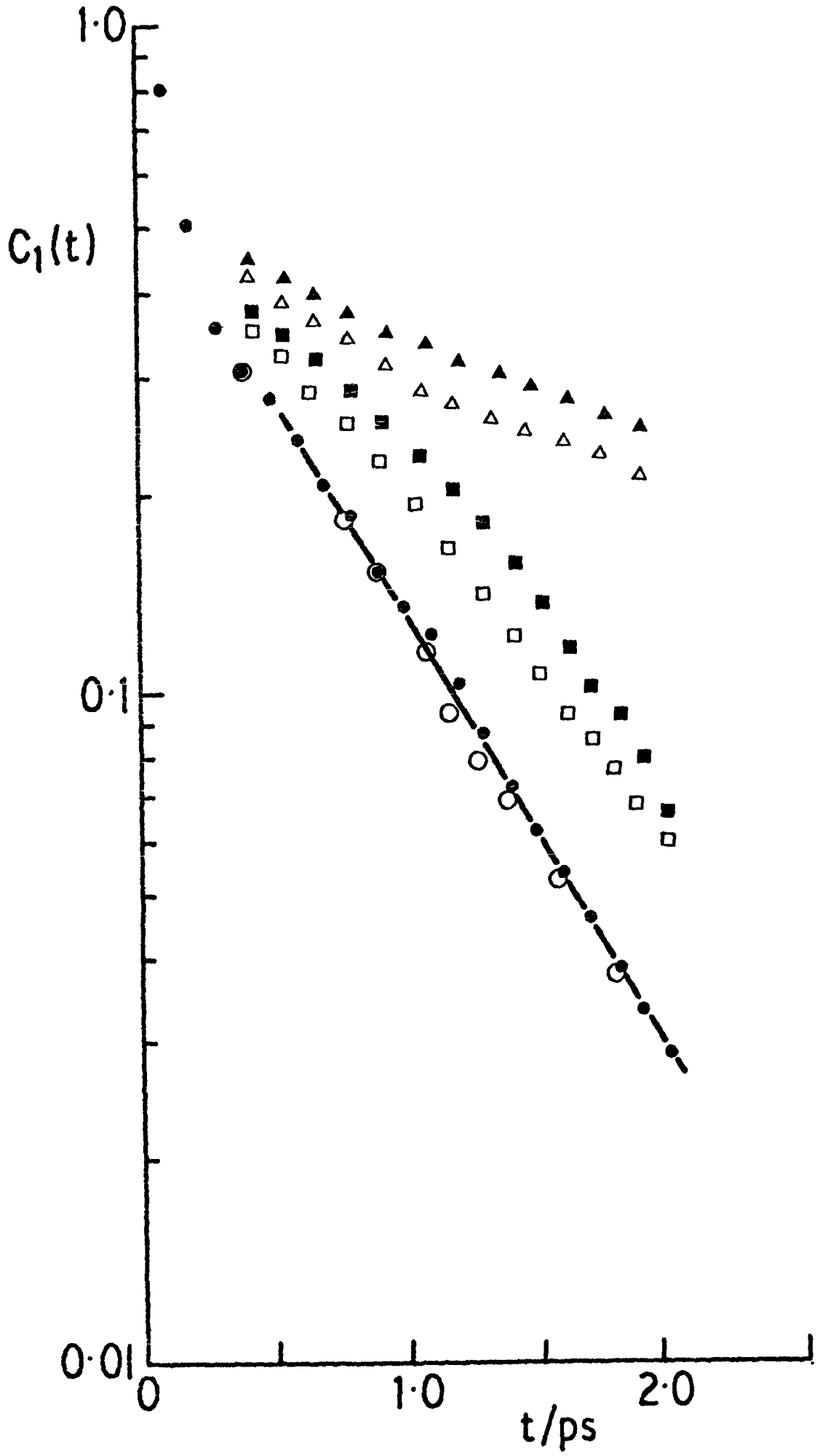
The first of these assumptions can be verified in the simulation by calculating the reorientational auto-correlation function,

$$C_\ell(t) = \langle P_\ell(\underset{\sim}{h}(t) \cdot \underset{\sim}{h}(0))\rangle \qquad (5.3.6)$$

where P_ℓ is the ℓ^{th} order Legendre polynomial and $\underset{\sim}{h}(t)$ is a unit vector in the body fixed system at time t. Since the methane is a symmetric top molecule any choice of a unit vector should give the same $C_\ell(t)$ if the molecule is rotating isotropically. $C_1^{\perp}(t)$ and $C_1^{\parallel}(t)$ are averaged for the adsorbed liquid at $\theta = 0.77$, $T = 94.4K$ and is shown in Figure 5.11. The molecule is rotating isotropically and at times greater than 0.5 ps $C_1(t)$ is approximately linear indicating some rotational diffusion. According to the Debye diffusion model (Singer et al., 1977)

$$\tau_1^{-1} = -\frac{d \log C_1(t)}{dt} = 2D_R/a^2 \qquad (5.3.7)$$

where D_R is the rotational diffusion coefficient and a is the radius of the molecule (4.091 Å for methane). The τ_1 reorientational time of the adsorbed methane calculated from



5.11 The reorientational auto-correlation functions plotted on a logarithmic scale. The slope of log $C_1(t)$ at long times is inversely proportional to the correlation time τ_1. The solid points are $C^{1}(t)$ and the hollow points are $C^{11}(t)$. The correlation functions reported here are ▲ θ = 0.52, T = 59K; ■ θ = 0.77, T = 72.1K and ● θ = 0.77, T = 90.4K.

Figure 3.10 is $0.67 \pm 0.05 \times 10^{-12}$ s.

In the limit of small Q, Sears (1966) shows that the quasi-elastic spectrum can be represented as a series of spherical Bessel functions $j_\ell(Qa)$. The first term is the Lorentzian from translational diffusion multiplied by the zero-order Bessel function. It is independent of the rotational diffusion. For small Q and for rapid rotation ($\tau_1 \simeq 0.5 \times 10^{-12}$ s) the higher order terms make broad, low-intensity contributions which effect the width of the main quasi-elastic peak. At a lower temperature of 72.1K the simulation shows that the reorientational motion is more anisotropic; $C_1^{\parallel}(t)$ reorients more rapidly than $C_1^{\perp}(t)$. The average value of τ_1 is approximately 1.2×10^{-12} s and the quasi-elastic spectrum should still be dominated by translation. As the temperature and coverage are further reduced the reorientation becomes even more anisotropic and the τ_1 reorientation time increases. At $\theta = 0.52$, $T = 59K$, τ_1 is approximately 2.2×10^{-12} s. It is not clear that $j_0(Qa)$ is the correct factor by which to modify the translational Lorentzian in the case of anisotropic orientation, and the question remains open whether the quasi-elastic spectrum will be significantly broadened by slow reorientation around the h_4 bond at moderately low temperatures $\simeq$ 60K. It is likely that the main peak in the spectrum does come from translation and the experiment does measure the translational self diffusion coefficient.

The experimental analysis also assumes that the self correlation

functions of methane adsorbed on graphite obeys Fick's equations of motion in 2-dimensions. The single particle distribution function, $g_s(r,t)$ is the solution of the diffusion equation

$$\frac{\partial\, g_s(r,t)}{\partial t} = D\,\nabla^2\, g_s(r,t) \qquad (5.3.8)$$

with the boundary condition $g_s(r,0) = \delta(r)$. In 2-dimensions

$$g_s(r,t) = \frac{\exp\,(-r^2/4D|t|)}{4\pi\, Dt} \qquad (5.3.9)$$

at all times $g_s(r,t)$ is normalized so that

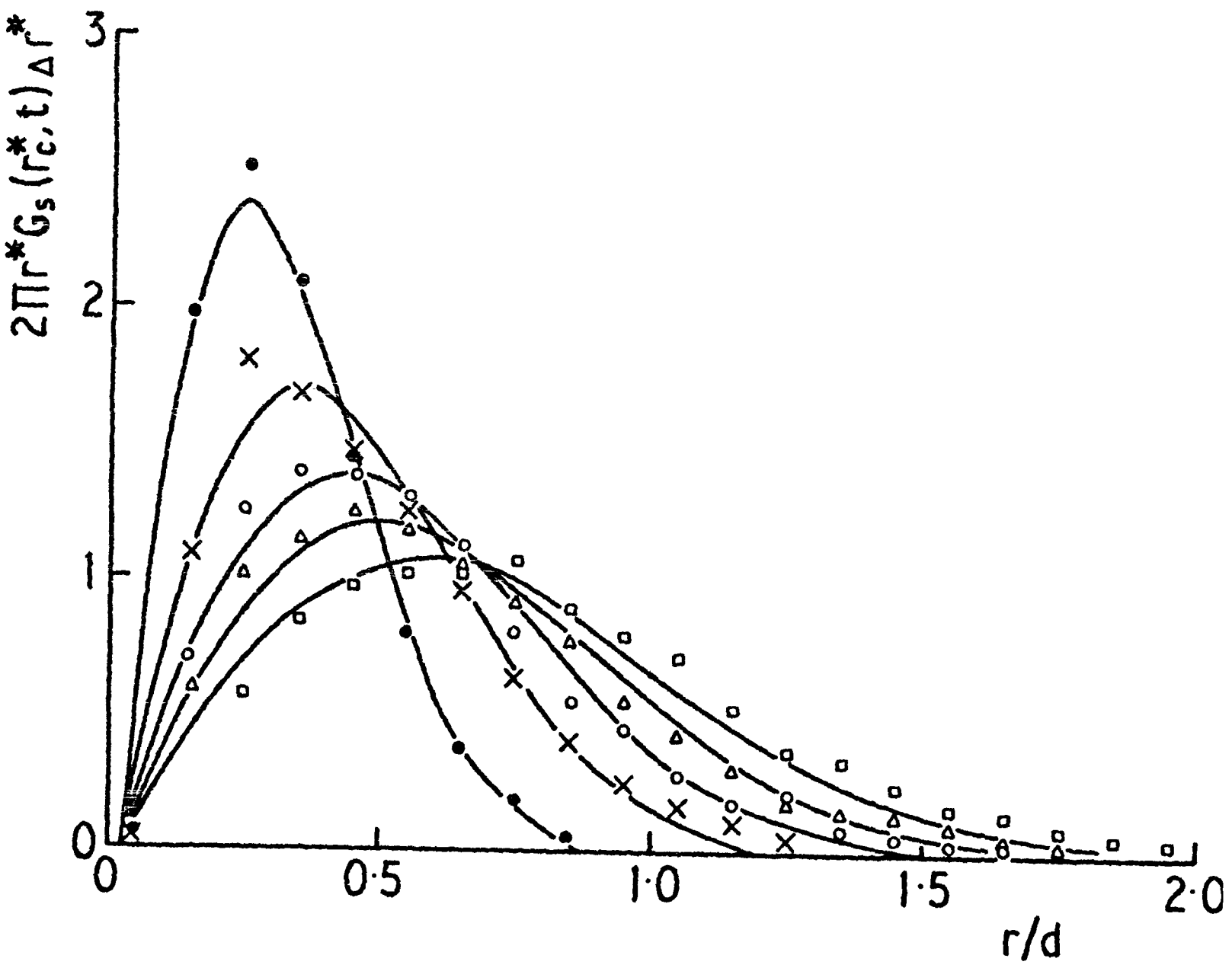
$$\int g_s(r,t)\, d\underset{\sim}{r} = 1. \qquad (5.3.10)$$

In the simulation we calculate the probability $f(r,t)$ that a molecule has diffused from its position at time zero and is in a shell Δr at a distance r from this original position. Using equation (5.3.9), $f(r,t)$ can also be written as

$$f(r,t) = \frac{r\,\Delta r\, \exp\,(-r^2/4D|t|)}{2Dt} \qquad (5.3.11)$$

and using the diffusion coefficients from table 5.2., the Fick equation above is compared to the simulation results in Figure 5.12. The agreement is excellent and improves at longer times towards the hydrodynamic limit, indicating that the diffusion is indeed Fickian in 2-dimensions.

Figure 5.12 The self part of the Van Hove function $G_s(r,t)$ at $\theta = 0.77$, $T = 94.4K$ v's distance at times of • 0.4 ps, x 0.8 ps, O 1.2 ps, Δ 1.6 ps and □ 2.0 ps. The solid lines are the solution to equation (3.5.11) at corresponding times to these simulation points.



The neutron scattering law for translation in 2-dimensions, $S(Q,\omega)$ is given by

$$S_s(Q,\omega) = \frac{1}{2\pi} \int_{-\infty}^{\infty} e^{i\omega t}\, dt \int_r g_s(\underset{\sim}{r},t)\, e^{-i\underset{\sim}{Q}.\underset{\sim}{r}} d\underset{\sim}{r} \qquad (5.3.11)$$

$$= \frac{1}{2\pi} \int_{-\infty}^{+\infty} (4\pi D\,|t|)^{-1}\, e^{i\omega t}\, dt\; 2\pi \int_0^{\infty} e^{-r^2/4\pi D|t|} J_0(Qr)\, r\, dr$$

$$= \frac{1}{\pi} \frac{DQ^2}{(DQ^2)^2 + \omega^2} \qquad (5.3.12)$$

Equation (5.3.12) modified by a zero-order spherical Bessel function is used to fit the experimental spectrum at a particular value of Q. In conclusion the simulation confirms the assumptions used to analyse the neutron scattering data.

5.4 The Spreading Pressure

Attempts have been made to measure the spreading pressure directly using a surface pressure gauge (Dash et al., 1976). The basic idea behind this gauge is that a surface film due to its 2-d pressure, will push on the edges of the adsorbent, causing it to expand. For a film adsorbed on a large area graphite sheet (formed by a large number of small crystals), a large amplification occurs and a measureable change in the length of the macroscopic piece of graphite is observed. Recent developments (Beaume et al., 1980) using an improved gauge have shown that not only expansion

but contraction may occur. However the quantity measured is not strictly ϕ (Halsey, 1978; Dash et al., 1978), because changes in the surface free energy caused by a film on the surface not only result from elastic stress but also from interactions between the adsorbate molecules and the internal degrees of freedom of the substrate. All the results reported so far must be interpreted using simplified models.

To obtain a statistical mechanical expression for the spreading pressure we use the approach in which the adsorbate is considered as a separate distinct phase formed on the surface of an inert solid. We assume that all the gas is adsorbed and the properties of this phase are given a subscript s; i.e V_s is the volume of adsorbate, A_s is the area of adsorbate and n_s is the number of adsorbed molecules. The spreading pressure is defined as

$$\phi = -\left(\frac{\partial A}{\partial A_s}\right)_{n_s,T,V_s} \qquad (5.4.1)$$

where A is the Helmholtz free energy of the adsorbate. Let us consider a block of material on the surface, (area A_s, volume V_s). As the surface area of the adsorbate changes the volume remains constant. Consider a box $\ell \times \ell \times (V_s/\ell^2)$ of the liquid, and let $\underset{\sim}{t}_i$ be a unit vector giving the position of the C.O.M. of molecule i in the box,

$$\begin{aligned} x_i &= \ell\, t_{ix} \\ y_i &= \ell\, t_{iy} \\ z_i &= V_s \ell^{-2} t_{iz} \end{aligned} \qquad (5.4.2)$$

The molecules i can take all positions in the volume by varying the scales t_{xi}, t_{yi}, t_{zi} between zero and one. The volume element, $d\underset{\sim}{r}_i = dx_i\, dy_i\, dz_i = V_s\, dt_{ix}\, dt_{iy}\, dt_{iz} = V_s\, d\underset{\sim}{t}_i$ and $\frac{d}{dA_s} = \frac{1}{2\ell}\frac{d}{d\ell}$.

The free energy in equation (5.4.1) can be expressed in terms of the partition function of the adsorbate and since the kinetic part of the partition function is independent of the surface area, ϕ can be expressed in terms of the configurational partition function, $Z_{n_s}(V_s,T)$,

$$\phi = - k_B T \frac{\partial}{\partial A_s} \left[\ell n\, Z_{n_s}(V_s,T)\right]_{n_s,T,V} \qquad (5.4.3)$$

where

$$Z_{n_s}(V_s,T) = \frac{1}{n_s!} \int \ldots \int \exp\left(-\beta U(\underset{\sim}{r}_1 \ldots \underset{\sim}{r}_n;\ \underset{\sim}{\omega}_1 \ldots \underset{\sim}{\omega}_n)\right) d\underset{\sim}{r}_n d\underset{\sim}{\omega}_n \qquad (5.4.4)$$

Rather than differentiate with respect to area, we differentiate with respect to the length of the surface A, and remove the ℓ dependence of the configurational integral using the transform above,

$$\phi = - \frac{k_B T}{2\ell} \frac{d}{d\ell} \left(\ell n\ \frac{1}{n_s!} V_s^{n_s} \int_0^1 \ldots \int_0^1 \exp\left[-\beta U(\underset{\sim}{r}_1 .. \underset{\sim}{r}_n; \underset{\sim}{\omega}_1 .. \underset{\sim}{\omega}_n)\right] d\underset{\sim}{t}_n d\underset{\sim}{\omega}_n \right. \qquad (5.4.5)$$

We can bring the differential inside the integral sign, assuming that as the box length changes the relative positions and orientations with respect to the sides of the box remain unchanged. Before differentiating we must consider the nature of the potential U. It is pairwise additive and of two parts,

$$U(\underset{\sim}{r}_1..r_n;\omega_1..\omega_n) = \sum_s \sum_i U_{is}(|\underset{\sim}{r}_i-\underset{\sim}{r}_s|,\omega_i)+\sum_{i,j>i}\sum U_{ij}(|\underset{\sim}{r}_i-\underset{\sim}{r}_j|,\underset{\sim}{\omega}_{ij}) \quad (5.4.6)$$ and

$$dU(r_i..r_n;\omega_1..\omega_n) = \sum_s \sum_i \frac{d\,U_{is}}{d(|\underset{\sim}{r}_i-\underset{\sim}{r}_s|)} \frac{d(|\underset{\sim}{r}_i-\underset{\sim}{r}_s|)}{d\ell} + \sum_{i,j>i}\sum \frac{dU_{ij}}{d(|\underset{\sim}{r}_i-\underset{\sim}{r}_j|)} \frac{d(|\underset{\sim}{r}_i-\underset{\sim}{r}_j|)}{d\ell} \quad (5.4.7)$$

All the differentials are carried out at constant relative orientation to the side of the box. Now

$$|\underset{\sim}{r}_i - \underset{\sim}{r}_s| = [(\ell t_{ix}-r_{sx})^2 + (\ell t_{iy}-r_{sy})^2 + (V_s\ell^{-2}t_{iz}-r_{sz})^2]^{\frac{1}{2}}$$

and

$$\frac{d|\underset{\sim}{r}_i-\underset{\sim}{r}_s|}{d\ell} = \frac{1}{2r_{is}}\left[2(\ell t_{ix}-r_{sx})t_{ix}+2(\ell t_{iy}-r_{sy})t_{iy}+2(V_s\ell^{-2}t_{iz}-r_{sz})-2V_s\ell^{-3}t_{iz}\right]$$

$$= \frac{1}{\ell r_{is}}\left[(x_i-r_{sx})x_i+(y_i-r_{sy})y_i-2(z_i-r_{sz})z_i\right]$$

$$= \frac{1}{\ell r_{is}}\left[(\underset{\sim}{r}_i \cdot \underset{\sim}{r}_i)-(\underset{\sim}{r}_i \cdot \underset{\sim}{r}_s)-3(z_i^2-z_iz_s)\right] \quad (5.4.8)$$

It is natural to take the z co-rodinate of the solid atoms as zero and

$$\frac{d(|\underset{\sim}{r}_i-\underset{\sim}{r}_s|)}{d\ell} = \underset{\sim}{r}_i \cdot \underset{\sim}{r}_i - \underset{\sim}{r}_i \cdot \underset{\sim}{r}_s - 3z_i^2 \qquad (5.4.9)$$

and similarly

$$\frac{d(|\underset{\sim}{r}_i-\underset{\sim}{r}_j|)}{d\ell} = \frac{r_{ij}^2 - 3z_{ij}^2}{\ell r_{ij}} \qquad (5.4.10)$$

The difference in the results stems from the fact that the surface atoms do not move during the scaling. Differentiating (5.4.5) and substituting (5.4.7), (5.4.9) and (5.4.10)

$$\phi = -\frac{k_B T}{2\ell}\ \frac{1}{n_s!}\ V_s^{n_s}\ \frac{\int_0^1 \cdots \int_0^1 \left[\sum_{is}\left(\frac{\underset{\sim}{r}_i\cdot\underset{\sim}{r}_i+\underset{\sim}{r}_i\cdot\underset{\sim}{r}_s-3z_i^2}{\ell r_{is}}\right)\frac{dU_{is}}{dr_{is}} + \sum\left(\frac{r_{ij}^2-3z_{ij}}{\ell r_{ij}}\right)\frac{dU_{ij}}{dr_{ij}}\right] e^{-\beta U}\, d\underset{\sim}{t}_n\, d\omega_n}{\frac{1}{n_s!}\ V_s^{n_s} \int_0^1 \cdots \int_0^1 e^{-\beta U}\ d\underset{\sim}{t}_n\ d\omega_n}$$

$$= \frac{1}{2A_s}\left\langle \sum_i \sum_s \frac{\underset{\sim}{r}_i\underset{\sim}{r}_i-\underset{\sim}{r}_i\underset{\sim}{r}_s-3z_i^2}{2r_{is}}\ \frac{dU_{is}(|\underset{\sim}{r}_i-\underset{\sim}{r}_s|,\omega_i)}{dr_{is}}\right.$$

$$\left. + \sum_i \sum_{j>i} \frac{r_{ij}^2-3z_{ij}^2}{2r_{ij}}\ \frac{dU_{ij}(|\underset{\sim}{r}_i-\underset{\sim}{r}_j|,\omega_i)}{dr_{ij}} \right\rangle \qquad (5.4.11)$$

An additional problem is created when a molecular liquid is involved. The differential of the potential must be broken up into the components of each site in the molecules, i.e.

$$\left(\frac{d\ U_{ij}(\underset{\sim}{r}_{ij},\omega_i,\omega_j)}{d\ r_{ij}}\right)_{\omega_i\omega_j} = \sum_{\alpha_i}\sum_{\beta_j}\left(\frac{\partial\ U_{\alpha\beta}(r_{\alpha\beta})}{\partial\ r_{ij}}\right)_{\omega_i\omega_j}$$

$$= \sum_{\alpha_i} \sum_{\beta_j} \left(\frac{d\, U_{\alpha\beta}(r_{\alpha\beta})}{d\, r_{\alpha\beta}} \frac{\partial\, r_{\alpha\beta}}{\partial\, r_{ij}} \right)_{\omega_i \omega_j} \qquad (5.4.12)$$

where there are α_i sites on molecule i and β_j sites on molecule j. Define $\underset{\sim}{r}_{\alpha\beta} = \underset{\sim}{r}_{ij} + \underset{\sim}{r}_{i\alpha} - \underset{\sim}{r}_{j\beta}$ and

$$\frac{\partial\, \underset{\sim}{r}_{\alpha\beta}}{\partial\, r_{ij}} = \frac{\partial\, \underset{\sim}{r}_{ij}}{\partial\, r_{ij}} = \frac{\underset{\sim}{r}_{ij}}{r_{ij}} = \hat{\underset{\sim}{r}}_{ij}$$

Now $\underset{\sim}{r}_{\alpha\beta} \cdot \underset{\sim}{r}_{\alpha\beta} = r_{\alpha\beta}^2$ and differentiating both sides gives

$$2\underset{\sim}{r}_{\alpha\beta} \frac{\partial\, \underset{\sim}{r}_{\alpha\beta}}{\partial\, r_{ij}} = 2r_{\alpha\beta} \frac{\partial\, r_{\alpha\beta}}{\partial\, r_{ij}}$$

or

$$\frac{\partial\, r_{\alpha\beta}}{\partial\, r_{ij}} = \frac{\underset{\sim}{r}_{\alpha\beta}}{r_{\alpha\beta}} \cdot \hat{\underset{\sim}{r}}_{ij}$$

$$= \hat{\underset{\sim}{r}}_{\alpha\beta} \cdot \hat{\underset{\sim}{r}}_{ij} \qquad (5.4.13)$$

Substituting (5.4.13) into (5.4.12) gives

$$\frac{d\, U_{ij}(\underset{\sim}{r}_{ij}, \omega_i, \omega_j)}{d\, r_{ij}} = \sum_{\alpha_i} \sum_{\beta_j} \frac{\partial\, U_{\alpha\beta}(r_{\alpha\beta})}{\partial\, r_{\alpha\beta}} \hat{\underset{\sim}{r}}_{\alpha\beta} \cdot \hat{\underset{\sim}{r}}_{ij} \qquad (5.4.14)$$

and similarly

$$\frac{d\, U_{is}(r_{is},\omega_i)}{d\, r_{is}} = \sum_{\alpha_i} \frac{\partial\, U_{\alpha}(r_{\alpha_i s})}{\partial\, r_{\alpha_i s}} \hat{\underset{\sim}{r}}_{\alpha_i s} \cdot \hat{\underset{\sim}{r}}_{is} \qquad (5.4.15)$$

Let us now consider the physical implications of above quantities. The first and seconds laws of thermodynamics are applicable to any volume element, a,

$$dU = T^a dS^a + W^a_{pV} + \sum_i \mu_i{}^a dn_i{}^a \qquad (5.4.16)$$

If a liquid is near a surface then the pV work in the volume element is not merely dependent on $dV^{(a)}$. The force per unit area normal to the surface, $p^{\perp,a}$, will be different to the force per unit area parallel to the surface $p^{\parallel,a}$. The pV work can be written as (Steele, 1974, Chap. 3)

$$W^a_{pV} = - p^{\parallel,a} z^a dA^a_s - p^{\perp,a} A^a_s\, dz^a \qquad (5.4.16)$$

The spreading pressure, $\phi^{(a)}$, for the element a is defined as

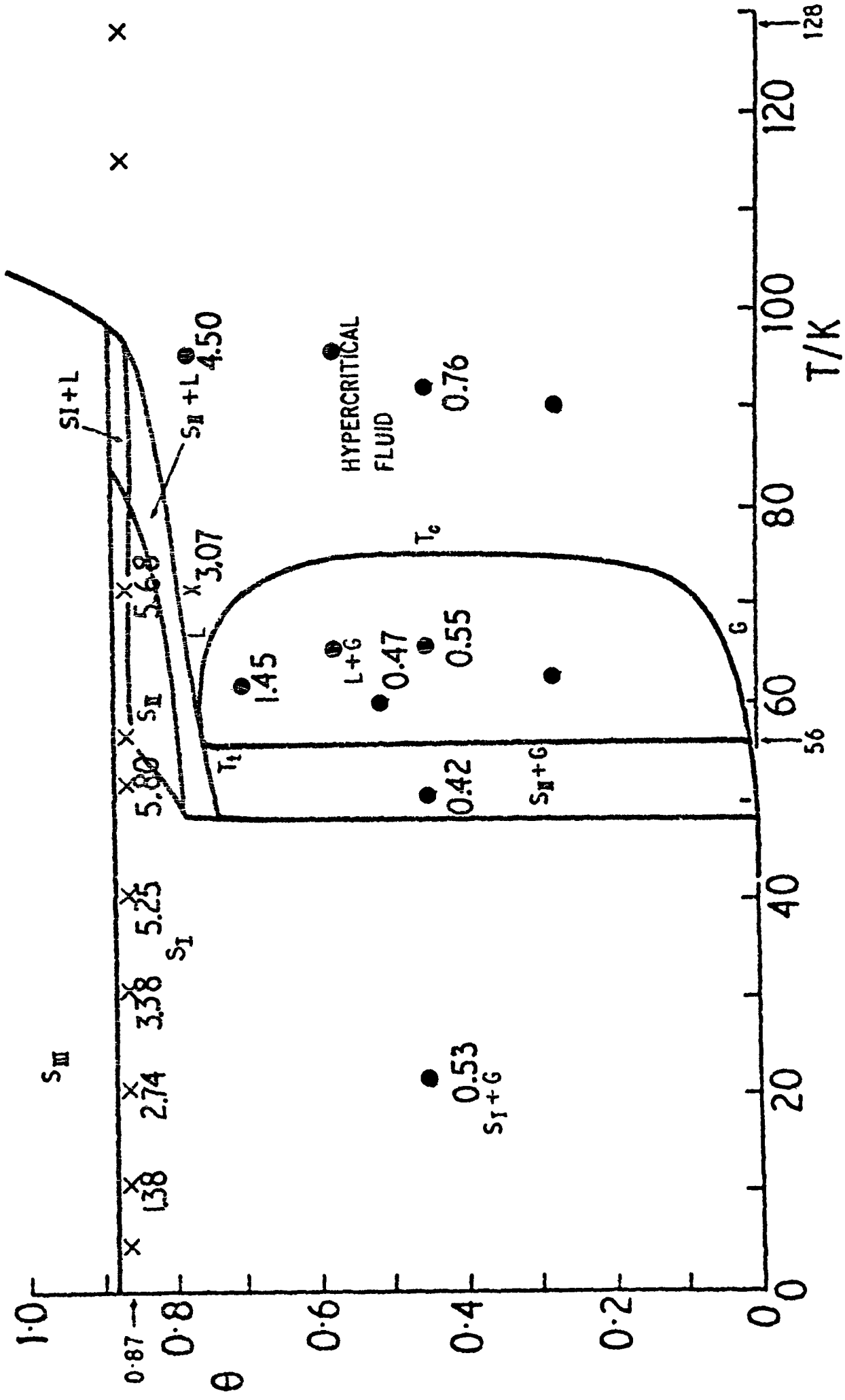
$$\phi^a = (p^{\parallel,a} - p^{\perp,a})\, z^a \quad , \qquad (5.4.17)$$

and in terms of this variable

$$W^a_{pV} = - \phi^a dA^a_s - p^a dV^a \quad , \qquad (5.4.18)$$

where $p^a \equiv p^{\perp,a}$. If the liquid is isotropic $p^{\parallel,a} = p^{\perp,a}$ and it is evident from (5.4.17) that the spreading pressure will be zero. If $p^{\parallel,a} > p^{\perp,a}$ the liquid will spread out and wet the surface; and the spreading pressure will be positive. It is not possible without further experimental results to deduce from this equation whether the liquid will spread isotropically across the surface or puddle to from liquid clusters plus gas. The spreading pressures for the simulated points are listed on the phase diagram in Figure 5.13. The general trend for the spreading pressure is to increase with increasing temperature and coverage. The isochores along $\theta = 0.87$ and $\theta = 0.46$ illustrate this trend: the drop in ϕ at $\theta = 0.87$, $T = 70K$ is probably due to a phase transition and not to the deviation of ϕ, which is less than 7% for all runs. A thorough investigation and interpretation of the statistical mechanical expression for the spreading pressure is not practicable until the pressure gauge experiments can yield accurate values of ϕ over a range of temperature and coverages. It is hoped that the results presented here will be a useful guide to the success of the model for methane adsorbed on graphite once the experiments have been performed.

Figure 5.13 The reduced spreading pressure ϕ^* over a range of simulation points (X,●) on the phase diagram.



CHAPTER 6

The Structure Factor of Benzene Adsorbed on Graphite

6.1 Introduction - Theory

If molecules in a system interact through pairwise-additive central forces, knowledge of the pair distribution function allows the calculation of thermodynamic properties such as the internal energy, pressure and compressibility. The Fourier transform of the pair distribution function is related to the experimental structure factor of the system. In this chapter we calculate the structure factor of a simple model for benzene adsorbed on graphite and compare the results to the recent neutron diffraction study of the same system (Meehan et al., 1980).

In our model we make the following assumptions that the benzene molecules lie flat on the surface at liquid densities and we represent the molecules by hard discs. This allows us to solve the Ornstein-Zernike (OZ) equation with the PY closure for this system to obtain the pair distribution function. In this model the adsorbed molecules must behave as 2-dimensional free rotors about their centre of mass, which has consequences for the functional form of the coherent structure factor.

In the remainder of this section we briefly discuss the relation between the distribution function and the experimental structure factor and we sketch the derivation of the OZ equation from

the Yvon equations (Yvon, 1958), and show how to obtain the pair distribution function using the PY closure with this integral equation. In section 2 the numerical method for solving the PY equation in 2-dimensions is discussed and in section 3 we describe the model for benzene and derive equations for its structure factor. In section 4 we compare the results of this model calculation to experiment.

The structure factor of a system can be measured directly through elastic scattering experiments, and is defined as the auto-correlation function of the Fourier components of the one-particle density (Hansen and McDonald, 1976), namely

$$S(k) = \frac{1}{N} \langle \rho_{\underset{\sim}{k}} \rho_{-\underset{\sim}{k}} \rangle \quad , \tag{6.1.1}$$

where

$$\rho_k = \int \exp\ (-i\ \underset{\sim}{k}.\underset{\sim}{r})\ \rho(\underset{\sim}{r})\ d\underset{\sim}{r} \quad . \tag{6.1.2}$$

We now define $\rho^{(1)}(r)$ in terms of the 3 dimensional Dirac delta function;

$$\rho^{(1)}(\underset{\sim}{r}) = \sum_{i=1}^{N} \delta\ (\underset{\sim}{r} - \underset{\sim}{r}_i) \tag{6.1.3}$$

The integral $\rho_{\underset{\sim}{k}}$ can now be rewritten as a sum,

$$\rho_{\underset{\sim}{k}} = \sum_{i=1}^{N} \exp\ (-i\ \underset{\sim}{k}.\underset{\sim}{r}_i) \quad , \tag{6.1.4}$$

and S(k) becomes

$$S(k) = \frac{1}{N} \sum_{i=1}^{N} \sum_{j=1}^{N} < \exp\ (-i\ \underset{\sim}{k}.\underset{\sim}{r}_i) \exp\ (i\ \underset{\sim}{k}.\underset{\sim}{r}_j)>$$

$$= 1 + \frac{1}{N} \sum_{i \neq j}^{N} \sum <\int\int \exp\ (-i\ \underset{\sim}{k}.(\underset{\sim}{r}-\underset{\sim}{r}'))\delta(\underset{\sim}{r}-\underset{\sim}{r}_i)\delta(\underset{\sim}{r}'-\underset{\sim}{r}_j)\ d\underset{\sim}{r}d\underset{\sim}{r}'$$

$$= 1 + \frac{1}{N} \frac{N(N-1)}{V^2} \int\int \exp\ (-i\ \underset{\sim}{k}.(\underset{\sim}{r}-\underset{\sim}{r}'))g(\underset{\sim}{r}-\underset{\sim}{r}')\ drdr'$$

$$= 1 + \rho \int \exp -i\ (\underset{\sim}{k}.\underset{\sim}{r})\ g(r)\ d\underset{\sim}{r} \tag{6.1.5}$$

The structure factor can be written in terms of h(r) = g(r) - 1, namely

$$S(k) = 1 + \rho \int \exp\ (-i\ \underset{\sim}{k}.\underset{\sim}{r})[h(r) + 1]\ d\underset{\sim}{r}$$

$$= 1 + \rho\ \hat{h}\ (k) + (2\pi)^3\ \rho\ \delta(\underset{\sim}{k}) \tag{6.1.6}$$

Yvon has shown that the linear response of a system to a static external field is related to the structure factor (Yvon, 1958). In establishing the link a new function, the direct correlation function appears in a natural way. The direct correlation function c(1,2) is defined as

$$c(1,2) = \frac{\delta \log [\rho^{(1)}(1)/z^*(1)]}{\delta \rho^{(1)}(2)} \qquad (6.1.7)$$

where δ is a functional derivative (Killingbeck and Cole, 1971), $\rho^{(1)}(1)$ is the singlet distribution function for particle (1), $\rho^{(1)}(2)$ for particle (2) and $z^*(i)$ is the activity of particle (i) in the presence of an external field ϕ_i; $z^*(i) = z \exp(-\beta \phi_i)$. (The notation has been contracted for ease of representation e.g. $\underset{\sim}{r}_3 \rightarrow 3$, $\underset{\sim}{r}_{12} \rightarrow 1,2$ etc.). The singlet distribution function is related to the grand canonical partition function (Ξ) (Nezbeda et al., 1980) by Yvon's first equation,

$$\rho^{(1)}(1) = \frac{\partial \log \Xi}{\partial \log z^*(1)} \qquad (6.1.8)$$

We now rearrange (6.1.7) to obtain a relation between z^* and $\rho^{(1)}$

$$\frac{\partial \log z^*(1)}{\partial \rho^{(1)}(2)} = -\frac{1}{\rho^{(1)}(1)} \frac{\partial \rho^{(1)}(1)}{\partial \rho^{(1)}(2)} - c(1,2)$$

$$= \frac{1}{\rho^{(1)}(1)} \delta(1,2) - c(1,2) \qquad (6.1.9)$$

This equation can be regarded as the inverse of Yvon's second equation (Nezbeda et al., 1980)

$$\frac{\partial\, \rho^{(1)}(1)}{\partial\, \log\, z^*(2)} = \frac{\partial^2\, \log\, \Xi}{\partial\, z^*(1)\, \partial\, z^*(2)}\; z^*(1)z^*(2)$$

$$= \rho^{(1)}\; \delta(1,2) + \rho^{(2)}(1,2) - \rho^{(1)}(1)\rho^{(1)}(2)\;,$$

$$= \rho^{(1)}\; \delta(1,2) + \rho^{(1)}(1)\rho^{(1)}(2)h(1,2) \qquad (6.1.10)$$

where $\rho^{(2)}(1,2)$ is the pair density given by

$$\rho^{(2)}(1,2) = \frac{1}{\Xi}\, z^*(1)z^*(2)\, \frac{\partial^2 \Xi}{\partial\, z^*(1)\, \partial\, z^*(2)}\;, \qquad (6.1.11)$$

and $\delta(1,2)$ is the '3-d' Dirac delta function in the contracted notation. We can relate (6.1.9) and (6.1.10) using a result of functional calculus (Killingbeck and Cole, 1971),

$$\delta(1,2) = \int \frac{\partial\, \log\, z^*(1)}{\partial\, \rho^{(1)}(3)}\; \frac{\partial\, \rho^{(1)}(3)}{\partial\, \log\, z^*(2)}\, d3 \qquad (6.1.12)$$

Substituting (6.1.10) and (6.1.11) into (6.1.12) we find that

$$h(1,2) = c(1,2) + \int \rho^{(1)}(3)\; c(1,3)\; h(2,3)\; d3$$

$$(6.1.13)$$

which is the fundamental equation linking the pair correlation function and the direct correlation function and is known as the

Ornstein-Zernike (OZ) relation (Ornstein and Zernike 1914). If we substitute for the pair correlation function h(2,3) in the integrand we get h(1,2) in terms of chains of direct correlation functions i.e.

$$h(1,2) = c(1,2) + \int \rho^{(1)}(3)\ c(1,3)\ c(2,3)\ d3\ +$$

$$\iint \rho^{(1)}(3)\ \rho^{(1)}(4)\ c(1,3)\ c(2,3)\ c(4,2)\ d3d4 + \ldots. \qquad (6.1.14)$$

We now consider some further functional expansions to derive a closure for the OZ equation. First we interpret the quantity $\rho g(0,1)$ as the local number density at point 1 from the origin when an external field, ϕ, is applied by a the particle at the origin (Percus, 1964). In other words g(0,1) predicts how much more likely a particle is to be at 1 when there is a particle at 0, compared to when there is no particle at 0. If there is no particle at the origin the local number density is ρ. The rigorous connection between the one-particle and two-particle densities (Percus, 1964) is

$$\rho^{(1)}(1|\phi) = \frac{1}{\rho}\ \rho^{(2)}\ (0,1|0)$$

$$= \rho\ g(0,1) \qquad (6.1.15)$$

It is possible to expand the variation of the one particle density in the presence of an external field in two ways. First we may expand in terms of the potential, i.e. the impulse on the system; or secondly in terms of the variation in density, i.e. the response of the system. In liquids potentials are rapidly varying at short distances so an expansion in $\Delta\phi$ cannot be expected to converge well. For short ranged potentials better results are obtained by expanding in powers of the smoothly varying response, $\Delta\rho^{(1)}$, (Hansen and McDonald, 1976). To first order we make a functional Taylor expansion of the one particle density,

$$\frac{\rho^{(1)}(1|\phi)}{z^*(1)} = \frac{\rho^{(1)}(1|0)}{z} + \int \frac{\partial}{\partial\, \rho^{(1)}(2|\phi)} \left(\frac{\rho^{(1)}(1|\phi)}{z^*(1)}\right)_{\phi=0} [\rho^{(1)}(2|\phi) - \rho^{(1)}(2|0)]\, d2$$

Substituting (6.1.15) gives

$$\frac{\rho^{(1)}(1|\phi)}{z^*(1)} = \frac{\rho}{z} + \int \left[\frac{\rho^{(1)}(1|\phi)}{z^*(1)} \frac{\partial}{\partial\, \rho^{(1)}(2|\phi)} \log\left(\frac{\rho^{(1)}(1|\phi)}{z^*(1)}\right)\right]_{\phi=0} \rho\, h(2,0)\, d2$$

and realizing the definition of c(1,2), equation (6.1.7), we obtain

$$\frac{\rho^{(1)}(1|\phi)}{z^*(1)} = \frac{\rho}{z} + \frac{\rho^2}{z} \int c(1,2)\, h(2,0)\, d2 \qquad (6.1.16)$$

Multiplying by z/ρ and using the relation

$$z^*(1) = z \exp[-\beta\, \phi(1)] = z \exp(-\beta\, U(0,1))$$

where U(0,1) represents the potential of the particle at the origin on particle 1, equation (6.1.16) becomes

$$g(0,1) = \exp(-\beta U(0,1))\,(1 + \rho \int c(0,2)\, h(2,1)\, d2)$$

$$= \exp(-\beta U(0,1))\,(g(0,1) - c(0,1)) \quad , \qquad (6.1.17)$$

where in taking the second step, use has been made of the OZ equation (6.1.13). Using this same relation we eliminate the direct correlation function to obtain an integral equation involving only g and U:

$$\exp(\beta U(1,2))\, g(1,2) = 1 + \rho \int [g(1,3)-1]\{1-\exp(\beta U(2,3)\}\, g(2,3)\, d23 \qquad (6.1.18)$$

This is the Percus-Yevick, PY equation obtained in a very different way by Percus and Yevick (1958). We now define a new function y(r) where

$$y(r) = \exp(\beta U(r))\, g(r). \qquad (6.1.19)$$

The density expansion of y(r) shows the function is continuous at $r = \sigma$ (Hansen and MacDonald, 1976). In terms of y(r) the direct correlation function in the PY approximation (from equation (6.1.17)) is

$$c(r) = y(r)\, f(r) \quad , \tag{6.1.20}$$

where f(r) is the Mayer-f function (exp ($-\beta$ U(r)) - 1).

In the case of hard discs (6.1.20) reduces to

$$\begin{aligned} c(r) &= -\, y(r), \quad r < \sigma \\ c(r) &= 0, \qquad r > \sigma \end{aligned} \tag{6.1.21}$$

In deriving the PY approximation we have been able to find a closure for the exact OZ equation. The PY approximation can be solved analytically for the special case of hard rods and hard spheres (Thiele, 1963; Werthiem 1963, 1964), and numerically for systems of even dimensionality.

6.2 Solution of the PY Approximation for Hard Discs

If we substitute the PY closure (equation (6.1.21)) into the OZ equation (6.1.13) we get,

$$y(r_{12})(e^{-\beta\, U\, 12} - 1) = c(r_{12}) + \rho \int c(r_{13})[y(r_{23})\, e^{-\beta\, U_{23}} - 1]\, d\underset{\sim}{r}_3$$

which is the PY equation for hard discs. Rearranging gives,

$$y(r_{12}) = 1 + \rho \int y(r_{13})[y(r_{23})\, \Delta\, (r_{23} - \sigma) - 1]\, d\underset{\sim}{r}_3 \quad , \tag{6.2.1}$$

where

$$\Delta = 1; \quad r_{23} - \sigma > 1,$$
$$\Delta = 0; \quad r_{23} - \sigma < 1. \qquad (6.2.2)$$

Rather than solve (6.2.1) and (6.2.2) directly we iterate the Fourier transform (Lado, 1971). Let us introduce two new variables H(r) and C(r) defined as

$$H(r) = y(r) - 1 \text{ , and}$$
$$C(r) = [1 + H(r)]\, f(r) \qquad (6.2.3)$$

Substituting (6.2.3) into (6.2.1) we arrive at a new expression for the PY equation, namely

$$H(r_{12}) = \rho \int [C(r_{13}) + H(r_{13})]\, C(r_{23})\, d\underset{\sim}{r}_3 \qquad (6.2.4)$$

Taking the Fourier transform of both sides of this equation, we obtain

$$\hat{H}(k) = \rho\, \hat{C}^2(k)/(1 - \rho\, \hat{C}(k)) \qquad (6.2.5)$$

The Fourier-Hankel transforms are defined as follows:

$$H(r) = \frac{1}{2\pi} \int_0^\infty \hat{H}(k)\, J_0(k.r)\, k\, d\, k,$$

and

$$\hat{H}(k) = 2\pi \int_0^{\infty} H(r)\, J_0(k.r)\, r\, dr; \qquad (6.2.6)$$

where $J_0(x)$ is the Bessel function of the first kind, and $C(r)$ and $\hat{C}(k)$ are defined in the same way. The integral equation (6.2.6) can be expanded as infinite series. Let $\lambda_1, \lambda_2 \ldots\ldots, \lambda_N$ be the first N positive roots of $J_0(x) = 0$, then we can replace equation (6.2.6) (Lado, 1971) by,

$$H(r_i) = \frac{1}{\pi R^2} \sum_{j=1}^{N-1} \hat{H}(k_j) \frac{J_0(k_j r_i)}{J_1^2(k_j R)}\ , \qquad (6.2.7)$$

$$\hat{H}(k_j) = \frac{4\pi}{K^2} \sum_{i=1}^{N-1} H(r_i) \frac{J_0(k_j r_i)}{J_1^2(K\, r_i)} \qquad (6.2.8)$$

where $r_i = \lambda_i/K$

$k_i = \lambda_i/R$,

and $R = r_N$, $K = k_N$ are the computational limits of r and k. The roots λ_i and hence the points r_i and k_i are equally spaced. Note that the choice of N and R is sufficient to determine all k_i and r_i, since $K = \lambda_N/R$.

Using the above transforms we solve the PY equation by the following method:

1) Store λ_i, $J_0(k_j r_i)$, $J_1(k_j R)$, $J_1(K\, r_i)$ in tables and make a simple estimate of $C(r)$; say

$C(R) = -R^2 + 2R - 2$; $r < \sigma$

$C(R) = 0$; $r < \sigma$

for $\rho\sigma^2 = 0.2$.

2) Calculate $\hat{C}(k)$ from $C(r)$ using equation (6.2.8) and $\hat{H}(k)$ from $\hat{C}(k)$ using equation (6.2.5).

3) Calculate $H(r)$ from $\hat{H}(k)$ using (6.2.7) and then test for convergence.

Convergence of the iterated solution is measured by the largest difference between successive iterates of H_j,

$$\Delta = \max_j |H_j^{new} - H_j^{old}| ,$$

which is required to be less than 10^{-4} in all cases. If convergence is achieved, we increase the density, and use the most recently calculated value of $C(r)$ and $H(r)$ as the initial guess for the new density point.

4) Calculate $C(r)$ from $H(r)$ using equation (6.2.3) and return to step (2).

Solutions of the integral equations were obtained for reduced densities ($\rho\sigma^2$) from 0.2 to 0.8 at intervals of 0.025. (The hard disc phase transition indicated by Monte Carlo (Wood, 1963) and Molecular Dynamics (Alder and Wainwright, 1962) sets in at $\rho\sigma^2 \sim 0.88$; at close packing $\rho\sigma^2 = 1.55$.) Up to $\rho\sigma^2 = 0.6$, a mean interval size $R/N = 0.025$ was maintained, with R_N being 5σ. In the upper density range, ($\rho\sigma^2 > 0.6$), R_N is increased to 10σ since $y(r)$ becomes long ranged at high densities, and R/N is increased to 0.05 to coincide with the increase in R_N.

We compare our results to those obtained by Lado (Lado, 1968) by calculating the virial equation of state,

$$\frac{\beta p}{\rho} = 1 + \tfrac{1}{2}\Pi\ \rho\sigma^2\ g(\sigma) \qquad (6.2.9)$$

Agreement between our work and Lado's is better than 0.1%.

6.3 Structure Factor for a Molecular Liquid in the Free Rotation Limit

The differential cross section for the elastic scattering of neutrons by a sample is given by (Gubbins et al., 1973),

$$\frac{d\sigma}{d\Omega} = \sum_i \sum_j \sum_\alpha \sum_\beta \langle \bar{b}_{i\alpha} \bar{b}_{j\beta} \exp\ (i\ \underset{\sim}{q}\cdot\underset{\sim}{r}_{i\alpha j\beta})\rangle \qquad (6.3.1)$$

where the sum is over all N molecules in the system and < > denotes an average over the grand canonical ensemble, nuclear isotope and spin states. $\bar{b}_{i\alpha}$ is the average scattering length of nucleus, α in molecule i and $\underset{\sim}{r}_{i\alpha j\beta} = \underset{\sim}{r}_{i\alpha} - \underset{\sim}{r}_{j\beta}$ is the site-site distance between two scattering centres. The differential cross section consists of two contributions, the coherent and incoherent parts,

$$\left(\frac{d\sigma}{d\Omega}\right)_{inc} = N \sum_\alpha \left[\overline{b_\alpha^2} - \bar{b}_\alpha^2\right] = N \sum_\alpha b_{inc,\alpha}^2 \ ; \qquad (6.3.2)$$

$$\left(\frac{d\sigma}{d\Omega}\right)_{coh} = \sum_{ij} \sum_{\alpha\beta} \bar{b}_\alpha \bar{b}_\beta \langle \exp\ (i\ \underset{\sim}{q}\cdot\underset{\sim}{r}_{i\alpha j\beta})\rangle$$

$$\equiv N \left[\sum_\alpha \bar{b}_\alpha\right]^2 S(\underset{\sim}{q}) \qquad (6.3.3)$$

We separate (6.3.3) into the i = j and i ≠ j terms namely,

$$S(q) = S_{intra}(q) + S_{inter}(q) \qquad (6.3.4)$$

where

$$S_{intra}(q) = \frac{1}{(\sum_{\alpha} \bar{b}_{\alpha})^2} \sum_{\alpha\beta} \bar{b}_{\alpha}\, \bar{b}_{\beta} < \exp\,[i\, \underset{\sim}{q}.(\underset{\sim}{r}_{Ci\alpha} - \underset{\sim}{r}_{Cj\beta})]> \,,$$

(6.3.5)

$$S_{inter}(q) = \frac{1}{N\,(\sum_{\alpha} \bar{b}_{\alpha})^2} \sum_{i\neq j} \sum_{\alpha\beta} \bar{b}_{\alpha}\, \bar{b}_{\beta} < \exp\,(i\, \underset{\sim}{q}.\underset{\sim}{R}_{ij})*$$

$$\exp\,[i\, \underset{\sim}{q}.(\underset{\sim}{r}_{Ci\alpha} - \underset{\sim}{r}_{Cj\beta})]>.$$

(6.3.6)

It is convenient to write $\underset{\sim}{r}_{i\alpha j\beta} = \underset{\sim}{R}_{ij} + (\underset{\sim}{r}_{Ci\alpha} - \underset{\sim}{r}_{Cj\beta})$ where $\underset{\sim}{R}_{ij}$ is the vector separating the molecular centres (defined arbitrarily) and $\underset{\sim}{r}_{Ci\alpha}$ is the vector from the centre of molecule i to the α nucleus of i.

We first consider a system where the substrate is orientated in parallel planes. Exfoliated x-y graphite (Thomas, 1981) is an example an orientated adsorbent. Attach $\underset{\sim}{q}$ without loss of

generality to the centre of a benzene molecule, that is $\underset{\sim}{q}$ makes some angles θ with the molecular fixed orientation of other molecules. Let the centre of mass of molecule i be located at the origin and θ_i be the angle between the space fixed orientation of the molecule and the y-axis, i.e.

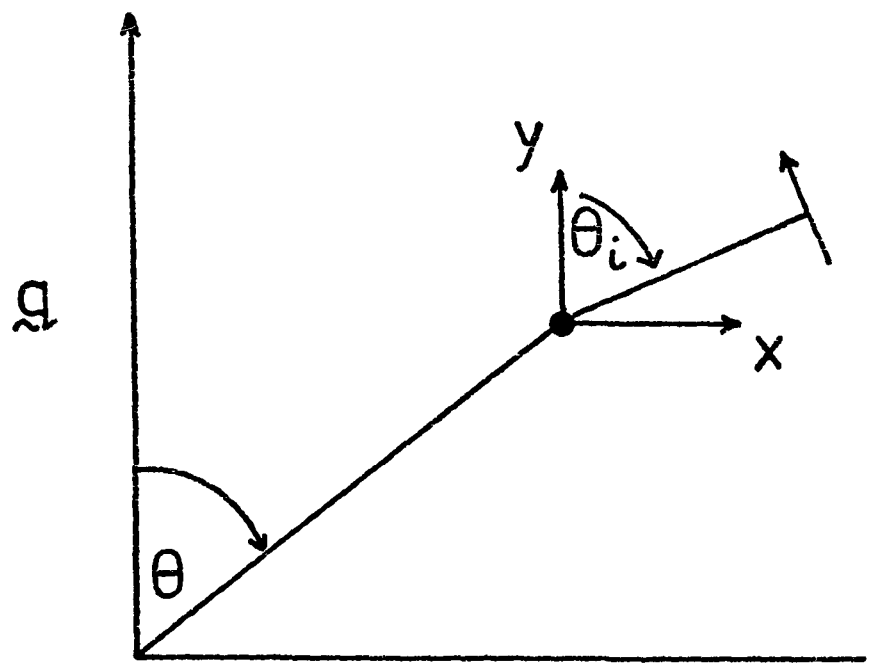


Figure 6.1 The Intra Axis System

S_{intra} is independent of the space fixed system since $\underset{\sim}{q}$ may be attached to the centre of molecule i, hence for θ_i constrained to a plane equation (6.3.5) becomes

$$S_{intra}(q) = \frac{1}{(\sum_{\alpha} \bar{b}_\alpha)^2} \int_0^{2\pi} \sum_{\alpha\beta} \bar{b}_\alpha \bar{b}_\beta \exp\,(i\, q\, r_{i\alpha\beta} \cos\theta_i)\, d\theta_i \qquad (6.3.7)$$

The standard integral gives (Lado, 1970)

$$S_{intra}(q) = \sum_{\alpha\beta} \frac{\bar{b}_\alpha \bar{b}_\beta J_0(q\, r_{\alpha\beta})}{(\sum_\alpha \bar{b}_\alpha)^2} \qquad (6.3.8)$$

Now consider the $i \neq j$ terms, S_{inter}. The average over S_{inter} can be written as

$$S_{inter}(q) =$$

$$\frac{N(N-1)}{N(\sum_\alpha \bar{b}_\alpha)^2} \frac{\int..\int \sum_{\alpha\beta} \bar{b}_\alpha \bar{b}_\beta \exp[i\, \underset{\sim}{q}.\underset{\sim}{r}_{i\alpha j\beta}] \exp(-\beta U(\underset{\sim}{r}_1..\underset{\sim}{r}_n, \theta_i..\theta_n) d\underset{\sim}{r}_1..d\underset{\sim}{r}_n\, d\theta_1..d_N}{\int..\int \exp -\beta U(\underset{\sim}{r}_1..\underset{\sim}{r}_n, \theta_1..\theta_n) d\underset{\sim}{r}_1..d\underset{\sim}{r}_N\, d\theta_1..d\theta_N}$$

(6.3.9)

where there are $N(N-1)$ equivalent terms in a homogeneous fluid.

Now

$$g(R_{12}, \theta_1, \theta_2) =$$

$$(2\pi)^2 \frac{N(N-1)}{\rho^2} \frac{\int...\int \exp\,(-\beta U(r_1...\theta_n) d\underset{\sim}{r}_3...d\underset{\sim}{\theta}_N}{\int...\int \exp\,(-\beta U(r_1..\theta_n) d\underset{\sim}{r}_1...d\underset{\sim}{\theta}_N}$$

(6.3.10)

and substituting into (6.3.9)

$$S_{inter} = \frac{\rho^2}{(2\pi)^2 (\sum_\alpha \bar{b}_\alpha)^2} \int_{r_1 r_2 \theta_1 \theta_2} \sum_{\alpha\beta} \bar{b}_\alpha \bar{b}_\beta \exp[i \underset{\sim}{q}.\underset{\sim}{r}_{i\alpha j\beta}] g(R_{12}\theta_1\theta_2) dr_1 dr_2 d\theta_1 d\theta_2$$

$$= \frac{\rho^2}{(2\pi)^2 (\sum_\alpha \bar{b}_\alpha)^2} \int_{R_{12}} \int_{\theta_1\theta_2} \sum_{\alpha\beta} \bar{b}_\alpha \bar{b}_\beta \exp(i \underset{\sim}{q}.\underset{\sim}{R}_{12}) \exp(i \underset{\sim}{q}.\underset{\sim}{r}_{Ci\alpha})$$

$$\exp(-i \underset{\sim}{q}.\underset{\sim}{r}_{Cj\beta}) g(R_{12}\theta_1\theta_2) R_{12} dR_{12} d\theta_1 d\theta_2 \quad , \qquad (6.3.11)$$

We simplify (6.3.11) by introducing

$\underset{\sim}{q}.\underset{\sim}{r}_{Ci\alpha} = q\, r_{Ci\alpha} \cos \theta^*_{i\alpha}$, and

$\underset{\sim}{q}.\underset{\sim}{r}_{Cj\beta} = q\, r_{Cj\beta} \cos \theta^*_{j\beta}$,

where $\theta^*_{i\alpha}$ is the body fixed molecular orientation, and $\underset{\sim}{r}_{Ci\alpha}$ is independent of R_{12} in the free rotor limit, i.e.

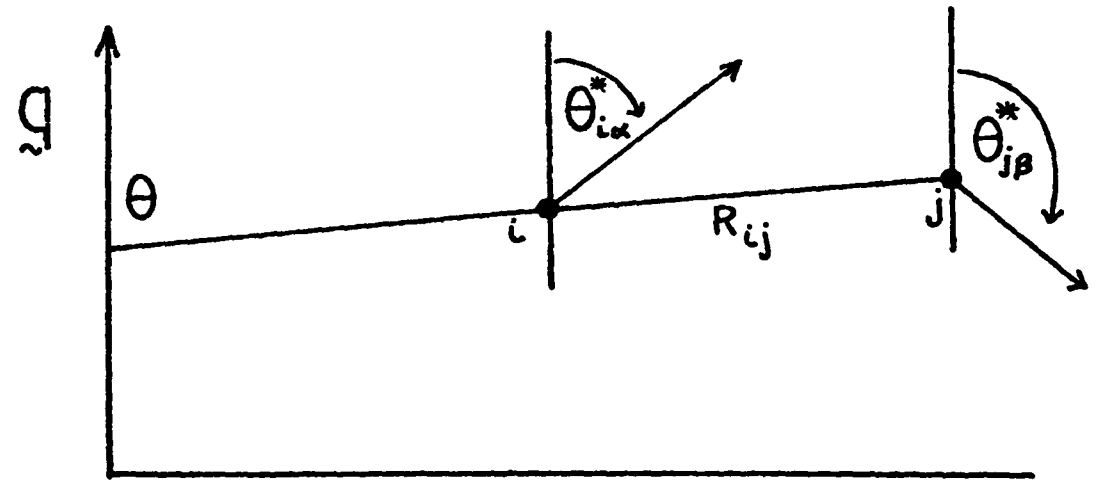


Figure 6.2 The Inter Axis System

We now integrate over the body fixed molecular orientation in equation (6.3.11), obtaining

$$S_{inter} = \frac{\rho\ 4\pi^2}{(2\pi)^2(\sum_\alpha \bar{b}_\alpha)} \left[\frac{1}{2\pi} \int_{\theta^*_{i=0}}^{2\pi} \sum_\alpha \bar{b}_\alpha \exp(i\ q\ r_{Ci\alpha} \cos\theta^*_{i\alpha}) d\theta^*_i \right]^2 *$$

$$\int \exp(i\ \underset{\sim}{q}.\underset{\sim}{R}_{12}) g(R_{12},\theta) R_{12} dR_{12} d\theta$$

$$= \frac{\rho}{(\sum_\alpha \bar{b}_\alpha)^2} \left[\sum_\alpha \bar{b}_\alpha J_0(q\ r_{C\alpha}) \right]^2 \int_{R_{12}=0}^{\infty} \int_{\theta=0}^{2\pi} \exp(i\ q\ R_{12} \cos\theta) g(R_{12}) R_{12} dR_{12} d\theta\ ,$$

(where $g(R_{12}) = g(R_{12},\theta)$),

$$= \frac{2\pi\ \rho}{(\sum_\alpha \bar{b}_\alpha)^2} \left[\sum_\alpha \bar{b}_\alpha J_0(q\ r_{C\alpha}) \right]^2 \int_{R_{12}=0}^{\infty} \left[\frac{1}{2\pi} \int_{\theta=0}^{2\pi} \exp(-i\ q\ R_{12} \cos\theta) d\theta \right] g(R_{12}) R_{12} dR_{12}$$

$$= 2\pi\rho \left[\frac{\sum_\alpha \bar{b}_\alpha J_0(q\ r_{C\alpha})}{\sum_\alpha \bar{b}_\alpha} \right]^2 \int_0^\infty g(R_{12}) J_0(R_{12} q) R_{12} dR_{12} \qquad (6.3.12)$$

Substituting (6.3.8) and (6.3.12) into (6.3.4) we obtain the total coherent structure factor,

$$S(q) = \sum_{\alpha\beta} \frac{\sum_\alpha \bar{b}_\alpha \bar{b}_\beta J_0(q\ r_{\alpha\beta})}{(\sum_\alpha \bar{b}_\alpha)^2} + 2\pi\rho \left[\frac{\sum_\alpha \bar{b}_\alpha J_0(q\ r_{C\alpha})}{\sum_\alpha \bar{b}_\alpha} \right]^2 \int_0^\infty g(R_{12}) J_0(q\ R_{12}) R_{12} dR_{12}$$

(6.3.13)

A model for benzene is required in order to calculate the structure factor. Our model is based on a previous model used in a simulation of liquid benzene (Evans and Watts, 1976). The Evans model is a site-site Lennard-Jones model from which we calculate the hard core diameter using the prescription (Hansen and McDonald, 1976),

$$\frac{d}{\sigma} = \int_0^{2^{1/6}} 1 - \exp\left[\frac{-1}{T^*}\left(4(r^{-12} - r^{-6}) + 1\right)\right] dr \quad . \qquad (6.3.21)$$

Table 6.1 lists the values of the hard disc diameter as a function of temperature. Since neutrons scatter from all nuclei we include twelve sites in the model. The carbon-carbon and carbon-hydrogen bond lengths are taken from a recent study of hydrocarbons (Murad et al., 1979). Figure 6.3 is a schematic representation of the model for benzene. The scattering lengths for carbon, hydrogen and deuterium are $\bar{b}_C = 0.665 \times 10^{-4}$, $\bar{b}_H = -0.374 \times 10^{-4}$ and $b_D = 0.667 \times 10^{-4}$ Å respectively (Bacon, 1977). The scattering experiments have used deuterated benzene as the adsorbate (Meehan et al., 1980) because it has a large coherent scattering cross section. As a result the model also uses the deuterium scattering length instead of hydrogen.

In the next section we discuss the results of the structure factor for the model described; using the PY hard disc solution for $g(R_{12})$. These results are compared to experiments performed

Table 6.1

The hard disc diameter as a function of temperature.

T(K)	σ_{LJ}(Å)	d/σ	σ_{HD}(Å)
100	7.0	1.01	7.07
150	7.0	0.992	6.94
200	7.6	0.985	6.89

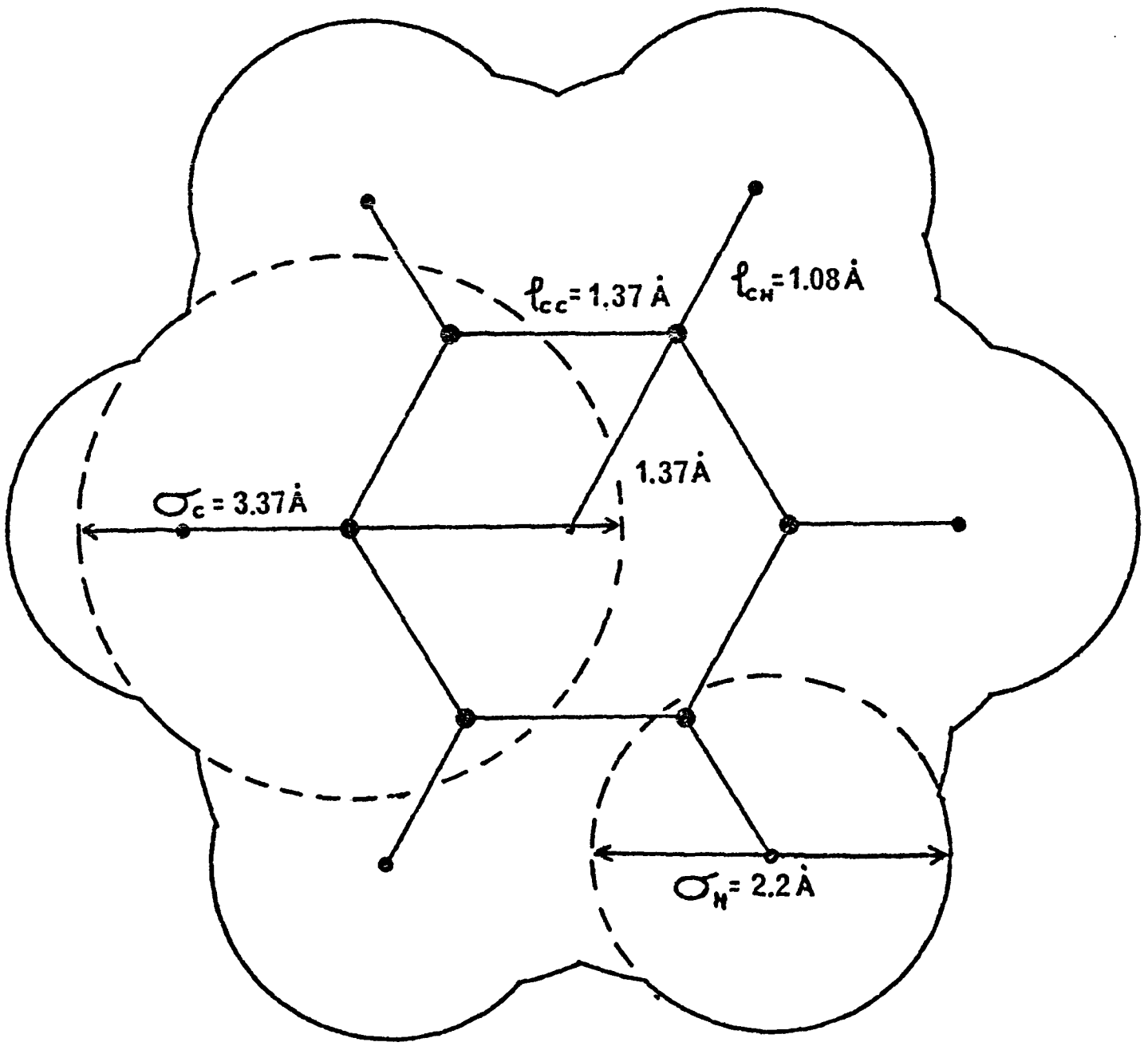


Figure 6.3 A schematic representation of the model for benzene. The dotted lines represent σ_C and σ_H. The hard sphere diameter, diameter not shown, is 6.92 Å.

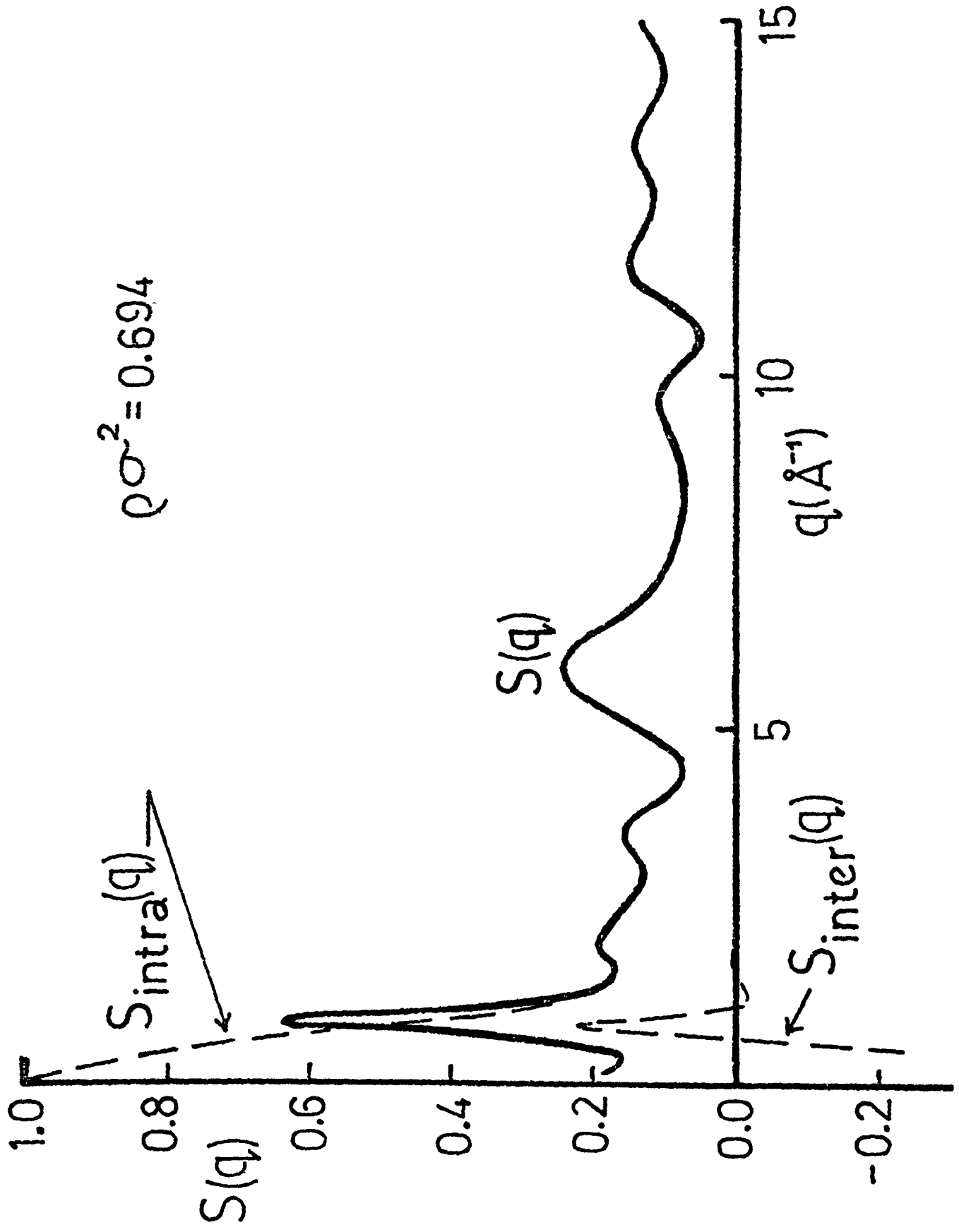
on a partially oriented adsorbent.

6.4 Results and Discussion

Equation (6.3.13) is solved numerically over a large range of q ($0 < q < 25$ Å^{-1}). The upper limit of the integral over R_{12} is truncated at the maximum value of R for which we have calculated g(R). At densities of $\rho\sigma^2 < 6$; $R_{max} = 5\sigma$ and for $\rho\sigma^2 > 0.6$; $R_{max} = 10\sigma$. The Bessel functions are calculated from standard NAG library routines. A listing of the programs PY, PYEX and SQ are given in the appendix to the thesis.

The structure factor is determined at four densities in the liquid range; $\rho\sigma^2 = 0.479$, 0.544, 0.694 and 0.760. These correspond to coverages of 100, 88, 69 and 63 Å^2/molecule. The onset of the liquid/solid phase transition for hard discs is at $\rho\sigma^2 \simeq 0.88$ and close packing is at $\rho\sigma^2 = 1.155$ (Lado, 1968). Figure 6.4 is a plot of $S_{intra}(k)$, $S_{inter}(k)$ and S(k) at $\rho d^2 = 0.694$. We observe S(k) is predominately affected by $S_{inter}(k)$ at low q. This is caused by the fundamental long range frequency in g(r). As q is increased the structure factor tends to $S_{intra}(k = \infty)$. In this region we observe the frequencies at small r, which result from intra molecular scattering. The first peak in S(k) describes the long range periodic behaviour in the liquid; for a crystal the first peak S(k) is equivalent to the reciprocal lattice spacing (Guinier, 1963). As we increase in density we expect to see a shift in the first

Figure 6.4 The structure factor of benzene adsorbed on graphite calculated from equation (6.3.13). At small q, S_{inter} dominates the shape of the structure factor while at large q, S_{intra} is the dominant contributor to the total structure factor.



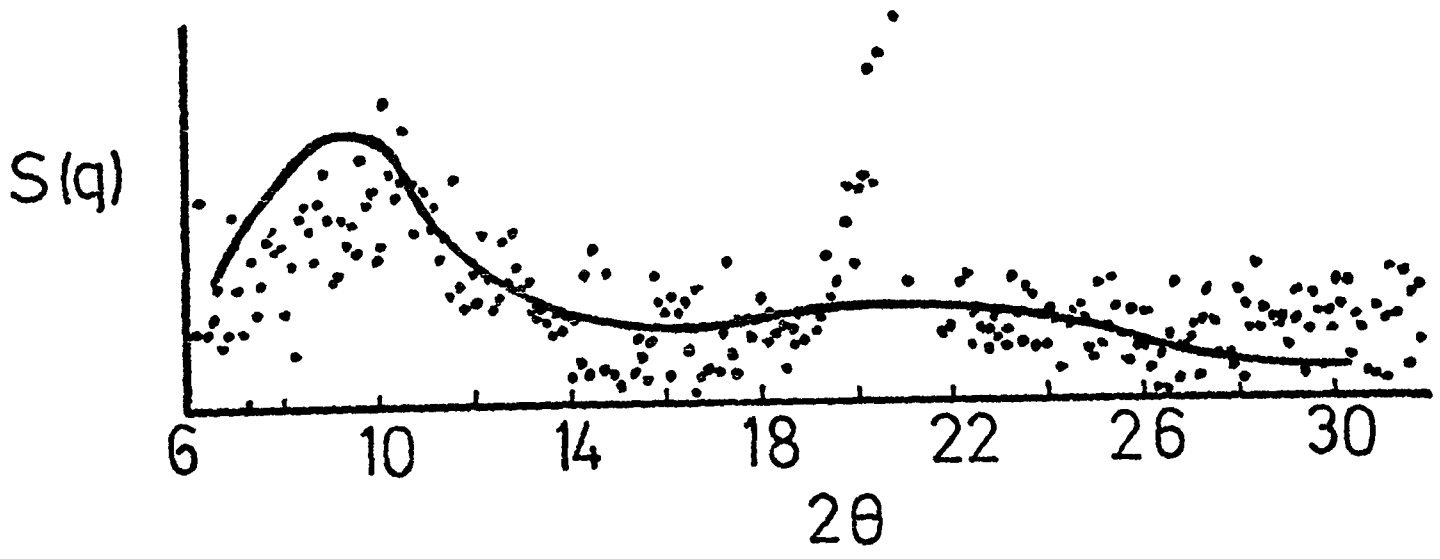
peak to larger q; i.e. the molecules come in closer contact with each other more often at high density. ~~Table 6.2 compares the shift in the first peak with density.~~

At present we can only compare our model calculations with one experimental result at a density of 63 $\mathring{A}^2$/molecule ($\rho\sigma^2$= 0.760) at 170K (Mathews and Thomas, 1980). In this system the substrate is exfoliated graphite, papyex. This substrate is only partially oriented, and the deviation from the plane parallel to $\underset{\sim}{q}$ is estimated to have a Gaussian distribution with a peak half height of $\approx \frac{\pi}{6}$ (Rayment, 1981). Figure 6.5 is a plot of S(q) superimposed on the experimental data. We have changed the scale of the x axis from q to the scattering angle θ. q is related to θ by

$$q = \frac{4\pi}{\lambda} \sin\theta \qquad (6.4.1)$$

where λ is the momentum of the incoming neutron,=1.22 $\mathring{A}$ (Mathews and Thomas, 1980). Agreement with experiment is quite good. The difference in shift between model and experiment can be attributed to two effects. First the substrate in the experiment is not totally oriented in two dimensions and second at the temperature studied it is unlikely the benzene molecules are lying absolutely flat on the surface. If the molecules are slightly tilted, closer packing is possible and therefore we would see a shift in θ to the right. However scattering studies of benzene adsorbed on Vulcan II (Meehan, et al., 1980), a powdered substrate, indicates the molecules do not rock more than 20^{o}.

Figure 6.5 Comparison of theory and experiment at $\rho\sigma^2 = 0.760$. The points are from the coherent neutron scattering experiment (Thomas and Mathews, 1980) at 170K. The large spike at $2\theta = 20^{o}$ is primarily from the background scattering from the substrate. The solid line is calculated from equation (6.3.13).



We have further investigated extensions of the model for the structure factor in 2 dimensions to systems of partially oriented substrates and randomly oriented powders. However we cannot show any rigorous connection between the local 2-d distribution function and a quasi-3d average over the orientations of the substrate. Until an experiment using an almost completely oriented substrate (for example graphite x-y) is performed, we are unable to quantitatively compare our model results with experiment.

CHAPTER 7

Summary

This thesis describes a number of studies of the interfacial-region and in particular, emphasis has been placed on the adsorption of gases onto solid surfaces. In Chapter 2 the Monte-Carlo method is developed to simulate a two component mixture of penetrable spheres governed by the potential

$$\begin{aligned} U_{\alpha\alpha},\ U_{\beta\beta} &= 0; && 0 < r < \infty, \\ U_{\alpha\beta} &= \infty; && 0 < r < \sigma_{\alpha\beta}, \\ U_{\alpha\beta} &= 0; && \sigma_{\alpha\beta} \leq r < \infty \ . \end{aligned} \qquad (7.1)$$

The equation of state is calculated in the one-phase region and used as a test for two virial expansions (Rowlinson, 1980). The simulation shows that these expansions predict the equation of state accurately in the one phase region. A simulation is also performed at high densities where the system separates into two phases. A density profile of the gas liquid surface is calculated and compared to analytic profiles obtained in the mean-field approximation. The mean-field profiles are too narrow by about 30%. In order to obtain one bulk liquid and one bulk gas region hard walls are introduced at the top and bottom of the box. In the absence of external potentials the liquid separates into randomly distributed droplets. The hard wall introduces a layering

effect in the liquid close to the wall and the mean field theory can be suitably extended to reproduce the simulation result.

In Chapter 3 a model for methane adsorbed on graphite is proposed. This system is chosen to study the adsorption problem because it exhibits a rich variety of phase behaviour at temperatures below 100K and there is an abundance of experimental data with which to compare the model results. It is necessary to introduce a number of simplifying assumptions in this work. The surface is assumed to be perfectly smooth and rigid. These two constraints could be relaxed by allowing the carbon sites in the first few layers of the graphite to move under the influence of other such sites, the adsorbate and the remainder of the bulk solid. A more difficult assumption to justify and correct is that quantum effects can be neglected. At low temperatures these can be important for such a light molecule as methane. Their effect on the equilibrium properties such as isosteric enthalpy can be included through the quantum correction to the partition function (Powles and Rickayzen, 1979). However the dynamical quantum effects could only be included by abandoning the classical equations of motion and solving the time dependent Schrödinger equation for the system. This approach seems unlikely to succeed and instead we have constructed an effective pairwise potential, which when used classically will reproduce the experimentally observable properties of the methane-graphite system. The de Broglie thermal wave length of methane at 30K is 0.79 Å, and the ratio of the wavelength to the lattice spacing in the S_I solid is 0.19. This quantity should be much

less than unity for a useful classical treatment and has values of 0.11 for liquid nitrogen and 0.08 for liquid argon at their respective triple points. Thus our potential, although purely classical, gives the experimentally observed rotational barriers. These rotations must, in part, be caused by quantum mechanical tunnelling and our potential is therefore "effectively" quantum mechanical.

The isosteric enthalpy is predicted by averaging the configurational energy during a molecular dynamics simulation of a single methane molecule. This quantity is within experimental error over the temperature range 110 - 150K. The surface second virial coefficients are calculated using a non-product integrating algorithm and with a predicted surface area of 10.5 $m^2\ g^{-1}$ of graphite, the virial coefficients agree almost exactly with experiment in the range T = 224 K to T = 300K. The effective pairwise potential also predicts the experimental height of the monolayer above the surface and the vibrational frequency against the surface. The translation and rotation of a single adsorbed particle are also monitored.

The molecular dynamics program has been extended in Chapter 4 to study the $\sqrt{3}$ x $\sqrt{3}$ solid methane adsorbed on graphite at a constant coverage of θ = 0.87. The configurational energies and specific heats are monitored, and respective changes in slope and discontinuities show that a slow phase transition occurs from 0 - 30K and a first order type of transition occurs at ≈ 90K. Centre of mass distribution

functions indicate that the solid structure persists above 52K, and the system has relaxed to a liquid above 100K. These results indicate that the low temperature transition is associated with a rotational phase change and the high temperature transition is due to some molecules leaving the surface, allowing the remaining bound molecules to relax into a quasi-2-dimensional fluid.

A quantitative analysis of the ordering in the solid is made by calculating the adsorbate-adsorbate, O_1, order parameter and the adsorbate-adsorbent, O_2 order parameter. The change in the O_1 order parameter as a function of temperature confirms the assignment of the phase transitions above. However anomalous behaviour is seen in the O_2 order parameter at low temperatures. Instead of observing a decay in the adsorbate-adsorbent order parameter as the temperature increases,the opposite trend occurs. In a small temperature range 10 - 25K the adsorbate-adsorbate interactions are not strong enough to randomize the translational motion of the methane and the barrier to translation is sufficiently low such that the adsorbate floats across the surface, resulting in a large O_1 but a small O_2 order parameter. It is possible that this phenomenon is an artifact of the simulation. The simulation result is reproducible but the question remains open whether the assumptions in the model cause the collective motion. In nature the adsorbate might exchange energy with the graphite to randomize the motion, and in addition real surfaces are not homogeneous and defects could destroy the collective nature of this motion.

This effect could be investigated by a neutron scattering experiment from Papyex (Thomas, 1981). There should be a measureable effect on the cross interference with the (10) reflection, and the Debye-Waller factor would contain a contribution that decreases as the temperature is raised above 20K. The simulation can be further extended to allow the first few layers of the graphite surface to move under the influence of the adsorbate and account for the effect of the coupling of the motion between the methane and graphite. The simplest model of a vibrating surface would be to join graphite sites by harmonic springs (McQuarrie, 1976).

The dynamical behaviour of the adsorbed monolayer has also been studied in Chapter 4, and compared to the phonon spectra of adsorbed methane on Vulcan and Papyex (Bomchil et al., 1980). In a homogeneous monatomic fluid the Fourier transform of the velocity auto-correlation function can be related to the incoherent structure factor. The incoherent scattering comes from the hydrogen atoms so that the spectra should be associated with the velocity auto-correlation function of the hydrogen atoms. However we expect the principal peaks in $S_s(0,\omega)$ to correspond to the peaks in the Fourier transforms of the velocity and angular auto-correlation functions. The velocity auto-correlation function is calculated parallel and perpendicular to the surface and the peaks in the Fourier transform of these functions confirm the assignment of the translational modes of motion in the spectra. Fourier transform of the angular velocity auto-correlation function has a number of peaks in common with the velocity auto-correlation

function but a peak at 68 cm^{-1} only appears in the librational motion and corresponds closely to the peak at 72 cm^{-1} in $S_s(0,\omega)$ which is assigned to rotational motion in the experimental spectra.

The reorientational motion in the monolayer is monitored and by analysis of the reorientation of vectors parallel and perpendicular to the surface it is observed that a slow rotational phase transition occurs from 0 - 30K. Above 30K the methane molecules are rotationally disordered. At low temperature the simulation enables us to infer there is little classical rotation and the spectra is the result of proton tunnelling.

In addition three methane molecules are scattered on top of the $\sqrt{3}$ x $\sqrt{3}$ monolayer at 30K. At this temperature it is observed that rotation is more strongly hindered for a single adsorbed molecule than for a molecule in the monolayer at the same temperature, and rotation is least hindered in the bilayer. These conclusions are in agreement with the qualitative description of rotation in adsorbed phases. The simulation program is at present constructed to simulate up to four adsorbed monolayers and further work could be undertaken to simulate multi-layer adsorption.

In Chapter 5 intermediate coverages of methane adsorbed on graphite are simulated in an attempt to unravel the various conflicting solid and liquid phases predicted by experiment (Coulomb et al., 1980; Vora et al., 1979). By monitoring the specific heat and configurational energy along an isochore at $\theta = 0.46$, and by calculating the C.O.M

distribution functions the model predicts a slow melting phase transition from 30K to 50K and the onset of a hypercritical fluid above 60K. Both experiments predict a solid S_I/gas phase up to 50K and an expanded solid S_{II}/gas phase between ≈ 50K and 60K; (the sets of results are slightly different in the exact assignment of the transition, see Figure 5.1). Above 56K Coulomb et al., postulate that there is a liquid/gas coexistence phase up to a critical point at 75K beyond which a hypercritical fluid exists. Vora et al., do not observe a liquid/gas phase and above 60K the fluid is hypercritical.

One route to determining the nature of the liquid phases is by monitoring the diffusion coefficient at constant temperature. If a liquid/gas phase coexists the diffusion coefficient is constant with a change in coverage, while in the hypercritical region the diffusion coefficient decreases with increasing coverage. The diffusion coefficients from the simulation show there is no gas/liquid coexistence but careful analysis of Coulomb et al., (1980) results indicates that their work has been interpreted correctly and a gas/liquid phase most likely exists in their system. The difference between the results may be due to the homogeneity of the surface in the model but it could also be due to the size of the system studied. The surface areas studied in the experiment are approximately forty times as large as the simulation cell and in these larger systems gas/liquid coexistence may be observed. A simpler simulation should be undertaken to study the effect

of system size on structure and diffusion. A simple model of Lennard-Jones discs in 2-dimensions could be studied. The LJ fluid would be placed as a cluster in the centre of the simulation cell of area ≃ 40000 $\mathring{A}^2$ with reflecting boundaries and the motion of the molecules monitored. Up to 1600 LJ particles would be needed to simulate the adsorbed liquid at a coverage of 0.5.

The statistical mechanical expression for the spreading pressure, a fundamental property describing an adsorbed fluid has been derived and the spreading pressure is reported over a wide range of temperature and coverage. Development of a surface pressure gauge which measures the spreading pressure directly is being undertaken by Beaume et al., and we await these experimental results to compare with the model calculations.

The structure of benzene adsorbed on graphite is studied in Chapter 6 by using numerical solutions in 2d to the OZ equation in the Percus-Yevick approximation. The coherent neutron scattering structure factor in the free rotor limit for benzene is derived. This limit allows us to describe the structure factor in terms of the centre-centre distribution function. There is only one experimental point in the liquid phase with which to compare our results. The theory is moderately successful in describing the structure; the first peak in S(q) is only slightly shifted from the experimental peak. The onset of the liquid phase in the experiment is above 150K and at these temperatures the benzene molecules

are rocking ± 20° from the inplane configuration (Meehan et al., 1980). This libration in the benzene allows closer packing of the molecules than if they were adsorbed flat discs. The experiment is also performed on Papyex which has a mozaic spread of ± 30° to the incident neutron beam and this may effect the exact position of the peaks in the spectrum. A better comparison with our model would be to perform the experiment on a more highly oriented substrate.

Appendix A

Program Listings:

MCPS	-	Monte Carlo simulation of the Penetrable Sphere Model.
MONOLAYER	-	Molecular Dynamics simulation of methane adsorbed on graphite. 4 adsorbed layers can be simulated.
PY	-	Solution to the Percus-Yevick equation for hard discs in the density range $\rho\sigma^2$ = 0.2 to 0.9 at intervals of 0.25.
PYEX	-	Solution to the Percus-Yevick equation at any density in the range $\rho\sigma^2$ 0.2 to 0.9 using the solutions of PY as an initial guess for y(r).
ROTBAR	-	The rotational barriers of methane adsorbed on graphite.
SQ	-	Structure factor of benzene adsorbed on graphite. The solutions of PYEX are used for g(r).
SURFACEONE	-	Molecular Dynamics simulation of one methane molecule adsorbed on graphite.
TPANALYSIS	-	Analysis of time dependent data stored on magnetic tape. Time correlation functions and diffusion properties are calculated.
VIRIAL	-	The surface second virial coefficient of methane adsorbed on graphite.

Accompanying material
stored separately.
Please check OLIS for
shelfmark

Bibliography

Abraham, F.F., Schreiber, D.E., Barker, J.A. (1975) J. Chem. Phys. 60, 1958.

Abramowitz, M., Stegun, A., (1975). A Handbook of Mathematical Functions, Dover, N.Y.

Alder, B.J., Wainwright, T.E. (1959) J. Chem. Phys. 31, 459.

Alder, B.J., Wainwright, T.E. (1962) Phys. Rev. 127, 359.

Alder, B.J., Wainwright, T.E. (1970) Phys. Rev. A1, 18.

Alder, B.J., Young, B.A., Mark, M.A. (1972) J. Chem. Phys. 56, 3013.

Andersen, H.C. (1980) J. Chem. Phys. 72, 2384.

Avgul, N.N., Kiselev, A.V. (1970) in Chemistry and Physics of Carbon Vol 6., Dekker, N.Y.

Bacon, G.E., 1977. Neutron Diffraction Newsletter, May, (Neut. Diff. Comm. Int. Union Crystallog.)

Barker, J.A., Henderson, D. (1967) J. Chem. Phys. 47, 4714.

Barojas. J., Levesque, D., Quentrec, B. (1973) Phys. Rev. A7, 1092.

Battezzati, L., Pisani, C., Ricca, F. (1975) J. Chem. Soc. Faraday II 71, 1629.

Beaume, R., Suzanne, J., Dash, J.G. (1980) Surface Sci. 92, 453.

Berne, B.J., Peccora, R., (1976) Dynamic Light Scattering, Wiley N.Y.

Bezus, A.G., Dreving, V.P., Kiselev, A.V. (1964) Russ. J. Phys. Chem. 38, 1589.

Bloom. M., Morrison, J.A. (1973) Chem. Soc. Spec. Per. Rep. Vol. 7, 140.

Bomchil, G., Huller, A., Rayment, T., Roser, S.J., Smalley, M.V., Thomas, R.K., White, J.W., (1980) Phil. Trans. R. Soc. London, B290, 537.

Chandler, D. (1978) Ann. Rev. Phys. Chem. 29, 441.

Chapela, G.A., Saville, G., Thompson, S.M., Rowlinson, J.S., (1977) J. Chem. Soc. Faraday II, 73, 1133.

Cheung, P.S.Y., Powles, J.G. (1975) Mol. Phys. 30, 921.

Cheung, P.S.Y., Powles, J.G. (1976) Mol. Phys. 32, 1383.

Cheung, P.S.Y. (1977) Mol. Phys. 33, 519.

Coulomb, J.P., Bienfait, M., Thorel, P. (1979) Phys. Rev. Lett. 42, 733.

Coulomb, J.P. , Bienfait, M., Thorel, P. (1980) J. de Physique. in press.

Crowell, A.D. (1958) J. Chem. Phys. 29, 446.

Crowell, A.D., Steele, R.B. (1961) J. Chem. Phys. 34, 1347.

Croxton, C.A. (1980) Statistical Mechanics of the Liquid Surface, Wiley, N.Y.

Dash, J.G. (1975) Films on Solid Surfaces, Academic Press, N.Y.

Dash, J.G., Suzanne, J., Shechter, H., Peierls, R.E. (1976) Surface Sci. 60, 411.

Dash, J.G., Suzanne, J., Shechter, H., Peierls, R.E. (1978) Surface Sci. 72, 219.

Dorfman, J.R., Van Beijeren (1977) Stat. Mech. B (ed. B.J. Berne) Plenum, N.Y., 65.

Evans, D.J., Watts, R.O. (1976) Mol. Phys.

Evans, D.J. (1977) Mol. Phys. 34, 317.

Everett, D.H. (1977) ed. Chem. Soc. Spec. Periodical Rep., Colloids Vol. 3.

Fehder, P.L., Emeis, C.A., Futrelle, R.A. (1971) J. Chem. Phys. 54, 4921.

Feller, W., (1950) An Introduction to Probability Theory and its Applications Vol. 1, Wiley, N.Y.

Feynman (1972) Statistical Mechanics a Set of Lecture Notes, Chapter 5, W.A. Benjamin Inc.

Freasier, B.C., Jolly, D., Bearman, R.J., (1976) Mol. Phys. 31, 255.

Frenkel, D., (1980) Intermolecular Spectroscopy and Dynamical Props. of Dense Systems, Proc. Int. School Physics "Enrico Fermi", LXXV, ed. J. Van Kranendonk.

Frenkel, D., McTague, J.P. (1980) Ann. Rev. Phys. Chem., 31, 491.

Gear, C.W. (1966) Argonne National Lab. Rep No ANL - 7126.

Giamano, E., Pisani, C., Ricca, F., Roetti, C., (1975) Surface Sci. 49, 401.

Gradshteyn, J.S., Ryzhik, I.M. (1965) Table of Integrals Series and Products, Academic Press, 480.

Griffiths, R.B., Wheeler, J.C. (1970) Phys. Rev. A2, 1047.

Gubbins, K.E., Gray, C.G., Egelstaff, P.A., Ananth, M.S. (1973) Mol. Phys. 25, 1353.

Guinier, A., 1963 X-ray Diffraction in Crystals, Imperfect Crystals and Amorphous Bodies, W. Freeman and Co., San Francisco.

Halsey, G.D. 1978 Surface Sci. 72, 1.

Hansen, J.P., (1973) Phys. Rev. A8, 3096.

Hansen, J.P., McDonald, I.R., (1976) Theory of Simple Liquids, Academic Press, London.

Hammmersley, J.M., Handscombe, D.C. (1964) Monte Carlo Methods, Wiley, N.Y.

Harp, G.D., Berne, B.J. (1970) Adv. Chem. Phys. 17, 63.

Heiney, P.A., Stephens, P.W., Birgeneau, R.J., Horn, P.M. (1980) Bull. Am. Phys. Soc. 25, 187.

Helfand, E., Stillinger, F.H. (1968) J. Chem. Phys. 49, 1232.

Helfand, E., Stillinger, F.H. (1972) J. Chem. Phys. 51, 1480.

Horn, P.M., Birgeneau, R.J., Heiney, P.A., Hammonds, E.M. (1978) Phys. Rev. Lett. 41, 961.

Huller, A., Kroll, D.M. (1975) J. Chem. Phys. 63, 4485.

Imry, Y., Gunther, L. (1971) Phys. Rev. B3, 3939.

Ising, E., (1925) Z. Physik, 31, 253.

James, H.M., Keenan, T.A. (1959) J. Chem. Phys. 31, 12.

Jansoone, V.M. (1974) Chem. Phys. 3, 78.

Killingbeck, J., Cole, G.H.A. (1971) Mathematical Techniques and Physical Applications, Academic Press, London.

Kiselev, A.V., Poshkus, D.P. (1963) Trans. Faraday Soc. 59, 428.

Kiselev, A.V., Poshkus, D.P. (1976) J. Chem. Soc. Faraday II. 72, 950.

Kitiagorodsky, A.E. (1973) Molecular Crystals, Academic Press, N.Y.

Kjems, J.K., Passell, L., Taub, H., Dash, J.G. (1974) Phys. Rev. Lett. 32, 724.

Klein, M.L., McDonald, I.R., O'Shea, S.F. (1978) J. Chem. Phys. 69, 63.

Klein, M.L., McDonald, I.R., O'Shea, S.F. (1979) J. Chem. Phys. 71, 298.

Lado, F., (1968) J. Chem. Phys. 49, 3092.

Lado, F., (1971) J. Comp. Phys. 8, 417.

Lane, J.E., Spurling, T.H. (1978) Aust. J. Chem. 31, 933.

Lal. M., Spencer, D. (1974) J. Chem. Soc. Faraday II, 70, 910.

Landau, L.D., Lifshitz, E.M. (1980) Statistical Physics 3rd Ed.
Pergamon, Oxford.

Lander, J.J., Morrison, J.A. (1967) Surface Sci. 6, 1.

Lebowitz, J.L., Percus, J.K., Verlet, J. (1967) Phys. Rev.
153, 250.

Lee, K.J., Barker, J.A., Pound, G.M. (1974) J. Chem. Phys. 60, 1976.

Lee, T.D., Young, C.N., (1952) Phys. Rev. 87, 410.

Leng, C.A., Rowlinson, J.S., Thompson, S.M. (1976) Proc. R. Soc.
London. A352, 1.

Levesque, D., Verlet, L. (1970) Phys. Rev. A2, 2514.

Levesque, D., Verlet, L., Kürkijarvi, J. (1973) Phys. Rev.
A7, 1690.

Lie, G.C., Clementi, E., Yoshimine (1976) J. Chem. Phys. 64, 2314.

Madden, P.A., Tildesley, D.J. (1981) Unpublished results.

Maki, K., O'Shea, S.F. (1980), J. Chem. Phys. 73, 3358.

Marlow, I., Thomas, R.K., Trewern, T.D., White, J.W. (1977)
J. Phys. (Paris) Colloq. 38, 3.

Mathews, E.A., Thomas, R.K. (1980) Unpublished results.

McDonald, I.R., Singer, K. (1972) Mol. Phys. 23, 29.

McDonald, I.R., Klein, M.L. (1976) J. Chem. Phys. 64, 4790.

McDonald, I.R., Klein, M.L. (1978) J. Chem. Phys. 68, 4875.

McDonald, I.R., O'Shea, S.F., Bounds, D.G., Klein, M.L.
J. Chem. Phys. 72, 5710.

McQuarrie, D.A., (1976) Statistical Mechanics, Harper and Bow, N.Y.

McTague, J.P., Nielsen, M., Passell, L. (1979) C.R.C. Critical Reviews in Solid State and Material Sci. 8, 125.

McTague, J.P., Nielsen, M., Passell, L. (1980) in Ordering in Strongly Fluctuating Condensed Matter Systems, ed. T. Risk, Plenum.

Meehan, P., Rayment, T., Thomas, R.K., Bomchil, G., White, J.W. (1980) R. Soc. Chem. Faraday I., 76, 2011.

Melnyk, T.W., Rowlinson, J.S., Sawford, B.L. (1972) Mol. Phys. 24, 809.

Mermin, N.D. (1968) Phys. Rev. 176, 250.

Metropolis, N., Rosenbluth, A.W., Rosenbluth, M.N., Teller, A.H., Teller, E. (1953) J. Chem. Phys. 27, 1087.

Murad, S., Gubbins, KE. (1978) Computer Modelling of Matter, ed. P. Lykos, A.C.S. Symposium Series Vol. 86, 62.

Murad, S., Evans, D.J., Gubbins, K.E., Streett, W.B., Tildesley, D.J. (1979) Mol. Phys. 37, 725.

Navescues, G. (1979) Rep. Prog. Phys. 42

Newbery, M.W., Rayment, T., Smalley, M.V., Thomas, R.K., White, J.W. (1978) Chem. Phys. Lett. 59, 461.

Nicolas, J.J., Gubbins, K.E., Streett, W.B., Tildesley, D.J. (1979) Mol. Phys. 37, 1429.

Novaco, A.D., McTague, J.P. (1979) Phys. Rev. B20, 2469.

Nezbeda, I., Boublik, T., Hlavaty, K. (1980) Statistical Thermodynamics of Simple Liquids and their Mixtures, Elsevier, Amsterdam.

Onsager, L. (1944) Phys. Rev. 65, 117.

O'Shea, S.F., Klein, M.L. (1979) J. Chem. Phys. 71, 2339.

Paneth, F., Radu, A. (1924) Chem. Ber. 57, 1221.

Parsonage, N.G., Staveley, L.A.K. (1978) Disorder in Crystals, O.U.P., Oxford, 1572.

Peierls, P.E. (1935) Ann. Inst. Henri Poincare. 5, 177.

Percus, J.K., Yevick, G.J. (1958) Phys. Rev. 110, 1.

Percus, J.K. (1964) in the Equilibrium Theory of Classical Fluids, ed. H.L. Firsh, J.L. Lebowitz, Benjamin, N.Y., II - 33.

Powles, J.G., Rickayzen, G. (1979) Mol. Phys. 38, 1975.

Pryde, J.A. (1969) The Liquid State, Hutchinson U.P. London.

Quentrec, B. (1974) Thesis No. 1197, Orsay, France.

Rahman, A. (1964) Phys. Rev. A136, 405.

Ramadas, S., Thomas, J.M. (1978) Chem. Soc. Spec. Per. Rep., Chemical Physics of Solids and their Surfaces, Vol 7.

Rayment, T. (1981) Private Communication.

Rosenfeld, Y., Thieberger, R., (1975) J. Chem. Phys. 63, 1875.

Rowley, L.A., Nicholson, D., Parsonage, N.G. (1976) Mol. Phys. 31, 365.

Rowley, L.A., Nicholson, D., Parsonage, N.G. (1976) Mol. Phys. 31, 384.

Rowlinson, J.S. (1969) Liquids and Liquid Mixtures, Butterworth, London.

Rowlinson, J.S. (1980) Adv. Chem. Phys. 41, 1.

Sams, J.R., (1965) J. Chem. Phys. 43, 2243.

Sams, J.R., Constabaris, G., Halsey, G.D., (1960) J. Am. Chem. Soc. 64, 1689.

Sears, V.F., (1966) Can. J. Phys. 44, 1279.

Shechter, H., (1977) J. Physique Colloq. C4, 38.

Shechter, H., Suzanne, J., Dash, J.G., (1979) J. Physique. 40, 467.

Singer, K., Taylor, A., Singer, J.V.L., (1977) Mol. Phys. 33, 1757.

Smith, E.B., Lea, K.R., (1963) Trans. Faraday Soc. 59, 1538.

Smith, E.R., Perram, J.W., (1975) Mol. Phys. 30, 31.

Specovius, J., Findenegg, G.H., (1978) Ber. Bunsenges. Phys. Chem. 82, 174.

Steele, W.A., (1974) Int. Encyc. of Phys. Chem. and Chem. Phys., The Interaction of Gases with Solid Surfaces, Pergamon, Oxford.

Stillinger, F.H., Rahman, A., (1974) J. Chem. Phys. 60, 1545.

Streett, W.B., Gubbins, K.E., (1977) Ann. Rev. Phys. Chem. 28, 373.

Streett, W.B., Tildesley, D.J., Saville, G., (1978) Computer Modelling of Matter, ed. P. Lykos, A.C.S. Symposium, Vol 86, 144.

Stroud, A.H., (1971) Approximate Calculation of Multiple Integrals, Prentice Hall, 229.

Tabony, J., (1980) Progress in NMR Spectroscopy (Ed. Emersley Feeney, Sutcliffe), Pergamon, Oxford.

Tabony, J., Cosgrove, T., (1979) Chem. Phys. Lett. 67, 103.

Tabony, J., White, J.W., Coulon, M., De la Chaume, J.C., (1980) in press.

Temperley, H.N.V., Rushbrooke, G.S., Rowlinson, J.S. eds. (1968) Physics of Simple Liquids, Nth. Holland Amsterdam.

Tildesley, D.J., Streett, W.B. (1980) Mol. Phys. 41, 85.

Tildesley, D.J. (1980) Mol. Phys. 41, 341.

Thomas, R.K. (1981) Private Communication.

Thompson, S.M. (1976) D. Phil. Thesis, Oxford University.

Thomy, A., Duval, X. (1970) J. Chim. Phys. 67, 1101.

Toxvaerd, S., (1975) J. Chem. Phys. 62, 1589.

Toxvaerd, S., (1979) Phys. Rev. Lett. 43, 529.

Thiele, E. (1963) J. Chem. Phys. 39, 474.

Valleau, J.P., Torrie, G.M. (1977) in Modern Theoretical Chemistry Vol. 5 ed. B.J. Berne, Plenum, Ch. 5.

Van Hove, L. (1954) Phys. Rev. 95, 249.

Verlet, L. (1967) Phys. Rev. 159, 98.

Verlet, L. (1968) Phys. Rev. 163, 201.

Verlet, L., Levesque, D. (1967) Physica. 36, 254.

Verlet, L. (1970) see Levesque (1970).

Verlet, L. (1973) see Levesque (1973).

Viellard-Baron, J. (1972) J. Chem. Phys. 56, 4729.

Vilches, O.E., (1980) Ann. Rev. Phys. Chem. 31, 463.

Vora, P., Shina, S.K., Crawford, R.K. (1979) Phys. Rev. Lett. 43, 704.

Weissmann, M., Cohen, N.V. (1980) J. Chem. Phys. 72, 4562.

Wertheim, M.S. (1963) Phys. Rev. Lett. 10, 321.

Wertheim, M.S. (1964) J. Math. Phys. 5, 643.

White, J.W., Thomas, R.K., Trewern, T., Marlow, I., Bomchil, G., (1978) Surface Sci. 76, 13.

Widom, B., Rowlinson, J.S., (1970) J. Chem. Phys. 52, 1670.

Williams, D.E., (1966) J. Chem. Phys. 45, 3770.

Williams, D.E., (1967) J. Chem. Phys. 47, 4680.

Wood, W.W., Parker, F.R., (1957) J. Chem. Phys. 27, 720.

Wood, W.W., (1959) Proc. Int. Joint Comp. Conf.

Wood, W.W., (1975) Fundamental Problems in Stat. Mech, III, Proc. Int. Summer School Fundam. Stat. Mech. III, The Netherlands, 1974, ed. E.D.G. Cohen, Nth Holland Amsterdam.

Wood, W.W., Erpenbeck, J.J., (1976) Ann. Rev. Phys. Chem. 27, 319.

Wood, W.W., (1963) Los Alamos Scientific Lab. Rep. LA-2827.

Young, D.A., Alder, B.J., (1974) J. Chem. Phys. 60, 1254.

Yvon, J., (1958) Suppl. Nuovo Cimento. 9, 144.

Zwanzig, R., Ailawadi, N.K., (1969) Phys. Rev. 182, 280.